

DESIGNING AND OPTIMIZING GRATINGS FOR SOFT X-RAY DIFFRACTION EFFICIENCY

A Thesis Submitted to the
College of Graduate Studies and Research
in Partial Fulfillment of the Requirements
for the degree of Doctor of Philosophy
in the Department of Physics and Engineering Physics
University of Saskatchewan
Saskatoon

By

Mark Boots

©Mark Boots, May 2013. All rights reserved.

PERMISSION TO USE

In presenting this thesis in partial fulfilment of the requirements for a Postgraduate degree from the University of Saskatchewan, I agree that the Libraries of this University may make it freely available for inspection. I further agree that permission for copying of this thesis in any manner, in whole or in part, for scholarly purposes may be granted by the professor or professors who supervised my thesis work or, in their absence, by the Head of the Department or the Dean of the College in which my thesis work was done. It is understood that any copying or publication or use of this thesis or parts thereof for financial gain shall not be allowed without my written permission. It is also understood that due recognition shall be given to me and to the University of Saskatchewan in any scholarly use which may be made of any material in my thesis.

Requests for permission to copy or to make other use of material in this thesis in whole or part should be addressed to:

Head of the Department of Physics and Engineering Physics

Rm 123 Physics Building

116 Science Place

University of Saskatchewan

Saskatoon, Saskatchewan

Canada

S7N 5E2

ABSTRACT

The *diffraction efficiency* is critical to the speed and sensitivity of grating-based spectroscopy instruments. This becomes particularly important for soft x-ray instruments, used on material science beamlines at synchrotrons around the world, where the low reflectivity of materials makes it challenging to create efficient optics.

The efficiency of soft x-ray gratings is examined from a rigorous electromagnetic approach, using the differential method of Neviere et. al. [43], adapted for deep gratings using the S-matrix propagation algorithm devised by Li [28][41]. New software is written to provide an open-source implementation with fast performance on cluster computing resources. Trends in diffraction efficiency are examined as a function of grating materials, coatings, groove geometry, and incidence conditions; these trends are used to provide recommendations for instrument design, including the identification of a new principle of optimal incidence angle.

Efficiency calculations and optimizations are applied to the design of a high-performance soft x-ray emission spectrometer for the REIXS beamline at the Canadian Light Source. The process produces an innovative design that exploits an efficiency peak in the third diffraction order to offer higher resolution than would otherwise be possible given the space constraints of the machine. Finally, the spectrometer's actual gratings are measured for diffraction efficiency as a function of wavelength. Although the real-world efficiencies differ substantially from the nominal calculations, the differences are explained by incorporating real-world effects: geometry errors, groove variation, oxidation, and surface roughness. A fitting process is proposed to match the calculated to the measured efficiency spectra. The geometry parameters predicted by the fitting process are found to agree exactly with atomic force microprobe (AFM) measurements for all the gratings studied. Because each grating parameter affects the shape of the efficiency spectrum in a different way, the spectrum can be considered as a unique “fingerprint” or “hash”; we conclude that this might be extended to use efficiency measurements and fitting calculations to characterize grating parameters that are difficult or impossible to measure directly.

ACKNOWLEDGEMENTS

The work described in this thesis represents the collaborative effort of many individuals, as well as the support and encouragement of many others; it has been a privilege to work with and learn from all of them.

In particular, it was my pleasure to work with David Muir along the entire journey from initial design concepts, through seemingly-endless technical problems, to the point of finally using an actual, working emission spectrometer. His undefeatable commitment and insights made the machine possible. (We joke that both of us are married to her, but that I never loved her the way he does.)

I am also extremely grateful to my supervisor, Alex Moewes, for providing a deft balance between setting challenges, issuing guidance, and providing the freedom to explore. The continuous encouragement and light-hearted pressure provided by the members of the material science research group (“*Does it work yet?*”) are also appreciated. I am grateful to Elder Matias, my supervisor in the controls group at the Canadian Light Source, for providing the flexibility and understanding that allowed me to finish this degree while simultaneously contributing to the instrumentation and software on the beamline. Finally, Professor Raymond Spiteri in the Computer Science department provided invaluable help as I was writing the numerical implementation of the grating software.

The real-world efficiency and AFM measurements, critical to many of the conclusions in this thesis, were only possible through the help of Dr. Eric Gullikson at Beamline 6.3.2 of the Advanced Light Source. The optimization and fitting calculations used computing resources provided by WestGrid (www.westgrid.ca) and Compute/Calcul Canada. I also gratefully acknowledge the funding provided by the NSERC undergraduate and postgraduate scholarship programs.

On a personal level, I am extremely grateful to Kelly Paton for inspiration, mathematical skill, and dedicated editing, as well as Scott Borys for irreplaceable and timely help developing the web application of the grating software. Last but most of all, I lack appropriate words to thank Joanne Newman for her endless encouragement, support, and love.

CONTENTS

Permission to Use	i
Abstract	ii
Acknowledgements	iii
Contents	iv
List of Tables	vii
List of Figures	viii
List of Abbreviations	xiv
1 Introduction	1
2 Motivation: Why grating efficiency matters	3
2.1 Soft x-ray spectroscopy techniques	7
2.1.1 Absorption spectroscopy	7
2.1.2 Emission spectroscopy	9
2.1.3 Importance of soft x-ray spectroscopy (SXS)	11
2.2 Spectroscopy instrumentation	13
2.2.1 Beamline optics: monochromators and spectrometers	14
2.2.2 Goals for soft x-ray instruments	18
2.2.3 Challenges of soft x-ray applications	22
2.3 REIXS spectrometer project	24
2.4 Summary: why grating efficiency matters	25
3 Theory: How to calculate grating efficiency	28
3.1 Introduction to grating theory	28
3.1.1 A brief history of grating theory	29
3.1.2 Comparison and applicability of grating theory families	31
3.1.3 Overview of the differential theory	38
3.1.4 Simplifying assumptions	43
3.1.5 Electromagnetic field and polarization	45
3.1.6 Maxwell's equations for sinusoidal time-varying fields	46
3.1.7 Periodicity of gratings and fields (Pseudo-periodic functions and the Fourier basis)	48
3.1.8 Deriving the Grating Equation	50
3.2 Defining Grating Efficiency	56
3.3 Solving for efficiency	60

3.3.1	Representing the grating	60
3.3.2	Matrix Formulation of Numerical Solution: Inside the Grooves	62
3.3.3	Boundary conditions at the top and bottom of the grooves	62
3.3.4	Solution implementation: The Shooting Method	63
3.3.5	Integration of growing exponentials: The S-matrix method	65
3.4	Interaction of X-rays and materials	75
3.4.1	Atomic scattering factors and the refractive index	76
3.4.2	Sensitivity of efficiency calculations to errors in the refractive index	79
4	Implementation of theory: How we calculated efficiency using computers	81
4.1	Pre-existing grating efficiency software	81
4.2	Improving the usability and efficiency of <code>Gradif</code>	82
4.2.1	Visual interface to the <code>Gradif</code> code	83
4.2.2	Detecting integration failures	87
4.2.3	Online access	89
4.3	Improved, open-source grating efficiency software	89
4.3.1	Motivation for new grating software	89
4.3.2	Features and limitations	90
4.3.3	Obtaining and running the new software	97
4.3.4	Parallel program design and performance	98
4.3.5	Validation of the new software	104
5	Trends: How different factors affect the grating efficiency	111
5.1	Effect of grating profile: groove shape	112
5.1.1	Note on grating manufacturing techniques	112
5.1.2	Profile geometry	117
5.1.3	Blazed optimization for triangular gratings	117
5.1.4	Efficiency comparison of common profiles	119
5.2	Effect of groove density	121
5.3	Effect of coating thickness	122
5.4	Comparison of coating materials	126
5.5	Effect of photon energy / wavelength	129
5.6	Effect of incidence angle	129
5.6.1	Optimal incidence for rectangular gratings	133
5.6.2	Optimal incidence for blazed gratings	138
5.7	Effect of anti-blaze angle for blazed gratings	139
5.8	Applications to beamline and instrument design	139
5.9	Validation: comparison of theory to experimental results	141
5.9.1	Note on incidence angle	142
5.9.2	Comparison to theory	142
6	Design: How we applied these tools to make the REIXS spectrometer optical design	147
6.1	Application to spectrometer design	147
6.1.1	Design goals	147

6.1.2	Comparative examples	149
6.2	Design Process	150
6.2.1	Justification of design choices	153
6.3	High resolution (3rd order) design	158
6.3.1	Options for reaching extreme resolution	158
6.3.2	Justification for 3rd order design	159
6.4	Coating choices	160
6.5	Tolerancing	162
6.6	Summary of final design	162
7	Characterization: How we measured the actual grating performance, and accounted for differences	168
7.1	AFM measurements of the manufactured grating profile	169
7.2	Diffractometer measurements of actual grating efficiency	172
7.2.1	Beamline 6.3.2 reflectometer	174
7.2.2	Diffraction experiment procedure	175
7.2.3	Sources of error	182
7.3	Real-world grating effects	186
7.3.1	Stray radiant energy	187
7.3.2	Manufacturing errors that <i>can</i> be modelled	194
7.4	Grating results, fitting, and comparison to theoretical efficiencies	197
7.4.1	Low Energy Grating (LEG)	198
7.4.2	Impurity Grating (IMP)	200
7.4.3	Medium Energy Grating (MEG)	203
7.4.4	High Energy Grating (HEG)	205
7.4.5	High resolution third-order gratings	208
8	What next: Real-world results and opportunities for future work	211
8.1	Spectrometer assembly, commissioning, and preliminary results	211
8.2	Future work: confirmation and extension of the fitting process	214
8.3	Future work: Efficiency calculation improvements and software-as-a-service .	216
References		218

LIST OF TABLES

4.1	Comparison of commercially-available grating efficiency software	82
4.2	Input command line arguments for the <code>pegSerial</code> and <code>pegMPI</code> programs.	99
4.3	Output file format for the <code>pegSerial</code> and <code>pegMPI</code> programs.	100
4.4	Time profile measurements of solver operations, averaged over 5 runs in single-threaded mode.	102
4.5	The run time, speedup, and efficiency attained using OpenMP fine-grained parallelization on a single <code>bugaboo</code> node using up to 12 processors.	104
4.6	The run time, speedup, and efficiency attained using MPI coarse-grained parallelization on the <code>bugaboo</code> cluster using 1 to 32 processors.	105
5.1	Critical incidence angles for “total external reflection” at 410 eV for the mirror and grating coatings shown in Figure 5.12.	131
5.2	Geometry parameters and incidence configuration for the gratings in Figures 5.19 to 5.22.	142
6.1	Gratings chosen for the REIXS spectrometer, with their target energies used for optimization, the energy ranges they will be able to cover, and the final optimized grating parameters	151
6.2	Predicted resolving power (RP, $E/\Delta E$) and grating efficiency (Eff) of the REIXS spectrometer at the emission lines of interest.	167
7.1	For higher-order suppression, Beamline 6.3.2 has a variable-incidence mirror and a set of transmission filter elements. The mirror coating, mirror angle, and filter need to be selected based on the energy range of the scan.	184
7.2	Comparison of actual and predicted grating parameters, using fitting to match the calculated efficiency spectra to the measured curves.	207

LIST OF FIGURES

2.1	Early spectroscopy would have involved long hours squinting through telescope eyepieces at barely visible lines.	4
2.2	A sensitive, compact, visible light spectrometer (Ocean Optics USB4000-UV-VIS).	5
2.3	X-ray absorption spectroscopy probes the density of <i>unoccupied</i> electronic states, modified by the presence of a core-hole: a vacancy left behind by the excited electron.	8
2.4	In this schematic of a grating monochromator, light from the source is focussed by mirrors and dispersed by the grating. An exit slit picks out the desired wavelength or energy range, and blocks the remaining light.	14
2.5	In this schematic of a grating spectrometer, mirrors are used to focus light from the source (or entrance slit) onto the detector.	15
2.6	The spectrometer in this schematic uses a curved grating to both disperse light by wavelength, and focus it onto the detector.	15
2.7	The Petersen Plane Grating Monochromator, as implemented on the HEPGM-3 beamline at BESSY.	17
2.8	The SXF endstation spectrometer on Beamline 8.0.1 of the Advanced Light Source.	19
2.9	A detector image and corresponding spectrum produced by the SXF spectrometer in Figure 2.8.	19
2.10	The spectrometer detector has an effective spatial resolution dx which is the minimum distance required to resolve two adjacent incident rays. To increase the spacing between adjacent wavelengths on the detector, we can either increase the grating-detector distance r' , or increase the angular dispersion. . .	21
2.11	The REIXS XES spectrometer, as built, in August 2012.	26
2.12	A variety of soft x-ray spectroscopy techniques, and the number of gratings required in the beam path to accomplish each one.	27
3.1	A one-dimensional grating with in-plane incidence.	28
3.2	The modal method and the RCW method approximate every real grating as a stack of rectangular gratings.	34
3.3	A visual comparison of the limitations and strengths of the main methods in grating theory.	37
3.4	Arbitrarily-complicated structures can be handled by dividing the grating into layers, where each layer is either homogenous (constant refractive index), or modulated (with a refractive index that changes periodically as a function of x at any given height y).	41
3.5	Modulated layers in a complicated stack of gratings. In between every layer, we can insert an imaginary, infinitely-thin homogenous layer where the Rayleigh expansion applies.	42

3.6	The Rayleigh expansion describes the electric field (TE polarization) or magnetic field (TM polarization) in homogenous media, above and below the grating.	53
3.7	The total electromagnetic flux through this highlighted area (Q_2) is used to define the grating efficiency of a diffraction order n , as the ratio of the flux of the diffracted wave $\bar{S}_n^{(2)}$ compared to the incident wave $\bar{S}^{(2)}$.	58
3.8	The $k^2(x, y)$ function for a simple groove profile.	61
3.9	Using the S-matrix method, thick gratings are divided into layers, where each layer is thin enough to avoid losing numerical significance during integration.	66
3.10	Comparison of a measured reflection curve around the total reflection cutoff region from a silicon(111) wafer under 1487 eV radiation, with that predicted by the Fresnel equations using atomic scattering factors from the Henke tables.	78
3.11	Experimental photoabsorption data for the CO ₂ molecule, compared with a plot calculated using the vector sum of atomic photoabsorption cross sections from the Henke tables.	78
3.12	Consistent overestimation or underestimation of the refractive index changes the magnitude, but not the overall shape, of the efficiency spectrum.	80
4.1	This web application provides a graphical user interface for calculating grating efficiencies. Forms prompt users for the grating parameters.	84
4.2	This web application provides a graphical user interface for calculating grating efficiencies. The results are plotted, and users can download a text-based table for further analysis.	86
4.3	This Options page configures the numerical precision of the calculations, the diffraction orders of interest, and the polarization of the incident light.	88
4.4	The difference in efficiency between TE and TM polarization is very small for grazing-incidence optics.	94
4.5	At more normal incidence, the efficiency is different for TE and TM polarization.	95
4.6	The S-matrix approach is the solution for this problem that becomes unstable at high energies when using the basic shooting method.	108
4.7	Shown over a range of coating thicknesses, the new software agrees with Gradif results to more than three significant figures.	110
5.1	5 common groove profiles and their geometry parameters.	113
5.2	Henry Rowland, supervising his mechanical engine ruling a grating.	114
5.3	The MIT ‘B’ ruling engine, now owned and operated by Richardson Gratings (a division of the Newport Corporation).	115
5.4	Master gratings can be replicated using a resin that hardens while in contact with the master (or subsequently, a submaster replicated from the first master).	116
5.5	The Sheridan technique for recording pseudo-blazed holographic gratings uses a single light beam reflected back on itself to make a regular interference pattern of standing waves. The master substrate consists of a <i>transparent</i> photoresist material that is hardened or weakened by exposure to the light.	117

5.6	In the blazed condition, the desired order diffraction angle – in this case, 1st order – is aligned with the direction of specular reflection off the groove surfaces. The angle at the base of the large facet is the <i>blaze angle</i> θ_b ; the angle at the base of the opposite facet is the <i>anti-blaze angle</i> θ_{ab}	119
5.7	0th order, 1st order, and 2nd order efficiency of three different groove profiles, all optimized for use at 400 eV.	120
5.8	Increasing the groove density always decreases the diffraction efficiency – at least for all the useful orders ($n \neq 0$).	123
5.9	0th order, 1st order, and 2nd order efficiency as a function of energy, for a range of groove densities from 300 to 2700 lines/mm. As the groove density increases, the maximum achievable efficiency drops, but the bandwidth of the blaze-optimization peak becomes wider.	124
5.10	In the soft x-ray regime under grazing incidence, metal-coated dielectric gratings are indistinguishable from pure metal gratings... as long as the coating is thicker than ~ 20 nm.	125
5.11	The reflectivity of a pure mirror at grazing incidence (88°), as a function of photon energy.	127
5.12	A comparison of the mirror reflectivity, 0th order, and 1st order efficiency for different coating materials, as a function of photon energy.	128
5.13	The reflectivity of a perfect platinum mirror as a function of incidence angle at 410 eV, calculated using the complex refractive index and the complex Fresnel equations.	131
5.14	The effect of incidence angle on diffraction efficiency for various grating profiles. While the 0th order efficiency/reflectivity always increases as the incident light becomes more grazing, there is an optimal incidence angle below 90° for higher-order light.	134
5.15	While the blaze angle can always be used to tune a grating for a required incidence angle, there is still a particular <i>optimal</i> incidence angle that – when combined with a corresponding optimized blaze angle – would produce the highest achievable efficiency.	135
5.16	Optimizing the incidence angle and groove geometry for a range of wavelengths and grating periods shows a $n = -1$ order maximum at the $n = +1$ order Wood anomaly: $\sin \theta_{max} = 1 - \lambda/d$	136
5.17	Unlike rectangular gratings, the optimal incidence angle for blazed gratings (marked points) does not follow the curve for the +1 order Wood Anomaly (dashed lines).	138
5.18	These calculations over a range of anti-blaze angles show that as long as the anti-blaze angle is greater than ~ 4 times the blaze angle, it has almost no effect on the efficiency.	139
5.19	Comparison of grating efficiency calculations to diffractometer measurements. Blazed grating, 1440 lines/mm, 2.2° blaze angle, 12.8° anti-blaze angle. Incidence: 160° constant included angle to the 1st inside order.	143
5.20	Comparison of grating efficiency calculations to diffractometer measurements. Rectangular grating, 600 lines/mm, 22.2 nm depth, 1.12 um valley width. Incidence: 167° constant included angle to the 1st inside order.	144

5.21 Comparison of grating efficiency calculations to diffractometer measurements. Trapezoidal grating, 300 lines/mm, 57° side angles, 49.3 nm depth, 2.46 um valley width. Incidence: 167° constant included angle to the 1st inside order.	145
5.22 Comparison of grating efficiency calculations to diffractometer measurements. Trapezoidal grating, 390 lines/mm, 57° side angles, 54 nm depth, 1.39 um valley width. Incidence: 160° constant included angle to the 1st inside order.	146
6.1 Resolving power performance comparison of existing spectrometer designs, calculated with all detectors having a 20 um pixel size.	150
6.2 Approximation of the process used to design the optics of the REIXS spectrometer.	152
6.3 The focal curve is the path in space the detector needs to move along to maintain focussing as a function of energy. This plot shows the effect of the b_2 VLS correction term.	155
6.4 Variable line space (VLS) corrections reduce aberrations that cause curvature, as seen in these ray-traced detector images of three adjacent emission lines. However, the increase in resolution due to better focussing is not able to make up for reduced dispersion across the surface of the detector.	156
6.5 Common errors in the manufacture of ruled and holographic gratings.	156
6.6 Justification for third-order design: At some points along the efficiency curve, the grating efficiency is actually higher in 3rd order than it would be in 1st order for an equivalent-resolution grating with three times the groove density.	161
6.7 The REIXS spectrometer design offers higher predicted resolution than the existing designs we surveyed in Figure 6.1.	163
6.8 Theoretical diffraction efficiency for the Low Energy Grating and Impurity Grating.	164
6.9 Theoretical diffraction efficiency for the Medium Energy and High Energy Gratings.	165
6.10 Theoretical diffraction efficiency for the High Resolution Gratings, optimized to be used in 3rd order.	166
7.1 Schematic diagram of an Atomic Force Microprobe (AFM), and a Scanning Electron Microscope image of the tip, showing a radius of approximately 10 nm.	170
7.2 The Low Energy Grating has a smooth regular profile, shown in this example image measured using an Atomic Force Microprobe (AFM).	171
7.3 The Calibration and Standards Beamline (6.3.2) at the Advanced Light Source consists of a bending magnet source, a VLS-PGM monochromator with three selectable gratings, a higher-order suppressor, and a two-circle reflectometer.	172
7.4 The reflectometer on Beamline 6.3.2 at the Advanced Light Source allows for independently setting the angle of the gratings in the beam, and setting the angle of a pinhole photodiode detector.	173
7.5 Reflectometer coordinates: the sample angle is measured up from grazing incidence, and the detector angle is measured up from grazing incidence.	174
7.6 The simplest diffractometer experiment scans the detector angle while illuminating the grating with a constant photon energy.	179

7.7	When the groove density of a grating is accurately known, the detector angle can be moved in tandem with the monochromator energy to keep it on the diffraction peak as the incident photon energy is scanned.	180
7.8	Roughness of the grating surface scatters stray light outside the diffraction orders. Typically, surface roughness is responsible for most of the reduction in real-world grating efficiency, compared to theoretical calculations.	188
7.9	The reflectivity factor calculated according to the Sinha expression (7.3) as a function of incidence angle and photon energy, assuming a refractive index of platinum.	191
7.10	A comparison of the Beckmann (solid) and Sinha (dashed) expressions for rough surface reflectivity shows the limitations of both approximations. . . .	192
7.11	Unprotected nickel quickly forms a surface oxide of NiO, which significantly reduces the reflectivity at the Oxygen edge (543 eV)	196
7.12	AFM measurements of the Low Energy Grating (LEG) profile, averaged along the grooves (10 um × 10 um). The best-fit blaze angle at the centre of the grating is $2.45^\circ \pm 0.20^\circ$	199
7.13	The blaze angle error of the manufactured LEG causes the efficiency peak to shift down in energy, and causes a transfer of energy from the first order to the second order. The fitting process predicts a blaze angle of 2.35° and an RMS roughness of 0.025 nm. (This assumes scaling factors of 0.93 and 0.84 for the first and second order respectively.) The predicted blaze angle agrees within error with the AFM estimate (2.45°).	200
7.14	When using a common scaling factor for fitting the LEG, we predict a blaze angle of 2.26° and a scaling factor of 0.95. However, this method provides less agreement and a less accurate blaze prediction than using independent scaling factors (Figure 7.13).	201
7.15	AFM measurements of the Impurity Grating (IMP) profile, averaged along the grooves (10 um × 10 um). The best-fit blaze angle at the centre of the grating is $1.60^\circ \pm 0.11^\circ$	201
7.16	Theoretical and measured efficiency of the Impurity Grating (IMP). The best-fit theoretical curve predicts a blaze angle of 1.65° , an anti-blaze angle of 5° , a 2.0 nm oxide layer, and an RMS roughness of 0.5 nm. (This assumes that the first order calculated efficiency is scaled by 0.91, and the second order is scaled by 0.62.) The fitting prediction agrees closely with the AFM estimate of the blaze angle (1.60°).	202
7.17	Using a common scaling factor for the first-order and second-order efficiency curves reduces the fitting accuracy and reduces the agreement between the predicted and AFM estimated blaze angles. For the impurity grating (left), this process predicts a 1.40° blaze angle, a 7 nm NiO surface layer, and a scaling factor of 0.9. For the MEG (right), it predicts a 1.7° blaze angle, a 4.5 nm NiO layer, and a scaling factor of 0.7.	203
7.18	AFM measurements of the Medium Energy Grating (MEG) profile, averaged along the grooves (5 um × 5 um). The best-fit blaze angle at the centre of the grating is $2.04^\circ \pm 0.22^\circ$	204

7.19	The real-world efficiency of the MEG can be explained by the fitting process, which predicts a blaze angle of 1.95° , an anti-blaze angle of 30° , a 1 nm coating of nickel oxide (NiO), and a surface roughness of 0.1 nm RMS. The scaling factors for first and second order are 0.70 and 0.37 respectively.	204
7.20	Theoretical and measured efficiency of the High Energy Grating (LEG). The solid theoretical curves were calculated using an arbitrary groove shape based on the AFM measurements (Figure 7.22). It cannot fully explain the reduction in real-world efficiency; therefore, we attribute the poor performance to groove-to-groove variation and scatter that we cannot model using the differential method.	205
7.21	AFM measurements of the High Energy Grating (HEG) profile, averaged along the grooves (5 um x 5 um). Severe ruling errors were apparent. The profile wasn't sufficiently triangular to attempt to fit a blaze angle, so we extracted one of the groove shapes to model as an arbitrary profile (Figure 7.22). . . .	206
7.22	Representative profile used to model the real-world HEG, extracted from the AFM measurements in Figure 7.21.	206
7.23	AFM measurements of the HighRes Medium Energy Grating (HRMEG) profile, averaged along the grooves (5 um x 5 um). The best-fit blaze angle at the centre of the grating is $4.43^\circ \pm 0.30^\circ$	209
7.24	AFM measurements of the HighRes High Energy Grating (HRHEG) profile, averaged along the grooves (3 um x 3 um). The best-fit blaze angle at the centre of the grating is $6.34^\circ \pm 0.28^\circ$	210
8.1	Nitrogen K α emission line of hexagonal boron nitride (hBN), taken using the IMP grating in 20 minutes. Total counts: 1892380.	213
8.2	Nitrogen K α emission line of hexagonal boron nitride (hBN), taken using the MEG. It offers the possibility for higher resolution than the IMP (Figure 8.1) at the expense of efficiency. (The energy axis for this plot is not calibrated.) Total counts: 288792.	214
8.3	Nitrogen K α emission line of hexagonal boron nitride (hBN), taken using the HRMEG in third order. The low count rate requires long count times; however, temperature shifts in the room cause the central detector energy to shift over this time, reducing the resolution. Work is still ongoing to focus the spectrometer for operation with the HRMEG, as well as stabilize the room temperature. Total counts: 112973.	215

LIST OF ABBREVIATIONS

AFM	Atomic Force Microprobe
API	Application Programming Interface
CEM	Channel Electron Multiplier
CIA	Constant Included Angle
EC2	Elastic Cloud Compute
EELS	Electron Energy Loss Spectroscopy
EUV	Extreme Ultra-violet
EXAFS	Extended X-ray Absorption Fine Structure
GUI	Graphical User Interface
HEG	High Energy Grating
HPC	High-performance Computing
HRHEG	High-Resolution High Energy Grating
HRMEG	High-Resolution Medium Energy Grating
IMP	Impurity Grating
IPES	Inverse Photoelectron Spectroscopy
LEG	Low Energy Grating
MEG	Medium Energy Grating
MIM	Modified Integral Method
MPI	Message Passing Interface
NEXAFS	Near-edge X-ray Absorption Fine Structure
PGM,	Plane Grating Monochromator
PSD	Power Spectral Density
RCW	Rigorous Coupled Wave
REIXS	Resonant Elastic And Inelastic X-ray Scattering
RIXS	Resonant Inelastic X-ray Spectroscopy
SRE	Stray Radiant Energy
SXE	Soft X-ray Emission Spectroscopy
SXS	Soft X-ray Spectroscopy
TER.	Total External Reflection
TEY	Total Electron Yield
TFY	Total Fluorescence Yield
TIR	Total Internal Reflection
UHV	Ultra-high Vacuum
VLS	Variable Line Spacing
XEOL	X-ray Excited Optical Luminescence
XPS	X-ray Photoelectron Spectroscopy

CHAPTER 1

INTRODUCTION

The *diffraction grating* is an optical component that exploits interference from a periodic surface of parallel grooves to control light based on its wavelength. For almost two hundred years, diffraction gratings have been – and still are – at the heart of many instruments responsible for breakthroughs in scientific understanding. Today, they are used in astronomy telescopes, chemistry spectrographs, spectrophotometers for life science, and in optics for material science experiments, over a range of wavelengths from the far infrared to soft x-rays. The sensitivity and acquisition time of these instruments depends on the efficiency of their gratings, i.e., the intensity of useful diffracted light compared to the incident light. In many cases – such as Peter Zeeman’s famous discovery of energy level splitting in a magnetic field – improvements in grating efficiency made a previously undetectable effect detectable.

To support and advance these techniques, this project sought to understand and improve the diffraction efficiency of gratings. While the research happens to be applicable to a wide range of scenarios – both theoretical and applied, it was focused on a tangible goal: designing and optimizing an innovative soft x-ray emission spectrometer for the REIXS beamline at the Canadian Light Source. Over the course of the project, we used and created new software tools based on rigorous electromagnetic theory (Chapter 3) to calculate diffraction efficiency. We applied these tools to understand efficiency trends, and used them to design the optics for the spectrometer. The software tools, described in Chapter 4, were written to harness high-performance computing resources where available, and have been released to allow other beamline designers to quantify and optimize their own designs. In examining the trends (Chapter 5), we compared different groove shapes, analyzed the effects of material and geometry parameters, and discovered new principles that can be applied to instrument design, including the principle of optimal incidence. We used this understanding to design

an innovative spectrometer that balances efficiency with high resolving power, and extended its performance by exploiting an efficiency peak in the third diffraction order. (Chapter 6 describes the design process we used.)

Once the spectrometer gratings were manufactured, we also measured their real-world efficiency and compared it with our calculations (Chapter 7). The measured efficiencies were very different from the original predictions, but we accounted for the discrepancy based on real-world effects and manufacturing differences: geometry errors, groove variation, surface roughness, and oxidation. We also discovered a fitting technique that could predict the real grating parameters based on the shape of the measured efficiency curves. Because each parameter affects the efficiency curves in a different way, we found that we could predict multiple parameters, and confirmed the accuracy of the geometry predictions using atomic force microprobe (AFM) measurements of the actual grooves. Other parameters like the surface roughness and the oxide thickness are difficult to measure, at least non-destructively; however, the exactness of the fit achieved for all gratings increases our confidence in the theoretical calculations, and suggests it might be possible to use the fitting technique to characterize grating parameters that are infeasible to measure directly.

In most cases of beamline design, the diffraction efficiency is hardly considered, or left up to the grating manufacturer. It is even more rare to actually *test* the gratings for their real efficiency. The REIXS spectrometer project was successful because we were able to combine rigorous efficiency calculations with ray-tracing predictions of the resolution, and use both to navigate the compromise between these two competing factors. Commissioning of the real-world spectrometer is still ongoing, but preliminary results (Chapter 8) confirm that our design process produced an effective and useful instrument for material scientists. In its high efficiency mode, the spectrometer offers competitive resolution and four to six times the throughput of a comparable spectrometer at the Advanced Light Source; it also offers a high resolution mode to push deeper into the electronic structure of new and novel materials. In addition to this physical instrument, we hope that our efficiency calculation methods and software will be useful in the design of future record-setting soft x-ray beamlines.

CHAPTER 2

MOTIVATION: WHY GRATING EFFICIENCY MATTERS

In 1821, when Joseph von Fraunhofer first resolved the sodium doublet lines using a diffraction grating he fashioned out of metal wire stretched between the grooves of two screws, he probably would not have anticipated the full scientific impact of his invention. Immediately, these observations helped reinforce Fresnel’s new wave theory of light [17]. More importantly, the diffraction grating quickly became the foundation of spectroscopy, superseding the prism as a wavelength-dispersive element with higher resolution, and applicable to radiation from the infrared to x-rays. Eventually it would enable a huge range of experiments and new discoveries in all fields of science:

- In astronomy, Fraunhofer himself was the first to conduct spectroscopic measurements on light from the sun, moon, planets, and stars. Shifts in the position of well-known absorption lines proved, using the Doppler Effect, that the universe was expanding. Today, the composition and temperature of galactic objects is routinely measured using grating-based spectroscopic techniques.¹
- In physics, visible spectroscopy of the hydrogen emission lines (Balmer Series) provided the data for Niels Bohr’s explanation of electron levels in the atom. Peter’s discovery of the Zeeman Effect – the splitting of emission lines in a magnetic field – was accomplished using a 20-foot Rowland Circle spectrometer [78]; his results back up the modern version of quantum theory and the magnetic and spin quantum numbers.
- In chemistry, many elements (such as caesium and rubidium, identified by Kirchhoff and Bunsen in 1860) were first discovered in trace amounts using spectral analysis.

¹In fact, the company that manufactured the gratings for this project also ruled the gratings used in the Hubble Space Telescope.

- Biologists and biochemists regularly use spectrophotometers to assay the concentration of a tagged reagent in a solution, making gratings a routine tool in life sciences, pharmaceutical, and genetic research.

One common lamentation of the early spectroscopists was the faintness of the light leaving the grating; indeed, we can imagine them in darkened rooms, peering through telescope objectives, straining to make out the faintest lines by eye (Figure 2.1):

Some lines can be distinguished in the spectrum of Procyon; but they are seen with difficulty, and so indistinctly that their positions cannot be determined with certainty. I think I saw a line at the position D in the orange.

Joseph Fraunhofer, in *Prismatic and Diffraction Spectra* [18, p. 61]



“But by examining the spectral lines you can see that the wine stains on the furniture were clearly from the previous tenants!”

Figure 2.1: Early spectroscopy would have involved long hours squinting through telescope eyepieces at barely visible lines... although we cannot argue with the value of the results! **Image credit:** JOHN McCLEOD, personal communication, August 2012.

Photographic film – and later, modern imaging devices like CCDs – have succeeded in removing at least the physical pain associated with spectroscopy. However, increases in grating efficiency are even more important and useful today as they would have been in 1830. At visible wavelengths, more efficient gratings have already enabled a range of compact spectrometers with very high sensitivity, such as the convenient USB-powered computer peripheral in Figure 2.2. Other wavelength ranges are more challenging; grating efficiency is especially critical to the variety of soft x-ray spectroscopy experiments now taking place at synchrotrons around the world, where the low reflectivity of optical materials makes it difficult to build highly efficient devices.



Figure 2.2: A sensitive, compact, visible light spectrometer (Ocean Optics USB4000-UV-VIS). It uses a blazed reflection grating optimized for 300 nm light, and connects to a personal computer using USB. **Image credit:** OCEAN OPTICS, INC. [45]

Put simply, the *diffraction grating efficiency* is the fraction of useful diffracted light outgoing from a grating relative to the amount of incoming light. (Chapter 3 offers a formal definition.) While spectroscopy experiments vary in hardware, instrumentation, and purpose, we can make a pair of general observations on why the grating efficiency is so important. From the point of view of an experimenter, it affects the amount of light available to the sample or detector, and therefore:

1. It affects the *speed* at which experiments can be done, by determining the exposure time required to record data of sufficient quality. In general, improvements in grating efficiency could reduce the amount of time for a given measurement – or equivalently, increase the number of measurements that could be taken in a certain time period. (For example, it takes anywhere from 3 minutes to several hours to measure a soft x-ray

emission spectrum on the 8.0.1 beamline at the Advanced Light Source, depending on the concentration of the sample and the desired resolution. One could argue that a factor of 2 optimization in the grating efficiency could almost double the number of users or the scientific throughput of the beamline.)

2. It affects the *feasibility* of doing an experiment in the first place. In situations where the experimental light source is extremely weak (for example, spectral analysis of faint stars in astronomy, or emission line measurements of trace elements in material science), the grating efficiency must be sufficient to raise the signal level above the background noise level seen by the detector. This is no longer a question of patience; if the signal level is below the background noise, our unhappy experimentalist could accumulate detector readings indefinitely to no avail.²

The motivation for this project was therefore to understand the factors affecting the efficiency of diffraction gratings, and to apply this knowledge to their optimization. To accomplish this, we sought the ability to model gratings numerically and calculate their efficiency – a useful outcome for all grating spectroscopy applications.

However, a more specific goal was actually our primary objective. At the onset of this project, we were involved in the optical design of a soft x-ray emission spectrometer, destined for use on the REIXS beamline at the Canadian Light Source. Working with David Muir, whose studies on spectrometer resolution are published in his M.Sc. thesis [40], we attempted to simultaneously achieve both *world-class resolution* and *record efficiency* for this machine.³ Therefore, although the calculation techniques presented in this thesis are general, our examination of trends in diffraction efficiency focusses on the types of gratings used in the soft x-ray regime.

Given our specific motivation, the following sections explain the ultimate goal of such a machine, and show how gratings are typically employed in soft x-ray spectroscopy.

²In fact, Zeeman mentions in the introduction to his paper that he was inspired by Faraday, who spent the last years of his life trying, “but in vain, to detect any change in the lines of the spectrum of a flame when the flame was acted on by a powerful magnet”. Zeeman decided “it might be yet worth while to try the experiment again with the excellent auxiliaries of the spectroscopy of the present time...” [78], brought on by Henry Rowland’s new mechanically-ruled reflection gratings.

³As it turns out, these two goals are implicitly in conflict; see Section 2.2.2.

2.1 Soft x-ray spectroscopy techniques

Soft x-rays are photons with energies in the range of approximately 100 to 10 000 eV (or wavelengths of about 10 to 0.1 nm). Unlike with hard x-rays, which are highly penetrating, soft x-ray energies correspond to the binding energies of core-level electrons in common, lightweight elements. This property is ironically responsible for both the experimental challenge of working with them – they are quickly absorbed by any matter over very short distances – as well as their inherent usefulness as a probe of the electronic structure in materials.

Soft x-ray experiments use this light – usually created by a tuneable source such as a synchrotron – and focus it onto a sample to be studied. Two techniques provide complementary information: absorption spectroscopy, and emission spectroscopy.

2.1.1 Absorption spectroscopy

Absorption spectroscopy measures the absorption rate of photons as a function of their wavelength (or energy). Experimentally, this is done by shining a monochromatic beam of light onto the sample and measuring the amount of light absorbed as the energy of the beam is changed.

Figure 2.3 shows the available absorption processes on the left side of the diagram (red). When the photon energy becomes sufficient to excite an electronic transition in the material, dramatically more photons will be absorbed; this is known as an *absorption edge*. Near the edge, as photons are absorbed by exciting electrons from the core level into unoccupied levels, adjacent unoccupied levels will have different probabilities of experiencing a transition, according to the quantum mechanical nature of the bonding in the material. (Note that according to the selection rule for dipole radiation, only electron transitions with a change in orbital angular momentum quantum number $\Delta l = \pm 1$ are allowed, since momentum must be conserved and photons have an angular momentum [spin] of one unit.) The absorption will increase for energies where the transition probability is higher; therefore, the absorption spectrum is actually a measure of the *density of unoccupied states* for electrons in the

material.⁴

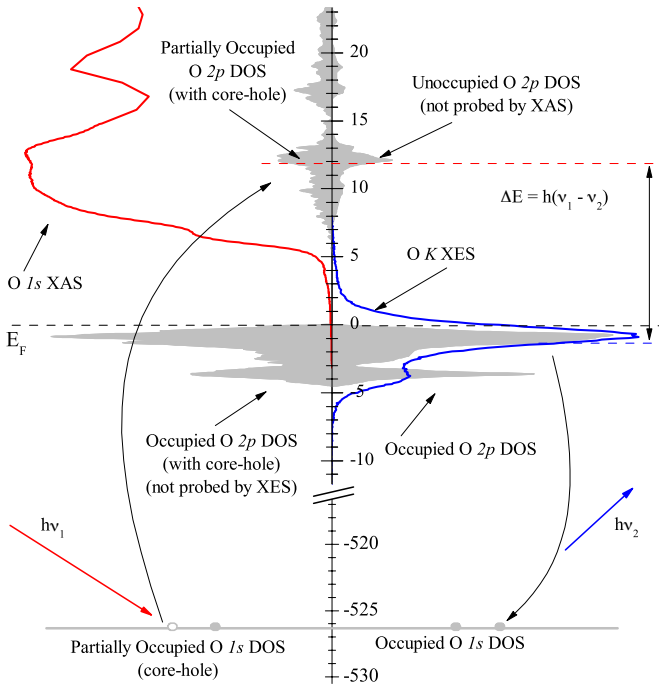


Figure 2.3: X-ray absorption spectroscopy (on the left, in red) probes the density of *unoccupied* electronic states, modified by the presence of a core-hole: a vacancy left behind by the excited electron. In this example for oxygen, the absorption edge starts at 6 eV above the Fermi level, labelled E_F .

X-ray emission spectroscopy (on the right, in blue) probes the density of *occupied* valence states, as a valence electron decays by emitting a photon to fill the core-hole. In this diagram, the absorption and emission spectrum have been plotted vertically to line up with the schematic of the energy levels; they are conventionally plotted on a horizontal energy axis. Grey areas represent the computed density of states. Reprinted from Reference [33].

One outstanding question concerns how the absorption rate is measured – how do we know how many photons were absorbed? Perfect absorption spectroscopy would shine the beam clear through the sample, and measure the intensity of the beam before and after to determine the fraction of light absorbed. While *transmission measurements* like this are feasible with hard x-rays, the short attenuation length of soft x-rays would require prohibitively thin samples for any beam to be left on the other side. Instead, different measurements are used as a proxy for the total absorption rate:

⁴To be accurate, we should say the ‘*partial* density of unoccupied states’, since the vacancy left behind in the original electron state (“core-hole”) will affect the energy of the unoccupied states.

Total electron yield

For the excited electron, the most probable decay mechanism is to quickly relax into a lower-energy state, transferring its energy to a more loosely bound electron in the process. This secondary electron, known as an Auger electron, can then be ejected from the sample – assuming it is close enough to the surface. The **total electron yield** (TEY) method determines the absorption rate by measuring the electric current that must flow into the sample to neutralize the ejected electrons and keep the sample uncharged. (Experimentally, this is done by simply connecting a wire to the sample holder, and placing a sensitive ammeter along the path to a solid ground connection.)

TEY measurements are difficult for some samples, either because an insulating sample doesn't allow current to flow in to replenish the ejected electrons ("sample charging"), or because electrons ejected deep in the material are reabsorbed elsewhere. This makes TEY measurements most sensitive to absorption events near the surface ($\sim 2\text{nm}$), and restricts them to conductive samples.

Total fluorescence yield

Total fluorescence yield (TFY) measurements overcome these problems by using a light-sensitive detector near the sample. Although several orders of magnitude less probable than the Auger decay process, excited states can also relax by emission of a photon. Instead of ejected electrons, TFY measures the intensity of all photons emitted during the decay, which makes it applicable to both insulating and non-insulating samples. Because photons have a greater escape depth than electrons, this technique is also able to probe deeper within a material than TEY can. Due to the low probability of fluorescence transitions compared to Auger transitions (several orders of magnitude), TFY measurements benefit greatly from concentrated samples and a light source which is capable of high intensity.

2.1.2 Emission spectroscopy

While absorption measurements provide information about the *unoccupied* states, we can also study what happens *after* the initial photon is absorbed. When a core-level electron is

promoted by the absorption of a photon, it leaves behind a “core-hole”, and the atom (or molecule, or crystal) is left in an excited state. While there are many ways for the system to collapse back to the ground state, there is a small probability that some valence-band electron will decay to fill the core-hole by the emission of another photon. Since the energy of the emitted photon will match the energy difference between that valence electron and the core level, the intensity distribution of *all emitted light* will correspond to the probability of finding electrons in the valence band at those energies. Therefore, if we could collect the *fluorescence* emitted from the sample and plot its intensity as a function of energy, we would have a measure of the *density of occupied states* for electrons in the material. In this way, emission spectroscopy provides information on the bound electronic states, which is not present in the absorption spectrum.

Experimentally, XES measurements are done by illuminating the sample with a fixed photon energy above the absorption edge. The fluorescence is captured using an energy- or wavelength-sensitive detector which is tuned to the energy range just below the absorption edge. Over time, an intensity spectrum is built up from the collected photons (Figure 2.3, Figure 2.9). Since fluorescence transitions are a random process, and highly improbable compared to other decay mechanisms like Auger decay, XES measurements require a sufficient exposure time to build up good statistics. They also benefit greatly from a high-intensity beam source and an efficient detector – such as a sensitive spectrometer with high-efficiency gratings.

Resonant inelastic x-ray scattering (RIXS)

An advanced form of XES is known as RIXS (*Resonant Inelastic X-ray Scattering*). Instead of exciting a sample with a photon energy well above the absorption edge, the energy of the beam is tuned to match transitions previously identified in the absorption spectrum (or stepped incrementally through this range). This allows the experimenter to preferentially excite into specific electronic states: at *resonance*, the transition probability will be extremely high because the exciting photon energy exactly matches the transition energy and the emitted photon energy.

RIXS is a one-step process, but it can be explained mathematically as a simultaneous

two-step process which combines absorption and emission: from the initial electronic state, an incoming photon is absorbed, creating a “core-hole” and an excited electronic configuration. This intermediate state decays by the emission of another photon into a final state, and this transition doesn’t necessarily need to involve the original electron. The difference in energy of the emitted and incident photons provides an *energy-loss spectrum* describing the nature of excitations within the material.

According to this two-step explanation, RIXS can probe transitions that would be forbidden by the dipole selection rule. For example, a 2p electron could be excited into a 3d state, and another 3d electron with a slightly different energy could collapse to fill the 2p hole, thereby effectively creating a ‘d-d’ excitation [9].

2.1.3 Importance of soft x-ray spectroscopy (SXS)

Soft x-ray spectroscopy is a valuable tool in material science for its ability to gain insight into the electron environment within a material. Since the electronic structure determines the bonding between atoms and thereby a material’s mechanical, chemical, and physical properties, this is a big deal indeed. Additionally, x-ray spectroscopy has a few complementary advantages over other analytical techniques like neutron diffraction and photoemission spectroscopy:

- It is **element-specific**: for a material containing a number of elements, it is usually possible to find absorption edges for each element that do not overlap with the others, making it possible to independently probe the bonding environment of each. For example, in an organic sample containing carbon, nitrogen, and oxygen, one can probe the oxygen using the O 1s absorption at 543 eV, and then separately excite the nitrogen 1s electrons at 410 eV.
- More than being just element-specific, it is also **site-specific**: soft x-ray spectra make it possible to distinguish, for example, single-bonded carbon atoms at one location in a molecule from double-bonded atoms at another.
- Depending on the detection technique, it can be **surface-sensitive** or **bulk-sensitive** (i.e.: it can probe through surface contamination or oxidation, testing the nature of

the material below).

Additionally, there are a few experimental considerations that make SXS desirable:

- It can be done **non-destructively** on whole samples, without having to crush them into powders, dilute them in solution, etc. It can also allow in-situ measurements of samples created directly within the vacuum chamber – for example, crystal samples created using sputtering or vapour deposition techniques.
- Because of the high brightness and small size of synchrotron beams, it can be done on **very small and thin samples**. Since the penetration depth of soft x-rays is so short, the interaction volume created by the beam will be tiny regardless of the sample thickness, making it a valuable characterization technique for thin film samples and even monolayers.

One obvious experimental disadvantage is that these techniques require access to synchrotron accelerators to produce the soft x-ray beam, which – for the foreseeable future – are not yet available in convenient desktop or bench-top models. Additionally, since soft x-ray experiments must be performed under ultra-high vacuum (UHV) conditions (see section 2.2.3), samples must either be UHV-compatible or carefully isolated from the vacuum environment behind thin windows.

Despite these limitations, SXS techniques have created some notable and very interesting discoveries in physics; some highlights are listed here:

- In 1990, de Groot et. al. presented the first comprehensive understanding of soft x-ray absorption in transition metal compounds. Not only did they produce some state-of-the-art experimental spectra for the time, but they also gave a thorough interpretation of them using crystal field atomic-multiplet theory [13].
- Butorin et. al. published the first RIXS studies of transition metals, and discovered *d-d* excitations in manganese oxide [9].
- Recently, Braicovich et. al. used RIXS to measure the dispersion of magnetic excitations in cuprate superconductors. This study also found a magnetic dispersion branch

that had never been found before using neutron scattering, and found that these types of materials are in non-homogenous spin states, revealing a bit more about the mysterious nature of cuprate superconductors [7].

- With the proper experimental equipment, RIXS studies can also be done on gaseous samples. In 2011, Pietzsch et. al. measured very high resolution RIXS on oxygen gas (O_2) to observe the vibronic structure. The exciting result from this study was the presence of spatial quantum beats in their spectra – essentially, an observation of quantum mechanical interference like the famous double-slit experiment, but using excitations into different states instead of transmission through different slits [53].

2.2 Spectroscopy instrumentation

The preceding sections make it clear that to perform soft x-ray spectroscopy experiments, we need three capabilities:

- Obviously, one needs a source of soft x-rays – usually, the brighter, the better. This became possible with the advent of synchrotron particle accelerator facilities, which emit broad-spectrum x-rays as relativistic electrons are forced to change their path by bending magnets.⁵

2. For absorption and emission spectroscopy:

From this broad spectrum of light, one needs to produce a nearly monochromatic beam of light to shine onto the sample, and must be able to adjust the energy of this beam. This is the role of a *monochromator*, which takes a broad-spectrum light source and extracts a small range of wavelengths from it (Figure 2.4).

3. Additionally, for emission spectroscopy:

One must be able to capture the light emitted from the sample and resolve it by

⁵Much more intense synchrotron light can be generated by “insertion devices” known as *undulators* and *wigglers*, in which an alternating array of magnets in a straight section of the accelerator forces the electron beam to bend many times over a distance of a few meters. Although light from insertion devices still contains a range of wavelengths, its spectrum consists of sharp intensity peaks which can be adjusted to the desired wavelength by changing the strength of the magnetic field. We intentionally avoid going into too much detail on synchrotron physics in this thesis; more information can be found in Reference [48].

wavelength. The end goal is to measure the relative intensity as a function of wavelength (or energy); this is accomplished using a *spectrometer* (Figure 2.6).

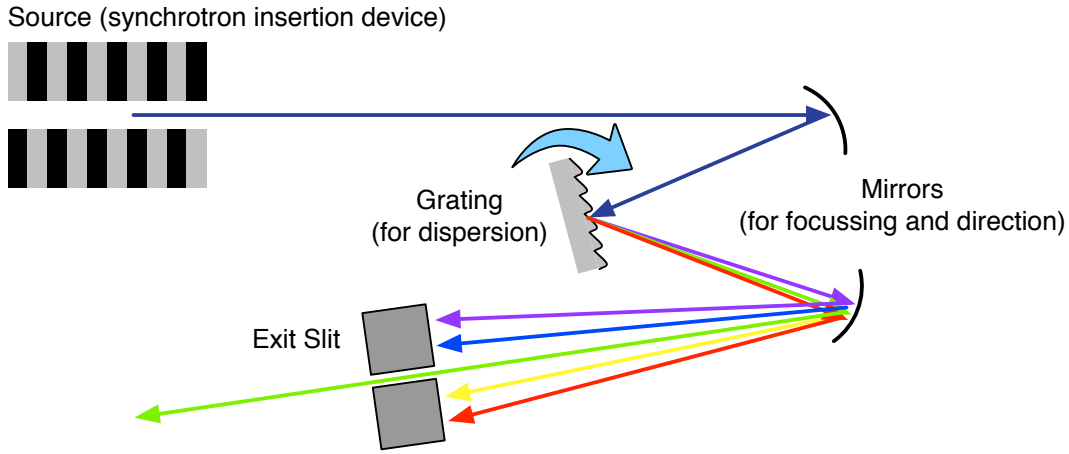


Figure 2.4: In this schematic of a grating monochromator, light from the source is focussed by mirrors and dispersed by the grating. An exit slit picks out the desired wavelength or energy range, and blocks the remaining light. Depending on the design, the output wavelength can be adjusted by changing the angle of the grating, the angle of the mirrors, and/or the position of the exit slit. (The resolution – the energy bandwidth of the outgoing light – depends on the dispersion of the grating, the geometry, and the size of the exit slit. An ideal monochromator would produce truly monochromatic light, but this would require an infinitely small slit.)

2.2.1 Beamlne optics: monochromators and spectrometers

Monochromators

The role of a monochromator (shown schematically in Figure 2.4) is to pick out a narrow range of wavelengths from a chromatic light source, and deliver the monochromatic beam to the experiment. For infrared light out to soft x-rays, diffraction gratings provide the most efficient way of separating the incoming beam based on wavelength.⁶ When the incidence angle and mounting angle of the grating are chosen to direct a single ($n \neq 0$) diffraction order

⁶For hard x-rays, monochromators use “natural” diffraction gratings consisting of atomic planes in blocks of single crystals, since the inter-atomic spacing is comparable to the short wavelength of the light; these might be analyzed more appropriately using Bragg scattering theory than the electromagnetic approach we take for the man-made structures in this thesis.

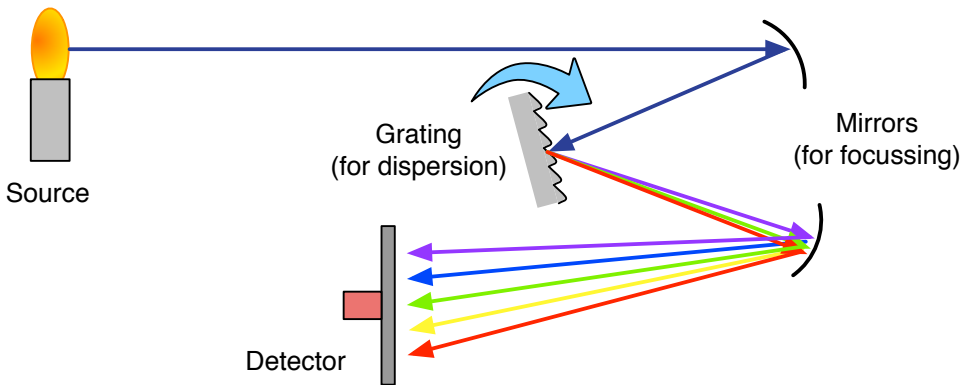


Figure 2.5: In this schematic of a grating spectrometer, mirrors are used to focus light from the source (or entrance slit) onto the detector, passing over a plane grating en-route to disperse the light by wavelength. (This is a *Czerny-Turner* arrangement, typical of compact visible-light designs like the one in Figure 2.2.) Since the grating diffracts different wavelengths at different angles, the intensity distribution across the detector surface creates a spectrum related to the wavelength (or photon energy).

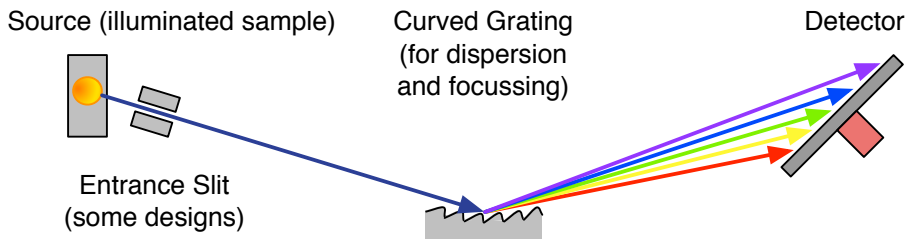


Figure 2.6: The spectrometer in this schematic uses a curved grating to both disperse light by wavelength, and focus it onto the detector. (This is typical of soft x-ray designs where the poor reflectivity of additional mirrors is usually avoided.) The intensity distribution along the surface of the detector can be converted into a spectrum with respect to wavelength or energy. Since the detector only captures a limited range of outgoing angles, it can be moved to pick out the desired wavelength window for each measurement.

toward the exit slit, the wavelength term in the grating equation (3.19)

$$n\lambda/d = \sin \theta_{2,n} - \sin \theta_2$$

creates a dependence on the sine of the outgoing angle $\theta_{2,n}$, so that shorter wavelengths leave more normal, and longer wavelengths leave at more grazing angles. Depending on the optical and mechanical design, the output wavelength can be selected by changing the angle of the grating, the angle of the mirrors (and hence the incidence angle onto the grating), and/or the position of the exit slit.

The resolution of the monochromator – ie: the bandwidth of wavelengths present in the output light – depends on the angular dispersion of the grating, the geometry, and the size of the exit slit; an ideal device would produce a perfectly monochromatic beam, but this would require an infinitely-small exit slit. (In practice, the size of the exit slit is used to adjust the resolution, in an unavoidable trade-off against the amount of flux produced.) Resolution is measured as the energy bandwidth ΔE (full width at half-maximum) for a given central energy; for example: $\Delta E = 500$ meV at 1000 eV. Often it is more convenient to normalize it as the *resolving power* $RP = E/\Delta E$, which has the benefit of being identical when measured in wavelength as well:

$$RP = \frac{E}{\Delta E} = \frac{hc/\lambda}{\Delta\lambda dE/d\lambda} = \frac{hc/\lambda}{\Delta\lambda (-hc/\lambda^2)} = \frac{\lambda}{-\Delta\lambda} \rightarrow \frac{\lambda}{\Delta\lambda}$$

In addition to dispersing the light by wavelength, monochromators must also act to *focus* light from the source, typically onto the exit slit, or onto the focal point of a downstream mirror. The schematic shown in Figure 2.4 is a *plane grating monochromator (PGM)*, where the focussing is accomplished using the two curved mirrors. Other designs use either a curved grating (*spherical grating monochromators*), or subtly change the line spacing of the grooves (*variable line space (VLS) grating monochromators*) to create the required focussing effect and reduce the number of optical elements. We avoid going into detail on focussing and monochromator design here; a good reference is provided by Petersen in Reference [48].

Our efficiency calculations in the rest of this thesis assume plane gratings and uniform line spacing; however, when curved gratings are used, the radius of curvature is typically so large – on the order of 10m – that the local changes over a grating surface (a few cm) do not

affect the efficiency. With VLS gratings, the groove spacing may change by a few percent from end-to-end, and we have modelled these situations by averaging the results of multiple efficiency calculations using a set of representative points.

Many monochromator designs offer multiple switchable gratings to let the user optimize between efficiency and resolution, since higher line density gratings are required to maintain the resolving power at higher energies. (As we will show in Chapter 5, the grating efficiency declines as both the line density and energy increase.) As a representative example, the HE-PGM-3 monochromator at Bessy [49] became the starting point for many soft x-ray beamline designs; it uses a 366 line/mm grating to cover the energy range between 30 eV and 700 eV, and a 1221 line/mm grating to cover the energy range between 120 and 1900 eV (Figure 2.7).

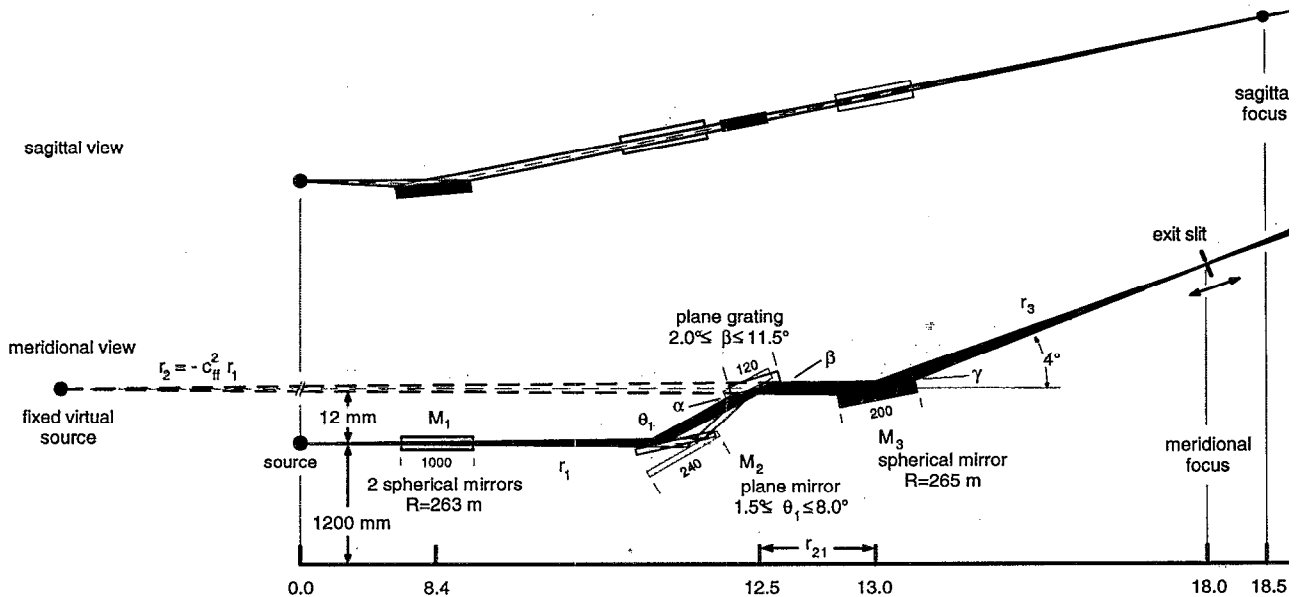


Figure 2.7: The Petersen Plane Grating Monochromator, as implemented on the HE-PGM-3 beamline at BESSY. In Reference [49], Petersen et. al. provide a good overview of monochromator focussing techniques, prior to the widespread adoption of VLS designs. Reprinted from Reference [49].

Spectrometers

If the goal of a monochromator is to produce monochromatic light, the goal of a spectrometer is to produce a *spectrum* – ie: to resolve the frequency components that exist in an unknown light source and measure their relative intensity. The device in Figure 2.5 is identical to

the monochromator shown in Figure 2.4, except that the exit slit has been replaced by an area-sensitive detector. With the grating positioned so that an outgoing diffraction order (typically the 1st order, for best efficiency) lands on the detector, the angular dependence on wavelength puts short wavelengths onto the top of the detector, and long wavelengths onto the bottom of the detector. The intensity profile recorded across the detector surface is a spectrum, although some mathematical correction will need to be done to calibrate the energy axis, by mapping detector positions to diffraction angles, and diffraction angles to energy using the grating equation.

The spectrometer in Figure 2.6 is more representative of those used in soft x-ray applications, where the low initial levels of fluorescence from the sample and the poor reflectivity of mirrors make it desirable to eliminate as many optical components as possible. Just like monochromators, spectrometers must focus light from the entrance slit – or directly from the source, in the case of slit-less designs – onto the detector. This is accomplished by using spherical gratings and arranging the geometry to exploit the *Rowland Circle* focussing condition discovered by Henry Rowland [48, p. 169], or again by using VLS gratings to alter the shape of the focal curve. More information on spectrometer focussing can be found in the M.Sc. thesis by David Muir [40].

Like monochromators, spectrometer designs usually offer switchable gratings with different line densities and coatings, optimized for different energy ranges. Figure 2.8 shows a top and side view of the SXF endstation on Beamlne 8.0.1 of the Advanced Light Source, a typical “workhorse” spectrometer, which balances moderate resolution with reasonable efficiency. It uses four gratings with groove densities of 600, 1000, 1000, and 1500 lines/mm to cover the energy range from 70 to 1200 eV, and uses a 40 mm wide multi-channel plate detector with an effective spatial resolution between 40 and 80 um. Figure 2.9 shows an image recorded by that detector, and the corresponding spectrum.

2.2.2 Goals for soft x-ray instruments

In the design of both spectrometers and monochromators, there are two goals we have already mentioned that are important from the experimenter’s perspective:

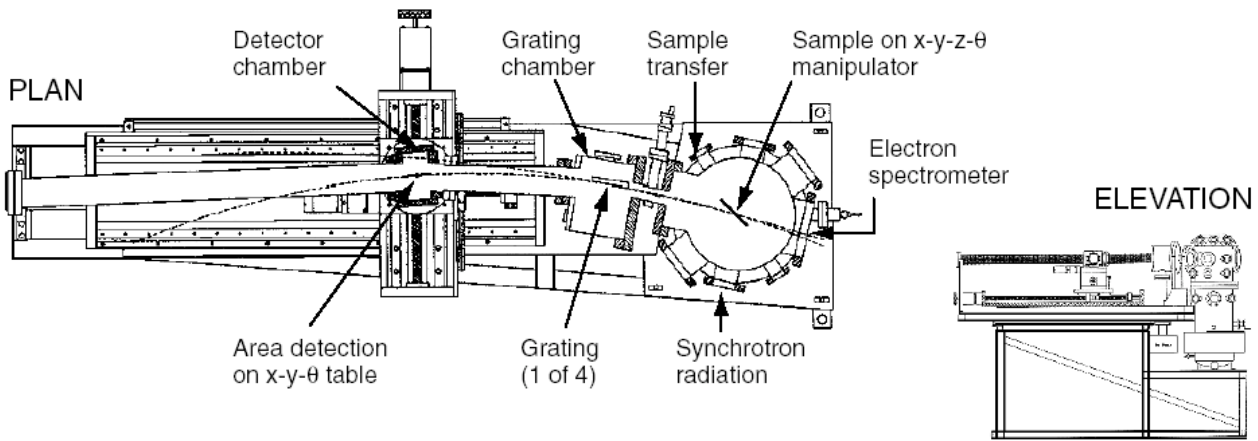


Figure 2.8: The SXF endstation spectrometer on Beamline 8.0.1 of the Advanced Light Source – a typical “workhorse” spectrometer. It uses spherical gratings in a Rowland Circle design; four gratings let users choose between higher resolution or higher efficiency at different energy ranges. The resolving power of this machine is compared with other leading spectrometers in Figure 6.1. Reprinted from Reference [25].

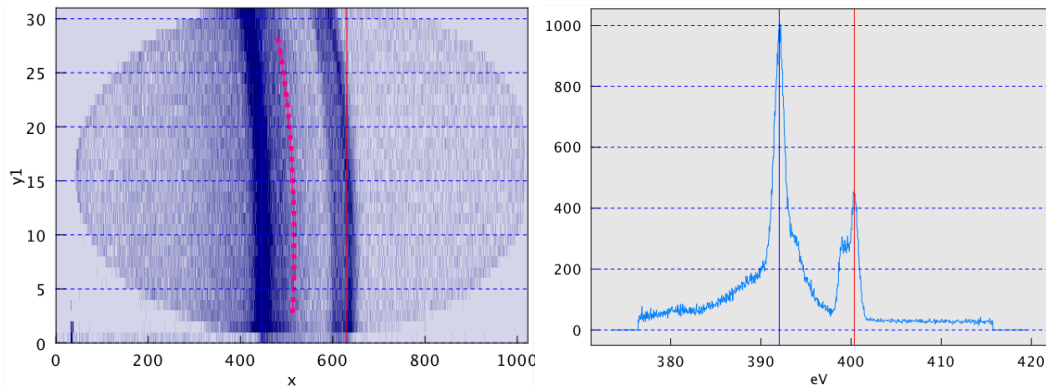


Figure 2.9: A detector image and corresponding spectrum produced by the SXF spectrometer in Figure 2.8. (This particular scan is of the nitrogen emission lines in nitrogen-doped zinc oxide.) The curvature of the spherical gratings provides focussing in the dispersion direction (x -axis), but unfortunately produces a curved image in the perpendicular direction (y -axis). This curvature is corrected by aligning rows along the red curve when the image is summed to produce the spectrum on the right.

- The **resolution** is important in order to see details in spectra and probe new science. On a soft x-ray beamline, the monochromator determines the resolution of an absorption scan, and the spectrometer determines the resolution of an emission scan. Both are involved in the experimental resolution of RIXS studies.
- The overall **efficiency** is important because it determines how much light is available, and indirectly how long it takes to generate enough photon interactions to record acceptable statistics. At a minimum, the efficiency must be high enough to produce a signal above the background noise level of the detector. Beyond this threshold, increases in efficiency make it faster to do experiments and let the user accomplish “more science” in a shift.

Since the probability of an excited atom decaying via fluorescence transitions is so low compared to other decay methods, the initial amount of light available in emission experiments is extremely low. This is further compounded in experiments on doped or dilute samples, when trying to observe the emission lines of the dopant elements. Finally, the entrance slit of a spectrometer can only capture a tiny geometric fraction of all photons out of the sample. All of these reasons combine to make emission spectroscopy experiments extremely “photon hungry”, which means that efficiency is especially critical here.

What makes these two goals challenging is that they are inherently in tension. To see why, we consider as an example a simple emission spectrometer like the one shown again in Figure 2.10.

The immediate result of a spectroscopy experiment is the image produced along the detector surface. For all detectors – be they photographic film, multi-channel plate detectors, or CCDs – there is an *effective spatial resolution*: the minimum distance along the detector that is required for two adjacent rays to be distinguished. For a given detector, if you want to increase the *energy resolution* of a design, you would need to either

1. increase the angular dispersion of the grating – thereby increasing the angular separation between adjacent wavelengths, or
2. put the detector a long way from the grating, so that over distance the angular dispersion creates a large spatial separation between adjacent wavelengths.

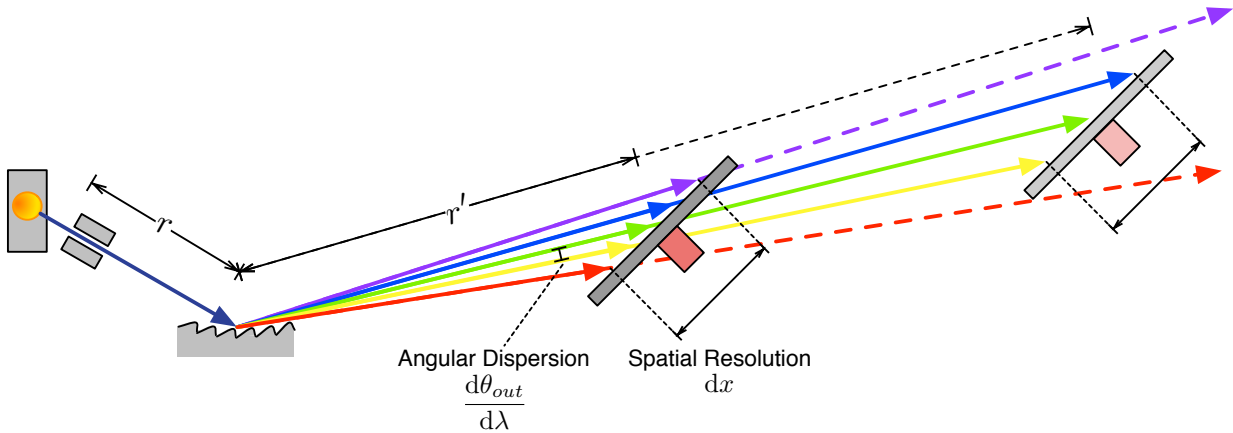


Figure 2.10: The detector has an effective spatial resolution dx which is the minimum distance required to resolve two adjacent incident rays. Except for the $n = 0$ order, the grating produces an angular dispersion $d\theta_{2,n}/d\lambda$, which is the angular separation between infinitesimally-adjacent wavelengths. To increase the spacing between adjacent wavelengths on the detector, we can either increase the grating-detector distance r' , or increase the angular dispersion.

Both of these solutions inherently reduce the *geometric efficiency* of the spectrometer: the fraction of all photons captured by the detector assuming perfect mirror and grating efficiency. In the dispersion direction (or *meridional* direction, vertical in Figure 2.10), the detector will now only capture photons from a smaller energy range; if the spectral line is wider than the detector, the corresponding reduction in light gathered is an unavoidable tradeoff no matter what scheme is used to increase resolution. However, the second method – increasing the distance from the grating to the detector – reduces the solid angle captured by the detector also in the perpendicular direction (or *saggital* direction, out of the page), further decreasing the geometric efficiency to an extent which depends on the nature of focussing in that direction.⁷ The only way to increase resolution with only the minimum essential reduction in geometric efficiency is by using the first method: increasing the grating’s angular dispersion. By differentiating the grating equation (3.19) with respect to wavelength (holding

⁷A complete analysis of focussing criteria would show that, at least for Rowland Circle spectrometers, increasing the source-grating distance requires an increase in both the entrance slit-grating distance, *and* an increase in the grating radius; both of these actions further decrease the geometric efficiency, possibly as a function of the cube of the distance. One could compensate by using larger gratings, but the maximum grating size must be limited to manage spherical aberrations; see Reference [40, p. 98].

the incident angle θ_2 constant):

$$\begin{aligned}\frac{n\lambda}{d} &= \sin \theta_{2,n} - \sin \theta_2 \\ \frac{n}{d} &= \cos \theta_{2,n} \frac{d\theta_{2,n}}{d\lambda} \\ \frac{d\theta_{2,n}}{d\lambda} &= \frac{n}{d \cos \theta_{2,n}}\end{aligned}\tag{2.1}$$

we derive an expression for the angular dispersion; it is clear that to create more dispersion, we can either increase the groove density (decrease the groove spacing d), or use a higher diffraction order n . Unfortunately, as will be shown in Chapter 5, both of these actions substantially reduce the *grating efficiency*. As an additional challenge, we can see that the dispersion will be reduced for higher energies, which leave the grating at more normal angles, creating a larger $\cos \theta_{2,n}$.

No matter which method is used, resolution and overall efficiency are in conflict. Whether it takes a hit to the grating or to the geometry, increasing the resolution demands a reduction in efficiency and vice-versa; the cleverness of the beamline designer is measured in his or her ability to negotiate this compromise.

While this example examined resolution as seen by a spectrometer detector, the same unfortunate principles also apply to monochromators.

2.2.3 Challenges of soft x-ray applications

All grating spectrometers, regardless of their wavelength range, are subject to the unavoidable tradeoff between resolution and efficiency. However, the nature of soft x-rays adds an additional set of challenges within this regime, which combine to make efficiency even more important.

UHV compatibility

Because the energy of soft x-ray photons matches the energy of core level electron transitions in all light elements, they are readily absorbed in matter over very short distances. (Just passing through 1 mm of nitrogen at atmospheric pressure is enough to attenuate a 200 eV beam by 63 percent!) This means that all SXS experiments must be done under *ultra-high*

vacuum (UHV) conditions, where the beam path has been evacuated of air and other contaminants, ideally to a pressure lower than 10^{-8} torr. This is accomplished by using vacuum chambers and sealed beam pipes, pumped down using turbo-molecular pumps, ion pumps, and/or cryogenic pumps. At these low pressures, most common materials would “out-gas”, boiling off contaminants into the vacuum environment. As a result, chambers and instrumentation must be built using a restricted set of UHV-compatible materials (certain grades of stainless steel and aluminum, copper, gold, and some special ceramics and high-temperature thermoplastics). Anything that comes into contact with the vacuum environment must be carefully cleaned prior to assembly, and it is often necessary to “bake out” the chambers by heating them to temporarily raise the vapour pressure while pumping in order to remove water and other contaminants adsorbed to the inside surfaces before eventually attaining UHV levels.

For the experimenter, UHV requirements also apply to samples. Liquid samples and non-UHV-compatible samples must be carefully enclosed and sealed behind thin windows to let the beam in. (Beryllium is often used in this application, due to its strength and relatively low absorption). Loading samples into the vacuum chamber must be done through an airlock, and remote actuators are required to adjust the sample position and the position of optical elements.

Low reflectivity and grazing incidence

Beamline designers face a more significant challenge when choosing optical elements. The easy absorption of soft x-rays means that mirror and grating surfaces have extremely low reflectivity at these wavelengths – at least at normal incidence. For visible light, the reflectivity of a polished aluminum surface approaches 90%; at 200 eV, the reflectivity of the same surface is less than 0.005% [12].

Two approaches are necessary to work around this challenge. Optical coatings need to be selected to avoid absorption edges in the region of interest. For example, carbon and nickel have relatively high peak reflectivities (Figure 5.11), but very strong absorption features at 284 eV and 853 eV respectively; these coatings would only be appropriate for optical elements used within a narrow wavelength range away from those edges. In many-electron materials

like gold and platinum, the most pronounced core-level absorption edges occur outside the soft x-ray region, and as result they have acceptable reflectivity over a wide bandwidth.⁸

Second, mirrors and gratings need to be aligned and used at *grazing incidence* – i.e., with the incident light striking them at glancing angles just a few degrees from parallel to their surface. At soft x-ray wavelengths, most materials have a refractive index with a real part *less than* one; the phase velocity of light is actually *faster* than it would be in a vacuum. This allows us to exploit the phenomenon of total internal reflection (TIR), except in this case it becomes a *total external reflection*, since the refractive index is higher in the grating material than it is in the vacuum above it. Just as with conventional TIR in glass and air, we can calculate a critical angle above which total external reflection will occur (see Section 5.6). For most metals, this turns out to be around 83 to 85 degrees from the surface normal.

2.3 REIXS spectrometer project

This thesis – and its motivation to establish a better understanding of diffraction grating efficiency – emerged from a primary engineering goal: to design and build a world-class emission spectrometer for the REIXS beamline at the Canadian Light Source. The REIXS (*Resonant Elastic and Inelastic X-ray Scattering*) beamline is optimized for material science experiments; it offers an elliptically-polarizing undulator to produce a high brightness beam of soft x-ray photons, and a high-resolution monochromator with a flux of $\sim 10^{13}$ photons/second and a resolving power greater than 5000. The beamline has room for two endstations; our task was to build the emission spectrometer, which will be used for inelastic scattering experiments, while a team from the University of British Columbia built the second endstation used for elastic scattering measurements.

In Chapter 6, I describe the design process and the resulting optical design of the spectrometer. Used in combination with the work of David Muir on spectrometer resolution [40], the ability to model grating efficiencies allowed us to optimize the design for an intelligent compromise between these two competing goals. In the process, we discovered an efficiency

⁸Gold and platinum do have absorption edges in the soft x-ray range, but these correspond to outer shell electrons (for example, gold 4s electrons bound at 802 eV) instead of core-level electrons. The outer electrons see shielding by the inner ones, and therefore have a lower transition probability.

peak in the 3rd order – typically assumed to be unusable – that prompted us to create an innovative design capable of reaching much higher resolution than would otherwise be possible given the space constraints of the beamline.

Figure 2.11 is a picture of the completed REIXS spectrometer as it nears the end of its commissioning phase in August 2012.

2.4 Summary: why grating efficiency matters

Figure 2.12 lists a variety of soft x-ray spectroscopy techniques, and shows the number of gratings in the beam path to the detector for each. Of these techniques, those in *italic text* are possible on the REIXS beamline; the remaining are possible on other beamlines at the CLS. For all of these techniques, the ability to create more efficient gratings would increase the speed of experiments, improve the quality of data, and increase the minimum concentration of samples that can be feasibly studied.

Conversely, during the design phase of these instruments, the unavoidable tradeoff between resolution and efficiency implies that accurate predictions of the grating efficiency could actually be used to improve *resolution*: by deliberately sacrificing efficiency, designers could push their resolving power to the limit once the efficiency is known to be “good enough”.

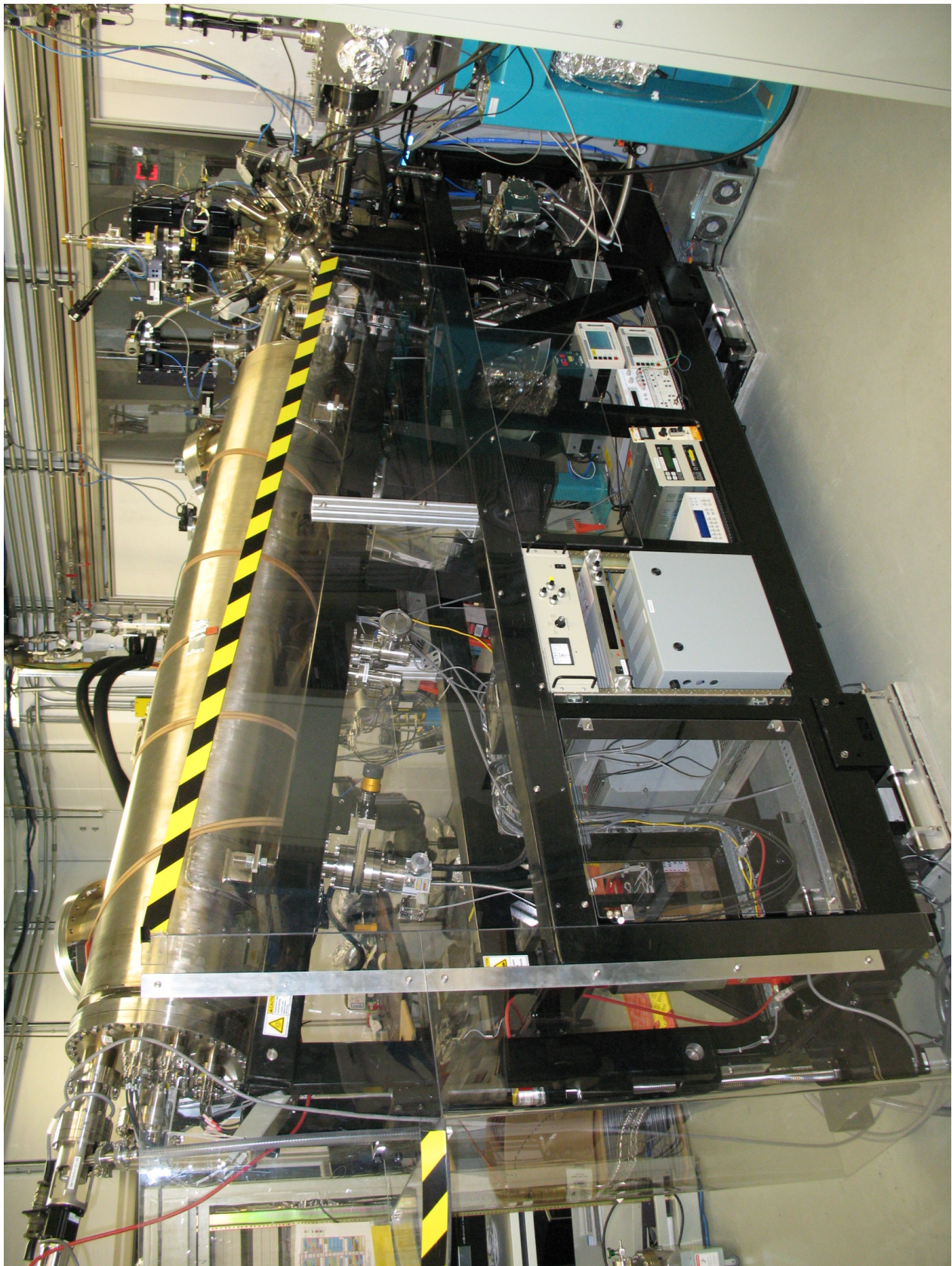


Figure 2.11: The REIXS XES spectrometer, as built, in August 2012.

	Photon In	Electron In
Electron Out	<p><i>Near-edge X-ray Absorption Fine Structure (NEXAFS): electron yield</i> </p> <p>Extended X-ray Absorption Fine Structure (EXAFS): electron yield </p> <p>X-ray Photoelectron Spectroscopy (XPS) </p>	
Photon Out	<p><i>Soft X-ray Emission Spectroscopy (SXE)</i> </p> <p><i>Resonant Inelastic X-ray Spectroscopy (RIXS)</i> </p> <p>X-ray Excited Optical Luminescence (XEOL) </p> <p><i>NEXAFS: fluorescence yield</i> </p>	<p>Electron Energy Loss Spectroscopy (EELS) </p> <p><i>Inverse Photoelectron Spectroscopy (IPES)</i> </p>

Figure 2.12: A variety of soft x-ray spectroscopy techniques, and the number of gratings required in the beam path to accomplish each one. Of these techniques, those in *italic text* are possible on the REIXS beamline using the emission spectrometer endstation. For all these techniques – and particularly those using two gratings – more efficient gratings would increase the speed of experiments, improve the quality of data, and increase the minimum concentration of samples that can be feasibly studied.

CHAPTER 3

THEORY: HOW TO CALCULATE GRATING EFFICIENCY

3.1 Introduction to grating theory

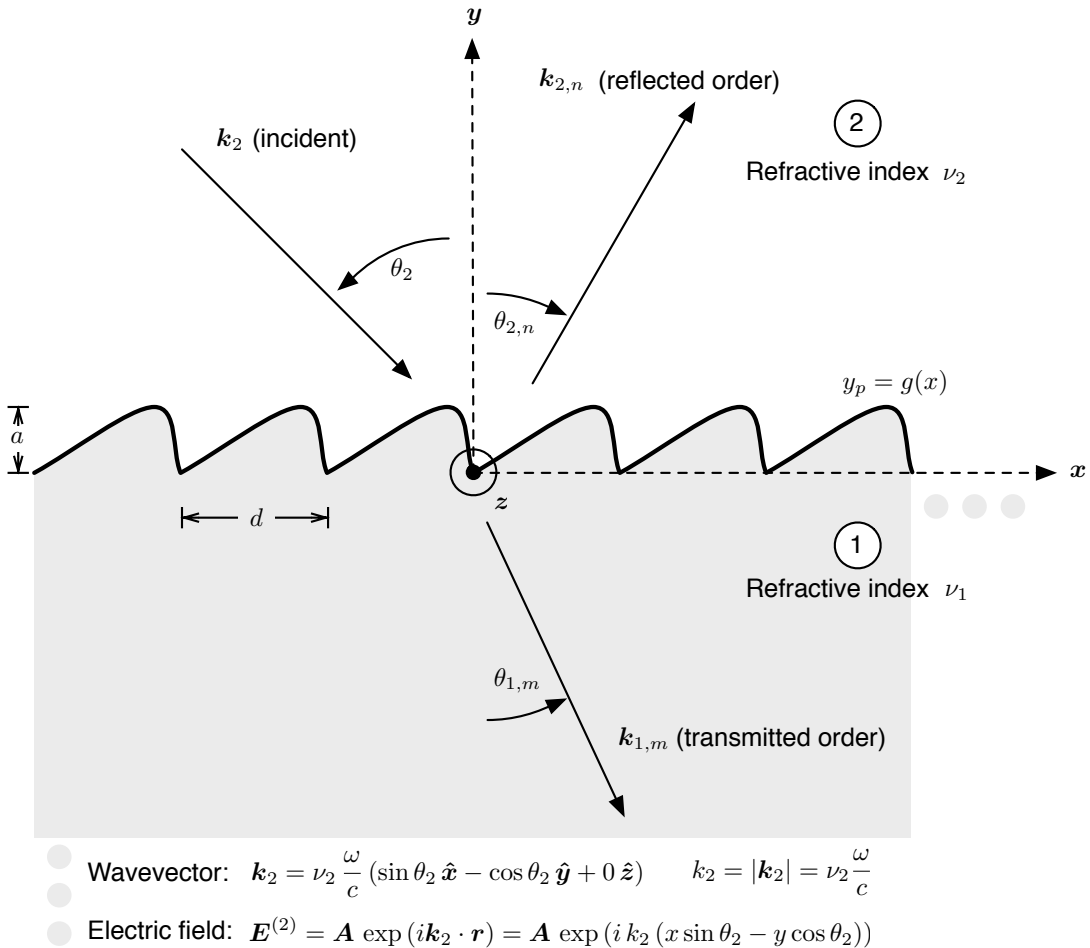


Figure 3.1: A one-dimensional grating with in-plane incidence.

For centuries, we have known that gratings reflect and transmit light at a set of discrete angles – called *orders* – where the angles depend on the wavelength (Figure 3.1). A variety of

simple proofs have been used to explain this. In undergraduate books, the grating equation is introduced as a consequence of constructive interference from a linear array of coherent emitters. (This makes sense for a slotted transmission grating, but it is less obvious why an arbitrarily-shaped periodic reflecting structure like the one in Figure 3.2 would behave the same way.) Other proofs – such as those using Fermat’s Principle to minimize an optical path function with a phase offset introduced by the grating [48, p. 93 – 99] – are general enough to explain the existence of diffraction orders, but they do not say anything about how much light goes into each.

This is unfortunate, because to determine grating efficiency, we must determine the intensity of the orders. A huge amount of research has gone into this question since Lord Rayleigh’s pioneering work in 1907 [61], and some clever analytical methods were even discovered that simplify the problem – but only for certain special groove shapes. It is only within the last twenty years that mathematical techniques and computational power have advanced enough to accurately model the electromagnetic field of light within and near the surface of an arbitrary grating, allowing us to actually determine how energy is distributed between the orders, and how much is absorbed within the grating. In this chapter, we look at a history of the key developments in grating theory, give a comparison of the current methods, and then set up the grating problem using the most general of these methods.

3.1.1 A brief history of grating theory

We define the “grating problem” as the problem of determining the intensity of a grating’s reflected and transmitted light everywhere. In general, this requires finding the solution to Maxwell’s equations for the electric and magnetic fields of the light, in the presence of the grating’s periodic boundary conditions, for a known incident field.

Prior to the availability of computers and numerical techniques, great attempts were made to solve this problem analytically. In 1907, Lord Rayleigh set up the problem¹ using a Fourier approach identical to the one we use later in this chapter [61]. However, without access to

¹Actually, Rayleigh’s first application of this technique was to the diffraction of sound waves [60]. It turns out that the wave equation for a pressure wave in compressible media is the same as for the fields in an electromagnetic wave, and the boundary conditions at interfaces are also analogous. In Reference [61] he shows applications to both sound and light.

powerful numerical methods, he could only make coarse approximations, using expansions truncated at the first or second power of the groove height.² This led to some obviously non-physical results, such as predictions of infinite intensity in any order when the outgoing angle of a higher order reached exactly 90 degrees. From 1907 until 1960, advancements in grating theory amounted to finding clever but limited simplifications to these expansions, which would work in the case of one particular groove profile, incidence angle, or approximation limit.

The introduction of computer-based numerical methods in the 1960s spawned a renewal of research into general solutions to the problem. The first “rigorous” algorithm³ was invented by several researchers in 1966:

The “integral” approach uses Maxwell’s equations in integral form and the Kirchhoff integral theorem [50][76][24]. It was generalized from perfectly conducting (i.e.: perfectly reflecting) gratings to finite-conductivity metallic gratings in an important paper in 1972 [32].

Alongside these “integral” methods, two other broad families of algorithms emerged based on Maxwell’s equations in differential form:

The “modal” method relates the electromagnetic field to a Fourier expansion in the vertical (y) direction with unknown coefficients, called modes. The total field satisfying the boundary conditions is solved algebraically as a linear combination of the modes [4][5][1].

The “differential” methods exploit the periodicity of the grooves to express both the grating boundary and the fields as Fourier expansions in the x -direction. The total field satisfying the boundary conditions is determined by numerically integrating a finite set of differential equations. (We explore the details of this method later in this chapter.)

²This was despite assuming a perfectly reflecting grating, exactly normal incidence, and only one term in the Fourier expansion for the groove shape – i.e., a sinusoidal grating.

³“Rigorous” here implies a method that does not introduce approximations into the theoretical equations, other than inevitably in the process of finite-precision numerical calculations.

The modal methods are not actually general because in their application of the boundary conditions, they require the edges of the grooves to be vertical; this limits them to rectangular gratings. However, they are accurate in this special case, and fast compared to the differential method because they avoid numerical integration. The other two approaches are general in representation, although the stability and accuracy of the integral approach is highly contingent on the groove geometry.

By 1980, grating theorists had devised a wide variety of implementations for each family. Reference [51] provides a comprehensive review of all the methods that were available by this date.⁴ Of the three families, the differential approach had proven to be the most general way of setting up the problem, but it ran into two numerical issues – particularly when used to describe TM-polarized light on highly-conducting metallic gratings. One issue was strictly computational: round-off errors when doing finite-precision computer arithmetic would lead to growing contamination during the numerical integration of exponential functions. This problem was solved by the introduction of the “S-matrix” propagation algorithm in 1996 [28][38]. The second problem was related to the mathematical implications of truncating an infinite Fourier series – unfortunately but obviously necessary for numerical calculations. This challenge was also finally resolved by the breakthrough work of Li [29] in 1996 on the factorization of truncated Fourier series; his method has been applied extensively by Neviere and Popov both to the simple cases of one-dimensional gratings like those shown in Figure 3.1 [57], and to complex three-dimensional periodic structures of anisotropic materials [56][42].

3.1.2 Comparison and applicability of grating theory families

To choose an appropriate method for a particular problem, we need to understand the assumptions and limitations of each one. As a “grating method user’s guide”, this section presents just enough theory to understand their areas of applicability. We cover the integral method, the modal method, and two variations of the differential method. This survey is not exhaustive; additional methods have been developed that are only applicable in specific cases. For example, for certain particular groove profiles, there exist coordinate transforma-

⁴The same author provides a follow-up paper, written ten years later on new methods that differ completely from the fundamentals used in 1980 [52].

tions and “conformal mappings”, which simplify the boundary conditions so that the grating problem can either be solved analytically, or reduced in complexity. We concentrate here on the methods that have been intended for general applications.

The Integral Method

For perfectly conducting metals, an electromagnetic field incident on a surface induces a surface current $\mathbf{j}_S(\mathbf{M}')$ at each point \mathbf{M}' . This surface current radiates a field – the diffracted electric field $\mathbf{E}(\mathbf{P})$ at a given point \mathbf{P} above the surface; the field is related to the surface current by the Kirchhoff Integral Theorem [26] using the Green’s function $G(\mathbf{P}, \mathbf{M}')$:

$$\mathbf{E}(\mathbf{P}) = \int_{\text{grating period}} G(\mathbf{P}, \mathbf{M}') \phi(\mathbf{M}') ds'$$

where ds' is a curvilinear coordinate along the grating profile, and $\phi(\mathbf{M}')$ is proportional to the surface current. Unfortunately, this becomes tricky, because the surface current is not only induced by the incident electric field, but also by the diffracted field radiated from all other points along the grating surface. This means that the surface current $\mathbf{j}_S(\mathbf{M}')$ at \mathbf{M}' depends not on the incident field, but also on the current $\mathbf{j}_S(\mathbf{M}'')$ at all coordinates \mathbf{M}'' . By substituting the corresponding $\phi(\mathbf{M}')$ into the equation above, this transforms it into a second-order integral equation for $\phi(\mathbf{M}')$.

Limitations

In practice, the numerical techniques required to solve this integral equation can be complicated, depending on the shape of the profile. For imperfectly-conducting gratings, the problem becomes even more difficult, and even harder still when the grating is made up of one or many layers – such as over-coated soft x-ray gratings and multilayers. Although it is universal, the main limitation of the integral approach is its computational cost, and the programming difficulty of applying it correctly to every unique grating situation. Numerical challenges abound, particularly regarding the discretization of the grating profile and how sharp corners and discontinuities are handled. Reference [54] presents an overview of integral implementations, as well as approximations for reducing the computation time and handling coating layers. The latest version – referred to as the “modified integral method” by Goray, has been the topic of many recent publications [22] [21] [68] [20].

Methods using Maxwell's Equations in differential form

The remaining two families (the modal method and the differential method) start from Maxwell's equations in differential form. Within the differential method, there are two variants: the “classical” differential method, and the “Rigorous Coupled Wave” (RCW) approach. We present all three here together because they share the same foundation. They all start by projecting the solution to Maxwell's Equations – i.e., the strength of the electric or magnetic field of the waves – onto some periodic basis in the x -direction, but with an unknown dependence on y . The task for each method is to determine the y -dependence by ensuring the total field satisfies the boundary conditions on the grating surface and at infinity. The modal method and the RCW method both assume a rectangular groove profile, so that the boundary conditions are simplified: this implies that the tangential and normal field components at the grating interface are purely along either the x - or y -direction.

The modal method assumes a basis of functions that are periodic in x , with “modes” F_m related to the field $u_m(x)$ as

$$F_m(x, y) = u_m(x) \exp(i\rho_m y)$$

where ρ_m is a “mode constant”. The total field is assumed to be a linear combination of the modes with unknown amplitudes, and since this field must satisfy the boundary conditions on the surface, it is possible to create a set of linear algebraic equations that can be solved for the mode amplitudes.

Limitations

For the modal method, the number of modes and the mode constants ρ_m must be sufficient to fully describe the actual field. For highly conducting materials, finding appropriate mode constants is difficult, but a technique is available in Reference [1].

The other obvious limitation of the modal method is to rectangular gratings with vertical groove boundaries. We can attempt to avoid this limitation by using stacks of thin rectangular gratings to represent an arbitrary shape, as shown in Figure 3.2. This is called the “staircase approximation” for obvious reasons, and is also used in the RCW method. Unfortunately, no matter how thin the slices are made, this approx-

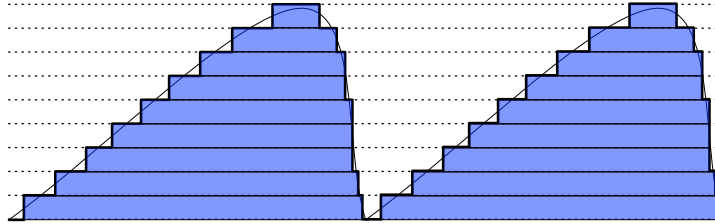


Figure 3.2: The modal method and the RCW method approximate every real grating as a stack of rectangular gratings. This simplifies the boundary conditions (the normal and tangential field components line up either along the x - or y -axis), so that the problem can be reduced to an algebraic solution for the eigenvalues of the modes or the Fourier coefficients. Every layer is treated as a separate grating with its own effect on the incoming and outgoing fields; the total grating effect is propagated up the stack using matrix methods.

imation creates sharp edges between the layers at the stair-step corners. Popov et. al. discovered that for TM-polarized light, this creates unrealistically strong electric fields at the corners, which cannot be physically representative of the true electric field near a smooth grating. Therefore, algorithms that use the staircase approximation require a larger number of basis components to represent this abruptly changing field, which slows down the computation. More importantly, even when there are enough components to let the solution converge, the results are not representative of reality. [58]

The differential method’s “classical solution” uses a periodic field similar to the modal method, except that the basis functions are Fourier expansions in the x -direction, and the unknown functions to solve are along the y -direction:

$$F(x, y) = \exp(ik \sin \theta_2 x) \sum_m F_m(y) \exp\left(\frac{2\pi i x}{d}\right)$$

By matching the total field to the boundary conditions at the top and bottom of the grooves, a set of coupled differential equations is created; this set is solved using a combination of numerical integration and linear algebra, which we describe later in this chapter.

Limitations

The advantage of the classical differential method is that it works for arbitrary groove

profiles. However, for rectangular profiles, it is slower than the other two options because of the necessity to perform a numerical integration for each basis component. The pure differential method originally suffered from numerical convergence problems in TM polarization on conductive gratings, but these were resolved in 1996 [29] [56]. The only remaining limitation is that the method assumes the material can be described by a well-behaved complex dielectric constant (or the related refractive index) both above and inside the grating material. This rules out “perfectly conducting” (i.e., perfectly reflecting) gratings, for which it is not reasonable to assign a dielectric constant. This limitation results in a numerical instability when trying to work with nearly perfectly conducting gratings – for example, gold and aluminum metallic gratings used with deep infrared or millimetre light – where the real part of the refractive index falls below 0.1. (A few suggestions have been proposed recently for extending the differential method to highly conducting gratings, such as by substituting a finite-thickness perfectly-conducting layer above an absorbing substrate. [55])

Because this method conducts a numerical integration using assumed starting values along the y -direction from the bottom to the top of the grooves, if the grooves are very deep, the long integration distance increases the computation time. The stability of the numerical integration process also suffers, because the exponential functions grow to span the precision available with standard floating-point (‘double’) variables. Therefore, the speed and accuracy of the basic differential method are only acceptable for gratings with a low depth-to-period ratio.⁵ Fortunately, the stability issue can be solved using the S-matrix modification to the differential method (Section 3.3.5).

The differential method’s “Rigorous Coupled Wave” approach is a simplification that can be applied for rectangular gratings. As we mentioned in the case of the modal method, when the groove edges are vertical, the boundary conditions within the grooves are invariant along the y -direction. This means that an eigenvalue technique can be used instead of a full numerical integration along y , which reduces the problem to an algebraic solution, speeds up the calculation, and removes the numerical challenges

⁵This limitation is not strictly limited to the differential approach; it affects the numerical integration of the integral method as well.

associated with integrating growing exponentials. As soon as this simplification was proposed, various authors [8] [65] [34] assumed that it could be generalized to arbitrary groove profiles by approximating them with rectangular slices, which could be made as thin as required for a given accuracy; this is the same “staircase approximation” used in the modal method (Figure 3.2). The RCW approach was used extensively for thirty years, and has been shown to produce fast and accurate results for TE-polarized light on dielectric and absorbing gratings. However, as we mentioned above, the fundamental validity of the staircase approximation was challenged in Reference [58].

Limitations

As a differential method, the RCW approach is limited to finitely-conducting materials. It is also limited to rectangular gratings, or (using the staircase approximation) to stacks of rectangular layers in TE polarization. It can also produce approximate results in TM polarization for dielectric gratings.

Figure 3.3 gives a visual comparison of the limitations and strengths of all four techniques. It shows that in general there is no clear “home-run” universal method; the techniques are complementary rather than supplementary. The optimal choice for a particular class of grating problems depends on the overlap between the grating characteristics and the limitations of each method.

Choosing a theoretical method

Since we were primarily interested in the efficiency of soft x-ray gratings used in grazing incidence, the limitations identified above provided clear guidance for choosing an appropriate method. At the frequency of soft x-ray radiation, metals behave as absorbing, weak dielectrics with a refractive index near $(0.999 - 0.001i)$; therefore, we do not need to worry about limitations on perfectly-conducting materials. At grazing incidence, polarization effects are also minimized; there turns out to be very little difference between measured and calculated results for TE and TM polarization.

However, we needed the ability to model a variety of groove profiles, including rectangular, triangular, trapezoidal, and sinusoidal shapes, with at least one coating layer. (The triangular, or “blazed” profile – featuring sharp vertices – turned out to be particularly important

Grating Shape	Conductivity	Polarization	Integral Method	Modal Method	Differential Method (post-2000)	
					RCWA	Numerically Integrated
Rectangular	Dielectric/Absorbing Metal	TE	●	●	●	●
		TM	● ● ● ●	● ●	●	● ● ●
	Perfect Conductor	TE	●	●	●	●
		TM	● ● ● ●	● ● ● ●	●	● ● ● ●
Arbitrary Smooth	Dielectric/Absorbing Metal	TE	●	●	●	●
		TM	● ● ● ●	● ●	●	● ● ●
	Perfect Conductor	TE	●	●	●	●
		TM	● ● ● ●	● ● ● ●	●	●
Very Deep Gratings	Dielectric/Absorbing Metal	TE	●	●	●	●
		TM	● ● ● ● ●	● ● ● ●	●	● ● ● ●
	Perfect Conductor	TE	●	●	●	●
		TM	● ● ● ●	● ● ● ●	●	● ● ● ●

Accuracy: ● Good ●● Approximate ●●● Poor ●●●● Not applicable

Calculation Time: ■ Fast ■■ Good ■■■ Acceptable ■■■■ Slow ■■■■■ Very Slow

Figure 3.3: A visual comparison of the limitations and strengths of the main methods in grating theory: the integral approach, the modal method, the full (numerically integrated) differential method, and the differential method’s “RCW” staircase-approximation simplification.

for our spectrometer design.) Therefore, we ruled out the modal and RCW methods, and were left with a choice between the integral method and the full differential method. Given the necessity of modelling coatings and sharp profiles, we selected the differential method for its simplicity and robustness. We used two implementations of this method for all the grating efficiency calculations, optimizations, and comparisons shown later in this thesis.

3.1.3 Overview of the differential theory

The rest of this chapter lays the groundwork for a full electromagnetic theory describing the interaction of light waves with periodic structures. The conventions we use here are applicable to either the classical differential or RCW methods, and the notation is consistent with the notation used by Neviere in [42]. However, before diving into the details of the mathematics, it might be useful to summarize the basic physical principles behind the solution:

1. The theory starts by using the Maxwell equations to derive a 2nd-order wave equation for the electric and magnetic field of the light. According to classical optics, the incoming light can be divided into two independent polarization components; the TE component has its *electric* field vector always parallel to the z -axis in Figure 3.1, and the TM component has its *magnetic* field vector always parallel to the z -axis. Due to the beautiful symmetry of the Maxwell equations, it turns out that the wave equation for the electric field in TE polarization is the same as the equation for the magnetic field in TM polarization, and for most of the theory we can use the same mathematics to work with both, referred to as the “general field” or just “the field”.⁶ Because the TE and TM polarizations are independent, we can solve the grating problem for both separately, and then combine the diffracted field solutions in proportion to the polarization of the incident light.
2. Because the grating is periodic, we use Fourier series expansions in the horizontal direction to express both the permittivity of the grating material, and the field itself. In the vertical direction, there are three distinct regions:

⁶While the wave equation is the same for both the TE electric field and the TM magnetic field, the boundary conditions for the fields at the grating interface are different and need to be handled separately. This is responsible for the difference in efficiency dependent on polarization.

- Region 2: above the grooves, where the refractive index is uniform ($\nu = \nu_2$);
- Inside the grooves – the “modulated region” – where the refractive index changes as a function of the x and y position: it is either ν_1 or ν_2 ;
- Region 1: below the grooves, inside the grating substrate, where the refractive index is again uniform ($\nu = \nu_1$).

3. Above and below the grooves:

By using the grating as a periodic operator and applying boundary conditions for the field at infinity, we can prove that light is reflected and transmitted at discrete angles, and that a sum of plane waves known as the Rayleigh Expansion can be used to express the total field that satisfies the wave equation in this region. Each propagating plane wave corresponds to a diffraction “order”, and once we know the angle of the incident light, we can determine the angles of the diffraction orders (Figure 3.6). At this point, the Rayleigh expansion still has unknown coefficients, and we need to determine these coefficients to find out how much energy is diffracted into each order.

4. Within the grooves:

However, the field within the grooves depends on the exact shape of the groove profile and the interaction of light within the material. It cannot be simply represented as a sum of plane waves, and the boundary conditions are complicated. There are two leading methods used to handle this. Both express the wave equation using Fourier expansions for the field and the grating permittivity. (These expansions would theoretically be infinite sums, therefore they need to be truncated for computer calculations. Special rules apply for accurately calculating the products of truncated Fourier series when they have discontinuities – for example, the normal component of the electric field at the grating boundary; these were discovered by Li in Reference [29].)

- (a) In the “Rigorous Coupled Wave” (RCW) approach [34] [37], the grating groove shape is sliced into thin layers (Figure 3.2) and approximated with vertical walls between layers: the “staircase approximation”. This simplifies the boundary conditions because the normal and tangential field components are either entirely

along the x - or y -axis; thus, at every layer the boundary value problem can be converted into a set of simultaneous linear equations and solved algebraically. Each layer is treated as a separate grating, and the effects of each layer on the up-going and down-going fields are propagated to the next using matrix methods. (As we describe in Section 3.1.2, the RCW accuracy and convergence suffers in TM polarization because the staircase approximation introduces sharp corners and artificially large electric field components at the step boundaries [58].)

- (b) In the “Differential Method” approach [56], we numerically integrate the wave equation many times using different assumed initial values, to generate a complete orthogonal set of particular solutions. Then we use techniques of linear algebra to solve for the coefficients of the general solution that satisfy the boundary conditions along the grating interface.
5. Finally, most common grating structures consist of one (or often many) stacked layers.⁷ (Typical and contrived examples are shown in Figures 3.4 and 3.5). In classical optics, the *reflection matrix* and *transmission matrix* are often used to propagate an incoming field through an optical layer. We can generalize this concept to gratings by defining a matrix that maps the Rayleigh coefficients of the incident field to the coefficients of the field that is reflected and transmitted by each layer. The matrices for each layer can then be multiplied together to find the effect of the complete grating; this is known as the “T-matrix” approach. While theoretically sound, the T-matrix becomes unstable in computer calculations because rounding errors introduce instability into growing exponential functions. An alternative formulation called the “S-matrix” approach defines a matrix at each layer that represents the cumulative effect of *all layers below and including that layer* on the incident field; by definition, this matrix remains bounded and is safe to use for numerical calculations [28]. This matrix links the Rayleigh coefficients of the up-going and down-going waves between each layer with the more complicated functions within the grooves of each layer, where the Rayleigh expansion does not apply.

⁷For example, dielectric gratings with a metal coating used for soft x-ray beamlines, gratings with thin-film multilayer coatings, etc.

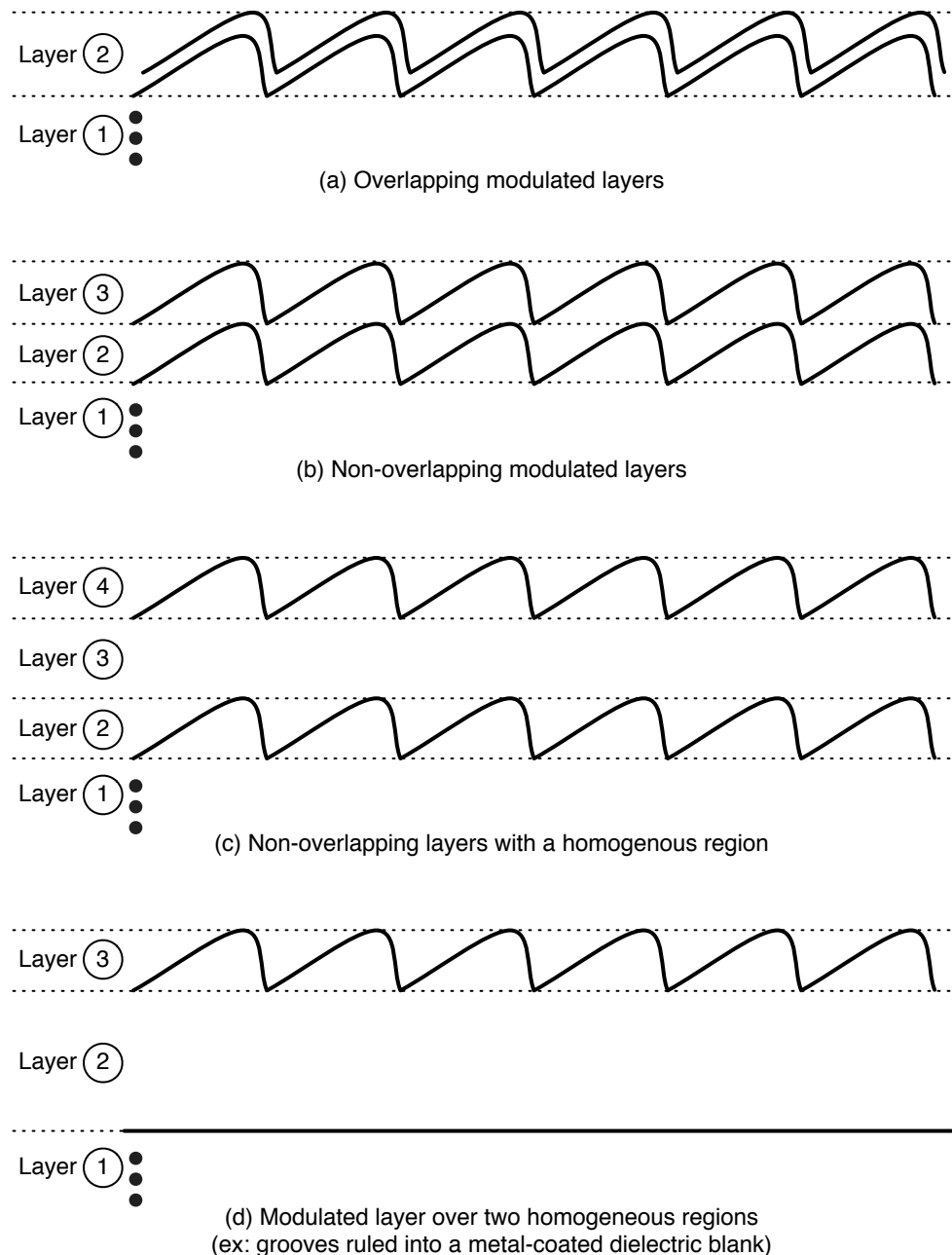


Figure 3.4: Arbitrarily-complicated structures can be handled by dividing the grating into layers, where each layer is either homogenous (constant refractive index), or modulated (with a refractive index that changes periodically as a function of x at any given height y).

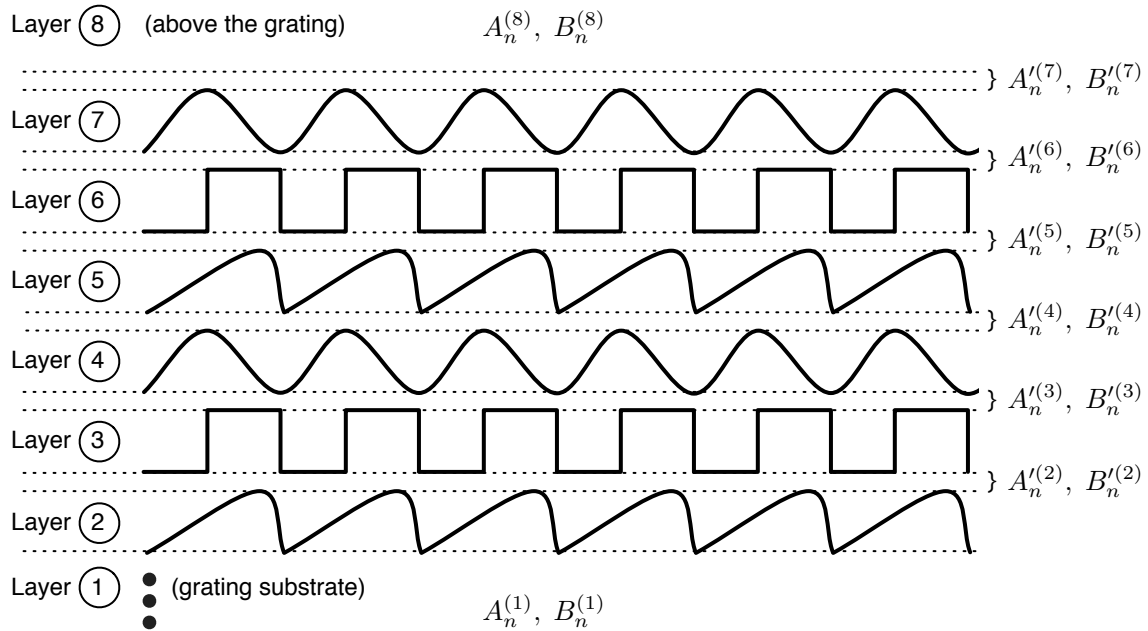


Figure 3.5: Modulated layers in a complicated stack of gratings. In between every layer, we can insert an imaginary, infinitely-thin homogenous layer where the Rayleigh expansion applies. The A'_n and B'_n expansion coefficients connect the boundary conditions between layers. Within each layer, the Rayleigh expansion does not apply – inside the grooves, the field cannot be represented as a simple sum of plane waves – and numerical methods are required to approximate it.

3.1.4 Simplifying assumptions

Before we tackle the mathematics of grating theory, this section defines the geometry and terminology we use throughout the text, and introduces some assumptions that simplify the problem. Figure 3.1 shows a side view of a reflection grating, in the following situation:

1. The mean surface of the grating is in the $x - z$ plane, with the grooves running parallel to the z -axis. The groove profile is periodic and repeats every distance d along the x -axis.
2. The grating is described by the profile function $y_p = g(x)$, which has a minimum of $y = 0$, a maximum $y = a$, and is periodic on d :

$$y_p = g(x) = g(x + d)$$

3. The grating is illuminated with a light ray travelling parallel to the $x - y$ plane (i.e.: within the plane of the page). This is referred to as “in-plane incidence”, and is typical of how most monochromators and spectrometers are used. (When the incident ray has a component in the z -direction, the diffraction peaks end up dispersed over the surface of a three-dimensional cone, and this is referred to as “conical mounting”.)

These first three simplifications reduce the grating problem to two dimensions, since the whole system is unchanged by translation along the z -axis.

Additionally, we assume that:

1. The incident light can be represented as a plane wave, infinite in extent.
2. The grating also stretches forever in the x - and z -directions.

Typical gratings used in soft x-ray devices are far, far larger (typically: 40 mm) than their groove spacing d (typically: a few μm). As long as they are illuminated with collimated light having a beam width much larger than the groove spacing, both of these assumptions seem reasonable.

Finally, to simplify the electromagnetic field calculations, we assume that

1. The grating material is non-magnetic, with a permeability of μ_0 .

2. The dielectric constant ϵ of the grating material is the same in all directions.

(These last two assumptions are also necessary to keep us within a two-dimensional problem. If the material is non-isotropic, then the dielectric constant ϵ becomes a tensor $[[\epsilon]]$ and the problem requires a full 3D analysis.)

These assumptions make the grating theory much simpler to present in this chapter. However, it should be noted that at the expense of larger matrices and higher mathematical complexity, it is possible to express the same theory in the full three-dimensional case, which enables the analysis of exotic situations like conical mount gratings, crossed 2D gratings, and non-isotropic materials. Reference [42, Chapter 5] provides a derivation of the full 3D version.

We assume that the grating surface exactly matches the periodic profile given by $y_p = g(x)$ in Figure 3.1. For real-world applications, this turns out to be the most unfounded assumption, since actual gratings vary from groove to groove due to imperfections in the manufacturing process, and their ideally smooth surfaces have an unavoidable amount of random roughness. Unfortunately, this assumption is necessary for any mathematical treatment; in Section 7.3, we look at the impacts of real-world imperfections on grating efficiency.

A few notes on notation:

- Quantities that change depending on the grating region are subscripted to indicate the region they are in. For example, k_2 and ν_2 designate the wave vector and refractive index, and $\theta_{2,n}$ the angle of the n -th order ray, in Region 2 above the grating. Eventually, we tackle layered gratings with many numbered regions, and this subscript convention becomes helpful.
- Angles are measured from the surface normal as shown in Figure 3.1. There are two different sign conventions in common use; we use positive angles for both the incident ray (θ_2) and the diffracted ray ($\theta_{2,n}$) when they are on opposite sides of the surface normal. Transmitted rays ($\theta_{1,n}$) are also measured using positive angles from the $-y$ axis, as shown in Figure 3.1.⁸

⁸The sign convention for diffraction angles affects the sign in the right-hand side of the grating equation

3.1.5 Electromagnetic field and polarization

In Figure 3.1, incoming light strikes the grating along wavevector \mathbf{k}_2 at an angle θ_2 from perpendicular to the grating plane:

$$\mathbf{k}_2 = \nu_2 \frac{\omega}{c} (\sin \theta_2 \hat{\mathbf{x}} - \cos \theta_2 \hat{\mathbf{y}} + 0 \hat{\mathbf{z}}).$$

We use ν to designate the refractive index. Here, ν_2 designates the refractive index in Region 2 above the grating, which is normally air or vacuum. (In Region 1, the grating material might be absorbing, which means the material's refractive index ν_1 would have an imaginary component greater than 0.) Frequency $\omega = 2\pi f$ is the angular frequency of the light, and c is the speed of light in vacuum.

The incoming light is a travelling electromagnetic plane wave with sinusoidal dependence on time. We can express the electric field vector using the complex exponential form

$$\mathbf{E}_{incident} = \mathbf{A} \exp(i(\mathbf{k}_2 \cdot \mathbf{r} - \omega t)) = \mathbf{A} \exp(i k_2(x \sin \theta_2 - y \cos \theta_2)) \exp(-i\omega t), \quad (3.1)$$

where the true (physical) field is contained in the real part. Since all fields will have the same harmonic dependence on time, we drop the $e^{-i\omega t}$ factor from here on. (The scalar k_2 is simply the magnitude of \mathbf{k}_2 , i.e.: $k_2 = |\mathbf{k}_2| = \nu_2 \omega / c$.)

The electric field vector is always perpendicular to the direction of the wave \mathbf{k}_2 , but can have an arbitrary polarization determined by \mathbf{A} . This can always be expressed as a superposition of two orthogonal components:

- The TE polarization represents the component of the electric field vector parallel to the z axis (i.e.: into the page). For a pure TE wave, the E_x , E_y , and B_z fields are always 0.
- The TM polarization represents the component of the electric field vector in the $x - y$ plane (i.e.: the *magnetic* field vector is along z). For a pure TM wave, the E_z , B_x , and B_y fields are always zero.

(3.19). In North American literature it is more common to measure all angles positive counter-clockwise from the surface normal; this creates a '+' rather than a '-' in the grating equation.

In general, the grating problem is solved by applying the Maxwell equations to the incident electric field, according to the boundary conditions imposed by the grating. By solving it separately for each polarization case (TE and TM), we can simplify these equations. In the end, we superpose the results calculated for the outgoing fields, weighted by the actual polarization of the incident light.

3.1.6 Maxwell's equations for sinusoidal time-varying fields

Our assumptions in Section 3.1.4 mean that the gratings are not loaded with free charge, or carrying free currents. Therefore, the two relevant Maxwell equations are:

$$\nabla \times \mathbf{E} = -\frac{\partial \mathbf{B}}{\partial t},$$

$$\nabla \times \mathbf{B} = \mu\epsilon \frac{\partial \mathbf{E}}{\partial t}.$$

For sinusoidal time-varying fields, both fields are proportional to $e^{-i\omega t}$, so the time derivatives reduce to:

$$\nabla \times \mathbf{E} = i\omega\mu\mathbf{H},$$

$$\nabla \times \mathbf{H} = -i\omega\epsilon\mathbf{E},$$

or, expressed in Cartesian coordinates:

$$\frac{\partial E_z}{\partial y} - \frac{\partial E_y}{\partial z} = i\omega\mu H_x, \quad (3.2)$$

$$\frac{\partial E_x}{\partial z} - \frac{\partial E_z}{\partial x} = i\omega\mu H_y, \quad (3.3)$$

$$\frac{\partial E_y}{\partial x} - \frac{\partial E_x}{\partial y} = i\omega\mu H_z, \quad (3.4)$$

$$\frac{\partial H_z}{\partial y} - \frac{\partial H_y}{\partial z} = -i\omega\epsilon E_x, \quad (3.5)$$

$$\frac{\partial H_x}{\partial z} - \frac{\partial H_z}{\partial x} = -i\omega\epsilon E_y, \quad (3.6)$$

$$\frac{\partial H_y}{\partial x} - \frac{\partial H_x}{\partial y} = -i\omega\epsilon E_z. \quad (3.7)$$

Since the grating and the incident light are uniform along the z -axis, all of the partial derivatives with respect to z are 0.

For TE polarization, since E_x , E_y , and H_z are 0, Equations (3.4), (3.5), and (3.6) become trivial, and Equations (3.2), (3.3), and (3.7) are decoupled into

$$\frac{\partial E_z}{\partial y} = i\omega\mu H_x, \quad (3.8)$$

$$-\frac{\partial E_z}{\partial x} = i\omega\mu H_y, \quad (3.9)$$

and

$$\frac{\partial H_y}{\partial x} - \frac{\partial H_x}{\partial y} = -i\omega\epsilon E_z. \quad (3.10)$$

We can use (3.8) and (3.9) to eliminate H_x and H_y in (3.10):

$$\frac{i}{\omega\mu} \frac{\partial^2 E_z}{\partial x^2} + \frac{i}{\omega\mu} \frac{\partial^2 E_z}{\partial y^2} = -i\omega\epsilon E_z.$$

Note that ϵ is a function of position $\epsilon(x, y)$, since it changes whether inside the grating or above the grating. Since

$$k^2(x, y) = \nu^2(x, y) \omega^2/c^2 = \omega^2\mu\epsilon(x, y),$$

we get a single second-order wave equation in E_z :

$$\nabla^2 E_z + k^2 E_z = 0, \quad (3.11)$$

where $E_z = E_z(x, y)$ and $k^2 = k^2(x, y)$ are both functions of position.

For the case of TM polarization, the Maxwell equations (3.5), (3.6), and (3.4) reduce to

$$\begin{aligned} \frac{\partial H_z}{\partial y} &= -i\omega\epsilon E_x, \\ -\frac{\partial H_z}{\partial x} &= -i\omega\epsilon E_y, \\ \frac{\partial E_y}{\partial x} - \frac{\partial E_x}{\partial y} &= i\omega\mu H_z, \end{aligned}$$

and an identical procedure produces the wave equation in H_z :

$$\nabla \left[\frac{1}{k^2} \nabla H_z \right] + H_z = 0. \quad (3.12)$$

In general, k here is still a function of position $k(x, y)$ depending on whether we are inside or outside of a groove valley, or above or below the modulated region. However, in the homogenous space above and below the modulated region, k is constant and both (3.11) and (3.12) reduce to the Helmholtz equation

$$\nabla^2 U_z + k^2 U_z = 0.$$

Due to the (near) symmetry of the Maxwell equations, the form of the wave equation in homogeneous space is the same for the $U_z = H_z$ field in TM polarization as it is for the $U_z = E_z$ field in TE polarization. To solve the grating problem, we need to find the solution to this wave equation in the presence of the grating boundary conditions.⁹

3.1.7 Periodicity of gratings and fields (Pseudo-periodic functions and the Fourier basis)

The periodic nature of the grating grooves immediately hints that we could represent them conveniently using a Fourier series. But can a Fourier expansion also be used to represent the fields E_z and H_z ?

Here we define $u = E_z$ when working in TE polarization, and $u = H_z$ when working in TM polarization; it represents the “generic field”. The grating can be imagined as an operator \mathbb{G} that transforms the incident field u_i into a diffracted field u :

$$u(x, y) = \mathbb{G} u_i(x, y).$$

Because the grating is periodic and extends to infinity, the operator \mathbb{G} is invariant (does not change) under translation by a grating period: $x \rightarrow x + d$:

$$u(x + d, y) = \mathbb{G} u_i(x + d, y).$$

Since the incident light arrives at an angle θ_2 , this translation adds an extra path distance $d \sin \theta_2$ to the incident wave u_i , for a phase change $e^{ik_2 d \sin \theta_2}$:

$$u_i(x + d, y) = e^{ik_2 d \sin \theta_2} u_i(x, y) = C u_i(x, y),$$

⁹Although the wave equation is the same, the boundary conditions for electric and magnetic fields are different at the grating boundary where ϵ and v change suddenly – for example, the normal component of the electric field is discontinuous, while the normal component of the magnetic field is continuous. This leads to a difference in the TE and TM efficiency.

where the constant C has been matched to $e^{ik_2 d \sin \theta_2}$.

Because the set of coupled Maxwell partial differential equations (3.2) to (3.7) is linear, any solution multiplied by a constant C is still a solution:

$$\begin{aligned} u(x, y) &= \mathbb{G}(u_i(x, y)) \\ C u(x, y) &= \mathbb{G}(C u_i(x, y)) \\ C u(x, y) &= \mathbb{G} u_i(x + d, y), \end{aligned}$$

but since $\mathbb{G} u_i(x + d, y) = u(x + d, y)$ also,

$$C u(x, y) = u(x + d, y).$$

In other words, the total field translated by one period d is equal to its untranslated self, multiplied by a complex constant:

$$u(x + d, y) = C u(x, y) = e^{ik_2 d \sin \theta_2} u(x, y) = e^{i\alpha_0 d} u(x, y),$$

where we have defined

$$\boxed{\alpha_0 \equiv k_2 \sin \theta_2}.$$

This is known as a *pseudo-periodic* relationship:

$$u(x + d, y) = e^{i\alpha_0 d} u(x, y),$$

since a true (strictly) periodic relationship would have the form

$$v(x + d, y) = v(x, y).$$

However, we can easily create such a function by defining $v \equiv e^{-i\alpha_0 x} u$. As a legitimately periodic function, v can be represented as a Fourier series expansion on the grating period d :

$$\begin{aligned} v(x, y) &= e^{-i\alpha_0 x} u(x, y) \\ v(x, y) &= \sum_{n=-\infty}^{\infty} u_n(y) e^{i2\pi n x / d} \\ u(x, y) &= e^{i\alpha_0 x} \sum_{n=-\infty}^{\infty} u_n(y) e^{i2\pi n x / d}. \end{aligned}$$

If we define

$$\alpha_n \equiv \alpha_0 + 2\pi n/d,$$

we can express the total field as something that looks *very close* to a Fourier series expansion:

$$u(x, y) = \sum_{n=-\infty}^{\infty} u_n(y) e^{i\alpha_n x}. \quad (3.13)$$

This is the Fourier basis for the total field $u = E_z$ or H_z , with an infinite number of Fourier coefficients u_n . (Eventually, we will need to truncate this series to work with it numerically.)

3.1.8 Deriving the Grating Equation

Equipped with a Fourier expansion for the total field and a wave equation, we can attempt to solve for the field. Figure 3.1 shows the coordinate system sliced into three regions:

- Region 2: Above the grooves where $y > a$, the impedance $k(x, y)$ is constant and proportional to the refractive index of the air/vacuum: $k_2(x, y) = v_2\omega/c$.
- Region 1: Below the grooves where $y < 0$, the impedance $k(x, y)$ is also constant and proportional to the grating's refractive index: $k_1(x, y) = v_1\omega/c$.
- Inside the grooves where $0 < y < a$, the impedance is changing as a function of position: whether inside or outside of a groove. We ignore this difficult region for now and try to work with the uniform regions as much as possible.

Where $k(x, y)$ is constant, the wave equations for both TE (3.11) and TM polarization (3.12) reduce to

$$\nabla^2 u + k^2 u = 0,$$

where $k = k_1$ above the grating, and $k = k_2$ below it. If we insert the Fourier expansion for the field $u(x, y) = \sum u_n(y) e^{i\alpha_n x}$ into the wave equation:

$$\begin{aligned} \nabla^2 \left(\sum_{n=-\infty}^{\infty} u_n(y) e^{i2\pi nx/d} e^{i\alpha_0 x} \right) + k^2 \sum_{n=-\infty}^{\infty} u_n(y) e^{i2\pi nx/d} e^{i\alpha_0 x} &= 0, \\ e^{i\alpha_0 x} \sum_{n=-\infty}^{\infty} \left(\frac{\partial^2}{\partial y^2} + (k^2 - (\alpha_0 + 2\pi n/d)^2) \right) u_n(y) e^{i2\pi nx/d} &= 0. \end{aligned}$$

For this Fourier sum to be equal to zero, all of the coefficients must be zero:

$$\begin{aligned} \left(\frac{\partial^2}{\partial y^2} + (k^2 - (\alpha_0 + 2\pi n/d)^2) \right) u_n(y) &= 0, \\ \left(\frac{\partial^2}{\partial y^2} + (k^2 - \alpha_n^2) \right) u_n(y) &= 0. \end{aligned}$$

This is a standard differential equation with the solution

$$u_n(y) = A_n e^{-i\beta_n y} + B_n e^{i\beta_n y},$$

where

$$\beta_n = \sqrt{k^2 - \alpha_n^2},$$

and A_n and B_n are unknown constants to be determined by the boundary conditions.

Special attention must be paid to the square root for β_n , depending on whether we are above or below the grating.

Above the grooves

Above the grating, we are likely inside air or vacuum ($k = k_2$), so the refractive index ν and k are real. Since $\alpha_n = \alpha_0 + 2\pi n/d$ increases with n , there is a finite number of n near $n = 0$ where $(k^2 - \alpha_n^2)$ is a positive number. However, there are also an infinite number of n (approaching $n \rightarrow \infty$ and $n \rightarrow -\infty$) where $(k^2 - \alpha_n^2) < 0$. This creates two possibilities for β_n (that we label $\beta_n^{(2)}$ because we are in Region 2):

$$\begin{aligned} \beta_n^{(2)} &= \sqrt{k^2 - \alpha_n^2}, & (k^2 - \alpha_n^2) > 0 && \text{(finite occurrences, } \beta_n^{(2)} \text{ real)} \\ \beta_n^{(2)} &= i\sqrt{\alpha_n^2 - k^2}, & (k^2 - \alpha_n^2) < 0 && \text{(infinite occurrences, } \beta_n^{(2)} \text{ complex)} \end{aligned}$$

Using this solution for the Fourier coefficients u_n , the total field is

$$u(x, y) = \sum_{n=-\infty}^{\infty} A_n^{(2)} e^{i\alpha_n x - i\beta_n^{(2)} y} + \sum_{n=-\infty}^{\infty} B_n^{(2)} e^{i\alpha_n x + i\beta_n^{(2)} y}.$$

This result is remarkable. The total field created above the grating is a finite sum of propagating plane waves (for all n where $\beta_n^{(2)}$ is real) and an infinite sum of decaying (when $\beta_n^{(2)}$ is complex) plane waves.

To expand on this conclusion: The first sum (with $A_n^{(2)}$ coefficients) are waves travelling in the $-y$ direction, down toward the grating. For the finite set of n where $\beta_n^{(2)}$ is real, these are non-decaying, normal waves. There is also an infinite number of exponentially growing waves that explode as $y \rightarrow +\infty$, for the remaining n that cause $\beta_n^{(2)}$ to be complex.

Similarly, the second sum (with $B_n^{(2)}$ coefficients) represents waves travelling away from the grating, in the $+y$ direction. There is a finite set of propagating waves, and an infinite set of exponentially decaying waves (“*evanescent waves*”) that tend to zero as $y \rightarrow +\infty$.

The total field has a unique solution only when the incident field u_i is totally specified. From the grating setup in Figure 3.1, we know that we only have a single down-going wave, corresponding to the incident plane wave; all of the $A_n^{(2)}$ for the other propagating waves must be 0. (We label this incident wave with $n = 0$.) We also need to reject the non-physical waves that explode as $y \rightarrow +\infty$, therefore the expansion of the field *above the grating* simplifies to

$$u(x, y) = A_0^{(2)} e^{i\alpha_0 x - i\beta_0^{(2)} y} + \sum_{n=-\infty}^{\infty} B_n^{(2)} e^{i\alpha_n x + i\beta_n^{(2)} y}. \quad (3.14)$$

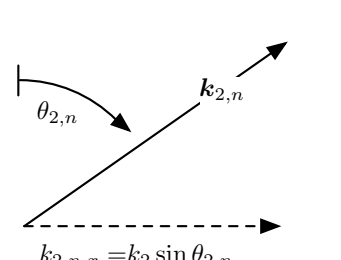
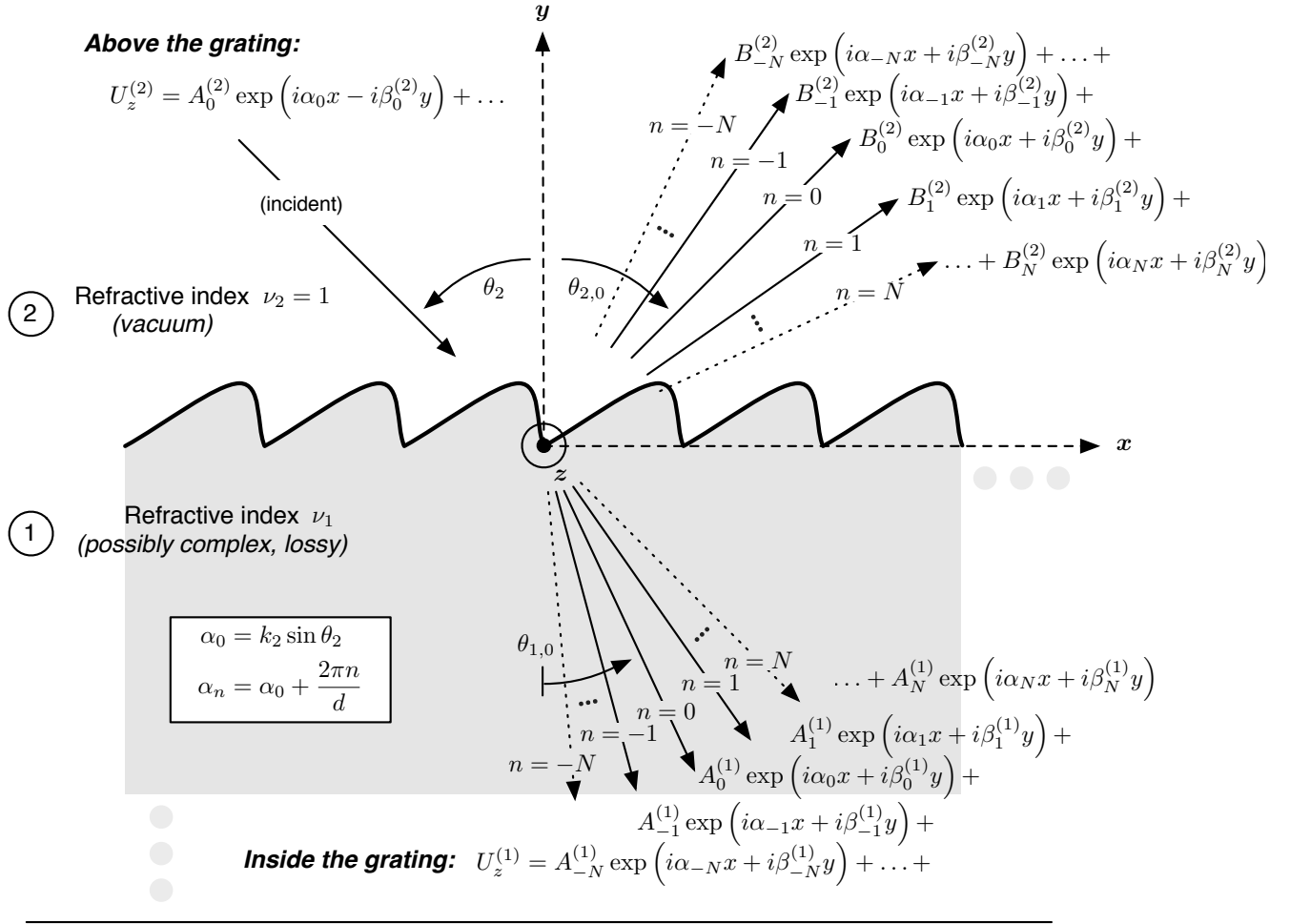
The diffraction grating’s reflected orders appear out of this expansion as the finite set of n , $\beta_n^{(2)}$, and $B_n^{(2)}$ values that create propagating plane waves travelling away from the grating. At this point, n can now be properly identified with the *diffraction order*. This is known as the *Rayleigh Expansion* for the diffraction field. (Rayleigh assumed this solution, but did not prove it, in Reference [61].) Figure 3.6 shows this visually and mathematically.

Below the grooves

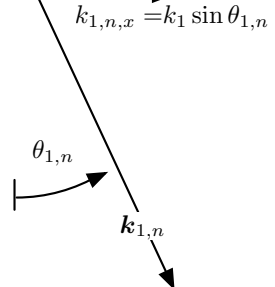
The field inside the substrate ($y < 0$) can be expanded using the same technique. One complication is that for grating materials that absorb energy, the refractive index (and hence $k = k_1$) is complex.¹⁰ In this situation there are two possibilities for the square root $\beta_n^{(1)} = \sqrt{k_1^2 - \alpha_n^2}$. The correct choice can be made by requiring that the diffracted waves remain bounded when $y \rightarrow -\infty$; this requires choosing the root where $\text{Im}(\beta_n^{(1)}) > 0$.

Applying the same process as above, we determine an expansion for the transmitted field,

¹⁰In fact, this is the case for all materials at soft x-ray wavelengths.



Reflected wavevectors $k_{2,n}$



Transmitted wavevectors $k_{1,n}$

Figure 3.6: The Rayleigh expansion describes the electric field (TE polarization) or magnetic field (TM polarization) in homogenous media, above and below the grating. The terms in the expansion include a finite number of propagating plane waves – the diffraction orders – and an infinite number of decaying, or “evanescent” plane waves. From the geometry of the diffracted and transmitted wave vectors, we can derive the grating equation, but we need to solve the A_n and B_n coefficients to determine the efficiency of each order.

corresponding to the transmitted orders. These are also shown visually in Figure 3.6:

$$u(x, y) = \sum_{n=-\infty}^{\infty} A_n^{(1)} e^{i\alpha_n x - i\beta_n^{(1)} y}. \quad (3.15)$$

The grating equations

These expansions for the reflected and transmitted fields show that as soon as the direction of the incident wavevector is fixed, the outgoing directions of light are determined. For the *reflected* orders, Equation (3.14) gives the x - and y -components of the wavevectors:

$$B_n^{(2)} e^{i(k_x x + k_y y)} = B_n^{(2)} e^{i(\alpha_n x + \beta_n^{(2)} y)},$$

where matching the x -components gives:

$$\begin{aligned} k_x &= \alpha_n \\ &= \alpha_0 + \frac{2\pi n}{d} \\ &= k_2 \sin \theta_2 + \frac{2\pi n}{d}. \end{aligned}$$

From the geometry analyzed in Figure 3.6, the x -component of the outgoing wavevector at angle $\theta_{2,n}$ is $k_2 \sin \theta_{2,n}$. Therefore,

$$k_x = k_2 \sin \theta_2 + \frac{2\pi n}{d} = k_2 \sin \theta_{2,n}, \quad (3.16)$$

and, after replacing the magnitude of the wavevector above the grating $k_2 = \nu_2 \omega/c = \nu_2 2\pi f/c = 2\pi/\lambda$, the famous grating equation (for reflected orders) is finally

$$\frac{n\lambda}{d} = \sin \theta_{2,n} - \sin \theta_2, \quad (3.17)$$

(where we have assumed that $\nu_2 = 1$ because we are in free space, and λ is also the free-space wavelength.) This is often called the *Fraunhofer Grating Equation*.

When $n = 0$, the grating equation reverts to the law of reflection ($\theta_{2,0} = \theta_2$, i.e.: the angle of reflection is equal to the angle of incidence.) This wave corresponds to a classically-reflected wave from a normal surface. The reflected orders that fall *between* the incident wave and the $n = 0$ reflection are referred to as *inside orders*; using our sign convention for

diffraction angles, they correspond to $n < 0$. The *outside orders* ($n > 0$, see Figure 3.6) are diffracted at angles beyond the $n = 0$ reflection.

We can also use the same technique to determine the angles of the transmitted orders. Equation (3.15) gives the x - and y -components of the transmitted wavevectors:

$$A_n^{(1)} e^{i(k_x x + k_y y)} = A_n^{(1)} e^{i(\alpha_n x + \beta_n^{(1)} y)},$$

$$k_x = \alpha_n = \alpha_0 + \frac{2\pi n}{d} = k_2 \sin \theta_2 + \frac{2\pi n}{d}.$$

From the geometry analyzed in Figure 3.6, the x -component of the outgoing wavevector at angle $\theta_{1,n}$ is $k_1 \sin \theta_{1,n}$. Therefore,

$$k_x = k_2 \sin \theta_2 + \frac{2\pi n}{d} = k_1 \sin \theta_{1,n}, \quad (3.18)$$

and, after again replacing k_1 , the magnitude of the wavevector below the grating with $k_1 = \nu_1 \omega/c = \nu_1 2\pi f/c = \nu_1 2\pi/\lambda$, the transmission grating equation is

$$\frac{n\lambda}{d} = \nu_1 \sin \theta_{1,n} - \nu_2 \sin \theta_2. \quad (3.19)$$

This time, instead of checking for the law of reflection, we can check that when $n = 0$, the transmission equation reverts to Snell's law of refraction ($\nu_1 \sin \theta_{1,0} = \nu_2 \sin \theta_2$).

Note: Simplifying β_n

Equations (3.16) and (3.18) provide a useful simplification for β_n . Since

$$k_2 \sin \theta_2 + \frac{2\pi n}{d} = k_2 \sin \theta_{2,n} = k_1 \sin \theta_{1,n},$$

we can go back to the expression for β_n , and easily show that

$$\begin{aligned} \beta_n^{(2)} &= \sqrt{k_2^2 - \alpha_n^2} = \sqrt{k_2^2 - (\alpha_0 + 2\pi n/d)^2} \\ &= \sqrt{k_2^2 - (k_2 \sin \theta_2 + 2\pi n/d)^2} \\ &= \sqrt{k_2^2 - (k_2 \sin \theta_{2,n})^2} \\ &= \sqrt{k_2^2 (1 - \sin^2 \theta_{2,n})} \\ &= \sqrt{k_2^2 \cos^2 \theta_{2,n}} \\ &= k_2 \cos \theta_{2,n}. \end{aligned}$$

Similarly, for the transmitted orders,

$$\beta_n^{(1)} = k_1 \cos \theta_{1,n}.$$

Finishing the grating problem

Based only on Maxwell's equations and an assumption of periodicity, we have shown that a grating reflects and transmits light into a set of discrete angles. Incredibly, this result is fully general – it does not depend at all on the shape or nature of the grating profile; all that's required is that it be periodic. Unfortunately, this impressive result still says nothing at all about the *grating efficiency*, or the *amount* of light diffracted into each order. We still do not know anything about the *amplitudes* B_n , A_n of the diffracted plane waves, and to determine these coefficients we will need to get down and dirty inside the grooves of the grating.

Within the grooves, the wave equations (3.11), (3.12) are much more difficult to solve due to the position-dependence of $k(x, y)$. The refractive index (and therefore the impedance k) changes whether inside or outside of a groove; if the grating shape is complicated, $k(x, y)$ is a complicated function indeed. At this point, we need to apply the numerical integration techniques of the classical differential method, or the eigenvalue method used in the RCW approach. Before going there, we take a closer look at defining grating efficiency.

3.2 Defining Grating Efficiency

In spectroscopy applications, experimenters typically illuminate a grating with light and use a single outgoing order ($n \neq 0$) to resolve the light by wavelength. If they are concerned about optimizing the amount of light delivered to their experiment, the efficiency question that matters to them is, “*How much light do we get out of the grating* (in the useful order), *compared to how much light went in?*” Fundamentally, this depends on how much energy is absorbed in the grating itself, and how the remaining energy is distributed between orders.

We can define the grating efficiency for a single order rigorously in the same way. For electromagnetic plane waves, the *Poynting Vector* represents the energy flux (or energy per

unit area, W/m²) carried by the wave:

$$\mathbf{S} = \mathbf{E} \times \mathbf{H}.$$

This gives the instantaneous energy flux, which oscillates in time with the wave. The *time-averaged Poynting vector* gives the average flux delivered over a full period of the wave. For harmonic waves, this works out to

$$\bar{S} = \frac{1}{2} \operatorname{Re}(\mathbf{E} \times \mathbf{H}^*),$$

where \mathbf{H}^* denotes the complex conjugate of \mathbf{H} .

Energy is conserved – between incidence, reflection, transmission, and absorption – over a constant grating area.¹¹ Therefore, we define the grating efficiency formally as *the ratio of the total time-averaged Poynting flux – through a surface parallel to the mean grating plane – of the outgoing order ($\bar{S}_n^{(2)}$) relative to the incident wave ($\bar{S}^{(2)}$)*. Figure 3.7 highlights a convenient surface Q_2 to use for reflected efficiencies ($e_n^{(r)}$), which spans one grating period d in the x -direction, and has unit length in the z -direction. (Due to the periodicity of the fields, any other surface spanning one or more complete grooves gives the same result.) For defining transmitted efficiencies $e_n^{(t)}$, we use a similar surface Q_1 at $y \leq 0$:

$$\begin{aligned} \text{Reflected order efficiency: } e_n^{(r)} &\equiv \frac{\iint_{Q_2} \bar{S}_n^{(2)} \hat{y} dz dx}{\iint_{Q_2} \bar{S}^{(2)} \hat{y} dz dx}, \\ \text{Transmitted order efficiency: } e_n^{(t)} &\equiv \frac{\iint_{Q_1} \bar{S}_n^{(1)} \hat{y} dz dx}{\iint_{Q_1} \bar{S}^{(2)} \hat{y} dz dx}. \end{aligned}$$

This definition for efficiency can be expressed in terms of the coefficients in the Rayleigh expansion for the reflected and transmitted fields (3.14), (3.15), so that if we could solve for these coefficients, we would have determined the grating efficiency.

¹¹Because the orders propagate away at different angles, it would not be correct to compare intensities based on areas of equal wavefront; instead we need to use an area of constant grating surface.

Time-averaged Poynting vectors:

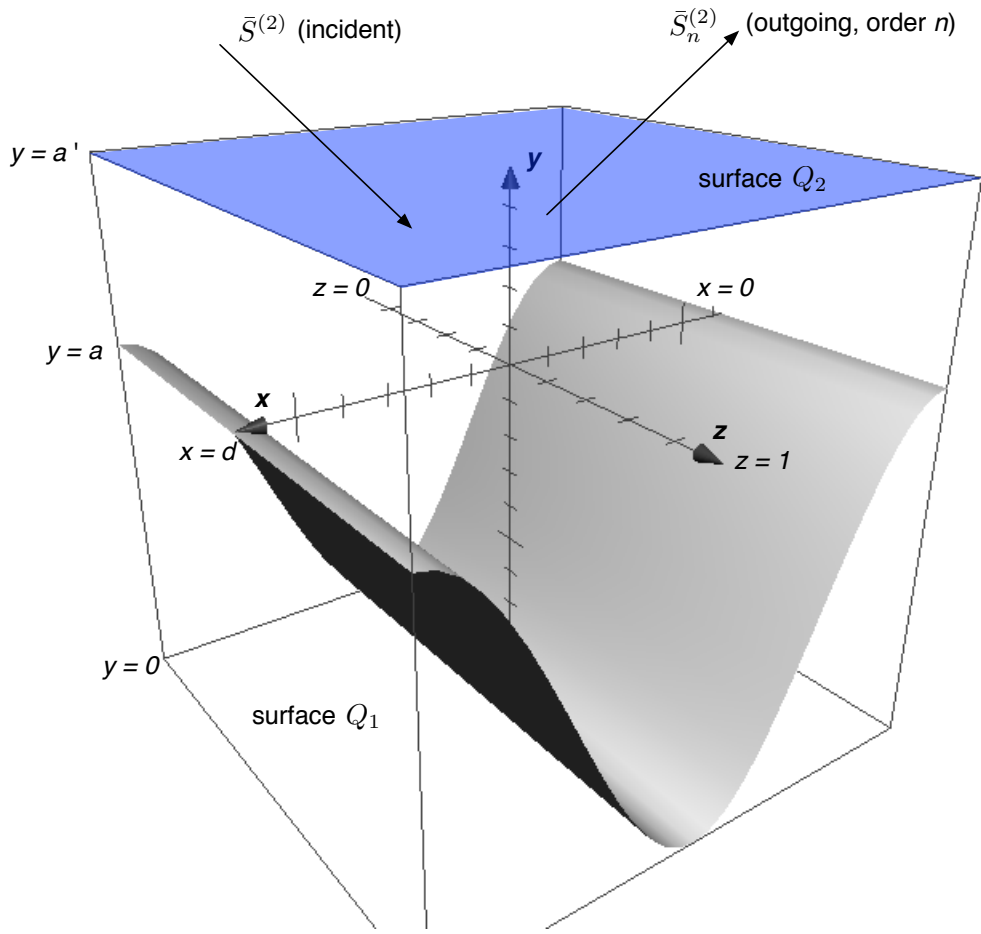


Figure 3.7: The total electromagnetic flux through this highlighted area (Q_2) is used to define the grating efficiency of a diffraction order n , as the ratio of the flux of the diffracted wave $\bar{S}_n^{(2)}$ compared to the incident wave $\bar{S}^{(2)}$.

Reflected Efficiencies

We know that the incident and diffracted orders are plane waves, so the magnetic field \mathbf{H} is related to the electric field \mathbf{E} as

$$|\mathbf{H}| = \frac{|\mathbf{E}|}{Z_2},$$

where $Z_2 = \nu_2 Z_0$ is the impedance of the space above the grating (usually free space, so $\nu_2 = 1$ and $Z_2 = Z_0 = 377\Omega$, the impedance of free space). Based on the Rayleigh expansion for the outgoing field (equation (3.14)), the magnitude of the time-averaged Poynting vector

for the *reflected order* is therefore

$$|\bar{S}| = B_n^{(2)} B_n^{(2)*} \eta_2,$$

where we have defined $\boxed{\eta_2 \equiv 1/(2Z_2)}$ in the case of TE polarization, and $\boxed{\eta_2 \equiv 2Z_2}$ for TM polarization. The direction of the vector is along the propagation direction, i.e.: at an angle $\theta_{2,n}$ to the y -axis, therefore the integrated flux through the surface is

$$\begin{aligned} \iint_{Q_2} \bar{S}_n^{(2)} \hat{y} dz dx &= \int_0^d \int_0^1 \bar{S}_n^{(2)} \hat{y} dz dx \\ &= B_n^{(2)} B_n^{(2)*} \eta_2 d \cos \theta_{2,n}. \end{aligned}$$

For the incident wave, the integrated flux is similarly

$$\iint_{Q_2} \bar{S}^{(2)} \hat{y} dz dx = A_0^{(2)} A_0^{(2)*} \eta_2 d \cos \theta_2,$$

and so the reflected efficiency in order n is

$$e_n^{(r)} = \frac{B_n^{(2)} B_n^{(2)*} \cos \theta_{2,n}}{A_0^{(2)} A_0^{(2)*} \cos \theta_2}.$$

We can simplify this somewhat by choosing a unit amplitude for the incident field, i.e.: $A_0^{(2)} = 1\text{V/m}$ for the TE electric field, or 1A/m for the TM magnetic field. Also, since $\beta_n^{(2)} = k_2 \cos \theta_{2,n}$, we can simplify this to

$$e_n^{(r)} = B_n^{(2)} B_n^{(2)*} \frac{\beta_n^{(2)}}{\beta_0^{(2)}}. \quad (3.20)$$

Transmitted Efficiencies

Gratings used in the soft x-ray regime are always used in reflection, due to the high absorption of materials at these wavelengths. However, since we are working on a general theory with application to all gratings, we can go through the same process for simplifying the transmitted efficiencies.

Again, we define $\boxed{\eta_1 \equiv 1/(2Z_1)}$ in TE polarization, and $\boxed{\eta_1 \equiv 2Z_1}$ in TM polarization, where $Z_1 = \nu_1 Z_0$ is the impedance of the grating substrate material. The same integrations

over the surface Q_1 give the ratio between the total transmitted and incident fluxes:

$$e_n^{(t)} = \frac{A_n^{(1)} A_n^{(1)*} \cos \theta_{1,n} \eta_1}{A_0^{(2)} A_0^{(2)*} \cos \theta_2 \eta_2}.$$

In this case, the difference in impedance above and below the grooves causes η_1 and η_2 to remain in the formula, so the final simplification depends on polarization:

$$\begin{aligned} e_n^{(t)} &= A_n^{(1)} A_n^{(1)*} \frac{\beta_n^{(1)}}{\beta_0^{(2)}} && \text{(TE Polarization)} \\ &= A_n^{(1)} A_n^{(1)*} \frac{\beta_n^{(1)}}{\beta_0^{(2)}} \left(\frac{v_2}{v_1} \right)^2 && \text{(TM Polarization)} \end{aligned} \quad (3.21)$$

3.3 Solving for efficiency

To determine A_n , B_n , and the efficiency, we need to find numerical solutions inside the modulated region for the general wave equations (TE polarization: (3.11), TM polarization: (3.12)). The solutions must match up to the boundary conditions at the top and bottom of the grooves, defined by the Rayleigh expansions (3.14), (3.15).

The wave equations and electromagnetic boundary conditions now depend on the polarization. **In this section, we present the analysis for TE polarization only.** The approach for TM polarization is similar, but the electromagnetic boundary conditions are different. The normal component of the TM electric field is discontinuous at the interface; this introduces convergence issues when the Fourier expansions are truncated. A small reformulation is necessary to ensure that the boundary conditions are uniformly satisfied everywhere [29]. For a detailed application of the differential method in TM polarization, see Reference [42, Chapter 4].

3.3.1 Representing the grating

As shown in Figure 3.1, the grating is described by the profile function $y_p = g(x)$, which has a minimum of $y = 0$, a maximum $y = a$, and is periodic on d :

$$y_p = g(x) = g(x + d).$$

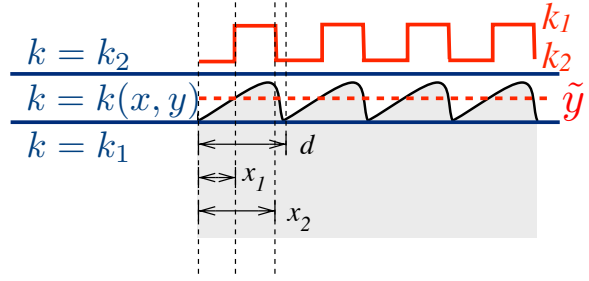


Figure 3.8: The $k^2(x, y)$ function for a simple groove profile. At any height ($0 < \tilde{y} < a$), the $k^2(x, \tilde{y})$ function be a periodic step function going from $k_1^2 = (\nu_1\omega/c)^2$ to $k_2^2 = (\nu_2\omega/c)^2$.

The exact groove profile is required to determine k^2 as a function of position. For a profile of arbitrary shape, at any height ($0 < \tilde{y} < a$), $k^2(x, \tilde{y})$ is a periodic step function going from $k_1^2 = (\nu_1\omega/c)^2$ to $k_2^2 = (\nu_2\omega/c)^2$. We can then determine a Fourier expansion for k^2 that applies inside the grooves: (Note that the expansion is only over x ; the Fourier coefficients $k_n^2(y)$ are still functions of vertical position y .)

$$k^2(x, \tilde{y}) = \sum_{n=-\infty}^{\infty} k_n^2(x, \tilde{y}) e^{2\pi i n x / d} \quad (3.22)$$

The coefficients k_n^2 can be computed using a Fast Fourier Transform of $k^2(x, \tilde{y})$ over the period d . Because this is a step function, for simple profiles with discontinuities at x_1 and x_2 (Figure 3.8), it can also be computed analytically. First, we define

$$\sigma_1 \equiv k_1^2 - k_2^2,$$

$$\sigma_2 \equiv k_2^2 - k_1^2.$$

Then, for $n = 0$:

$$k_0^2 = \frac{1}{d} (k_2^2 d - \sigma_1 x_1 - \sigma_2 x_2).$$

For $n \neq 0$:

$$k_n^2 = \frac{-1}{2\pi n} \left[\sigma_1 \left(\sin \left(\frac{2\pi n x_1}{d} \right) + i \cos \left(\frac{2\pi n x_1}{d} \right) \right) + \sigma_2 \left(\sin \left(\frac{2\pi n x_2}{d} \right) + i \cos \left(\frac{2\pi n x_2}{d} \right) \right) \right].$$

3.3.2 Matrix Formulation of Numerical Solution: Inside the Grooves

When we put the Fourier expansions for $u_z = E_z$ (3.13) and k^2 (3.22) into the general differential equation (3.11) and truncate to $n = [-N, N]$, we get one second-order differential equation for every n :

$$\frac{d^2 E_n(y)}{dy^2} + \sum_{m=-N}^N k_{(n-m)}^2(y) E_m(y) - \alpha_n^2 E_n(y) = 0,$$

where E_n is the n^{th} Fourier coefficient in the expansion of the electric field. This is conveniently expressed by defining the column vector $[E(y)]$ with $2N + 1$ components $E_n(y)$, and the $(2N + 1) \times (2N + 1)$ square matrix M as

$$M_{nm}(y) = -k_{(n-m)}^2(y) + \alpha_n^2 \delta_{nm} \quad \delta_{nm} = \begin{cases} 1, & \text{if } n = m \\ 0, & \text{if } n \neq m \end{cases}$$

giving the matrix equation

$$\frac{d^2 [E(y)]}{dy^2} = M(y) [E(y)]. \quad (3.23)$$

This is now a set of second order differential equations in y that need to be solved so that the values of the field coefficients $E_n(y)$ satisfy boundary conditions at the top and bottom of the grooves: $y = a$ and $y = 0$.

3.3.3 Boundary conditions at the top and bottom of the grooves

Regardless of the shape of the profile, it always has a maximum value at $y = a$, and a minimum value at $y = 0$. The Maxwell Equations provide two additional boundary conditions here:

1. The tangential component of the electric field \mathbf{E} must be continuous at an interface.

For TE polarization, the tangential component is just the E_z component, so we require that the electric field is continuous at $y = 0$ and $y = a$. Therefore, the field must match up to the Rayleigh expansion solutions found for Region 2 and Region 1:

$$E_n(a) = A_0^{(2)} e^{-i\beta_0^{(2)} a} \delta_{n,0} + B_n^{(2)} e^{i\beta_n^{(2)} a}, \quad (3.24)$$

$$E_n(0) = A_n^{(1)}. \quad (3.25)$$

At this point, both the A_n and B_n coefficients are still unknown.

2. The tangential component of the magnetic field \mathbf{H} must be continuous at an interface.

In TE polarization, the tangential magnetic field is proportional to the normal derivative of the electric field. At $y = a$ and $y = 0$, regardless of the profile shape, the normal vector to the grating surface is along the y -direction, so we need dE_z/dy to be continuous; this gives the remaining two boundary conditions:

$$\frac{dE_n(y)}{dy} \Big|_{y=a} = -i\beta_0^{(2)} A_0^{(2)} e^{-i\beta_0^{(2)} a} \delta_{n,0} + i\beta_n^{(2)} B_n^{(2)} e^{i\beta_n^{(2)} a}, \quad (3.26)$$

$$\frac{dE_n(y)}{dy} \Big|_{y=0} = -i\beta_n^{(1)} A_n^{(1)}. \quad (3.27)$$

Optionally, these four requirements can be combined to give two equations that link the function $E_n(y)$ to its derivative at $y = 0$ and $y = a$:

$$\begin{aligned} \frac{dE_n(y)}{dy} \Big|_{y=0} &= -i\beta_n^{(1)} E_n(0) \\ \frac{dE_n(y)}{dy} \Big|_{y=a} &= \begin{cases} i\beta_n^{(2)} E_n(a) & (n \neq 0) \\ -i\beta_0^{(2)} A_0^{(2)} e^{-i\beta_0^{(2)} a} + i\beta_n^{(2)} (E_n(a) - A_0^{(2)} e^{-i\beta_0^{(2)} a}) & (n = 0) \end{cases} \end{aligned}$$

The four boundary equations ((3.24), (3.25), (3.26), (3.27)), along with the matrix differential equation (3.23), establish the grating boundary value problem (BVP) in the Fourier space, for TE polarization.

3.3.4 Solution implementation: The Shooting Method

At this point, we have $2N + 1$ second-order boundary value problems that need to be integrated in the y -direction (3.23). In this BVP, the boundary conditions do not provide any values; only a link between the unknown function and its derivative. To handle this complication, the original theory authors used a technique called the **shooting method** [57].

Because the differential equation is a linear system, we can construct a general solution that matches the boundary conditions out of a linear combination of trial solutions. The Fourier expansion for the field represents a complete basis, so we can use it to generate a

complete set of $2N + 1$ trial solutions $[\tilde{u}(y)]_p$ for the vector $[u(y)]$, where $p = [-N, N]$. Any orthogonal set of particular solutions that satisfies the boundary conditions at $y = 0$ (3.27) is acceptable, so we choose these values for the p -th trial solution at $y = 0$:

$$\begin{aligned}\tilde{E}_n(0)_p &= \delta_{p,n}, \\ \tilde{E}'_n(0)_p &= -i\beta_n^{(1)}\delta_{p,n}.\end{aligned}\tag{3.28}$$

This transforms the $2N + 1$ boundary value problems into $(2N + 1) \times (2N + 1)$ initial value problems. All of the trial solutions can now be individually integrated from $y = 0$ to $y = a$, using Equation (3.23):

$$[\tilde{E}''(y)]_p = M(y)[\tilde{E}(y)]_p\tag{3.29}$$

using any reliable numerical integration routine.

Finally, we need to find a linear superposition of the trial solutions that satisfies the boundary conditions at $y = a$ (3.24), (3.26):

$$\begin{aligned}\sum_{p=-N}^{+N} c_p \tilde{E}_{np}(a) &= A_0^{(2)} e^{-i\beta_0^{(2)}a} \delta_{n,0} + B_n^{(2)} e^{i\beta_n^{(2)}a}, \\ \sum_{p=-N}^{+N} c_p \tilde{E}'_{np}(a) &= -i\beta_0^{(2)} A_0^{(2)} e^{-i\beta_0^{(2)}a} \delta_{n,0} + i\beta_n^{(2)} B_n^{(2)} e^{i\beta_n^{(2)}a}.\end{aligned}\tag{3.30}$$

Because of the $y = 0$ boundary condition (3.25) and our choice of starting values (3.28), the superposition constants c_p can be identified with the coefficients $A_n^{(1)}$: $c_p = A_n^{(1)}$ for $n = p$. Therefore, these represent $2(2N + 1)$ linear equations for the $2(2N + 1)$ unknowns $A_n^{(1)}, B_n^{(2)}$. If we eliminate $B_n^{(2)}$, we can express the resulting equations in linear matrix form $A\mathbf{x} = \mathbf{b}$:

$$T [A^{(1)}] = [V^{(2)}],\tag{3.31}$$

where $[A^{(1)}]$ is the vector of $A_n^{(1)}$ coefficients, $[V^{(2)}]$ is a vector defined by the incident wave (which has a single component when there is only one incident plane wave):

$$V_n^{(2)} = \delta_{n,0} e^{-i\beta_0^{(2)}a},$$

and T is the square matrix with elements

$$T_{np} = \frac{1}{2} \left[\tilde{E}_{np}(a) - \frac{\tilde{E}'_{np}(a)}{i\beta_n^{(2)}} \right].$$

Because the grating problem has a unique solution, T must be invertible (as long as the numerical integration process was stable and accurate). Using LU decomposition or any other standard matrix method to solve the linear system of Equation (3.31) provides the coefficients for the transmitted orders $A_n^{(1)}$. In the final step, Equation (3.30) provides the $B_n^{(2)}$ coefficients, from which we can compute the reflected efficiencies using Equation (3.20).

This concludes the basic formulation of the differential method. However, there are two numerical challenges that complicate its implementation. One is the truncation convergence issue in TM polarization, which we have already mentioned [29]. The other is introduced by growing exponential functions that cause a loss of significance during the numerical integration.

3.3.5 Integration of growing exponentials: The S-matrix method

The integration process (3.29) requires numerically integrating a set of growing and decaying exponential functions. As the groove depth, or integration distance a increases, the values of \tilde{u}_p and \tilde{u}'_p become very large – for example, on the order of 10^{22} for a depth of just $a = 0.1$ um. However, the algebraic process (3.31) requires taking the sum and difference of many large \tilde{u}_p values to produce a number less than unity. On a computer with finite-precision floating point numbers, this results in a loss of significance that can make the final result meaningless.

For example, standard double-precision (IEEE 754) variables have a decimal precision of approximately 16 digits. The subtraction of two numbers on the order of 10^{22} will have a result precision of $\pm 10^6$. Obviously, a final efficiency result of $e_{r,1} = 0.21 \pm 10^6$ would be of little use. To mitigate this, we need a strategy to keep the \tilde{u}_p values bounded within the significant range; the only way to accomplish this is to limit the integration distance.

The solution to this problem was originally developed for handling stacks of grating layers, like those shown in Figure 3.4. Here, the grating is sliced into layers between modulated regions (Figure 3.5). However, the technique can also be applied to a single deep grating, as shown in Figure 3.9, where the layer thicknesses are chosen small enough to keep the integration values bounded. The basic concept is to conduct separate numerical integrations using assumed starting values from the bottom to the top of each layer, and then to combine

the effects of all layers using a stable matrix algorithm.

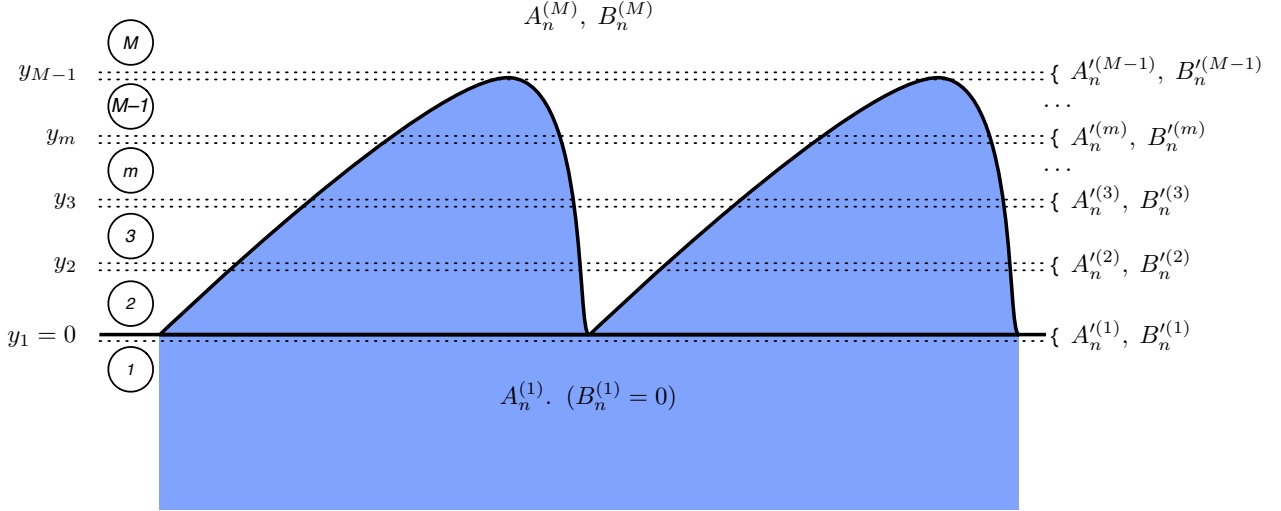


Figure 3.9: Using the S-matrix method, thick gratings are divided into layers, where each layer is thin enough to avoid losing numerical significance during integration. Conceptually, we insert a zero-thickness homogeneous layer between each “real” region, so that Rayleigh expansions with coefficients A'_n , B'_n are valid. (These conceptual layers have the same impedance (k_M^2) and $\beta_n^{(M)}$ as the vacuum region M .)

Between each “real” grating layer (Figure 3.9), we can conceptually insert a homogeneous layer with zero thickness. By giving the conceptual layer the same refractive index as the vacuum, we ensure that the Rayleigh expansion that applies within it has the same β_n values and propagation angles as the Rayleigh expansion above the grating. (Introducing this conceptual layer has no effect on the grating efficiency, because it has zero thickness; we introduce it only to make the mathematics convenient.)

Previously, in the single-layer formulation, we had a single down-going wave $A_0^{(2)}$ above the grating, and a set of up-going reflected waves $B_n^{(2)}$. Below the grooves (inside the substrate) there was a set of down-going transmitted waves $A_n^{(1)}$. In the multi-layer formulation, we now have down-going and up-going waves within each conceptual layer. Instead of just one incident wave, all except the external layers have a complete set of waves incident from both above and below. Transmitted light from the region above creates down-going incident waves; reflected light from the region below creates up-going incident waves.

Figure 3.9 shows the numbering we adopt now for the conceptual homogeneous layers. They are numbered from $m = 1$ (the substrate) to $m = M - 1$. The number of “real”

grating slices is $M - 2$, and the vacuum region above the grating is labelled M . Within each conceptual layer m , at a height y_m , the field is described by a Rayleigh expansion with coefficients $A_n'^{(m)}$ and $B_n'^{(m)}$:

$$E_z(x, y) = \sum_{n=-N}^N \left[A_n'^{(m)} e^{-i\beta_n^{(M)} y_m} + B_n'^{(m)} e^{i\beta_n^{(M)} y_m} \right] e^{i\alpha_n x}. \quad (3.32)$$

Because we have chosen the conceptual layers to have the same refractive index as the vacuum, $\beta_n^{(m)} = \beta_n^{(M)}$. Since the top conceptual layer is in the vacuum above the grating, $A_n'^{(M-1)} = A_n^{(M)}$ and $B_n'^{(M-1)} = B_n^{(M)}$.

To simplify the matrix calculations, we define a vector $V^{(m)}$ with two blocks to represent the up-going and down-going waves inside each conceptual layer. Each block contains the components for all orders n :

$$V^{(m)} \equiv \begin{pmatrix} & \vdots \\ & A_n'^{(m)} e^{-i\beta_n^{(M)} y_m} \\ \hline & \vdots \\ & \vdots \\ & B_n'^{(m)} e^{i\beta_n^{(M)} y_m} \\ & \vdots \end{pmatrix}.$$

We can then define a (yet unknown) **transmission matrix** $T^{(m)}$ for the m -th conceptual layer that describes the effect of the region directly below it:

$$V^{(m)} = T^{(m)} V^{(m-1)}.$$

This relates the waves in the $(m - 1)^{\text{th}}$ conceptual layer to the m^{th} conceptual layer.

If we could compute the $T^{(m)}$ matrix for each layer, the transmission matrix for the total stack T could be found, relating the waves at the top of the stack ($m = M$) to the waves at

the bottom ($m = 1$, $y = 0$):

$$\begin{pmatrix} \vdots \\ A_n^{(M)} e^{-i\beta_n^{(M)} y_m} \\ \vdots \\ \hline \vdots \\ B_n^{(M)} e^{i\beta_n^{(M)} y_m} \\ \vdots \end{pmatrix} = T \begin{pmatrix} \vdots \\ A_n^{(1)} \\ \vdots \\ \hline \vdots \\ B_n^{(1)} \\ \vdots \end{pmatrix},$$

where

$$T = T^{(M-1)} \dots T^{(m)} \dots T^{(3)} T^{(2)}.$$

There are no up-going waves incident from below the substrate, so $B_n^{(1)} = 0$:

$$\begin{pmatrix} \vdots \\ A_n^{(M)} e^{-i\beta_n^{(M)} y_m} \\ \vdots \\ \hline \vdots \\ B_n^{(M)} e^{i\beta_n^{(M)} y_m} \\ \vdots \end{pmatrix} = T \begin{pmatrix} \vdots \\ A_n^{(1)} \\ \vdots \\ \hline \vdots \\ 0 \\ \vdots \end{pmatrix}. \quad (3.33)$$

This equation is sufficient to calculate the outgoing transmitted waves $A_n^{(1)}$ and reflected waves $B_n^{(M)}$ for any incidence condition $A_n^{(M)}$.

Determining the T-matrix for one layer

To determine the $T^{(m)}$ matrix that describes the region below the m^{th} conceptual layer, we again apply the shooting method. Like in Section 3.3.4, we generate a set of P orthogonal trial solution vectors $V_p^{(m-1)}$ that satisfy the boundary conditions at the bottom of the region, and integrate them numerically from y_{m-1} to y_m . Then, we choose a linear combination of the resulting $V_p^{(m)}$ that satisfy the boundary conditions at the top (y_m). However, because

we now have up-going *and* down-going incident waves within the region, we need twice as many trial solutions as before: $P = 2(2N + 1)$.

As a reminder, the boundary conditions now require that our numerical solution within the modulated region below y_m must match up to the Rayleigh expansions defined in the conceptual layers above and below. The boundary conditions come from the continuity of the tangential electric field ($E_z = \sum E_n(y) \exp(i\alpha_n x)$) and its first derivative at y_{m-1} and y_m :

$$E_n(y_{m-1}) = A_n'^{(m)} e^{-i\beta_n^{(M)} y_{m-1}} + B_n'^{(m)} e^{i\beta_n^{(M)} y_{m-1}},$$

$$\left. \frac{dE_n}{dy} \right|_{y_{m-1}} = -i\beta_n^{(M)} A_n'^{(m)} e^{-i\beta_n^{(M)} y_{m-1}} + i\beta_n^{(M)} B_n'^{(m)} e^{i\beta_n^{(M)} y_{m-1}},$$

$$E_n(y_m) = A_n'^{(m)} e^{-i\beta_n^{(M)} y_m} + B_n'^{(m)} e^{i\beta_n^{(M)} y_m}, \quad (3.34)$$

$$\left. \frac{dE_n}{dy} \right|_{y_m} = -i\beta_n^{(M)} A_n'^{(m)} e^{-i\beta_n^{(M)} y_m} + i\beta_n^{(M)} B_n'^{(m)} e^{i\beta_n^{(M)} y_m}. \quad (3.35)$$

Therefore, we choose the following trial solutions at y_{m-1} . For the first $2N + 1$ solutions (from $p = [-N, N]$), we use a vector

$$V_p^{(m-1)} = \begin{pmatrix} \vdots \\ A_n'^{(m-1)} e^{-i\beta_n^{(M)} y_{m-1}} \\ \vdots \\ \vdots \\ B_n'^{(m-1)} e^{i\beta_n^{(M)} y_{m-1}} \\ \vdots \end{pmatrix} = \begin{pmatrix} \vdots \\ \delta_{n,p} \\ \vdots \\ 0 \\ \vdots \end{pmatrix},$$

and derivatives

$$\frac{V_p^{(m-1)}}{dy} = \begin{pmatrix} \vdots \\ -i\beta_n^{(M)}\delta_{n,p} \\ \vdots \\ \vdots \\ 0 \\ \vdots \end{pmatrix}.$$

From (3.32), these correspond to starting integration values for the trial electric field components $\tilde{E}_{n,p}$ at y_{m-1} :

$$\tilde{E}_{n,p}(y_{m-1}) = A_n'^{(m-1)}e^{-i\beta_n^{(m-1)}y_{m-1}} + B_n'^{(m-1)}e^{i\beta_n^{(m-1)}y_{m-1}} = \delta_{n,p} + 0,$$

$$\left. \frac{d\tilde{E}_{n,p}}{dy} \right|_{y_{m-1}} = -i\beta_n^{(M)}\delta_{n,p}.$$

For the second set of $2N+1$ trial solutions (from $p = [N+1, 3N+1]$) we choose down-going waves for starting values:

$$V_p^{(m-1)} = \begin{pmatrix} \vdots \\ A_n'^{(m-1)}e^{-i\beta_n^{(M)}y_{m-1}} \\ \vdots \\ \vdots \\ B_n'^{(m-1)}e^{i\beta_n^{(M)}y_{m-1}} \\ \vdots \end{pmatrix} = \begin{pmatrix} \vdots \\ 0 \\ \vdots \\ \vdots \\ \delta_{n,p-(2N+1)} \\ \vdots \end{pmatrix},$$

with derivatives

$$\frac{V_p^{(m-1)}}{dy} = \begin{pmatrix} & & & \\ & \vdots & & \\ & 0 & & \\ & \vdots & & \\ & & \vdots & \\ & i\beta_n^{(M)}\delta_{n,p-(2N+1)} & & \\ & \vdots & & \end{pmatrix}.$$

These correspond to starting values of the electric field components

$$\tilde{E}_{n,p}(y_{m-1}) = A_n'^{(m-1)}e^{-i\beta_n^{(m-1)}y_{m-1}} + B_n'^{(m-1)}e^{i\beta_n^{(m-1)}y_{m-1}} = 0 + \delta_{n,p-(2N+1)},$$

$$\left. \frac{d\tilde{E}_{n,p}}{dy} \right|_{y_{m-1}} = i\beta_n^{(M)}\delta_{n,p-(2N+1)}.$$

Now we can numerically integrate the electric field components from y_{m-1} to y_m as before, using Equation (3.23). From the second pair of boundary conditions (3.34)(3.35), we can compute $V_p^{(m)}$ at the end of the integration:

$$V_p^{(m)} = \begin{pmatrix} & & & \\ & \vdots & & \\ & A_n'^{(m)}e^{-i\beta_n^{(M)}y_m} & & \\ & \vdots & & \\ & & \vdots & \\ & B_n'^{(m)}e^{i\beta_n^{(M)}y_m} & & \\ & \vdots & & \end{pmatrix} = \begin{pmatrix} & & & \\ & \vdots & & \\ & \frac{1}{2} \left(\tilde{E}_{n,p}(y_m) - \frac{1}{i\beta_n^{(M)}} \frac{d\tilde{E}_{n,p}}{dy}(y_m) \right) & & \\ & \vdots & & \\ & & \vdots & \\ & \frac{1}{2} \left(\tilde{E}_{n,p}(y_m) + \frac{1}{i\beta_n^{(M)}} \frac{d\tilde{E}_{n,p}}{dy}(y_m) \right) & & \\ & \vdots & & \end{pmatrix}.$$

Because of the fortunate choice of starting values $V_{n,p}^{(m-1)} = \delta_{n,p}$, the solution to the matrix equation

$$V^{(m)} = T^{(m)}V^{(m-1)}$$

is easy and direct:

$$T_{n,p}^{(m)} = V_{n,p}^{(m)}.$$

The shooting method, when used with this choice of starting values, directly determines the components of the m -th layer's $T^{(m)}$ matrix.

The combined efficiency of a stack of layers

Mathematically, having determined the $T^{(m)}$ matrix for each layer, we can compute the combined effect of the whole stack through matrix products

$$T = T^{(M-1)} \dots T^{(m)} \dots T^{(3)} T^{(2)},$$

and use Equation (3.33) to determine the final transmitted waves $A_n^{(1)}$ and reflected waves $B_n^{(M)}$ for any incidence condition $A_n^{(M)}$. Numerically, however, this matrix multiplication results in the exact same large numbers and loss of significance that we originally set out to avoid.

We recall that the layers were chosen sufficiently thin to keep the $T^{(m)}$ matrix for each layer bounded within significance; the problem enters in the multiplication. Fortunately, we can use an algebraic re-formulation to avoid ever having to compute the full matrix product T . The **S-matrix propagation algorithm** was discovered by Li [28] and applied to the differential method by Neviere and Montiel [41]. Instead a matrix $T^{(m)}$ that describes the effect of one layer, it defines the matrix $S^{(q)}$ that describes the cumulative effect of *all layers from $m = 1$ up to the q^{th} layer*:

$$\left(\begin{array}{c} \vdots \\ B_n'^{(q)} e^{i\beta_n^{(M)} y_q} \\ \hline \vdots \\ A_n^{(1)} \\ \vdots \end{array} \right) = S^{(q)} \left(\begin{array}{c} \vdots \\ B_n^{(1)} \\ \vdots \\ A_n'^{(q)} e^{-i\beta_n^{(M)} y_q} \\ \vdots \end{array} \right). \quad (3.36)$$

The S matrix is bounded by definition, and its blocks have well-defined physical interpretations as reflection and transmission matrices [42, Chapter 3]. The algorithm re-arranges the blocks of the T-matrices so that the growing exponential functions never appear in the result.

The S-matrix algorithm is derived in inductive fashion by writing out (3.40) at levels q and $q + 1$. We omit the algebra here and state only the final results. To start, we split the T and S matrices into square blocks of size $2N + 1$:

$$T = \left[\begin{array}{c|c} T_{11} & T_{12} \\ \hline T_{21} & T_{22} \end{array} \right],$$

$$S = \left[\begin{array}{c|c} S_{11} & S_{12} \\ \hline S_{21} & S_{22} \end{array} \right].$$

Defining a temporary matrix $Z^{(q)}$:

$$Z^{(q)} \equiv \left(T_{11}^{(q+1)} + T_{12}^{(q+1)} S_{12}^{(q)} \right)^{-1}, \quad (3.37)$$

the results allow us to express the S matrix up to the $q + 1$ layer based on the S matrix at the q^{th} layer and the T-matrix of the $(q + 1)^{\text{th}}$ layer:

$$S_{22}^{(q+1)} = S_{22}^{(q)} Z^{(q)}, \quad (3.38)$$

$$S_{12}^{(q+1)} = \left(T_{21}^{(q+1)} + T_{22}^{(q+1)} S_{12}^{(q)} \right) Z^{(q)}. \quad (3.39)$$

(The other two blocks of the S matrix can also be calculated, but are not actually required to determine the efficiencies, nor proceed with the algorithm.)

$$S_{21}^{(q+1)} = S_{21}^{(q)} - S_{22}^{(q+1)} T_{12}^{(q+1)} S_{11}^{(q)}$$

$$S_{11}^{(q+1)} = -S_{12}^{(q+1)} T_{12}^{(q+1)} S_{11}^{(q)} + T_{22}^{(q+1)} S_{11}^{(q)}$$

Equation (3.37), (3.38), and (3.39) give us exactly what we need to iterate vertically through a stack of grating layers. The calculation of the S matrix for a full grating begins at layer 1, where no reflection occurs and the transmission is unity for all incoming waves:

$$S_{12}^{(1)} = 0,$$

$$S_{22}^{(1)} = \mathbb{1}.$$

Applying the inductive step at the top of the first layer ($y = y_2$) gives

$$\begin{aligned} Z^{(1)} &= \left(T_{11}^{(2)} \right)^{-1}, \\ S_{12}^{(2)} &= T_{21}^{(2)} \left(T_{11}^{(2)} \right)^{-1}, \\ S_{22}^{(2)} &= \left(T_{22}^{(2)} \right)^{-1}. \end{aligned}$$

The rest of the stack is solved inductively by computing the $T^{(q+1)}$ matrix at each layer $q+1$, and then using Equation (3.37), (3.38), and (3.39) to determine $S^{(q+1)}$, until we reach the top layer.

Finally, we can use the blocks of the final $S^{(M-1)}$ matrix to relate the incident waves at the top of the grating to the diffracted and transmitted waves, using Equation (3.40). Since there are no up-going waves incident from below the substrate ($B_n^{(1)} = 0$):

$$\left(\begin{array}{c} \vdots \\ B_n^{(M)} e^{i\beta_n^{(M)} y_{M-1}} \\ \hline \vdots \\ A_n^{(1)} \\ \vdots \end{array} \right) = \left[\begin{array}{c|c} S_{11}^{(M-1)} & S_{12}^{(M-1)} \\ \hline S_{21}^{(M-1)} & S_{22}^{(M-1)} \end{array} \right] \left(\begin{array}{c} \vdots \\ 0 \\ \vdots \\ A_n^{(M)} e^{-i\beta_n^{(M)} y_{M-1}} \\ \vdots \end{array} \right). \quad (3.40)$$

For a single incident plane wave with normalized intensity, $A_n^{(M)} = \delta_{n,0}$. From this we can work out the transmitted Rayleigh coefficients below the grating

$$A_n^{(1)} = S_{22,n,0}^{(M-1)} e^{-i\beta_0^{(M)} y_{M-1}},$$

and the reflected Rayleigh coefficients above the grating

$$B_n^{(M)} = S_{12,n,0}^{(M-1)} e^{-i(\beta_n^{(M)} + \beta_0^{(M)}) y_{M-1}}.$$

Having computed the outgoing Rayleigh coefficients without loss of significance, Equations (3.20) and (3.21) compute the final reflected and transmitted efficiencies in each diffraction order.

3.4 Interaction of X-rays and materials

In setting up the differential theory, we assumed that light propagation within the grating material could be described by a refractive index, but we failed to suggest what this refractive index would be, and how it would vary with wavelength. In this final theory section, we verify the assumption and suggest one source of refractive index data.

In the soft x-ray region, the refractive index description is generally valid – both for conventional dielectrics like SiO_2 , and for metals. In metals, the frequency of x-ray light is much higher than the plasma frequency; free electrons cannot respond fast enough to follow the changing electric field, so the material behaves as a weak dielectric rather than a conductor. However, the incident x-rays are sufficiently energetic to cause electronic state transitions in bound electrons (**photoabsorption**); the result is substantial attenuation of the beam as it propagates through the material. Energy in the beam is also lost through **coherent scattering** of photons off electrons in the material. These two processes mean that attenuation is always present, but it becomes extremely strong at photon energies immediately above the material's **absorption edges**.

The complex refractive index ν :

$$\nu(\lambda) = n + i\kappa,$$

can describe both the dielectric strength and the attenuation. The real component n is analogous to the conventional refractive index; it describes the phase velocity v of the light in the material,

$$n = c/v,$$

while the **extinction coefficient** κ describes the amount of attenuation. When using the sign convention for the electric field in Equation (3.1),

$$E \propto \exp(i(kz - \omega t)) = \exp(i\omega(\nu z/c - t)),$$

the sign of κ must be positive for absorption. ($\kappa < 0$ would imply amplification as the light travelled through the material.) For almost all materials at x-ray wavelengths, n is smaller

than, but very close to one, so the refractive index is often listed as

$$\nu = 1 - \delta + i\kappa.$$

3.4.1 Atomic scattering factors and the refractive index

At soft x-ray wavelengths, it is nearly impossible to measure the refractive index directly. Instead, scattering theory and absorption measurements can be used together to determine semi-empirical values. Scattering of electromagnetic waves from single point charges (e.g., electrons) is well described by classical **Thomson scattering**. To extend this to multi-electron situations, the **atomic scattering factor** f describes the amplitude of an electromagnetic wave scattered by a complete atom, compared to what would be scattered by a single electron:

$$f = f_1 + if_2.$$

It is complex because all of the atom's electrons might not scatter in phase. It can be separated into a forward-scattering component $f(0)$ and a correction Δf_0 that depends on the scattering angle θ :

$$f = f_1 + if_2 = f_1(0) - \Delta f_0(\theta) + if_2(0).$$

The “Henke Data” publication [23] tabulates the atomic scattering factors for all elements from Hydrogen to Uranium over the energy range from 50 eV to 30 000 eV. The authors calculate the scattering factors from a survey of all existing available photoabsorption measurements. The measured absorption cross section directly provides the imaginary part of the scattering factor (f_2). Since it is practically impossible to empirically measure the speed of x-ray light in absorbing materials, the Kramers-Kronig dispersion relations are used to determine the real part (f_1) from the imaginary part [27]. (A modified Kramers-Kronig dispersion relation is used to correct for relativistic effects.) Across energy regions where photoabsorption measurements were not available, the values were interpolated using theoretical calculations.

If the atoms within a material (metal, crystal, or gas) can be assumed to scatter as dipoles, the complex refractive index can be determined from the scattering factors of all

the constituent atoms. This allows us to estimate the refractive index – even for compound grating materials like SiO_2 and MgF_2 – as a function of wavelength:

$$\tilde{n} = 1 - \delta - i\beta = 1 - \frac{r_e}{2\pi} \lambda^2 \sum_{q=1}^Q n_q f_q(0), \quad (3.41)$$

where there are Q different types of atoms in the material, n_q is the number density of atoms of type q , $f_q(0)$ is the complex forward scattering factor $f(0)$ for atom q , and r_e is the classical electron radius [23]. (Note that the refractive index \tilde{n} here uses the opposite sign convention to ν defined above; if $\tilde{n} = 1 - \delta - i\beta$, $\nu = 1 - \delta + i\beta$.)

Using this method to calculate the refractive index assumes that the photoabsorption cross section does not depend on the bonding environment of atoms in the material; i.e., *it assumes that the individual atoms scatter independently*. In the vicinity of absorption edges, two processes invalidate this assumption: transitions to weakly bound excited states produce fine structure near the absorption edge (NEXAFS), and backscattering of outgoing photoelectrons from the atoms in a crystal causes oscillations above the edge (EXAFS).

Given these effects, is it acceptable to use refractive indexes derived from the Henke data? Two examples from Reference [23] show the limits of validity. Figure 3.10 compares the reflectivity of a pure silicon wafer calculated from atomic scattering factors against measurements of the real crystal; in this case the agreement is good. In Figure 3.11, the near-edge absorption fine structure of CO_2 causes deviation in the measured absorption spectrum compared to the vector sum of the atomic photoabsorption in the vicinity of the Carbon K 1s and Oxygen K 1s absorption edges.

Far away from absorption edges, the semi-empirical nature of the data gives us a high degree of trust in the accuracy of the Henke-based refractive indexes; however, we need to remember that they do not reflect reality in the vicinity of a material’s absorption edges.

The Center for X-ray Optics website [12] offers an online calculator to estimate the refractive index of a compound material using Equation (3.41) based on its chemical formula and density, subject to the atomic-like assumption. We used this service to build a database of complex refractive indexes for common grating materials over the 50 eV to 10 000 eV range. These values were used in all calculations shown later in the text.

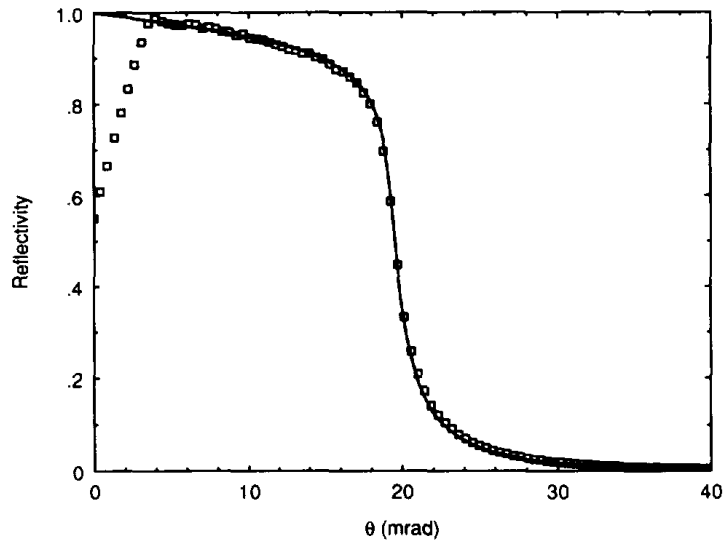


Figure 3.10: Comparison of a measured reflection curve around the total reflection cutoff region from a silicon(111) wafer under 1487 eV radiation, with that predicted by the Fresnel equations ((5.2), (5.3)) using the atomic scattering factors from the Henke tables. (The low-angle cutoff is instrumental.) Reprinted from Reference [23, Figure 18].

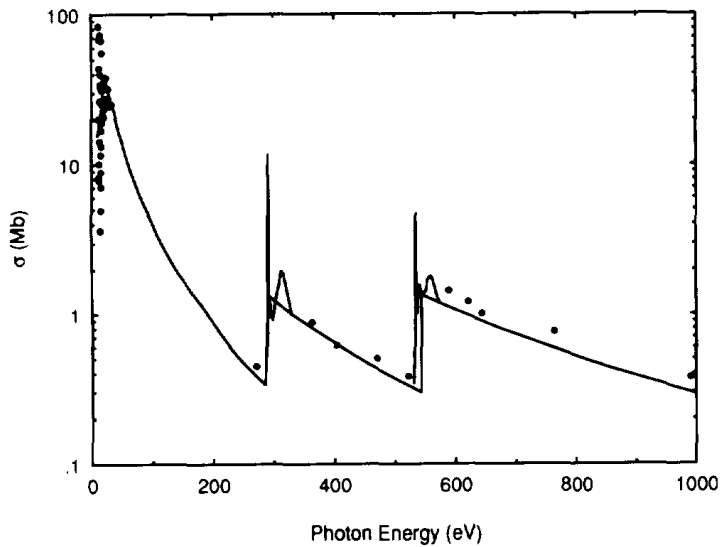
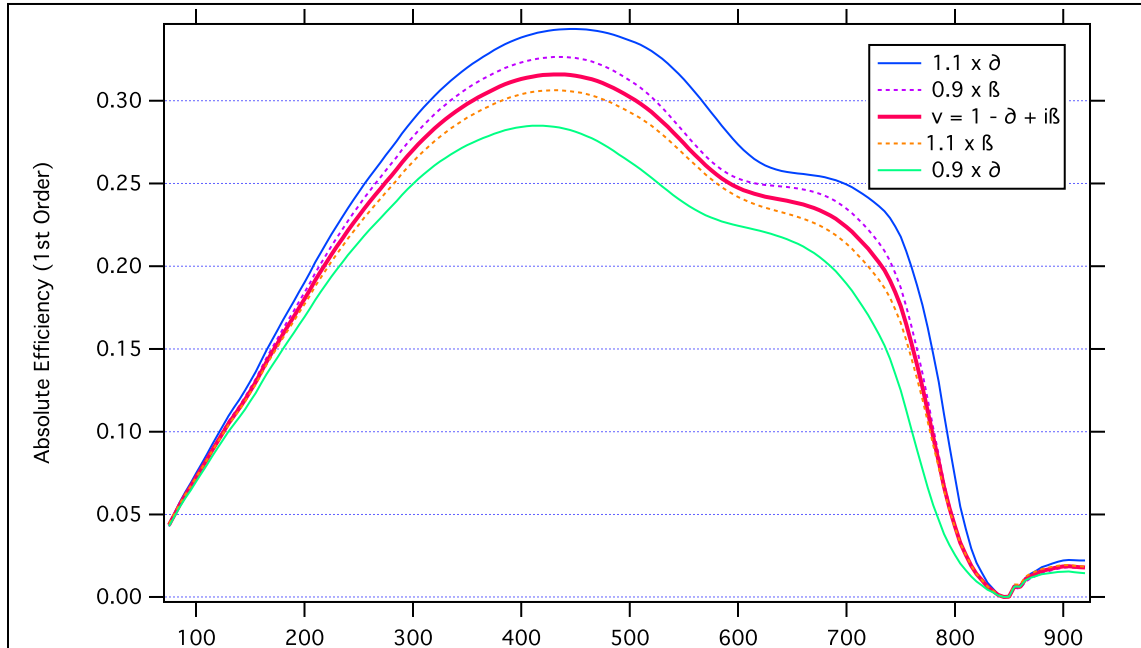


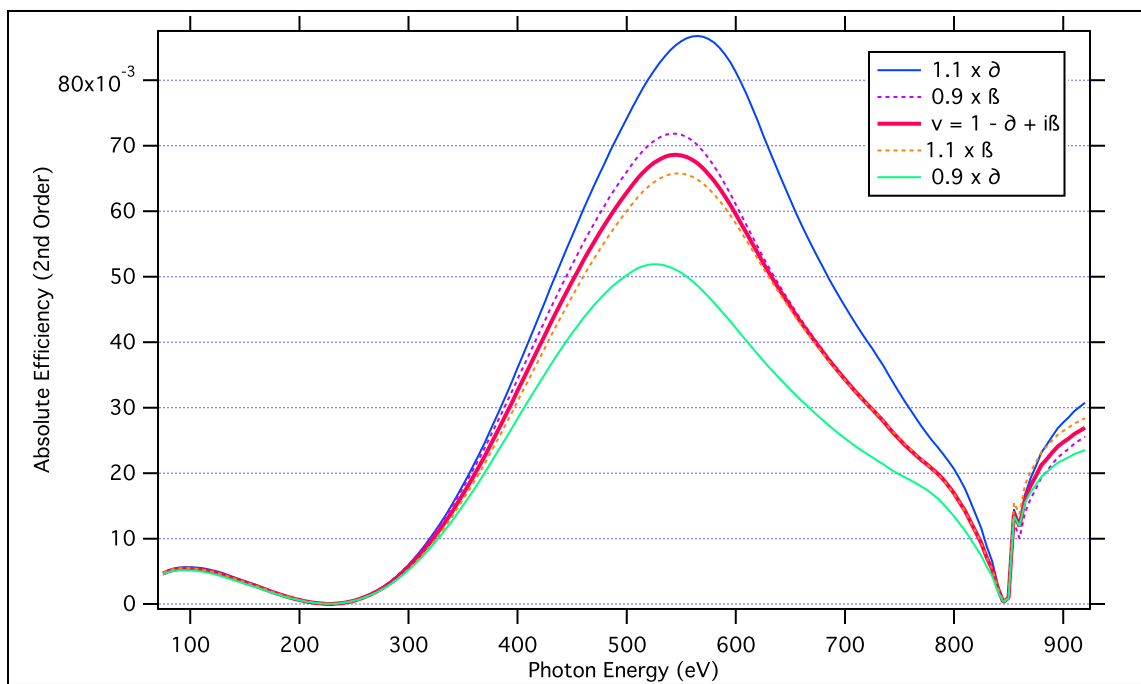
Figure 3.11: Experimental photoabsorption data for the CO₂ molecule, compared with a plot calculated using the vector sum of atomic photoabsorption cross sections from the Henke tables. The near-edge fine structure causes differences in the vicinity of the C K 1s (284 eV) and O K 1s (543 eV) absorption edges. Reprinted from Reference [23, Figure 15].

3.4.2 Sensitivity of efficiency calculations to errors in the refractive index

Figure 3.12 examines the sensitivity of the efficiency calculations to the refractive index, to determine the effect of any potential inaccuracy introduced by using the Henke data. For this example, we chose a nickel grating to include a strong absorption edge near 850 eV. The thick red curves represent the default grating with a refractive index given by $\nu = 1 - \delta + i\beta$, which obviously varies as a function of wavelength. The additional curves show the effect of a consistent 10% overestimation or underestimation in δ or β ; for example, $\nu' = 1 - 1.1\delta + i\beta$. We note that a *consistent* error in a component of the refractive index changes the magnitude but not the overall shape of the curves; therefore, an error like this would not mislead us when doing optimizations or comparisons of grating designs. A more significant problem would occur if the error in the Henke-based refractive index changes over the wavelength range of interest, as it is known to near absorption edges.



(a) 1st (-1) Order



(b) 2nd (-2) Order

Figure 3.12: Consistent overestimation or underestimation of the refractive index changes the magnitude, but not the overall shape, of the efficiency spectrum. Here we show the efficiency of a Nickel grating featuring an absorption edge at 853 eV. The thick red curve represents the efficiency based on refractive indexes calculated from the Henke data, in the form $\nu(\text{eV}) = 1 - \delta + i\beta$. The additional curves show the effect of a consistent relative error in either δ or β ; for example, $\nu' = 1 - 1.1\delta + i\beta$, or $\nu' = 1 - \delta + 0.9i\beta$. (Blazed grating, 1000 lines/mm, 1.11° blaze angle, 87° incidence angle.)

CHAPTER 4

IMPLEMENTATION OF THEORY: HOW WE CALCULATED EFFICIENCY USING COMPUTERS

In the initial stages of the spectrometer design project, we used `Gradif` – a program written by Michel Neviere, one of the original authors of the differential theory – for all of our calculations and optimizations. We also built a user interface for this program, to speed up the process of entering input and running multiple calculations. More recently, we implemented a new, open-source grating efficiency calculator from scratch to address some shortcomings of the `Gradif` code: performance, stability, and the ability to handle arbitrary grating shapes. A secondary benefit of this last project is the opportunity to share it freely with the grating/beamline design community, and to extend it in conjunction with other researchers.

In this chapter, we examine the existing grating software options, describe our experience using the `Gradif` code, and review the development and validation of new grating efficiency software.

4.1 Pre-existing grating efficiency software

Currently there are four commercial or closed-source programs available for calculating diffraction grating efficiencies (Table 4.1). `PCGrate` implements the modified integral method [22] and is the most general, although also the slowest and most expensive. `GSolver` uses the Rigorous Coupled Wave approximation [35][36] and can therefore handle any grating shape, subject to the previously noted issues with the staircase approximation in TM polarization. Two implementations of the differential method are available: Professor Neviere sells an

Table 4.1: Comparison of commercially-available grating efficiency software

Name and Organization	Method	Price (USD)	Graphical User Interface	Arbitrary Shapes
PCGrate-SX 6.5 IIG, Inc. http://www.pcgrate.com	Modified Integral Method (MIM)	GUI: 15749 Console: 11249 Both: 22499	Available	Yes
GSolver 5.2 Grating Solver Development Co. http://www.gsolver.com	Rigorous Coupled Wave (RCW)	795	Yes	Yes
Gradif Dr. Michel Neviere m.neviere@free.fr	Differential Method	6090	No	No
REFLEC Dr. Michael Krumrey Michael.Krumrey@ptb.de	Differential Method	0	No	No

implementation called **Gradif**, and the **REFLEC** program is used internally at the BESSY synchrotron. Although the differential method is general, both of these implementations are limited to predefined grating profiles (rectangular, blazed, trapezoidal, and sinusoidal).

Table 4.1 compares the methods, features, and cost of these programs.

4.2 Improving the usability and efficiency of Gradif

The Canadian Light Source purchased the **Gradif** code and made it available for this project. However, there were two challenges involved in applying the code:

1. The code itself is a Fortran-language program that provides no user interface. Instead, to calculate an efficiency data point for a grating at just one energy, approximately 30 numbers must be entered into a blank screen, with no prompts, in the correct order. These numbers define the grating geometry, the coating/layer thicknesses, the incidence conditions, the integration parameters, and also the complex refractive indices of the layers and the substrate.¹ Using this program requires a time-consuming and error-

¹These last two values will change as a function of photon energy, since the refractive index varies with wavelength, so we need to look them up for each data point.

prone data entry process.

2. In the event of an error made during data entry, one of many grating parameters could end up outside the narrow region of convergence where the code is able to numerically integrate a solution successfully. When this happens, the program runs forever in an infinite loop, with no feedback that the calculation has failed. This region of convergence is not well established, so even when data entry errors are avoided, it is possible for a user to specify a valid grating that is – for example – too deep to be calculated. Without user feedback, it is impossible to know if the calculation is still running successfully, or if it has failed into this infinite loop.

To beat these two challenges, we built a web-based graphical interface, and carefully modified the Fortran source code to detect convergence failures.

4.2.1 Visual interface to the `Gradif` code

Figure 4.1 shows a screenshot of the graphical user interface (GUI) that we built to help us perform efficiency calculations efficiently. The interface served as a wrapper to generate input for the `Gradif` code, manage running a set of calculations, and extract the results.

The interface was implemented as a web-based application, so it could be used from anywhere through a browser, without having to distribute the `Gradif` code or install anything on a person’s individual computer. Users described the grating parameters and incidence scenario through a form that prompted them for the necessary information based on the type of grating (Figure 4.1). When the calculation finished, an efficiency plot would be generated, and users could also download data tables of their calculations. These tables were also archived so they could be retrieved later.

It supported the following features:

- **Grating types**

The form would request the geometry parameters required for each of the supported grating types: rectangular, blazed, trapezoidal, and sinusoidal profiles.

- **Order and polarization**

1

Nephiere: A Program for Modelling Diffraction Grating Efficiencies

[Intro](#) | [Single Grating](#) | [Complex Scan](#) | [Mirror](#) | [Plot](#) | [Optimize](#) | [Files](#) | [Options](#)

Diffraction Efficiency (Single Grating)

Grating Type:

[beamteam.usask.ca](#) dev: [\[email\]](#) [Mark Boots](#) [University of Saskatchewan](#)

2

Nephiere: A Program for Modelling Diffraction Grating Efficiencies

[Intro](#) | [Single Grating](#) | [Complex Scan](#) | [Mirror](#) | [Plot](#) | [Optimize](#) | [Files](#) | [Options](#)

Diffraction Efficiency (Single Grating)

Grating Parameters: Triangular (Blazed) Grating

General Parameters

Groove Density /mm

Incidence Angle(deg)

Energy eV

Geometry

Blaze Angle (deg)

Opposite Angle (deg)

Grating Material

Material

Coating

Coating

Coating Thickness um

VLS Parameters

Linear correction /cm²

Quadratic correction /cm³

Cubic correction /cm⁴

Grating Size mm

Number of VLS points

Rock and Roll

Log File Name

Figure 4.1: This web application provides a graphical user interface for calculating grating efficiencies. Forms prompt users for the grating parameters.

Users could configure which inside and outside orders were plotted, and specify the polarization of the incident light: TE, TM, or natural light (randomly polarized).

- **VLS gratings**

To model variable line space (VLS) gratings, the interface accepted the VLS parameters in conventional notation (linear, quadratic, and cubic corrections) and used these to calculate the groove density and corresponding efficiency at a user-determined number of points along the grating surface; the overall efficiency was taken as an average of these.

- **Efficiency plots as a function of wavelength**

In the simplest mode, the system generated a plot of the efficiency in the desired orders as a function of wavelength, holding all the other parameters constant (Figure 4.2). This would represent the typical case of testing how a grating would perform in a beamline.

- **Complex scans over arbitrary grating parameters**

The interface also offered flexibility to test arbitrary relationships along incidence angle, energy, geometry, and other parameters. This feature was most efficiently used in conjunction with a spreadsheet or other data analysis program to fill in the grating parameters and interpret the output tables.

- **Database of optical materials and refractive index**

We also developed a database of common grating substrate and coating materials, so that the interface could automatically look up their complex refractive index as a function of photon energy. This information was calculated using the semi-empirical Henke data tables of the x-ray atomic scattering factor [23] discussed in Section 3.4.1. The library is valid from 30 eV to 10 000 eV, but is known to have poor accuracy in the vicinity of absorption edges.

- **Mirror reflectivity**

As an additional tool for beamline designers, we implemented the ability to calculate the reflectivity of a simple mirror using any of the materials in the refractive index

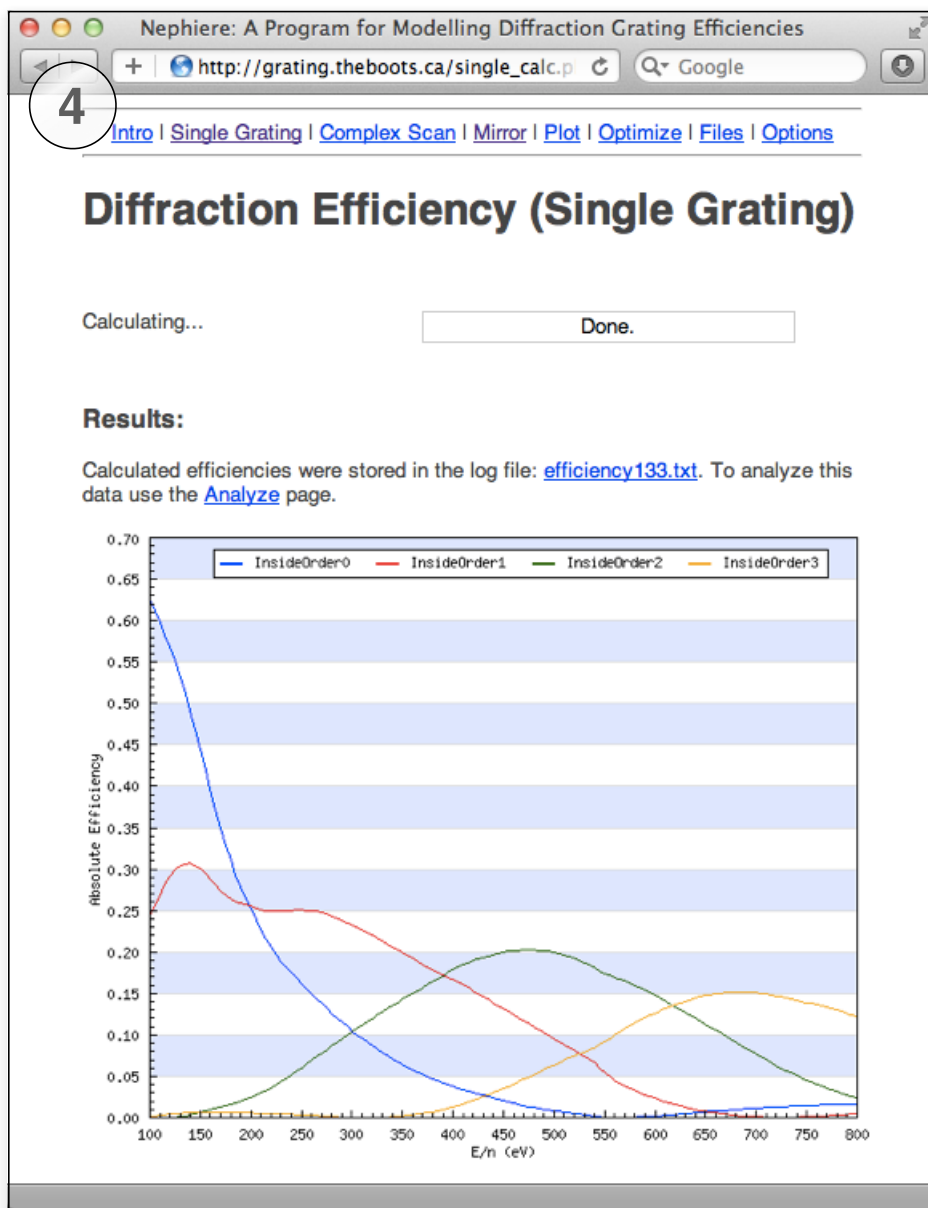
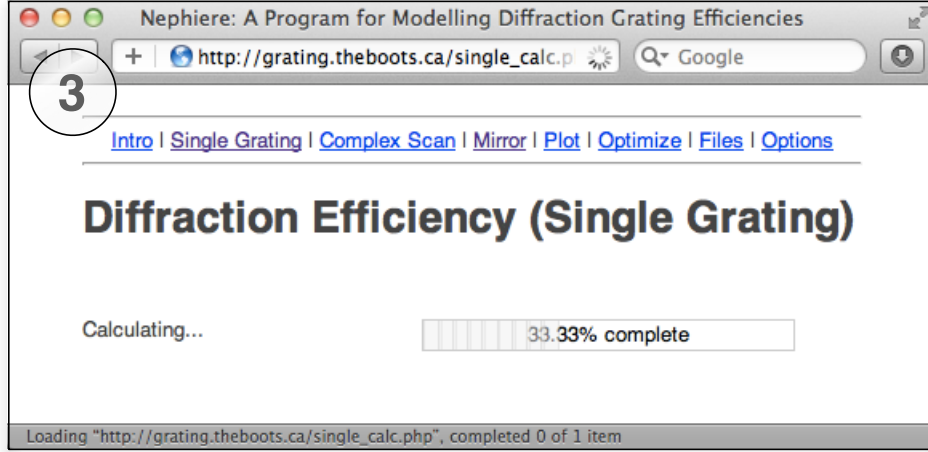


Figure 4.2: This web application provides a graphical user interface for calculating grating efficiencies. The results are plotted, and users can download a text-based table for further analysis.

database. Mirror reflectivity was computed as a function of incidence angle and photon energy using the complex Fresnel equations [16, p. 40] for both polarizations.

- **Control of numerical precision**

An ‘Options’ page (Figure 4.3) allowed users to configure the numerical precision used in the calculations. The two critical factors are the number of integration steps used in the numerical integration of the particular solutions for the $A_n^{(m)}$ and $B_n^{(m)}$ coefficients at each layer, and the number of Fourier coefficients $2N + 1$ used in the truncated sum. The defaults we chose ($N = 31$; 401 integration steps) were found to produce accurate results and reasonable performance across the entire soft x-ray range, as long as the coating thickness was less than 0.5um. However, prudent designers should still do convergence tests for any high-stakes results, by repeating the calculations and comparing against efficiencies computed using larger values. This technique can also be used to find the minimum number of Fourier coefficients that are required before the results start to disagree. (This can be helpful to optimize the computation speed before running a large number of calculations on similar gratings at similar wavelengths.)

4.2.2 Detecting integration failures

When an integration fails, the original `Gradif` code is programmed to repeatedly retry the calculation using successively thinner S-matrix layers. Sometimes this strategy is successful, but in many cases the integration fails regardless of the layer thickness, leading to an infinite loop. The Fortran code was written using a 1970’s-era programming approach, including substantial use of global variables and GOTO statements. (These two features are heavily discouraged in modern programming methodologies.) As a result, the code is hard to trace, but we were able to insert a counter to detect when a numerical integration fails after many repeated attempts. Our modification allows the calculation to exit with an error message, rather than run indefinitely.

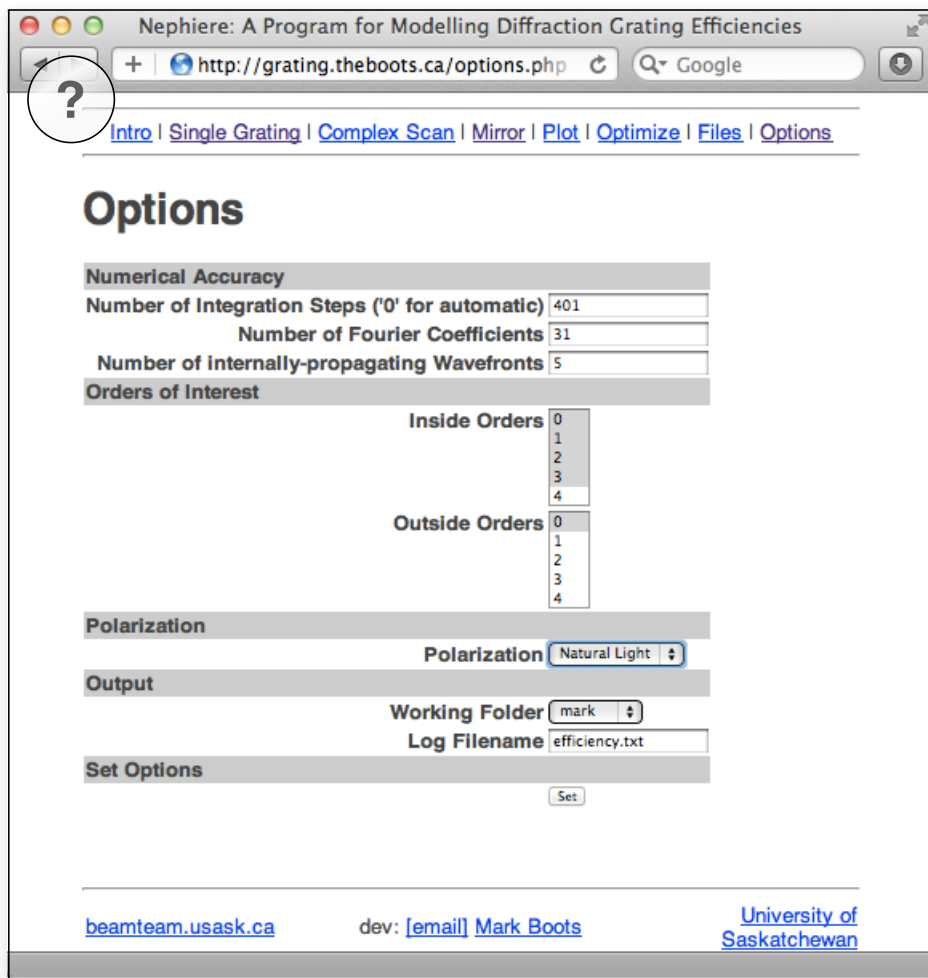


Figure 4.3: This Options page configures the numerical precision of the calculations, the diffraction orders of interest, and the polarization of the incident light.

4.2.3 Online access

Because the user interface ran as a web application, it could be (and was) accessed by beamline designers from all over the world. In one example, it was used by Professors Coryn Hague and Gheorghe Sorin Chiuzbaian to improve the design of a new beamline for the SOLEIL synchrotron. The calculations could be requested by anyone from anywhere, but they all ran on a single server computer at the University of Saskatchewan. Unfortunately, the underlying `Gradif` code is commercial software, and while we were licensed to run it on this machine, recent communication from Professor Neviere indicated that he was unhappy with this level of access to results calculated using his code. As a result, we disabled public access to the original website.

4.3 Improved, open-source grating efficiency software

4.3.1 Motivation for new grating software

The `Gradif` code allowed us to complete the design and optimization of the REIXS spectrometer in Chapter 6; however, several limitations provided motivation for improvement:

1. **Unpredictable instability:** For some rare but reasonable grating inputs, the numerical integration process becomes unexpectedly unstable. We expect this to happen for deep gratings outside of `Gradif`'s convergence range, but in other cases the failed calculations are surrounded by successful calculations. The random failures can usually be avoided by tweaking the number of integration steps or the number of Fourier coefficients, but not in a consistent or predictable way.
2. **Performance:** The run time of a single calculation depends on the grating depth, number of Fourier coefficients, and number of integration steps required for convergence; it can range from two seconds for shallow gratings to well over 30 seconds. At this speed, it is feasible to calculate the efficiency of a single grating over a range of wavelengths; however, if we want to do global optimization or fitting (Chapter 7), faster run times are desired. The `Gradif` code is inherently single-threaded, although

independent calculations can be run simultaneously by invoking the program multiple times.

3. **Arbitrary groove profiles:** As we will see in Chapter 7, grating manufacturing rarely produces the perfect, intended groove profile. To model real-world gratings, we need the ability to represent profiles of arbitrary shape; for example, point-wise defined curves derived from atomic force microprobe (AFM) measurements.
4. **Open online access:** Finally, since grating efficiency has rarely been considered during many past beamline designs, we believe the soft x-ray instrument design community would benefit from having access to an easy-to-use, easy-to-access grating efficiency calculator. It became obvious after taking down the original web interface to **Gradif** that there was a strong demand for this service.

These four factors motivated us to write a new implementation of the differential method from scratch.

4.3.2 Features and limitations

We envision two different software activities (“*use-cases*”) that would be helpful during the design phase of a soft x-ray instrument:

1. **Producing efficiency curves:** For a potential grating specification, a designer might want to predict its efficiency over the range of wavelengths or photon energies where that grating would be used. (For examples, see Figures 6.8, 6.9, and 6.10 in Chapter 6.)

These curves might assume a constant incident angle (for example, in a fixed-incidence spectrometer), or the designer might want to vary the incidence angle according to some function of the wavelength (for example, when designing a constant included angle (CIA) monochromator).

2. **Optimization:** Instead of simply predicting the efficiency, a designer probably wants to optimize it by varying the grating parameters within an acceptable range. The grating

parameters also affect the focussing and resolution characteristics of the instrument, therefore there will usually be constraints for some of the parameters. In other cases, the designer might wonder if a certain increase in efficiency is worth the trade-off it causes in resolution.

A global optimization method is desired here for two reasons: the efficiency function may have several local maxima, and the parameters have hidden dependencies. (For example, we show in Section 5.1.3 that the optimal “blaze angle”, or the angle at the base of a triangular groove profile, is highly coupled to the incident angle, order, groove width, and wavelength.)

Finally, there is one computationally intensive use-case that would be valuable to grating manufacturers and theorists:

3. **Fitting grating parameters to measured efficiency:** To validate and improve any of the modelling methods, we need to actually measure the efficiency of real gratings. This can be done on special beamlines that have been designed with **diffractometer** chambers for this purpose; we discuss our own measurements in Chapter 7. Some of the real-world grating parameters are hard to measure; for example, we found that the micro-structure of the surface (oxidation and roughness) dramatically affects the efficiency, but it is difficult to measure the roughness and oxidation levels directly. If these parameters could be incorporated into the efficiency model, a curve-fitting search could determine the parameters that best match the theoretical to the measured efficiency curves.

We wrote the new grating software in modular components so that it could be applied to all three of these use-cases. The grating solver (implementation of the differential method) is complete, along with an *application programming interface* (API) to integrate the solver into third-party programs. A command-line user interface enables single efficiency calculations or the calculation of efficiency curves in three different incidence modes. Work continues toward a web-based user interface, and a built-in global optimization and fitting facility. (Optimization and fitting can already be done using third-party tools, using the command-line interface or API to evaluate single efficiencies.)

Features

The solver and command-line interface support the following features:

- **Standard grating shape profiles:** rectangular, triangular, trapezoidal, and sinusoidal.
- **Custom grating shape profiles:** any point-wise defined profile.
- **Coatings:** an optional coating layer of a different material on top of the grating, generated by translating the grating profile vertically. The coating can be thicker than the groove depth, leaving a homogeneous layer between the coating grooves and the grating grooves, or it can interpenetrate the grating grooves. (Note: Coatings are not yet supported on custom profiles.)
- **Material Database:** automatic lookup of complex refractive indexes for common materials based on the Henke tables.
- **Incidence scanning modes:** calculation of common efficiency curves with a single command:

1. `constantIncidence` mode calculates the efficiency over a range of wavelengths (or photon energies) at a constant incidence angle.
2. `constantIncludedAngle` mode automatically varies the incidence angle as a function of wavelength, to satisfy a condition of a constant deviation from the incident light to the outgoing order n . (This is the operating mode for many monochromator designs.) The incidence angle θ_2 is computed from the grating equation (3.19) and the requirement that the included angle $\phi = \theta_2 + \theta_{2,n}$:

$$\theta_2 = \arcsin\left(\frac{-n\lambda}{2d\cos(\phi/2)}\right) + \phi/2$$

3. `constantWavelength` mode calculates the efficiency over a range of incidence angles at a constant wavelength.

- **Parallel calculations:**

- Fine parallelization of a single calculation
- Coarse parallelization of many efficiency calculations using high-performance computing resources

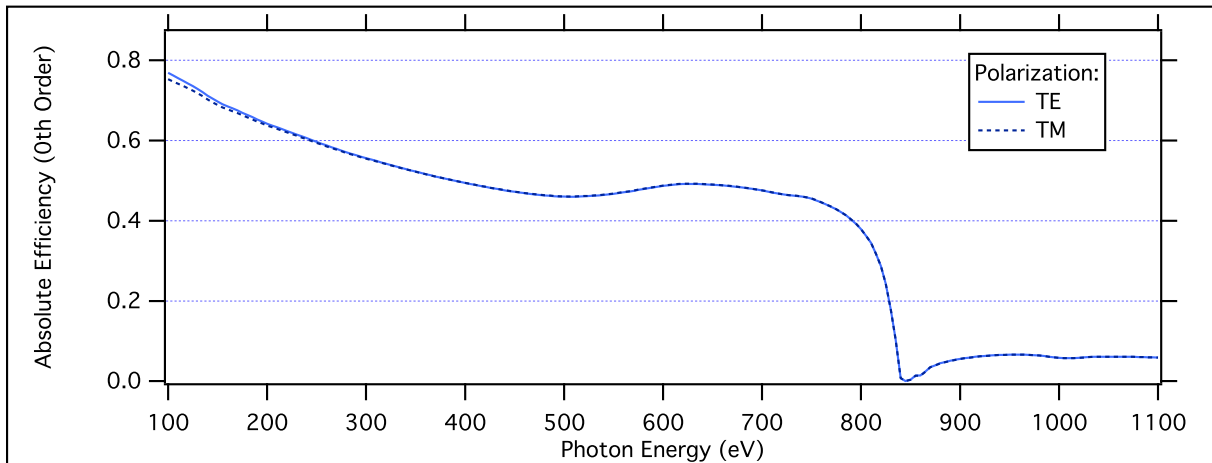
Limitations

The current version has two main limitations; work is ongoing to address both of these:

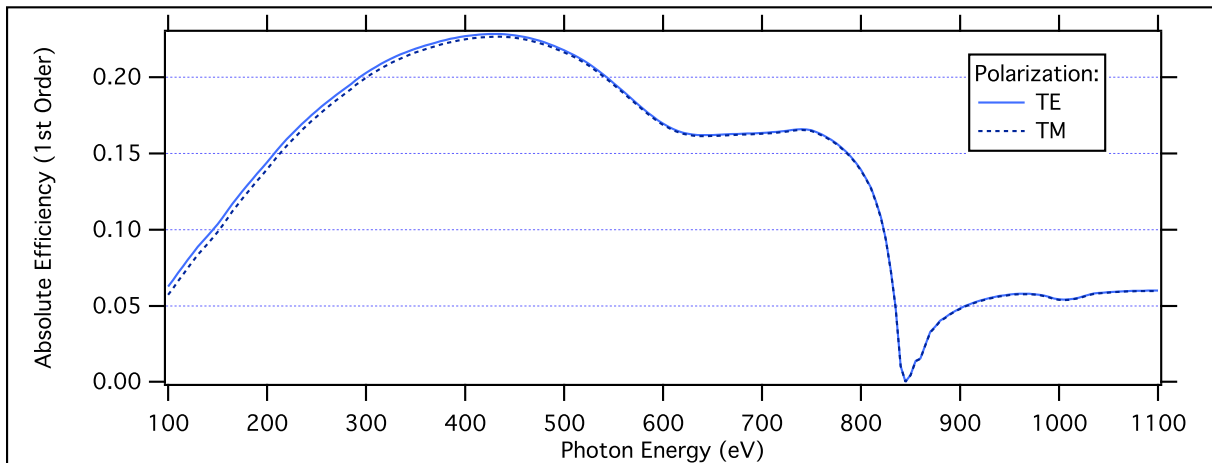
1. The solver currently only calculates the efficiency for TE polarization. Since the TE and TM polarization efficiencies converge at grazing incidence, for soft x-ray optics used in grazing incidence there is very little difference between the TE and TM polarization. Figure 4.4 shows a grating at 88 degrees incidence calculated using the **Gradif** program; the difference between TE and TM efficiency is generally less than 5% (relative). The shape of the TE and TM curves are also identical; therefore, designers currently using the TE results for optimization should not be misled even if their actual incidence configuration includes TM light. However, implementing the TM solver is necessary for completeness, and accuracy at more normal incidence angles (Figure 4.5).
2. Interpenetrating coatings are not yet supported for custom (point-wise defined) groove profiles.

Improving Stability

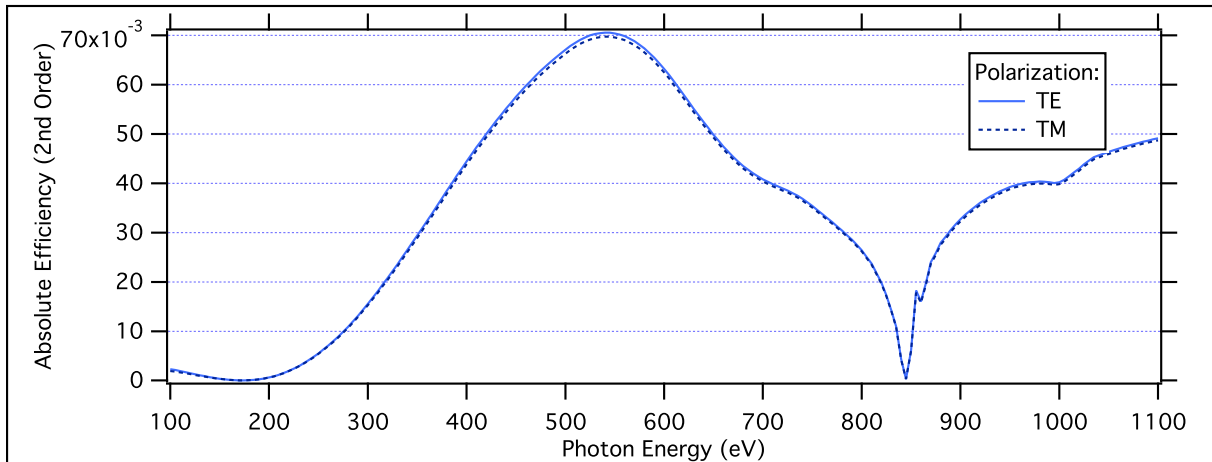
The solver uses two techniques to improve integration stability of the ordinary differential equation (3.23). **Gradif** uses a fixed number of vertical integration steps, regardless of the height of the grating or the thickness of the S-matrix layers. Therefore, the user needs to manually estimate the appropriate number of integration steps necessary for convergence of a specific problem. Instead of a fixed step size, we use an adaptive step size integration algorithm with error prediction, to ensure that the error at every integration step remains under a defined tolerance. This allows us to automatically use smaller steps where the problem is sensitive, and larger steps for faster performance whenever possible. Users no longer need to manually estimate the appropriate number of integration steps, although



(a) 0th Order

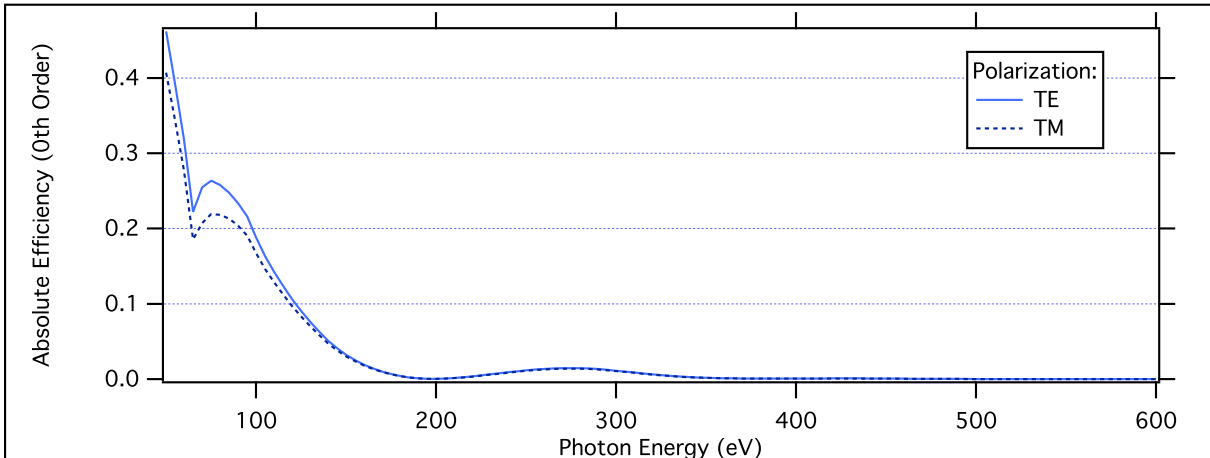


(b) 1st Order

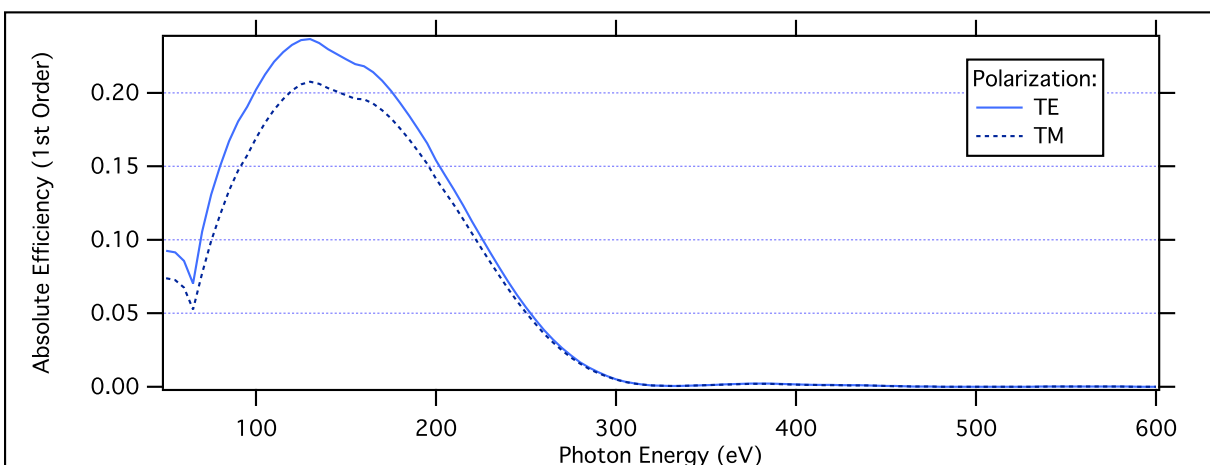


(c) 2nd Order

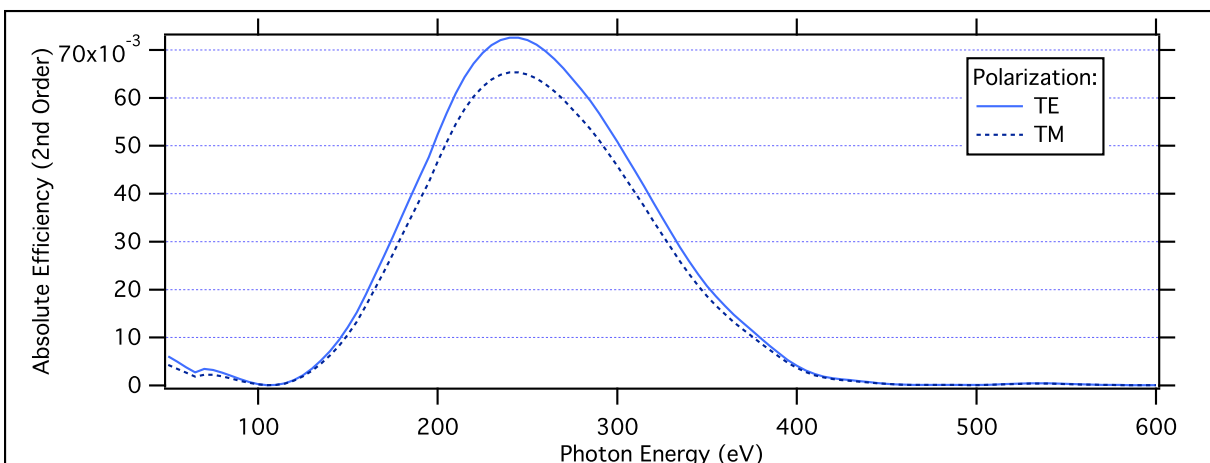
Figure 4.4: The difference in efficiency between TE and TM polarization is very small for grazing-incidence optics. For this grating at 88 degrees incidence, the difference is less than relative 5%. Grating: 1200 lines/mm, 1.48° blaze angle, Nickel coating.



(a) 0th Order



(b) 1st Order



(c) 2nd Order

Figure 4.5: At more normal incidence, the efficiency is different for TE and TM polarization. This is the same grating as Figure 4.4 but at 80 degrees incidence; the difference becomes up to relative 20%. However, because the shapes of the curves are identical, optimization of the TE efficiency provides the same results as optimization of the TM efficiency. Grating: 1200 lines/mm, 1.48° blaze angle, Nickel coating.

they can adjust the tolerance setting if required for exceptional problems. (The default tolerance setting was determined over a range of typical soft x-ray grating inputs to offer good performance while ensuring convergence and a wide margin of stability.) Although the variable step size method offers better accuracy, better reliability, and less possibility of operator error, it comes with one performance trade-off: we can no longer share computations of the $M(y)$ matrix and $k_n^2(y)$ expansions across all the trial solutions; each trial solution will potentially need to evaluate them at different values of y .

For the ODE integration algorithm, we experimented with a variety of explicit methods,

- classical 4th order Runge-Kutta,
- Runge-Kutta-Fehlberg,
- multistep Adams-Bashforth,

and implicit methods,

- second and fourth-order Runge-Kutta,
- Bulirsch-Stoer, and
- multi-step backward difference.

We found that the results were insensitive to the integration method to more than six significant figures, and that the explicit methods (predictably) ran much faster than the implicit ones. Currently, we use a method under the family of *Adams-Bashforth multistep methods*, which uses an explicit Adams-Bashforth predictor and an implicit Adams-Moulton corrector [10]. It was found to offer the highest performance, since the error estimation requires far fewer function evaluations than the classical Runge-Kutta algorithm.

The solver's second stability improvement comes from automatically estimating the number of S-matrix layers required to keep the integration values bounded within significance. The largest values of the exponential functions [$\exp(i\beta_n y)$] occur for the largest orders $-N$ and N when they are evanescent, where $\beta_{(\pm N)} \approx \pm i2\pi N/d$. To estimate the maximum size these will reach after integration over a layer of thickness h , we can bound them with an

assumed homogeneous layer with the same index as the vacuum:

$$\text{Maximum Value} \approx \left| e^{i\beta_{(\pm N)}^{(M)} h} \right|$$

Double-precision variables have a precision of approximately 16 decimal digits. To keep a significance of (for example) 10^{-6} in the final result, we need to keep the maximum value below $10^{15} \times 10^{-6} = 10^9$. From this, we can estimate the maximum layer thickness h :

$$\text{Maximum Value} = 10^9 = \left| e^{i\beta_{(\pm N)}^{(M)} h} \right|$$

There should always be sufficient orders to ensure that the highest outside orders are evanescent, so $\beta_{(+N)}^{(M)}$ should always be fully imaginary. Therefore,

$$h \approx \frac{\ln(10^9)}{\text{Im}(\beta_N^{(M)})}$$

Experimentation has shown that using a layer thickness of approximately $h/2$ gives a reliable margin of stability.

The two stability controls – the integration error tolerance and the layer thickness – are related. Thicker layers can sometimes become stable when the integration tolerance is decreased, but only to a limit; increasing the number of S-matrix layers is always the most reliable way to achieve stability.

4.3.3 Obtaining and running the new software

Work is still ongoing on a new web-based graphical user interface. However, the command-line version of the program is ready for use, and can be downloaded and run following the instructions on the project repository:

Instructions and introduction: <https://github.com/markboots/peg>

Download: <https://github.com/markboots/peg/zipball/master>

Check out with git: `git://github.com/markboots/peg.git`

Revision history: <https://github.com/markboots/peg/commits/master>

The program accepts input via command-line arguments, and writes efficiency results to an output file. It can optionally update a progress file while the calculations are running; this allows other processes (such as a graphical front-end or web interface) to monitor the status of the run, check for failures, and see what fraction of the total calculations are finished. Table 4.2 documents the command-line arguments for specifying the grating and incidence configuration. An example of the output file format is shown in Figure 4.3.

4.3.4 Parallel program design and performance

Over the past forty years, the power and speed of scientific software has increased exponentially. Part of this has been the result of improved algorithms in numerical analysis, but most of it has come from a similar exponential increase in the processor speed and memory capacity of computer hardware. Recently, however, physical limits have started to encroach on “Moore’s Law”, which originally suggested a doubling in chip performance every 18 months: as transistors approach the atomic scale, quantum effects will set a hard lower limit on their size. In the future, software will no longer be able to count on perpetually-increasing processor speeds; instead, the only path to higher performance will come from exploiting *parallelism*: the ability to compute parts of the problem simultaneously on multiple processors. (This is already evident in the hardware trend of the past 4 years, where computer processor clock speeds have nearly stagnated, but the average number of cores per processor has increased from one to four.)

For the present, parallel processing can provide a solution in two scenarios: when a numerical problem is too big to fit in a single computer’s memory, or when the problem takes too long to run. In our case, optimization and fitting tasks fall into the second category. If we assume that **Gradif** is already implementing the differential method efficiently, then the *only* way to beat its performance on the same hardware is by using parallelism.²

For both of these reasons, we designed the new software to support parallel calculations from the start.

²In fact, because our software’s variable step size integration method requires more calculations of the grating expansion k_n^2 in exchange for better stability, we should expect it to be slower than **Gradif** *unless* we find a way to exploit parallelism.

Table 4.2: Input command line arguments for the pegSerial and pegMPI programs.

Required	
Grating Specification:	
--gratingType	One of: [rectangular blazed sinusoidal trapezoidal]
--gratingPeriod	[grating period in um]
--gratingGeometry	command-delimited list of geometry parameters, in um and/or degrees] Rectangular profile: depth, valley width Blazed profile: blaze angle, anti-blaze angle Sinusoidal profile: depth Trapezoidal profile: depth, valley width, blaze angle, anti-blaze angle
--gratingMaterial	[grating substrate material]: This should be a name corresponding to a refractive index database filename, e.g., Au, Ni, C, SiO2, etc.
--N	[truncation index]: Specifies the number of positive and negative orders to include in the Fourier expansion. Will also determine the number of orders that are calculated, although if you only want to calculate 3 orders, you will still need a much larger truncation index for accurate results. In the soft X-ray range, convergence is usually attained with $N \sim [15\ldots45]$.
Operating Mode:	
--mode	One of: [constantIncidence constantIncludedAngle constantWavelength]
--min	[min]
--max	[max]
--increment	[increment]
Required, depending on the mode:	
--incidenceAngle	[incidence angle in degrees]
--includedAngle	[deviation angle in degrees]
--toOrder	[diffraction order for the included angle]
--wavelength	[wavelength in um]
In constant incidence mode, a calculation is performed for wavelengths from --min to --max in steps of --increment, at a fixed incidence angle given by --incidenceAngle.	
In constant included angle mode, the incidence angle is calculated at each wavelength to ensure a constant included angle of --includedAngle between the incident light and the order specified in --toOrder. This is the operating mode for many monochromators. (Inside orders are negative, outside orders are positive.)	
In constant wavelength mode, a calculation is performed for incidence angles from --min to --max in steps of --increment, for a fixed wavelength given by --wavelength.	
Output:	
--outputFile	[file name]: The calculation output will be written to this file.
Optional	
--progressFile	[file name]: If provided, the current status of the calculation will be written in this file; it can be monitored to determine the progress of long calculations. This provides an interface for other processes to monitor the status of this calculation (for example, a web-based or GUI front-end, etc.).
--eV	If this flag is included, all wavelength inputs (-min, -max, -increment, and -wavelength) will instead be interpreted as photon energies in electron volts (eV).
--printDebugOutput	If this flag is included, each calculation will print intermediate results to standard output.

Table 4.3: Output file format for the pegSerial and pegMPI programs. The Input section restates the program input, the Progress section is updated as the calculation completes, and each row of the Output section lists the independent variable (wavelength, eV, or incidence angle, depending on the mode) followed by the calculated efficiencies for all orders from $-N$ to N .

```
Test      executed      with:      ./pegSerial --mode constantIncidence --min 100 --max 120  
--increment 5 --eV --incidenceAngle 88 --gratingType blazed --gratingPeriod 1  
--gratingMaterial Au --N 15 --gratingGeometry 2.5,30 --outputFile testOutput.txt  
--progressFile testProgress.txt
```

```

# Input
mode=constantIncidence
incidenceAngle=88
units=eV
min=100
max=120
increment=5
gratingType=blazed
gratingPeriod=1
gratingGeometry=2.5,30
gratingMaterial=Au
coatingMaterial=[none]
coatingThickness=0
N=15
integrationTolerance=1e-05
# Progress
status=succeeded
completedSteps=5
totalSteps=5
# Output
100      4.86049e-06,5.73524e-06,1.15331e-05,2.26984e-05,3.40043e-05,3.20538e
         -05,1.09471e-05,2.46656e-05, 0.000207617,0.000525489,0.000402885,9.29454e
         -05 ,0.00604008,0.0202516,0.193704,0.688149, 0,0,0,0,0,0,0,0,0,0,0,0,0,0,0,0,0,0
105      5.17974e-06,4.87572e-06,8.75638e-06,1.96591e-05,3.6063e-05,4.48567e
         -05,2.63319e-05,8.62826e-06, 0.000156884,0.000572518,0.000629053,6.95573e
         -06 ,0.00581251,0.0252621,0.200502,0.678858, 0,0,0,0,0,0,0,0,0,0,0,0,0,0,0,0,0,0
110      5.85305e-06,4.91785e-06,6.66783e-06,1.53924e-05,3.35836e-05,5.23866e
         -05,4.57548e-05,9.18712e-06, 9.75067e-05,0.000564861,0.000862771,2.38342e
         -05 ,0.00534777,0.0305067,0.205757,0.669051, 0,0,0,0,0,0,0,0,0,0,0,0,0,0,0,0,0,0
115      6.70782e-06,5.76303e-06,5.81191e-06,1.15465e-05,2.8753e-05,5.44993e
         -05,6.33855e-05,2.451e-05,4.82133e-05,
         0.000510943,0.00107579,0.000154448,0.00472995,0.0359483,0.209988,0.658912,
         0,0,0,0,0,0,0,0,0,0,0,0,0,0,0,0,0,0
120      7.51931e-06,7.11245e-06,6.20636e-06,8.89412e-06,2.30516e-05,5.20039e
         -05,7.60472e-05,4.85705e-05,1.87322e-05,
         0.000421879,0.00124637,0.000396847,0.00401002,0.0415518,0.213464,0.648892,
         0,0,0,0,0,0,0,0,0,0,0,0,0,0,0,0,0,0

```

Fine-grained Parallelization

Computing the grating efficiency in all orders n at a single wavelength λ can be viewed as a single “calculation” of the efficiency function:

$$e_n = \text{eff}(\lambda, p_1, p_2, \dots),$$

where the parameters p_1, p_2, \dots represent the grating parameters.

Based on our experience with `Gradif`, we expect that this calculation can take from two seconds up to several minutes depending on the grating. **Fine-grained parallelization** attempts to speed up a single calculation, which should benefit desktop users with multi-core processors. By analyzing the differential method, we identified the following possibilities for decomposing the problem into parallel tasks:

- **Option 1:** In the shooting method, all of the $P = 2(2N + 1)$ trial solutions need to be numerically integrated from y_{m-1} to y_m in each slice. All of the trial solutions are independent, allowing parallelization of this process over p . Profiling results (Table 4.4) show that the integration process, including calculation of the permittivity matrix $M(y)$ at each step, represents 99.99% of the total calculation time. This suggests that this is the (only) worthwhile candidate for parallelization. When using the S-matrix method, if there are more processors available than trial solutions P , we can also parallelize the independent integrations over each layer m .
- **Option 2:** The permittivity matrix $M(y)$ must be calculated based on the grating profile, for each grid value along the y -axis. If the integration routine uses a fixed step size, the computation of all the M matrices could be parallelized over grid points. This is not directly possible if the integration routine uses a variable step size, in which case M needs to be evaluated at each integration step.
- **Option 3:** The final step of the shooting method requires inversion of a $2N + 1$ linear algebraic system; this could optionally use a parallel iterative solver, but for typical N values from 15 to 45, there is little room for improvement here: the matrix calculations are already small, fast, and fit easily within a single processor’s memory space. With

$N = 15$, they account for less than 0.02% of the total run time of the serial program (Table 4.4).

Table 4.4: Time profile measurements of solver operations, averaged over 5 runs in single-threaded mode. Essentially all of the time is spent in the integration of the trial solutions, which includes the required calculation of $M(y)$ at each integration step. This example is for a blazed grating, using $N = 15$.

```
Test executed with: ./pegSerial --mode constantIncidence --min 100 --max 120
--increment 5 --eV --incidenceAngle 88 --gratingType blazed --gratingPeriod 1
--gratingMaterial Au --N 15 --gratingGeometry 2.5,30 --outputFile testOutput.txt
--progressFile testProgress.txt --measureTiming
```

Solver Operation	Percent of Run time
Allocate Memory	0.0003%
Look up refractive index	0.6803%
Compute α_n , β_n values and layers	0.0006%
Numerically integrate trial solutions	99.3011%
S-matrix operations	0.0174%
Compute Rayleigh coefficients $B_n^{(M)}$	0.0003%
Compute and package efficiencies	0.0001%

Coarse-grained Parallelization

Fine-grained parallelization over trial solutions has a limit to scaling: it can only use up to $P \times (M - 1)$ processors, if we distribute every trial integration within every layer. (This is obviously not a practical limit for desktop users with four or eight cores, but it does limit the theoretical scalability of the program in a high-performance computing (HPC) facility.) However, all three of the use-cases – efficiency curves, optimization, and fitting – require repeated calculations of the efficiency function over different wavelengths or parameters. Because all of these calculations can be done independently, we can obtain a nearly linear speedup using

an “embarrassingly parallel” distribution of separate calculations to each processor. This avoids nearly all the overhead of synchronization and communication that can limit parallel performance. Due to the small amount of information that needs to be shared across processes, this approach could scale to effectively use hundreds or thousands of nodes in a HPC facility.

Parallel Implementation Details

The fine-grained approach requires substantially more inter-process communication than the coarse-grained approach. Therefore, we implemented it using the shared-memory programming paradigm using the OpenMP library [46]. Based on the profiling results (Table 4.4), we determined that any performance gained from Option 3 would not be significant enough to make it worth attempting. Because we chose an adaptive step-size integration algorithm to increase the integration stability, Option 2 was not possible, so we concentrated on implementing parallelization over trial solutions (Option 1).

Fine-grained parallelization is built into the `pegSerial` program, and enabled using the `--threads` command-line argument. We tested the parallel efficiency of this mode using one of the machines in the `bugaboo.westgrid.ca` cluster, part of the WestGrid high-performance computing resource that is made available to academic researchers through Compute Canada. On this machine, we could use up to 12 processors; the results in Table 4.5 show that our code achieves a parallel utilization efficiency of 94% using 4 threads, dropping to 81% as the overhead increases with 12 threads.

The coarse-grained parallelization lends itself naturally to a distributed-memory computing paradigm, so we implemented it using the Message Passing Interface (MPI) standard [39]. In this environment, the same program (`pegMPI`) is launched simultaneously on multiple processors in a cluster computer. Each program determines for itself which wavelengths/energies/incidence angles it should calculate. After every calculation, each program broadcasts its results over the network to the “root node”, which is responsible for writing a single output file and progress file.

Table 4.6 shows that the coarse-grained parallelization is extremely efficient; in fact, it seems to run more efficiently than the single-threaded program. This is of course impossible;

Table 4.5: The run time, speedup, and efficiency attained using OpenMP fine-grained parallelization on a single `bugaboo` node using up to 12 processors. Reported results are based on the minimum run time of five runs.

```
Test format: ./pegSerial --mode constantIncidence --min 100 --max 131
--increment 1 --incidenceAngle 88 --outputFile timingTestOutput.txt
--gratingType blazed --gratingPeriod 1 --gratingMaterial Au --N 15
--gratingGeometry 2.5,30 --eV --threads t
```

Threads t :	1	2	4	6	8	10	12
Runtime (s):	94.55	48.50	25.27	17.80	13.35	11.33	9.71
Speedup:	1	1.95	3.74	5.31	7.08	8.35	9.73
Efficiency:	100%	97%	94%	89%	89%	83%	81%

the efficiencies over 100% are timing artifacts caused by the fact that some `bugaboo` nodes are faster than others.

Modern cluster architectures often contain many independent computers (“nodes”) connected via a local area network, with every node having four to eight local processor cores. To take advantage of this architecture, the two parallel modes can be used simultaneously in a hybrid execution model using fine-grained distribution over the local processor cores, and coarse distribution over cluster nodes.

4.3.5 Validation of the new software

We tested the new software extensively for logical self-consistency, and for consistency with `Gradif`. In this section, we list examples of the tests that gave us confidence that its output is physically reasonable; in the next chapter, we validate both `Gradif` and our new software against experimental measurements.

Table 4.6: The run time, speedup, and efficiency attained using MPI coarse-grained parallelization on the `bugaboo` cluster using 1 to 32 processors. Reported results are based on the minimum run time of five runs. The efficiencies larger than 100% are measurement artifacts, due to some `bugaboo` nodes being faster than others; there is no way for the `pegMPI` program to exceed a theoretical efficiency of 100%.

```
Test      format: mpiexec -n P ./pegMPI --mode constantIncidence --min
100 --max 131 --increment 1 --incidenceAngle 88 --outputFile
timingTestOutput.txt --gratingType blazed --gratingPeriod 1
--gratingMaterial Au --N 15 --gratingGeometry 2.5,30 --eV
```

Processors P :	1	2	4	8	16	32
Runtime (s):	112.73	54.33	27.14	13.64	6.37	3.23
Speedup:	1	2.07	4.15	8.27	17.70	34.91
Efficiency:	100%	104%	104%	103%	111%	109%

Physical Principles

- **Conservation of Energy** requires that the sum of transmitted and reflected efficiencies must be unity for lossless (non-absorbing gratings), and always less than unity for absorbing gratings. If we set the imaginary component of the refractive index to 0, we can confirm that the sum of all reflected and transmitted efficiencies is exactly 1.0:
 - Example triangular grating: 1000 lines/mm, 2.5° blaze angle, 88° incidence angle, 410 eV, $N = 15$:
 - * With refractive index $\nu_1 = (1.4 + 0i)$, the efficiency sum is $\sum e_{r,n} + \sum e_{t,n} = 0.703347 + 0.296606 = \mathbf{0.999953}$.
 - * With refractive index $\nu_1 = (0.993 + 0i)$, the efficiency sum is $\sum e_{r,n} + \sum e_{t,n} = 0.983451 + 0.016549 = \mathbf{0.999999}$.

Real gratings are absorbing materials, such as Platinum at 410 eV:

- With refractive index $\nu_1 = (0.993 + 0.00754i)$, the efficiency sum is $\sum e_{r,n} +$

$$\sum e_{t,n} = 0.45904 + 0.000782219 = \mathbf{0.459822}.$$

- The **Reciprocity Theorem** requires that the intensity of an electromagnetic signal should not change when swapping the source and the detector. For gratings, this would represent an exchange of the incident plane wave and the outgoing diffraction order of interest. Surprisingly, this means that the efficiency of order n at an incidence angle θ_2 should be the same as the efficiency of the corresponding order at incidence angle $\theta'_2 = -\theta_{2,n}$.
 - Example triangular grating: 1000 lines/mm, 2.5° blaze angle, 30° anti-blaze angle, 410 eV, $N = 15$:
 - * At $\theta_2 = 88^\circ$ incidence, the calculated (-1) order efficiency is **8.23519%**. The outgoing angle is $\theta_{2,-1} = 85.114^\circ$.
 - * At $\theta'_2 = -85.114^\circ$ incidence, the calculated (-1) order efficiency is **8.23339%**. (The outgoing angle is -88° as required.)

For another test, instead of using a negative incidence angle, we mirrored the grating geometry horizontally and extracted the outside order instead:

- * At $\theta''_2 = 85.114^\circ$ with a 30° blaze angle and 2.5° anti-blaze angle, the calculated $(+1)$ order efficiency is **8.23339%**.

One consequence of the reciprocity theorem is that the 0th order reflection efficiency should not change when rotating a grating around its y -axis by 180° . Although this might be obvious for symmetric gratings, it is rather surprising for gratings with asymmetric groove profiles. For example, the 0th order efficiency for the 2.5° blazed grating calculated above was **18.1245%** at 88° incidence. Flipping the grating to obtain a 30° blaze angle and 2.5° anti-blaze angle, we calculated an identical 0th order efficiency of **18.1245%**.

Logical consistency for coatings

When the software was extended to handle coatings, there were several opportunities to check for logical situations where the efficiencies should remain the same. Because the coating

amounts to a vertical extension of the grating profile, a coating of material X on top of a substrate of the same material should represent the same physical grating – despite being calculated differently. If we know the efficiency of a bare grating of material X, all of the following coating scenarios should (and do!) produce the exact same results, albeit with longer calculation times:

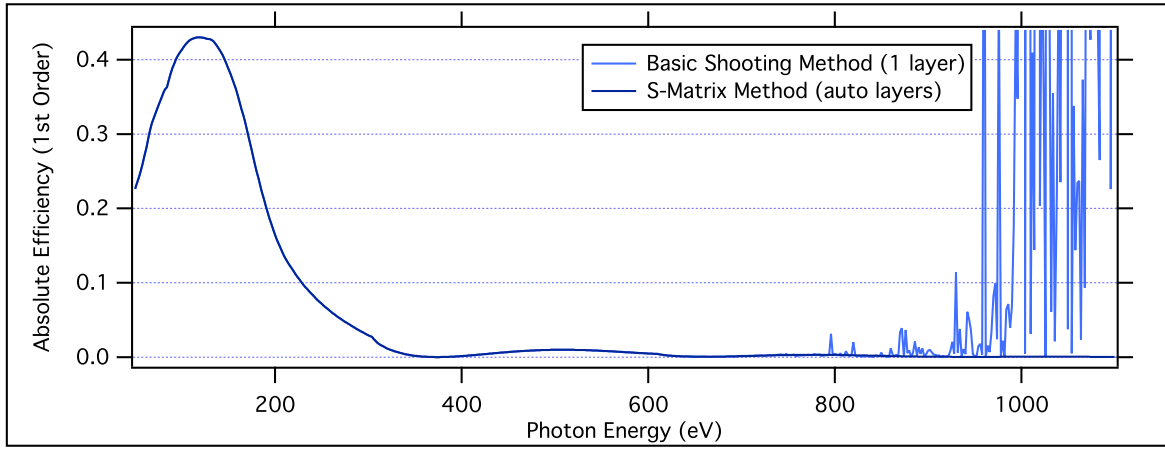
- A 0-thickness coating of any material Y on X
- A thin (interpenetrating) coating of material X on X
- A thick coating of material X on X
- A very thick coating of material X on any material Y

Logical consistency for S-matrix layers

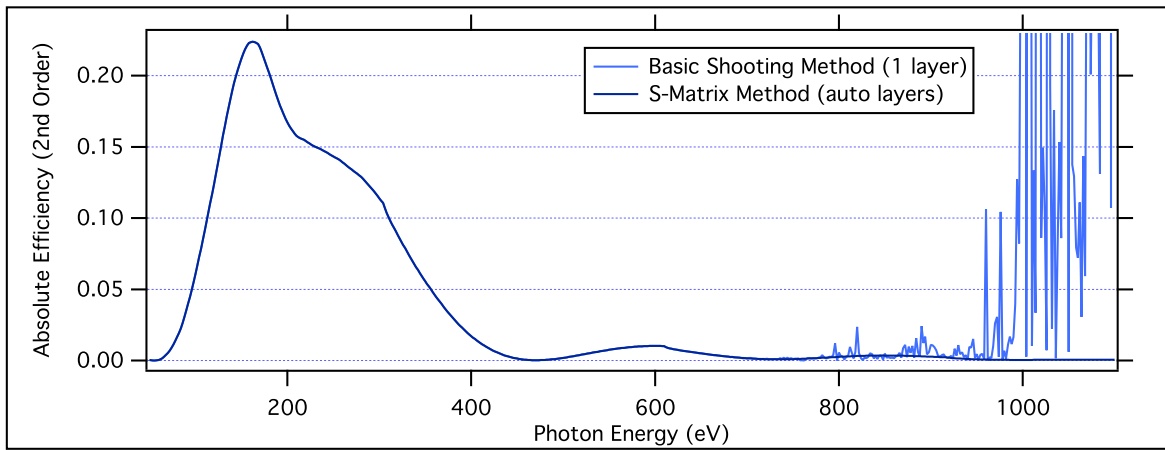
When the software was extended to use the S-matrix algorithm, we expected that:

- For thin gratings that were previously stable, it should reproduce the same results as the basic shooting method (Section 3.3.4).
- For thick gratings that were previously unstable, it should produce stable results.
- For gratings that previously showed wavelength regions of stability and instability, the new results should converge with the previous regions of stability.
- As long as sufficient layers are used, the results should be invariant to the number of layers.

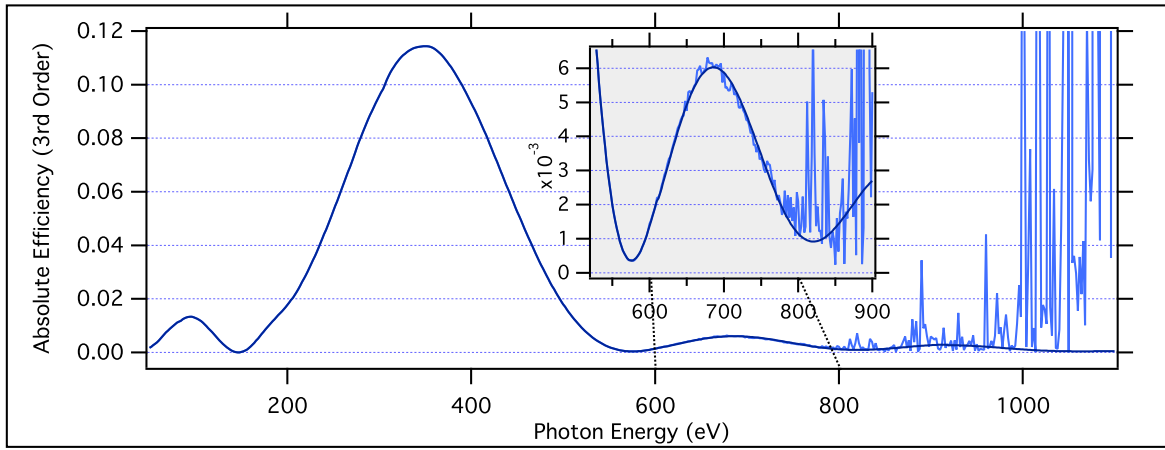
All of these criteria are satisfied. For thin gratings, the results using 1, 2, 5, 10, and 100 layers are identical to more than six significant figures. Figure 4.6 shows a great example of a problem that was unstable at high energies when using a single layer; using just a few layers, the S-matrix approach eliminates these instabilities but converges smoothly with the valid parts of the original curve.



(a) First Order



(b) 2nd Order



(c) 3rd Order

Figure 4.6: The S-matrix approach is the solution for this problem that became unstable at high energies when using the basic shooting method. The software automatically determines the number of layers required, ranging here from one layer at low energies to three layers at high energies. The inset in the 3rd-order curve shows that the numerical error “noise” is also reduced, even for calculations that remain “stable”. (Blazed grating, 600 lines/mm, 1.85° blaze angle, gold substrate, 86° incidence.)

Logical equivalence for point-wise defined profiles

When the software was extended to handle arbitrary groove shapes based on a set of (x, y) points defining the surface function $y_p = g(x)$, we confirmed that although the method for calculating the k_n^2 expansion differs, we produced the same results for the basic profiles (rectangular, blazed, and trapezoidal) and their point-wise defined equivalents.

Comparison to **Gradif**

We compared the new software to previous **Gradif** calculations of the TE efficiency for a wide range of gratings. We found that both programs are in agreement, typically to at least three significant figures. (The exact agreement depends on the number of integration steps chosen for **Gradif**; increasing the number of steps generally improves the agreement.) Figure 4.7 shows a set of comparison calculations over a range of coating thicknesses. The red curve shows the relative difference in the efficiencies calculated by the two programs for the 50 nm-thick grating; it is less than 1000 parts per million everywhere. For all practical purposes, the results are identical. Work is ongoing to examine whether the new software can handle calculations that previously fell outside **Gradif**'s domain of convergence.

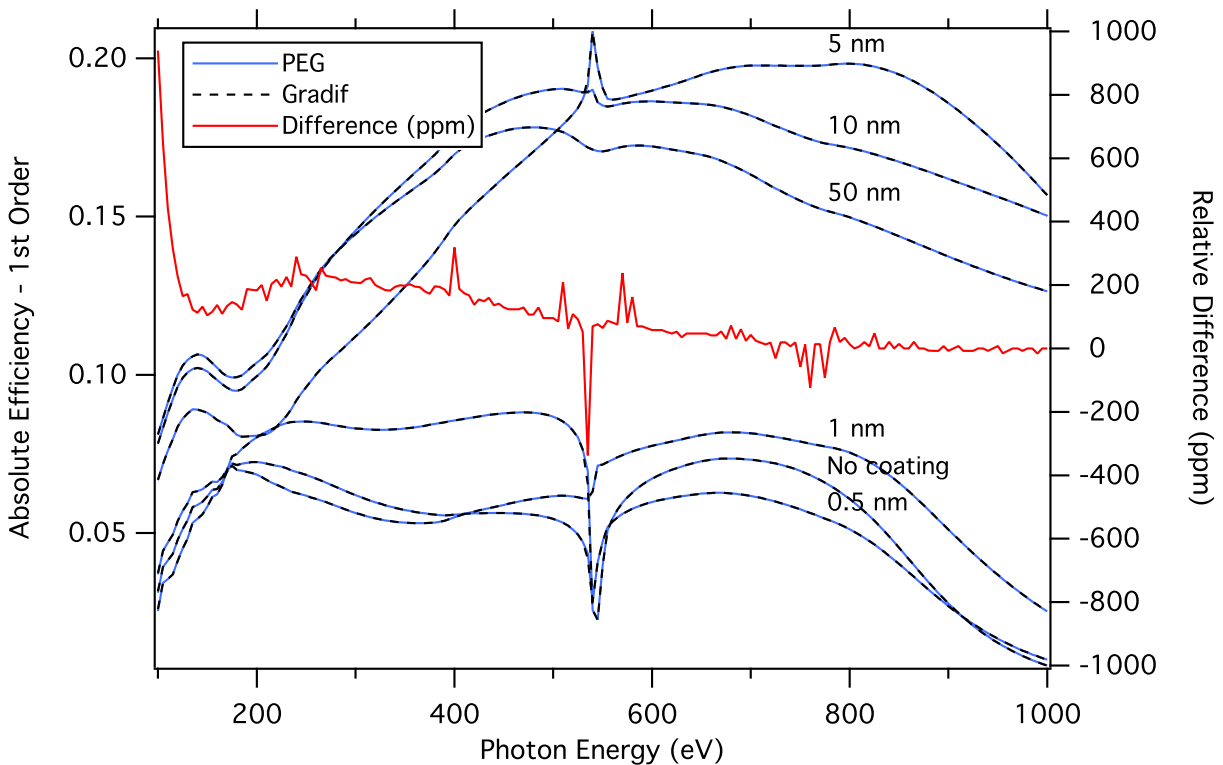


Figure 4.7: The new software agrees with **Gradif** to more than three significant figures. These calculations show the TE efficiency for a blazed grating on an SiO_2 substrate, with a range Pt coating thicknesses. The red curve is the relative difference between the two programs for the 50 nm calculation, in parts per million. (Blazed grating, 1200 lines/mm, 1.46° blaze angle, 88° incidence.)

CHAPTER 5

TRENDS: HOW DIFFERENT FACTORS AFFECT THE GRATING EFFICIENCY

With new software tools in-hand, we move on to the next question: What can we learn from them about the efficiency of gratings, especially those used in typical soft x-ray instruments?

This chapter looks at the theoretical effects caused by changes to grating parameters: groove profile, shape (depth, duty cycle, angles, etc.), line density, coating material, coating thickness, and incidence angle. We can think of the grating efficiency as a scalar function of this many-dimensional parameter space, but it is impossible to capture its complexity in a simple analytical equation. None the less, the results in this chapter should give beamline designers an understanding of trends along each dimension within this space, and how to apply these trends to the optimization of gratings.

We attempt to isolate the effects of each parameter as much as possible. However, many parameters are linked together so that they cannot be made independent. For example, as we show in Section 5.1.3, gratings with triangular profiles have an optimal *blaze angle* (the angle at the base of the light-facing facet, Figure 5.6) that aligns the outgoing diffraction order with the specular reflection for maximum efficiency. For this type of grating, changing only the groove density will change the outgoing diffraction angle, and therefore change the optimal blaze angle. Simply plotting the efficiency as a function of groove density while holding all other parameters constant would confuse the blaze effect with the density effect; instead, we correct for this by adjusting the angle to keep the grating “on-blaze” as we vary the groove density in Figure 5.8.

All of the calculations in this chapter were computed with the differential method, using

either **Gradif** or our new PEG implementation. Unless otherwise noted, results are shown for randomly polarized (natural) light, which is an average of the TM and TE efficiency. When we refer to 1st and 2nd order efficiencies without clarification, we implicitly mean the inside orders ($n < 0$).¹

5.1 Effect of grating profile: groove shape

As we showed in Chapter 3, any kind of periodic groove structure will have a diffraction effect, regardless of the nature of the groove shape. However, the grating efficiency – particularly in the order the experimenter wants to use – depends substantially on the groove shape.

Five common groove profiles are shown in Figure 5.1: a classic rectangular profile, a triangular profile (also known as a “sawtooth” or “blazed” pattern), a trapezoidal profile, a sinusoidal profile, and an approximated triangular profile.

5.1.1 Note on grating manufacturing techniques

These types of profiles emerged largely as a consequence of grating manufacturing techniques. To understand the impact of manufacturing on groove shape, we take a look at two techniques for creating gratings: mechanical and holographic ruling.

Mechanical Ruling

In 1880, Henry Rowland invented a method for machining long, precise screws [64], and this enabled him to create a “ruling engine” (Figure 5.2) for mechanically scratching fine parallel lines into a layer of metal on a substrate material. His version was much more accurate than previous machines because it self-compensated for systematic errors in the screw pitch, and his efficient production of high-quality gratings “revolutionized spectroscopy” [75]. Today, there are several extremely precise ruling engines around the world, using diamond tips and interferometric position feedback to mechanically engrave groove densities approaching 3 000 lines/mm.²

¹At grazing incidence, the outside orders are usually suppressed completely, since they would end up inside the grating. In the Rayleigh expansion (3.14), they end up as evanescent (decaying) rather than propagating orders.

²The Michelson ruling engine, now owned by the Newport Corporation, can rule up to an astonishing

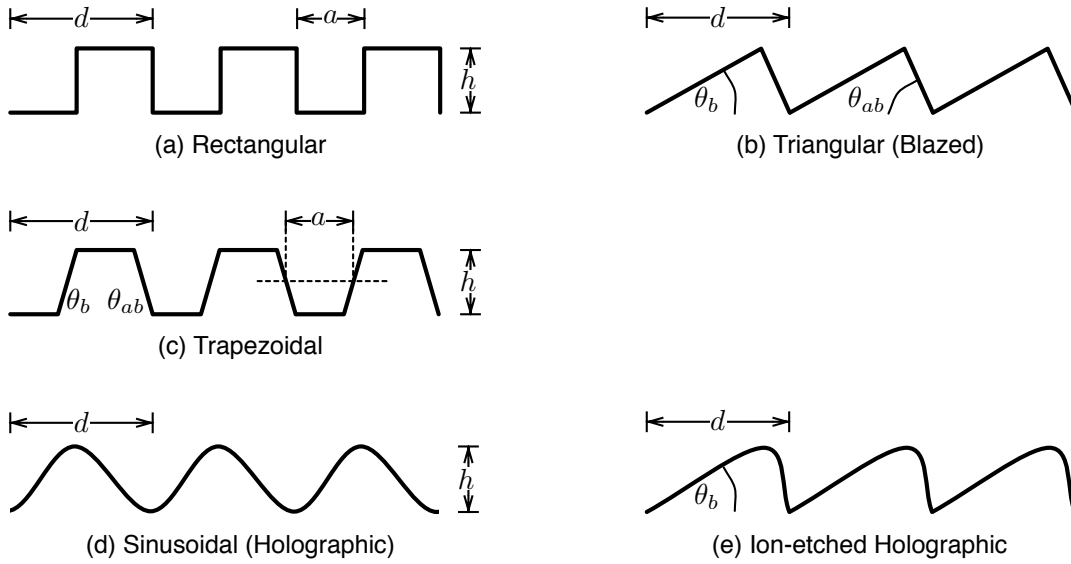


Figure 5.1: 5 common groove profiles and their geometry parameters. The rectangular profile (a) and triangular profile (b) are idealized versions of those produced by mechanical ruling. The trapezoidal profile (c) is usually produced accidentally while trying to rule a rectangular profile with an imperfect ruling tip. The sinusoidal profile (d) is the natural shape produced by holographic ruling; the result can be ion-etched to approximate a triangular profile (e).

The rectangular and triangular profiles in Figure 5.1 are a consequence of the shape of mechanical ruling tips. The trapezoidal profile is often produced accidentally when attempting to rule a rectangular profile with a non-ideal tip, as was the case for the gratings shown in Figures 5.21 and 5.22.

The setup and operation of mechanical ruling engines is a long, elite, and painstaking process; for gory details, see *The Diffraction Grating Handbook* [47] by the Newport Corporation, which operates three ruling engines within its Richardson Grating Lab. To reduce the cost of ruled gratings, often a “master grating” is ruled mechanically and then used to create a mould for replicating other gratings; the groove shape is transferred using a thin layer of liquid resin that is hardened while in contact with the master grating surface (Figure 5.4).³

Holographic Ruling

10 800 lines/mm.

³The gratings used for the REIXS spectrometer were all master gratings. They were ruled directly into a gold coating on top of a quartz grating blank, and then top-coated with an evaporated platinum or nickel surface.

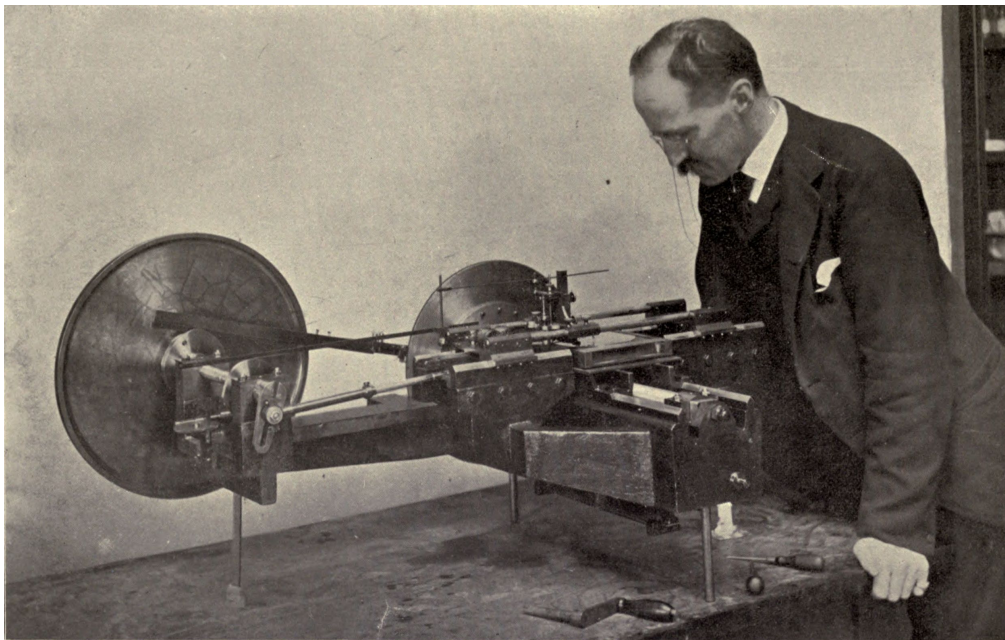


Figure 5.2: Henry Rowland, supervising his mechanical ruling engine ruling a grating. Photographed at Johns Hopkins University, Baltimore. Reprinted from THE PHYSICAL PAPERS OF HENRY AUGUSTUS ROWLAND [64, page 715]

A more recent technique was invented in the late 1960s for manufacturing gratings faster and with more repeatability. It uses two sources of coherent light to project a holographic interference pattern of regular standing waves onto a grating master. The grating master consists of a photoresist material that is either strengthened or weakened by exposure to light. After the master has been exposed to the interference pattern for a sufficient time, it is bathed in a developer chemical, which washes away either the exposed or unexposed parts, leaving behind a sinusoidal relief pattern that corresponds to the original intensity of light [30].

The last groove profile shown in Figure 5.1 represents an attempt to turn holographically-ruled sinusoidal gratings into triangular gratings using ion etching to partially eat away the groove surface while holding the finished photoresist master at an angle to the ion beam [2]. Another technique for pseudo-blazed holographic gratings is known as Sheridan's Method [70], which uses a transparent photoresist exposed to the intersection of a coherent light source with its reflected self (Figure 5.5). Because the master is inclined relative to the interference pattern, the intensity profile is asymmetric and produces a lopsided sinusoidal shape.

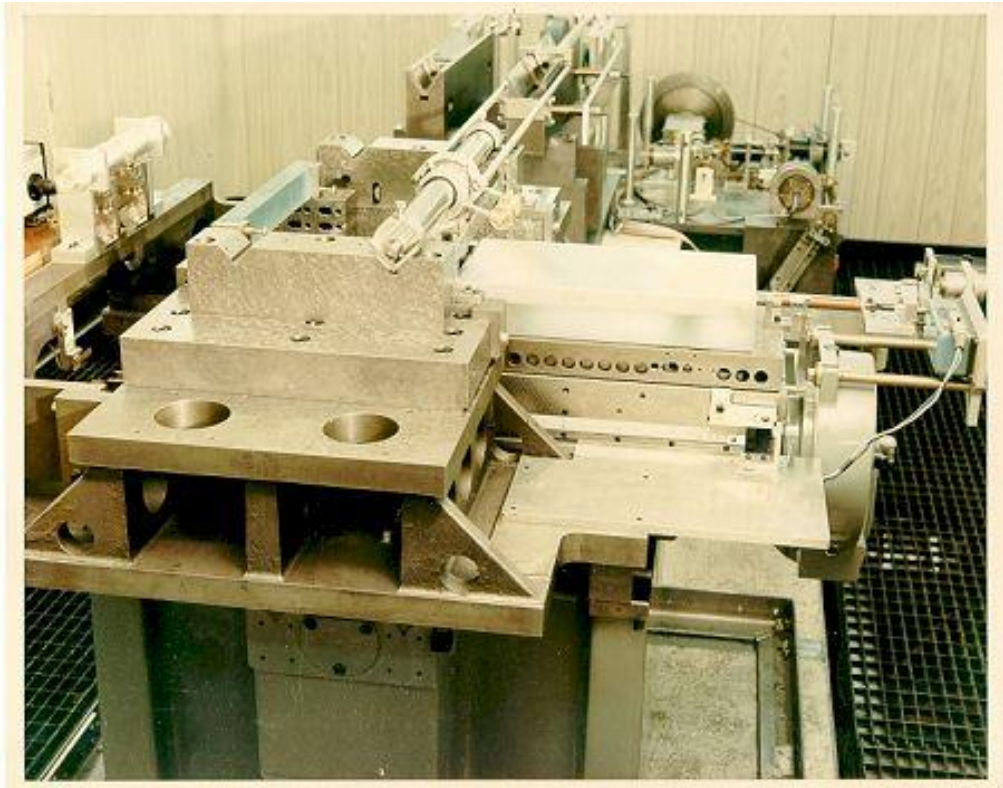


Figure 5.3: The MIT 'B' ruling engine, now owned and operated by Richardson Gratings (a division of the Newport Corporation). It can rule gratings up to 420 mm wide, with grooves up to 320 mm long. The maximum groove density is 1500 lines/mm. Equipped with a servo system for advancing the grating carriage and interferometric feedback using frequency-stabilized lasers, it is the most accurate ruling engine in the world. To control for thermal expansion of the engine, the room temperature is controlled to 0.005°C; the system even compensates for changes in room air pressure since a change of just 2.5 mm of mercury will affect the refractive index of air (and therefore the interferometer wavelength) by one part per million. The entire engine is suspended from springs to dampen vibrations between 3Hz to 60Hz, which could otherwise be transmitted to the diamond tip. Reprinted from THE DIFFRACTION GRATING HANDBOOK [47]

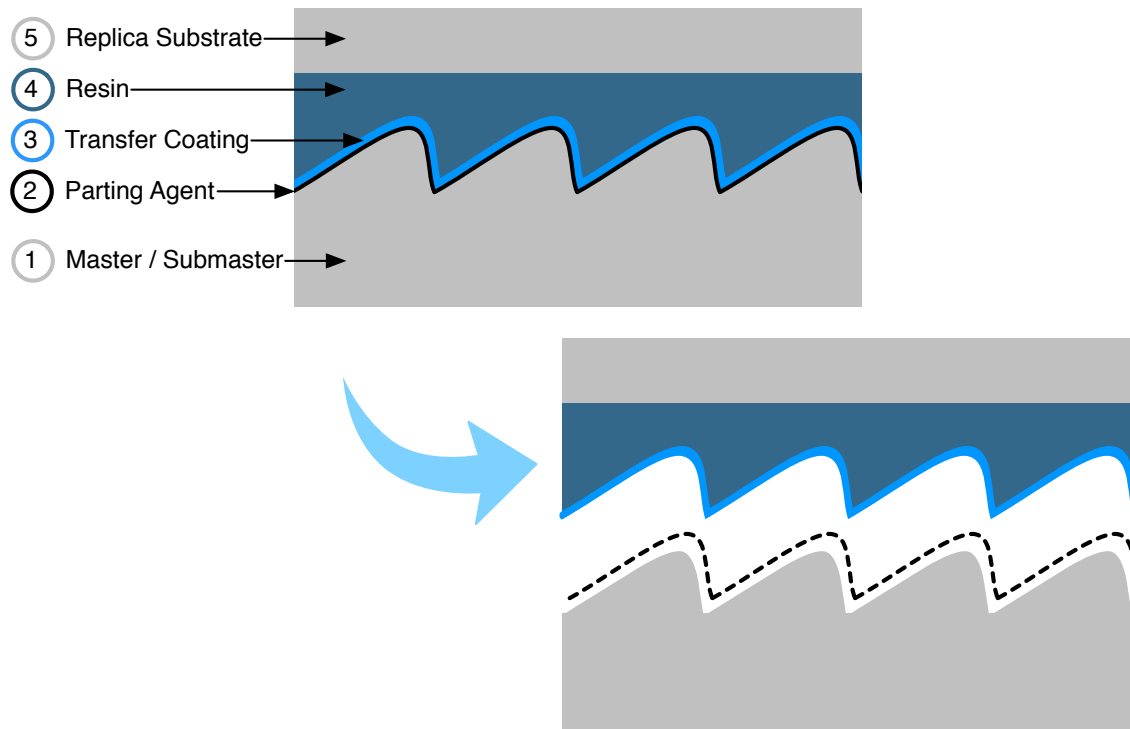


Figure 5.4: Master gratings can be replicated using a resin that hardens while in contact with the master (or subsequently, a submaster replicated from the first master). First, a parting agent (2) is applied to the surface of the master; it must be thin and uniform otherwise it will affect the profile. A metallic (aluminum or gold) coating about 1um thick is then applied above the parting agent; this coating will eventually end up as the top surface of the replicated grating, and is called the *transfer coating* (3). Finally, the replica blank (5) is cemented from above using a resin (~10um thick) that hardens under UV exposure or over time (4). Once the resin is cured, the gratings are separated at the parting agent layer, leaving the hardened resin in the shape of the grooves, with the metal coating adhered to the top. This will produce a mirror image of the master grating; to create a perfect replica, this first replica needs to be replicated again.

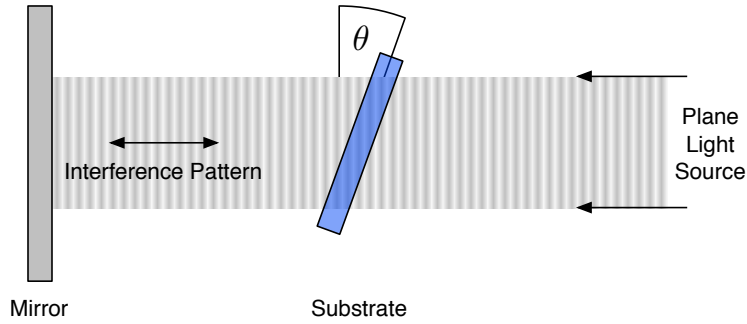


Figure 5.5: The Sheridan technique for recording pseudo-blazed holographic gratings uses a single light beam reflected back on itself to make a regular interference pattern of standing waves. The master substrate consists of a *transparent* photoresist material that is hardened or weakened by exposure to the light. By placing the substrate at an angle θ to the light path, the light and dark fringes are stretched out parallel to the grating surface; additionally, the angled incidence creates a lopsided sinusoidal intensity pattern that mimics blazed gratings.

5.1.2 Profile geometry

Figure 5.1 shows the parameters that describe the geometry of each profile. In addition to the groove spacing d , rectangular gratings are characterized by a groove depth h (or duty cycle) and a groove width a . Ruled triangular gratings are described by their blaze angle θ_b , and the opposite angle (or “anti-blaze angle”) θ_{ab} .⁴ Trapezoidal gratings are described by a groove depth h , a groove width a , and their blaze and anti-blaze angles θ_b and θ_{ab} . Sinusoidal gratings are fully described by just their groove depth h , and an assumption of a sinusoidal variation $y(x) = y_0 + \frac{h}{2} \sin(2\pi x/d)$.

5.1.3 Blazed optimization for triangular gratings

The triangular profile in Figure 5.1 (b) is much more than an accidental artifact of mechanical ruling. This shape is optimal for concentrating as much energy as possible into a single order, and therefore boosting the grating efficiency in that order. Intuitively, we might imagine that to increase efficiency, we should line up the direction of classical “reflection” off the majority

⁴Ideally the anti-blaze angle should be 90° , but it is usually less than 30° due to constraints on the ruling tip shape.

of the grating surface with the direction of the diffracted ray. Still thinking classically, we might also want to minimize shadowing in the corners of the grooves.

The ideal blazed grating meets both of these criteria. By carefully choosing a blaze angle θ_b we can – at least at one wavelength of interest – line up the specular reflection of the angled surface with the diffraction direction in order n . Using the law of reflection from geometric optics ($\theta_{\text{incident}} = \theta_{\text{reflected}}$), we can easily⁵ derive the optimized condition for a blazed grating. From the geometry in Figure 5.6, where N' is normal to the angled surface:

$$\theta_{\text{incident}} = \theta_{\text{reflected}}$$

$$\theta_2 - \theta_b = \theta_{2,n} + \theta_b$$

$$\theta_{2,n} - \theta_2 = -2\theta_b$$

Applying a trigonometric identity to the grating equation (3.19):

$$\begin{aligned} n\lambda/d &= \sin \theta_{2,n} - \sin \theta_2 \\ \frac{n\lambda}{2d} &= \cos\left(\frac{\theta_{2,n} + \theta_2}{2}\right) \sin\left(\frac{\theta_{2,n} - \theta_2}{2}\right) \\ \frac{n\lambda}{2d} &= \cos\left(\frac{\theta_{2,n} + \theta_2}{2}\right) \sin(-\theta_b) \end{aligned}$$

or

$$\theta_b = -\arcsin\left(\frac{n\lambda}{2d \cos\left(\frac{\theta_{2,n} + \theta_2}{2}\right)}\right) \quad (5.1)$$

Textbooks and resources on beamline design universally provide this derivation and formula for the optimal blaze angle θ_b [73, page 4-17] [47, Section 9.1] [48]. Using efficiency calculations, we confirmed that this intuitive argument is a good approximation for what happens in the full electromagnetic picture; the actual ideal blaze angle is usually slightly but insignificantly lower. For a 1200 line/mm grating used at an incidence angle of 88 degrees with 400 eV photons in the first inside order ($n = -1$) (Figure 5.7), Equation (5.1) would recommend a blaze angle of 1.67°. We used this as the starting point to conduct a

⁵Setting up a ruling engine to correctly and accurately engrave this angle is another story...

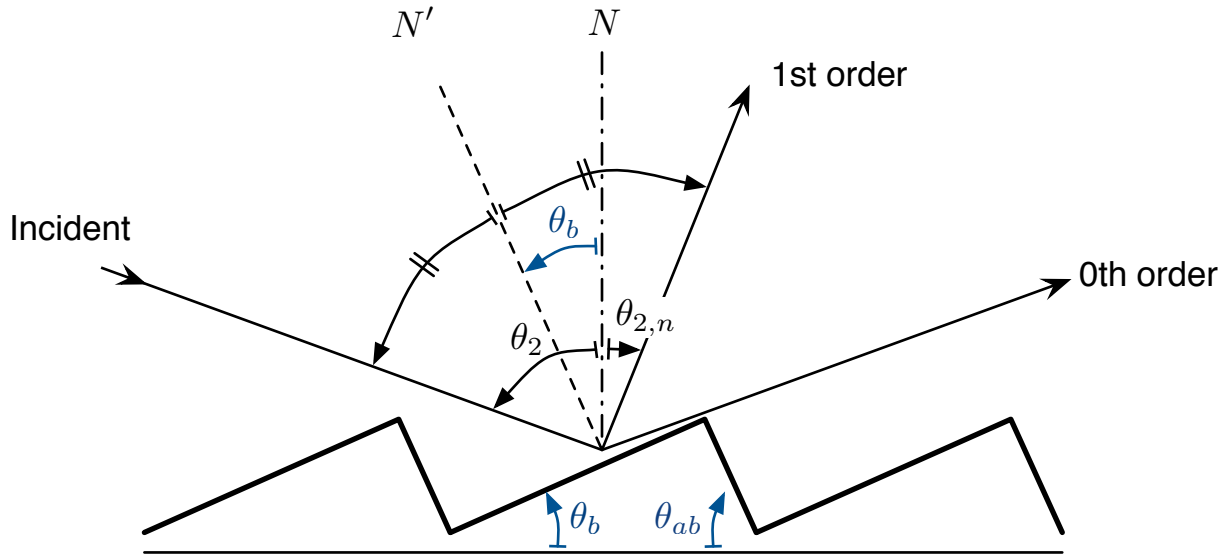


Figure 5.6: In the blazed condition, the desired order diffraction angle – in this case, 1st order – is aligned with the direction of specular reflection off the groove surfaces. The angle at the base of the large facet is the *blaze angle* θ_b ; the angle at the base of the opposite facet is the *anti-blaze angle* θ_{ab} .

software optimization using efficiency calculations, and were only able to increase the 1st order efficiency from 16.2% to 16.8% by reducing the blaze angle from 1.67° to the optimal 1.46° .

Because the blaze angle depends on the $n\lambda$ term in the grating equation, a grating optimized for a wavelength x in 1st order will also be optimized for a wavelength $x/2$ in 2nd order (or, in terms of energy, optimization for x eV in 1st order would imply optimization for $2x$ eV in 2nd order). We can confirm this for the blazed grating in Figure 5.7, where the 1st-order efficiency peak occurs at 450 eV, and the 2nd order efficiency peak occurs near 900 eV.

5.1.4 Efficiency comparison of common profiles

For comparison, Figure 5.7 shows the 0th order, 1st order, and 2nd order efficiency for three common grating profiles: blazed, sinusoidal, and rectangular (commonly referred to as *laminar*). All three gratings have a groove density of 1200 lines/mm, are shown at an incidence angle of 88 degrees, and have had their geometry optimized for maximum efficiency in 1st-order with 400 eV photons. (The coating is platinum, and the substrate is quartz

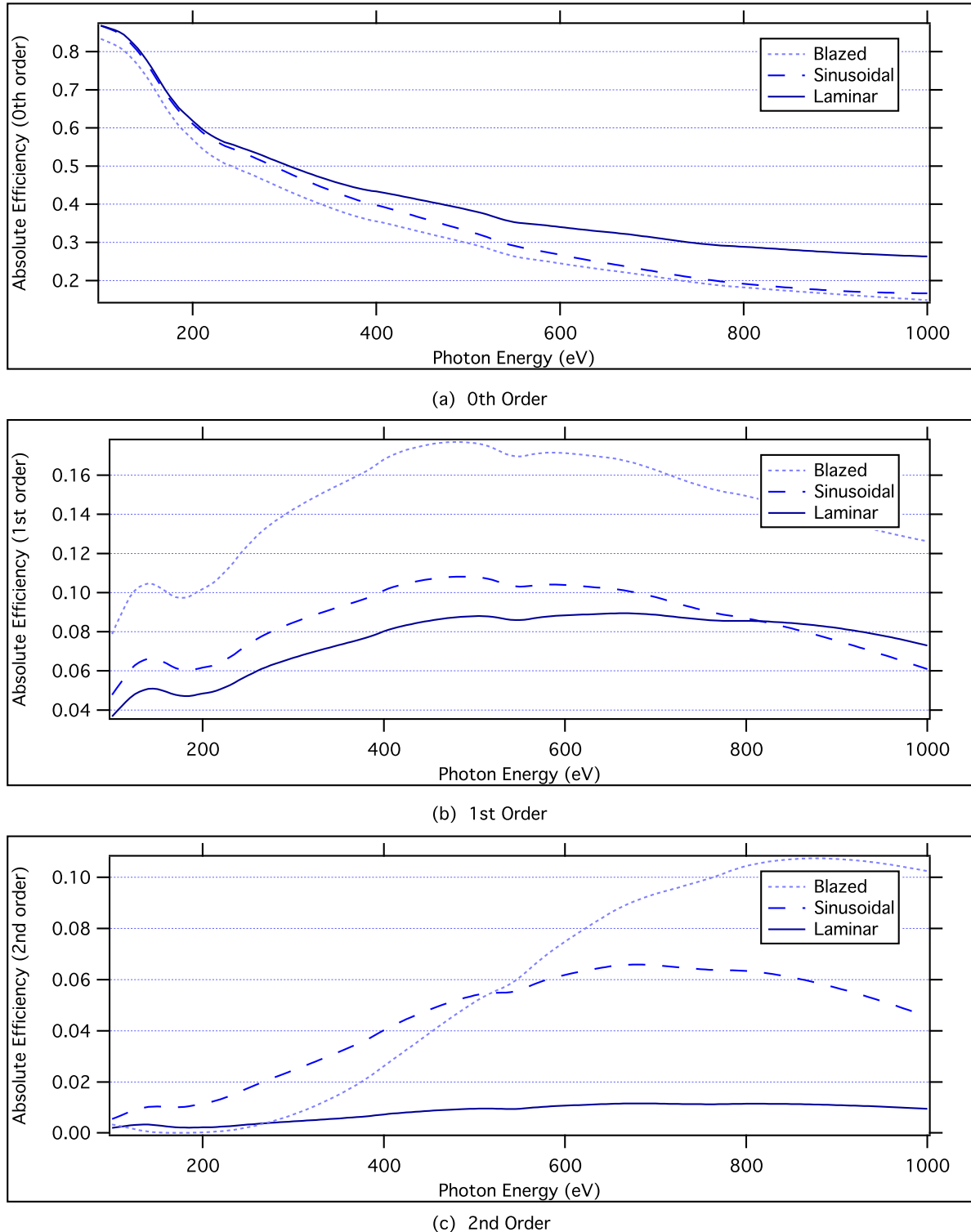


Figure 5.7: 0th order, 1st order, and 2nd order efficiency of three different groove profiles, all optimized for use at 400 eV. The blazed grating is superior in both 1st and 2nd order. All gratings: 1200 lines/mm, Platinum coating. Blazed: 1.46° angle, 60° anti-blaze angle. Sinusoidal: 13.7 nm groove depth. Laminar (rectangular): 9.6nm groove depth, 50% duty cycle.

[SiO_2 .]) The blazed grating was optimized by adjusting the blaze angle; the sinusoidal grating by adjusting the groove depth, and the rectangular grating by adjusting the groove depth and assuming a duty cycle of 50%.

The blazed profile is substantially superior to both the sinusoidal and laminar alternatives. In first order, even though the efficiency curve peaks near the design energy of 400 eV, the performance is better across the entire range from 100 eV to 1000 eV (and beyond). The blaze effect causes this curve to be shifted up in energy by a factor of two in 2nd order, so that again the blazed grating out-performs the other profiles, but only above 500 eV. The sinusoidal grating has relatively flat efficiency across the energy range, even though it still shows the energy-dependence of its optimization for 400 eV. (We have chosen a platinum coating for these examples since its reflectivity is relatively constant across the energy range (Figure 5.12). The small universal dip in efficiency at 180 eV is due to a drop in the Pt reflectivity here.)

5.2 Effect of groove density

Because the groove density directly affects the angular dispersion, using a higher-density grating is the most direct path to designing a higher-resolution instrument (Section 2.2.2). Unfortunately, Figure 5.8 shows that increasing the groove density universally decreases the grating efficiency in all orders except the 0th order, even when the remaining parameters are adjusted to keep the grating optimized. This turns out to be true, not only in this example for two grating profiles, but as a general principle. Intuitively, we can argue that as the groove density approaches infinite, the grating will look more and more like a flat mirror – with microstructure becoming smaller and smaller. Therefore, it makes sense that the amount of light in the 0th-order specular reflection will increase at the expense of the diffracted orders.

Figure 5.9 explores the groove density effect in more detail, with an efficiency spectrum for a series of blazed gratings from 300 lines/mm to 2700 lines/mm, all optimized for 400 eV at 88° incidence. It confirms that as the groove density increases, the 0th order efficiency increases, and the $n \neq 0$ order efficiencies decrease. However, one fortunate outcome is that as the groove density increases, the width of the efficiency peak caused by the blazing

optimization becomes wider; therefore, higher groove-density blazed gratings can be used optimally over a wider energy range than low-density gratings.

5.3 Effect of coating thickness

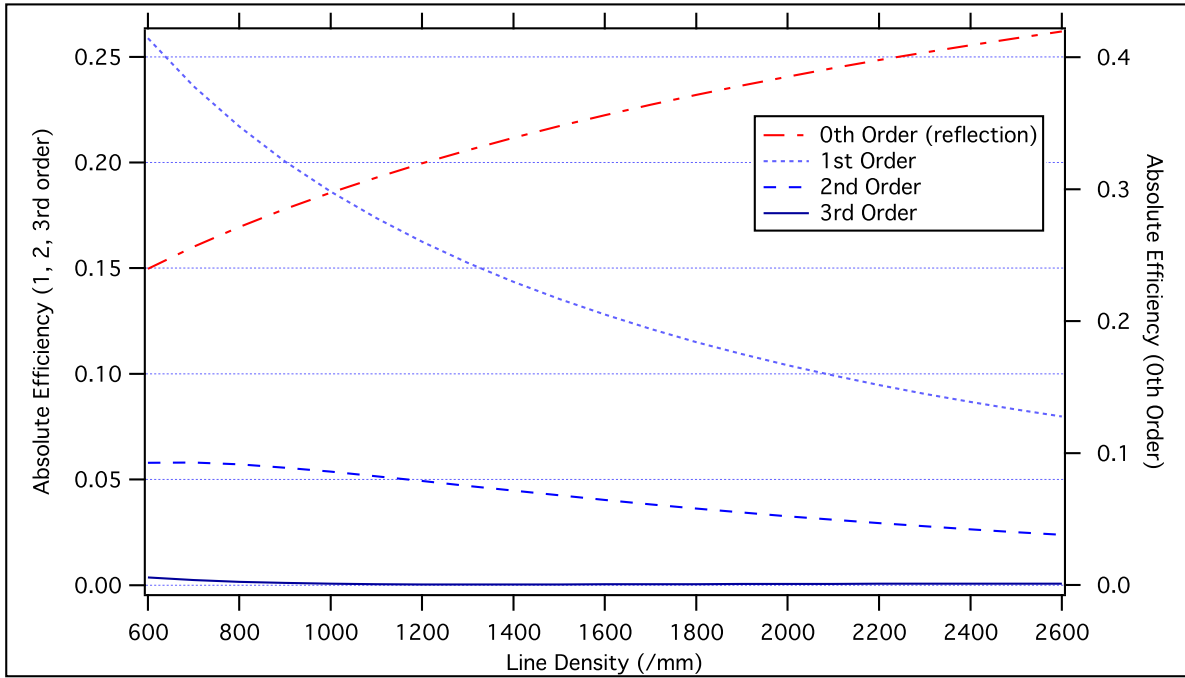
Gratings intended for use in soft x-ray instruments are manufactured on precision-ground blanks, usually consisting of fused quartz (SiO_2) or other amorphous glasses. The insulating (dielectric) blank is coated in a layer of metal, where the smoothness of the surface is absolutely critical. Often gold is used as a first coating, since it can be applied with very low roughness, and because it provides a soft layer in which to rule the grooves. If another type of coating is required (such as nickel and platinum, in our case), these coatings are applied on top of the gold after ruling.

The required thickness of the coating is another question that can be answered by efficiency calculations. Thin coatings can be applied more smoothly than thick ones [48], so the question is: how thick must a coating be for a given photon energy and incidence angle, so that photons are fully reflected or absorbed before reaching the substrate interface? If the coating is too thin, the absorption characteristics of the glass oxide substrate will start to show up in the efficiency spectrum.

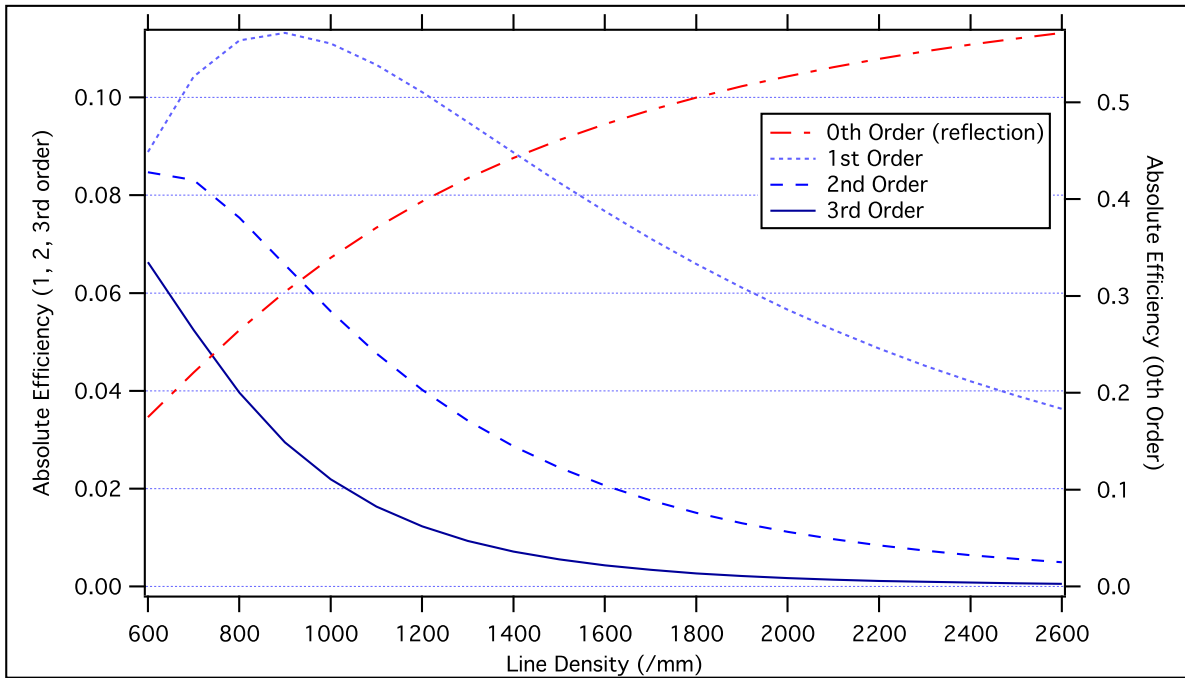
Figure 5.10 shows calculations for various thicknesses of platinum coatings above an SiO_2 substrate, compared with a theoretical solid platinum grating of infinite thickness. The 0.5nm and 1nm coatings show the oxygen absorption edge at 525 eV, as well as significantly reduced reflectivity over the whole energy range. The 5 nm layer shows a thin-film interference effect that actually boosts the efficiency above 600 eV.⁶ As we should expect, at a thickness of 50nm and above, the coated gratings become indistinguishable from an infinitely-thick platinum substrate.

In general, the required minimum thickness will depend on the photon energy, incidence angle, and the x-ray form factor of the coating material – all of which affect the x-ray penetration depth. These results show that for thin coatings, the efficiency calculations are

⁶The sharp peak in this spectrum at 525 eV might be anomalous; the Henke data used to derive the complex refractive index of all these materials is not accurate in the vicinity of absorption edges.



(a) Blazed grating, maintaining the blaze condition as the groove density changes.
Platinum coating, 88-degree incidence, 400eV photon energy.



(b) Sinusoidal grating. Groove depth optimized at 1200 lines/mm; maintaining the depth-to-period ratio as the line density changes. Platinum coating, 88-degree incidence, 400eV photon energy.

Figure 5.8: Increasing the groove density always decreases the diffraction efficiency – at least for all the useful orders ($n \neq 0$). In these plots, we tried to control for inter-related factors: For the blazed grating in (a), the blaze angle has been adjusted with the groove density (using Equation (5.1)) to maintain the on-blaze condition. In (b), the sinusoidal grating depth was optimized at 1200 lines/mm, and then the depth-to-period ratio was maintained across changes to the groove density.

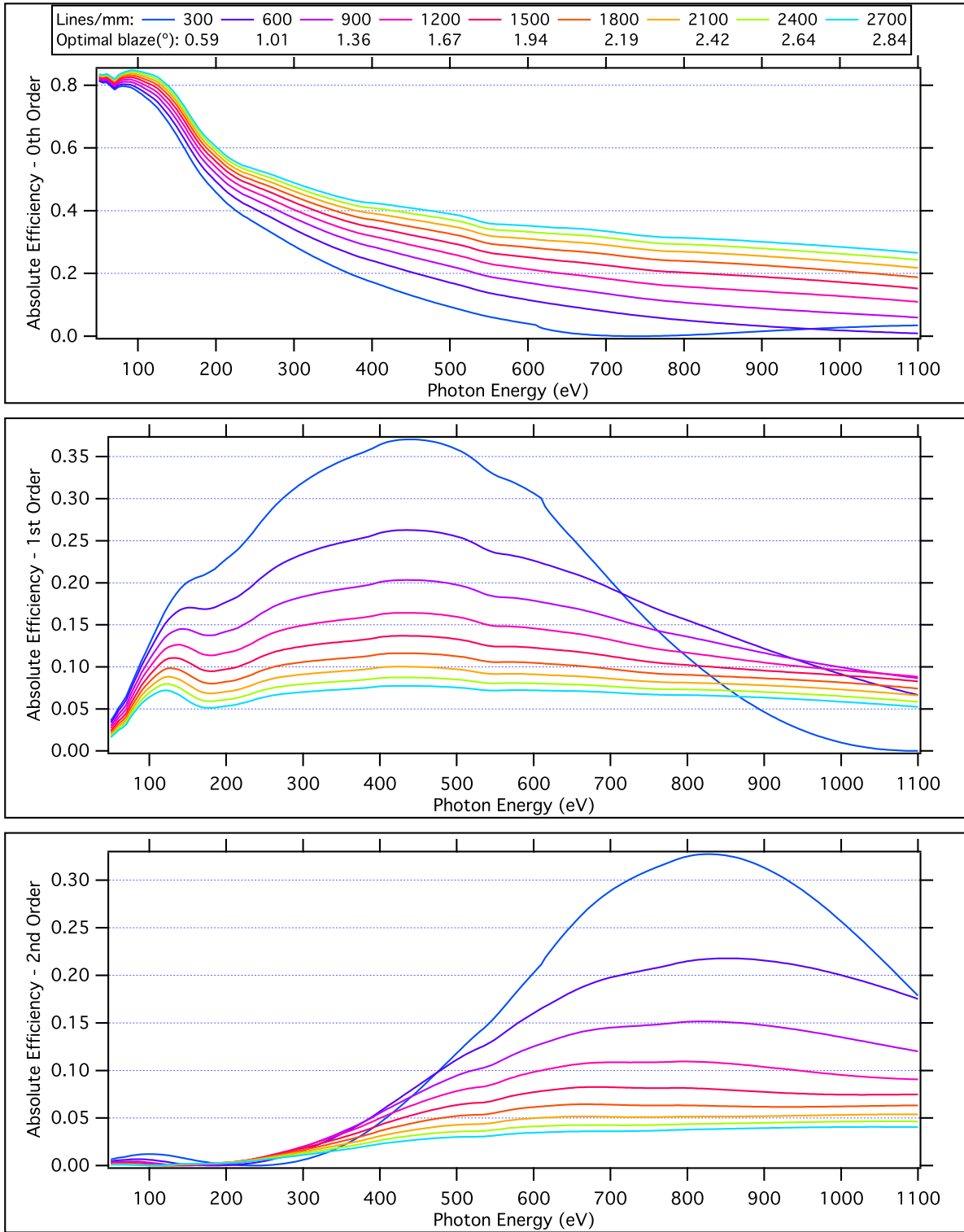
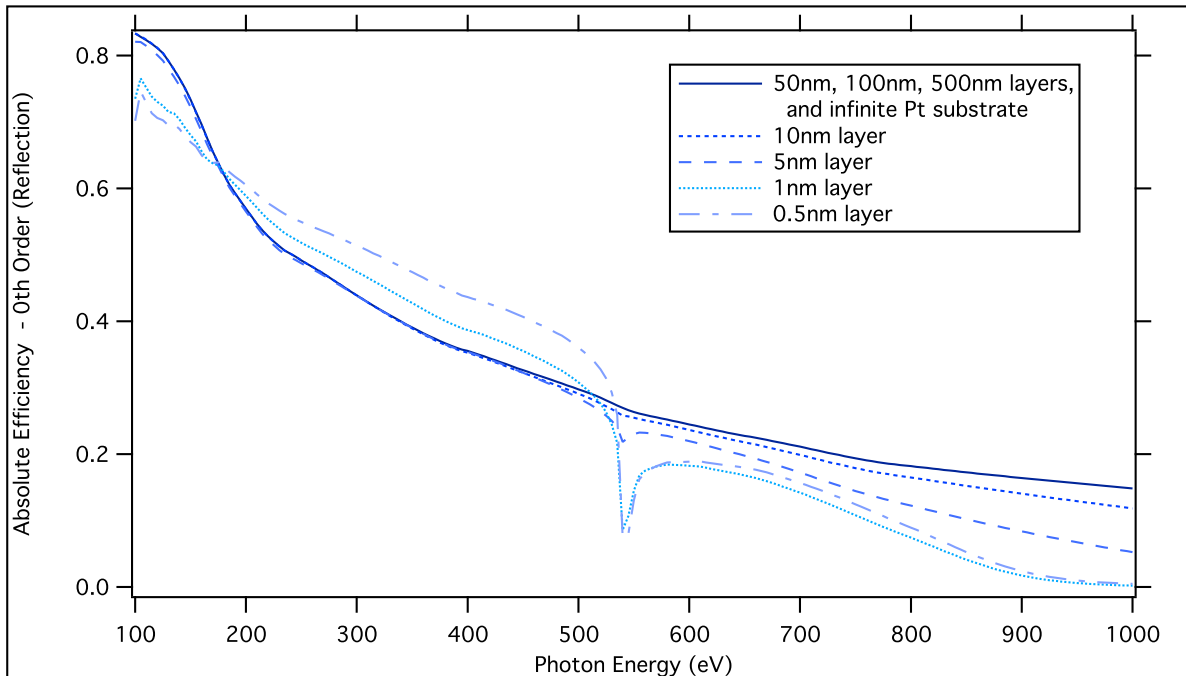
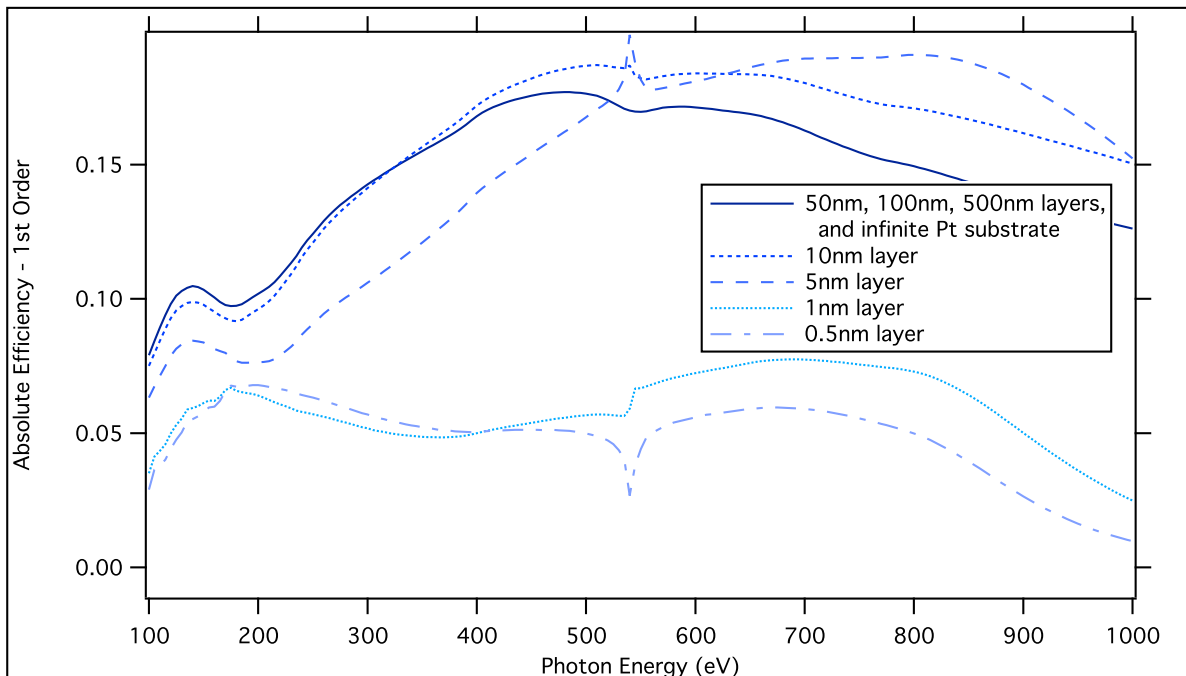


Figure 5.9: 0th order, 1st order, and 2nd order efficiency as a function of energy, for a range of groove densities from 300 to 2700 lines/mm. All gratings are triangular, platinum-coated, with an optimal blaze angle dependent on the groove density according to Equation (5.1). (Blaze angles are shown in the legend.) As the groove density increases, the maximum achievable efficiency drops, but the bandwidth of the blaze-optimization peak becomes wider.



(a) 0th Order



(b) 1st Order

Figure 5.10: In the soft x-ray regime under grazing incidence, metal-coated dielectric gratings are indistinguishable from pure metal gratings...as long as the coating is thicker than ~ 20 nm. (The exact required thickness depends on the material, photon energy, and incidence angle). These calculations show Pt coatings of varying thickness over an SiO_2 substrate, as well as an infinitely thick pure Pt grating. (Blazed grating, 1200 lines/mm, 1.46° blaze angle, 88° incidence.

able to rigorously incorporate the effects of interference and absorption at the interface with the substrate.

5.4 Comparison of coating materials

All materials suffer from inherently low reflectivity at soft x-ray energies. Even when gratings are used at grazing incidence, designers must carefully choose coating materials to maximize efficiency considering the desired wavelength range of the instrument. (This becomes particularly frustrating when a material with otherwise high reflectivity has an absorption edge right in the middle of the region of interest.)

To help in selecting materials, Figures 5.11 and 5.12 show several possibly grating coatings: carbon, nickel, gold, platinum, and iridium. (Figure 5.11 shows the reflectivity of a plain mirror made out of these materials over the energy range from 100 to 1000 eV, at 88° grazing incidence. Figure 5.12 compares the mirror reflectivity with the 0th order and 1st order efficiency of a sinusoidal grating, which had its groove depth optimized for 400 eV.)

The heavy precious metals (Au, Pt, Ir) are commonly chosen for grating coatings because they have a relatively constant reflectivity over this energy range. This is because their core-level electrons are so tightly bound that their strongest absorption features occur well above the soft x-ray range. (For example, the Pt K 1s absorption edge is at 78.4 keV.) Their outer-shell electrons fall within the soft x-ray range (for example, the platinum N and O transitions), but these absorption features are not nearly as strong, and therefore do not seriously affect the reflectivity. Gold has better reflectivity than Pt and Ir below 200 eV, and also has the previously-mentioned desirable property of being easy to apply smoothly and rule mechanically. Above 200 eV, platinum has been the de-facto choice for high-energy wide-bandwidth gratings for many years. Iridium (and rhodium, not shown) actually have even better reflectivity and corrosion resistance than platinum, and are becoming standard coating options with some manufacturers.

In contrast, carbon and nickel offer much higher reflectivity over some parts of this energy range, but unfortunately have strong absorption features right in the middle. The carbon K 1s absorption edge at 284 eV makes it restricted to, but excellent for, low-energy applications.

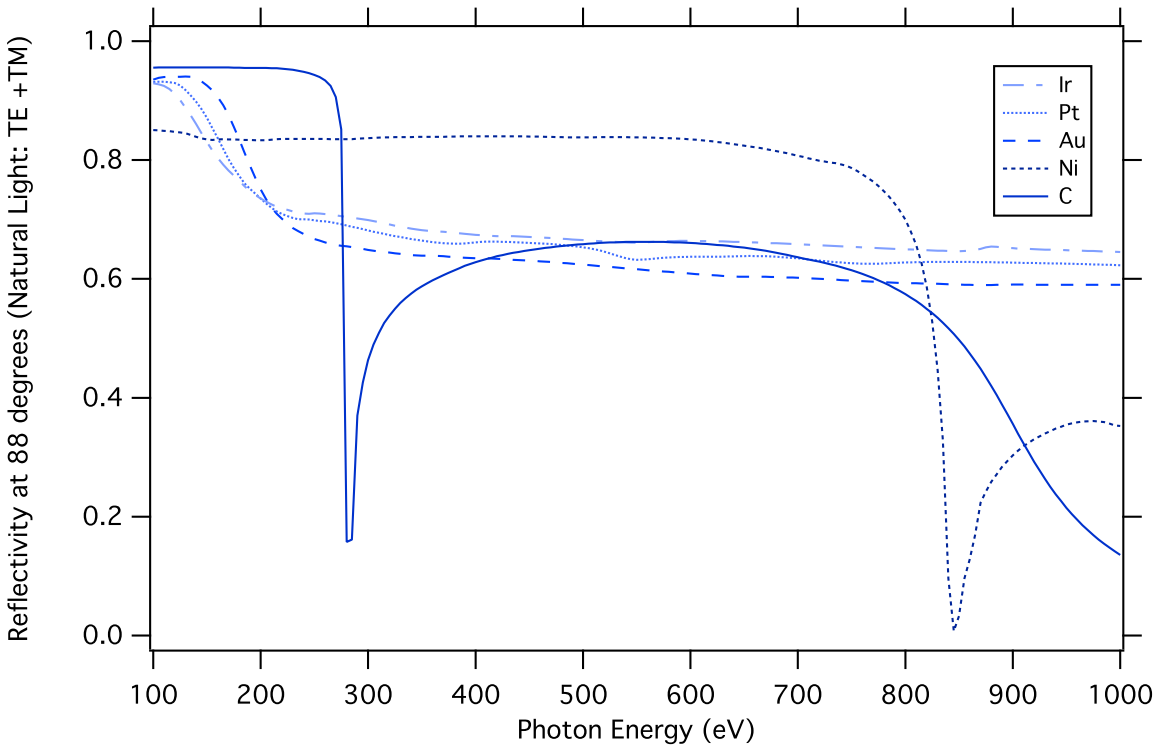


Figure 5.11: The reflectivity of a pure mirror at grazing incidence (88°), as a function of photon energy. Lighter elements like carbon and nickel have the highest peak reflectivity, but have strong absorption features. Heavier metals, particularly those within the platinum group, have reasonable reflectivity over the entire soft x-ray region of interest. Up to 200 eV, gold has a higher reflectivity than Pt and Ir.

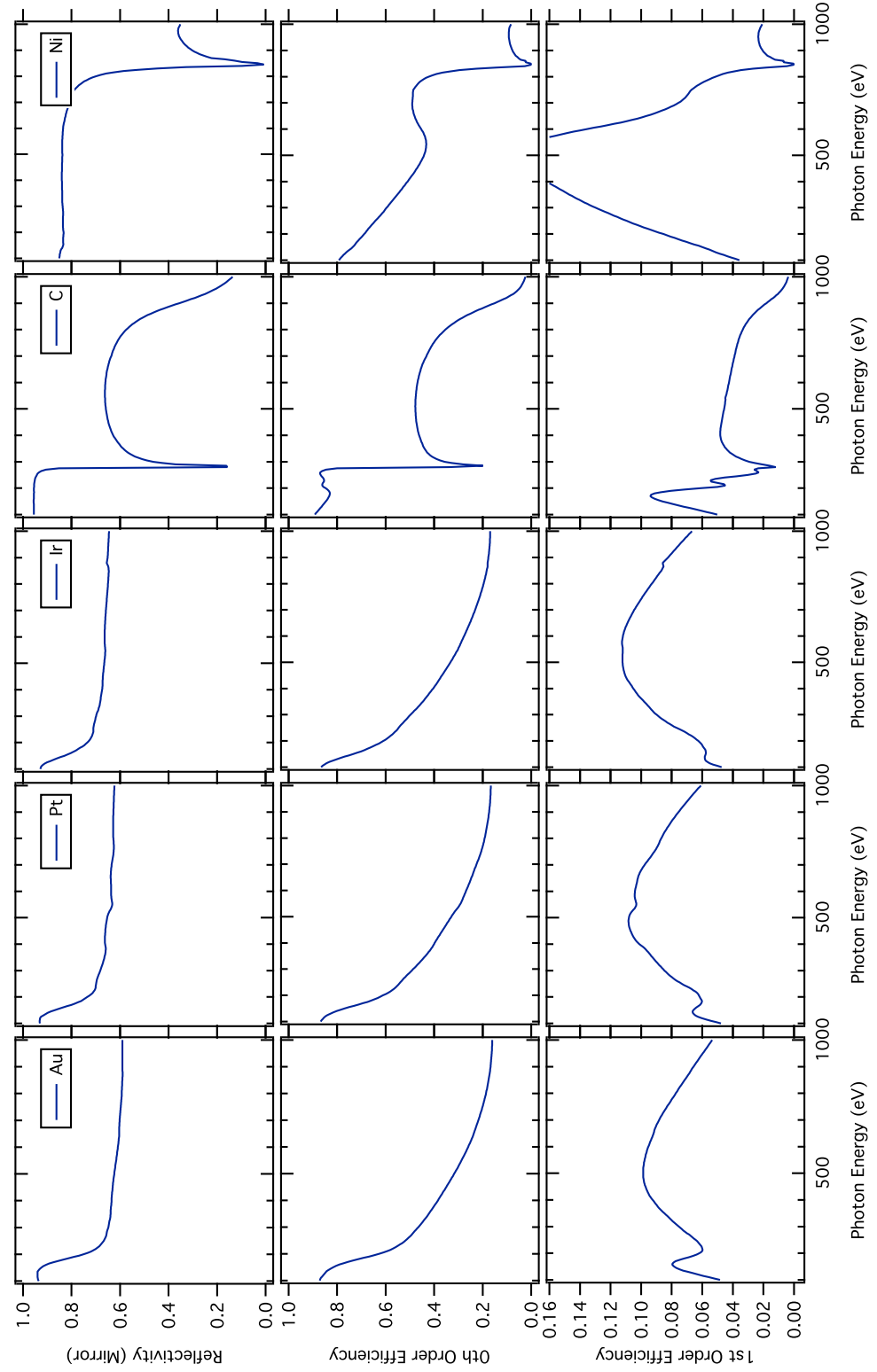


Figure 5.12: A comparison of the mirror reflectivity, 0th order, and 1st order efficiency for different coating materials, as a function of photon energy. (Gratings: Sinusoidal profile, 88° incidence angle, 1200 lines/mm, 13.7 nm groove depth.) Note that the 1st order efficiency has energy-dependent features that are not visible in the simple reflectivity.

The nickel L₂/L₃ edges do not occur until 870/853 eV, and Figure 5.12 seems to suggest that nickel would be the clear winner over much of the soft x-ray range. This prompted us to use it for two of the REIXS spectrometer gratings, with one obvious but unforeseen consequence (Section 7.3.2).

Not shown in these plots, silicon also has a very high reflectivity up to its L₂/L₃ absorption edge at 100 eV. Therefore, bare Si and SiO₂ mirrors are often used for extreme ultra-violet (EUV) and very low-energy soft x-ray beamlines [48]; Si-coated gratings might be useful here as well.

5.5 Effect of photon energy / wavelength

The energy-dependence (or wavelength-dependence) of grating efficiency is shown in many of the previous plots, where we display the efficiency as a function of photon energy. However, it is impossible to isolate trends for this relationship on its own, because the photon energy is inherently coupled to the grating efficiency in multiple ways. For starters, the complex refractive indexes of grating materials always vary as a function of energy. Additionally, the photon energy also determines the angle of the outgoing diffraction orders, which can be seen in both the Rayleigh expansion for the total field, and in the simplified grating equation (3.19). Therefore, optimizations for geometry parameters that depend on outgoing angles – like the blaze angle and groove depth – are inherently coupled to the photon energy. The plots in Figure 5.12 highlight this by showing the difference between the energy-dependent reflectivity of a plain flat mirror, versus the more complicated diffraction efficiency.

5.6 Effect of incidence angle

In the soft x-ray regime, the real part of the refractive index for metals is less than unity. This means that the phase velocity for light in the material is actually *faster* than the speed of light in a vacuum.⁷ As mentioned in Section 2.2.3, we can exploit this phenomenon to

⁷Because the refractive index changes with wavelength, dispersion causes a *group velocity* $v_g < c$, therefore Einstein's speed limit is not violated.

increase the reflectivity of gratings and mirrors by using them at grazing incidence, creating what is sometimes referred to non-rigourously as “*total external reflection*” (TER).

Total internal reflection (TIR) happens in conventional materials when a light ray travels from a slower optical medium (refractive index n_2) toward a faster optical medium (refractive index $n_1 < n_2$). Snell’s law of refraction would relate the angles of the incident (θ_2) and transmitted (θ_1) waves:

$$n_2 \sin \theta_2 = n_1 \sin \theta_1$$

$$\sin \theta_1 = \frac{n_2}{n_1} \sin \theta_2$$

By choosing an incident angle θ_2 for which there is no possible solution to θ_1 , we can ensure that there is no transmitted wave – the incident wave must be completely reflected.

$$\frac{n_2}{n_1} \sin \theta_2 > 1$$

This will happen for all incident angles θ_2 beyond a critical angle:

$$\theta_{\text{critical}} = \arcsin \left(\frac{n_1}{n_2} \right)$$

In the case of soft x-ray mirrors and gratings, if we make a crude approximation and ignore the imaginary component of the mirror’s refractive index, the same situation happens when light from the (slower) vacuum is incident on the (faster) medium of the mirror.⁸ Here the vacuum refractive index is $\nu_2 = n_2 = 1$, and the mirror refractive index is $\nu_1 \approx n_1 < 1$. (For example, at 410 eV, the real part of the refractive index of platinum is $n_1 = 0.99321$.) We can therefore calculate the critical angle for *total external reflection*; for incident angles larger than this, there should be no transmitted wave into the mirror:

$$\theta_{\text{critical}} = \arcsin (n_1)$$

(where n_1 is the real part of the mirror’s complex refractive index.) Critical angles for the coatings in Figure 5.12 at 410 eV are given in Table 5.15.

⁸This assumption is necessary because Snell’s law in the form $n_1 \sin \theta_1 = n_2 \sin \theta_2$ only makes sense for real n . If n_1 and θ_1 were real, but the mirror’s n_2 was complex, this would require a complex “angle” θ_2 , which would have no direct physical interpretation.

Table 5.1: Critical incidence angles for “total external reflection” at 410 eV for the mirror and grating coatings shown in Figure 5.12.

Material	θ_{critical} for TER (°)
Carbon (C)	85.92
Nickel (Ni)	83.20
Gold (Au)	83.85
Platinum (Pt)	83.32
Iridium (Ir)	83.10

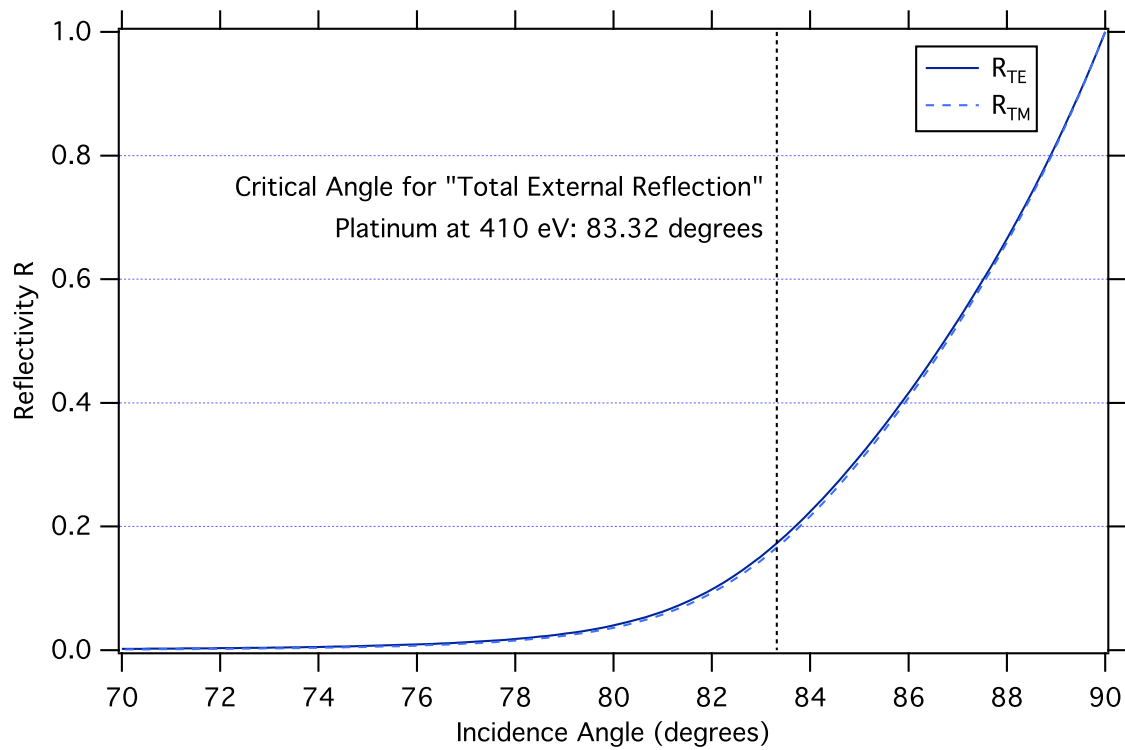


Figure 5.13: The reflectivity of a perfect platinum mirror as a function of incidence angle at 410 eV, calculated using the complex refractive index and the complex Fresnel equations. The “total external reflection” approximation suggests a critical angle of 83.3° for total reflection, but due to absorption within the material, the reflectivity only reaches 1 at complete grazing incidence (90°). There is no substantial difference between TE and TM polarization.

Because we ignored the imaginary component $i\beta$ of the full refractive index ($\nu = n + i\beta$), the concept of TER is just an approximation for what happens in the rigorous electromagnetic picture. The imaginary component represents absorption of the electromagnetic wave within the material, and as a result, no soft x-ray mirrors are ever totally reflecting – Figure 5.13 shows that a reflectivity of 1 only occurs at complete grazing incidence (90°). Reference [16] gives a rigorous derivation of reflection and transmission from absorbing materials: the reflection coefficients for TE and TM polarization, from a material with complex refractive index ν at incidence angle θ , are known as the *complex Fresnel equations*:

$$\cos \phi \equiv \sqrt{1 - \frac{\sin^2 \theta}{\nu^2}} \quad (5.2)$$

$$r_{TE} = \frac{\cos \theta - \nu \cos \phi}{\cos \theta + \nu \cos \phi} \quad (5.2)$$

$$r_{TM} = \frac{-\nu \cos \theta + \cos \phi}{\nu \cos \theta + \cos \phi} \quad (5.3)$$

In general, the reflection coefficients r_{TE} and r_{TM} are also complex, so they give both the amplitude and phase shift of the reflected electric field vector. The reflectivity R is given by the squared magnitude of the reflection coefficient:

$$R_{TE} = |r_{TE}|^2 = r_{TE} r_{TE}^*$$

$$R_{TM} = |r_{TM}|^2 = r_{TM} r_{TM}^*$$

These are plotted in Figure 5.13 as a function of incidence angle for a smooth platinum mirror at 410 eV.

Moving from mirrors to gratings, Figure 5.14 shows the effect of incidence angle on diffraction efficiency for several different geometry profiles. Even though TER is a crude approximation, this figure does confirm that the grating efficiencies in the 0th, 1st, and 2nd orders are indeed extremely low below platinum’s “critical incidence angle” of 83.3° . By comparison with the mirror plot in Figure 5.13, we might expect that as the incidence angle becomes more and more grazing, the efficiency should increase continuously... and that is certainly the case for the $n = 0$ order. However, this turns out to be not true for the remaining orders; *there is actually an optimal incidence angle below 90° where efficiency is maximized*. At first glance, it might seem like this is an accidental side-effect of the blazed optimization; since the

optimal blaze angle depends on the incidence angle, it might have been possible that all the gratings in Figure 5.14 had their geometry optimized for a sub-90° incidence angle. However, by exploring the effect of incidence angle on efficiency over a range of blaze angles, Figure 5.15 dispels this idea; it shows that for $n \neq 0$ orders, there is indeed an optimal incidence angle, which depends only on the groove density (period) and the energy.

We found that the same effect happens for rectangular and sinusoidal gratings as well. In each case, finding the optimal incidence requires a simultaneous optimization of the geometry parameters at each incidence angle tested: the blaze angle for triangular gratings, and the groove depth for rectangular and sinusoidal gratings. (Because of the coupling between groove geometry and incidence angle, non-optimal geometry can otherwise hide the incidence maximum.)

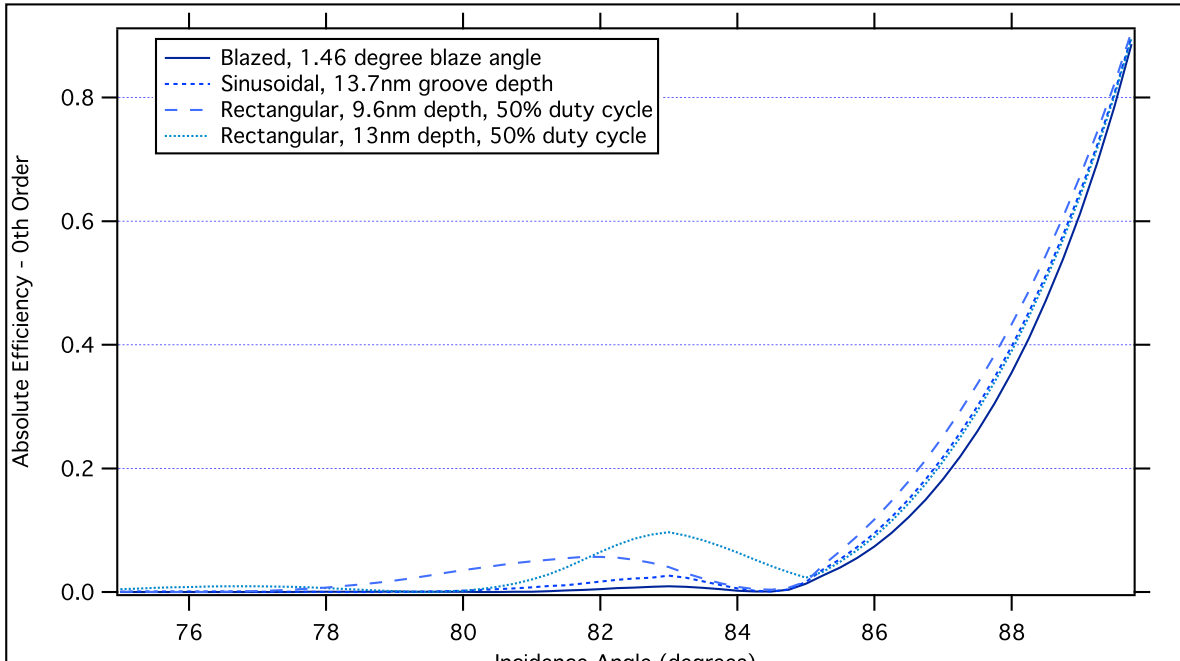
Figure 5.15 contains an important take-away message for instrument designers: if an arbitrary incidence angle is required for some external reason, the geometry (blaze angle, depth, etc.) can be adjusted to optimize for that incidence. However, in the absence of constraints, there exists a unique optimal incidence angle (and corresponding groove geometry) where the efficiency reaches an absolute maximum.

Can we predict the optimal incidence analytically? And does it actually only depend on the period and wavelength? To answer these questions, we conducted a comprehensive search of the incidence angles that optimize first-order efficiency over a range of wavelengths and grating periods, for both blazed and rectangular gratings. For every combination of wavelength and period, we needed to perform a global optimization of the incidence angle and groove geometry.⁹ We used the new PEG software, running massively in parallel on one of the Westgrid high-performance cluster computers, to conduct the optimizations.

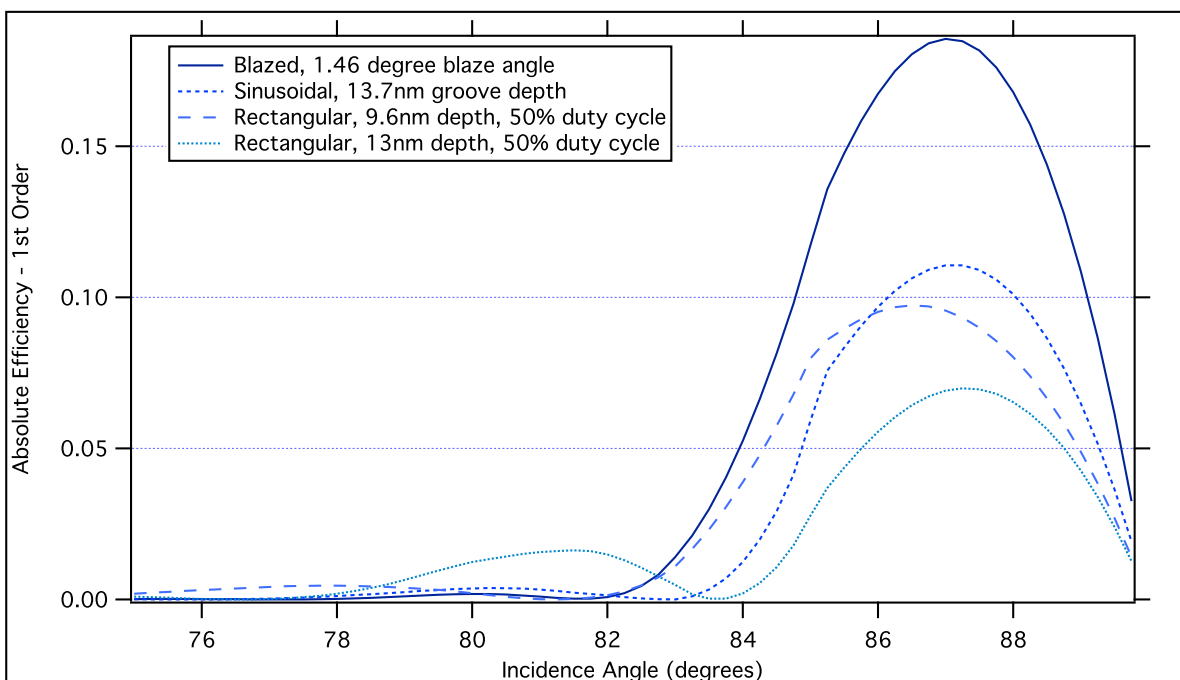
5.6.1 Optimal incidence for rectangular gratings

Figure 5.16 shows the optimal incidence angles found for rectangular gratings as a function of period and wavelength. We discovered that we can accurately predict the optimal incidence

⁹A global optimization was necessary particularly for the rectangular gratings, which exhibit periodic local maxima over the search space.



(a) 0th Order



(b) 1st Order

Figure 5.14: The effect of incidence angle on diffraction efficiency for various grating profiles. While the 0th order efficiency/reflectivity always increases as the incident light becomes more grazing, there is an optimal incidence angle below 90° for higher-order light. The critical angle for total external reflection in Platinum is 83.3° ; clearly both the 0th-order and 1st-order efficiency drop off significantly below this angle. (Gratings: 1200 lines/mm, platinum coating, 400 eV; blaze angles and profiles as indicated.)

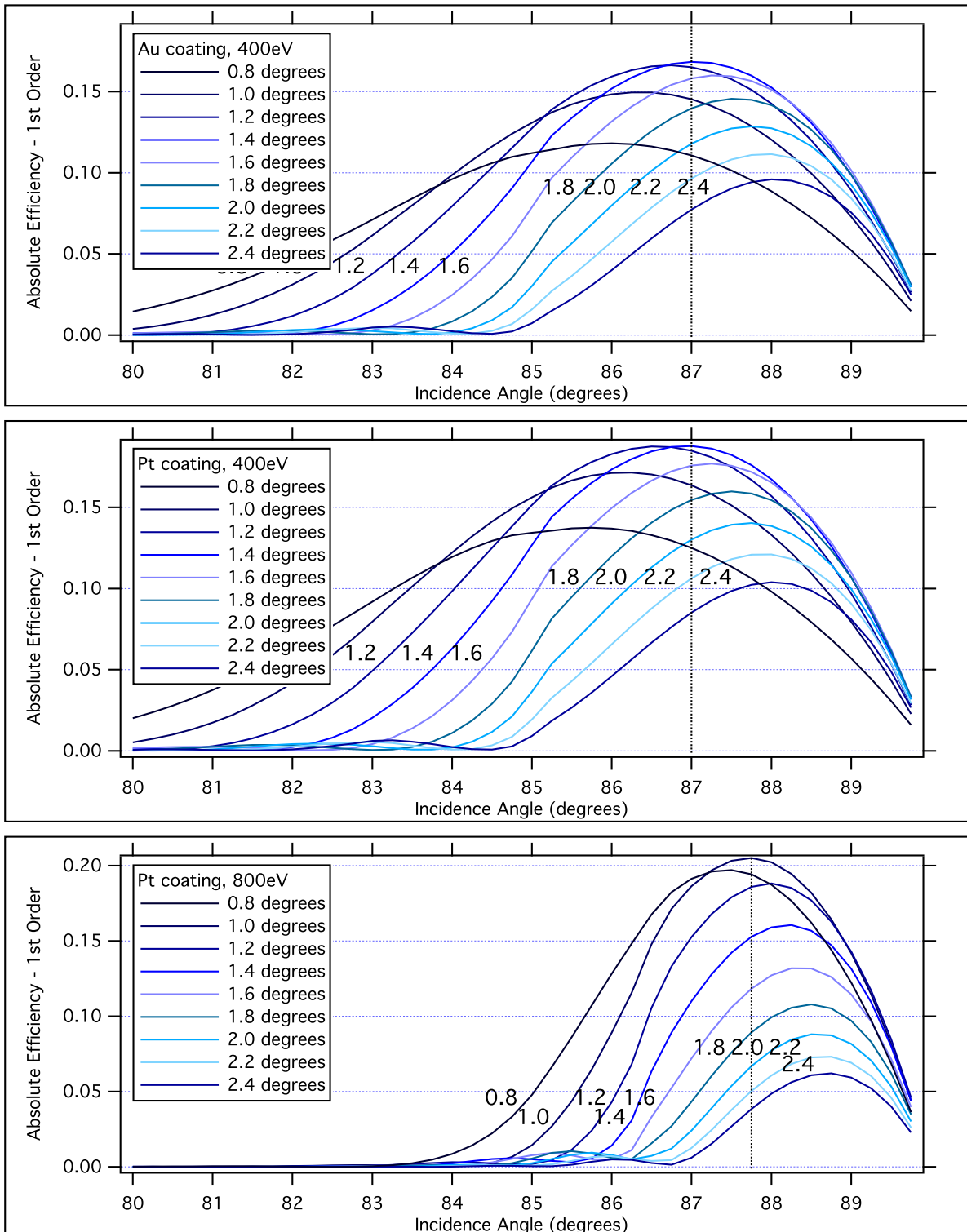


Figure 5.15: While the blaze angle can always be used to tune a grating for a required incidence angle, there is still a particular *optimal* incidence angle that – when combined with a corresponding optimized blaze angle – would produce the highest achievable efficiency. This optimal angle depends only on the groove density and energy. (Gratings: all 1200 lines/mm; coatings, blaze angles, and energies as indicated.)

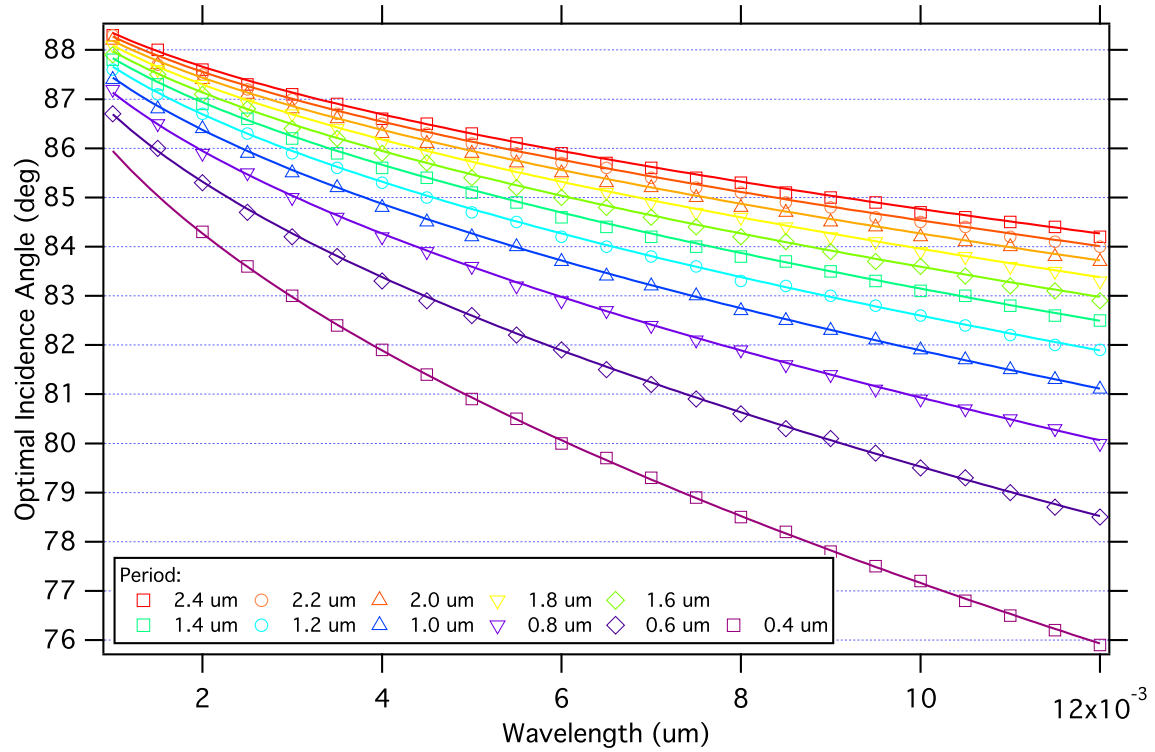


Figure 5.16: Optimizing the incidence angle and groove geometry for a range of wavelengths and grating periods shows a $n = -1$ order maximum efficiency at angles described by $\sin \theta_{max} = 1 - \lambda/d$ [smooth curves]. This is the angle where the $n = +1$ order reaches 90° : a Wood anomaly. The optimization was conducted on a grid with an incidence step of 0.1° and a groove depth step of 0.002 um , using rectangular platinum gratings.

angle θ_{max} according to the formula

$$\theta_{max} = \arcsin\left(1 - \frac{\lambda}{d}\right), \quad (5.4)$$

plotted in the smooth curves for each period. (Deviation from this formula and the optimized points is only due to the 0.1° precision of our optimization.)

There is a clear physical explanation for this result. At grazing incidence, most of the outside ($n > 0$) orders are evanescent, depending on the incidence angle. If we assume an incidence angle so that an outside order n' is propagating, and then we increase the incidence just to the point where it becomes evanescent, all of the energy previously carried by that wave will suddenly need to be re-distributed, increasing the efficiency of the remaining propagating orders. The incidence angle where this happens occurs when the n' outgoing angle reaches 90° . The effect is strongest in the case of the $n' = +1$ outside order; from the grating equation, we find:

$$\begin{aligned} \sin \theta_{2,n'} &= \sin \theta_2 + n' \lambda / d \\ \sin \theta_{2,+1} &= \sin \theta_2 + \lambda / d \\ \sin(90^\circ) &= \sin \theta_2 + \lambda / d \\ \sin \theta_2 &= \sin \theta_{max} = 1 - \lambda / d \end{aligned}$$

Therefore, the incidence angle for maximum inside first-order efficiency is the one that *just* causes *all* of the outside orders to be evanescent. Historically, this has been referred to as a *Wood anomaly of the Rayleigh type*, and it has been observed experimentally in visible light gratings as early as 1902 [77]. Here, we show that we can predict it well using rigorous electromagnetic calculations via the differential method.

In visible light applications, Wood anomalies can be very sharp, and constitute a problem rather than an advantage by hiding or masking spectral lines; they can also be sensitive to polarization [72]. In the grazing incidence soft x-ray domain, the efficiency increases and decreases smoothly on both sides of the peak; it does not drop off sharply even when the $+1$ order is actually propagating, but still close to 90° . (We also confirmed using **Gradif** that it is insensitive to polarization.) Therefore, we actually suggest *exploiting* the $+1$ Wood anomaly as a starting point when designing constant-incidence x-ray instruments. For photon energies

above 100 eV, the peak width should provide a usable instrumental range, but designers should always check the efficiency spectrum over wavelength to ensure that it is wide enough for their range of interest. At low photon energies, an incidence angle slightly higher than θ_{max} can widen the range with only a small decrease in the peak efficiency.

5.6.2 Optimal incidence for blazed gratings

From these results, we would also expect to find the optimal incidence for blazed gratings at the +1 Wood anomaly. However, the actual optimal incidence angle turns out to significantly more grazing than predicted by Equation (5.4); the results are shown in Figure 5.17. The difference is significant: in some cases we have observed a doubling in the efficiency from the angle predicted in Equation (5.4) and the true optimal incidence. The explanation for the difference is related to the blazing effect, but we have not yet discovered an analytic formula to predict it. So far, it must be determined via optimization.

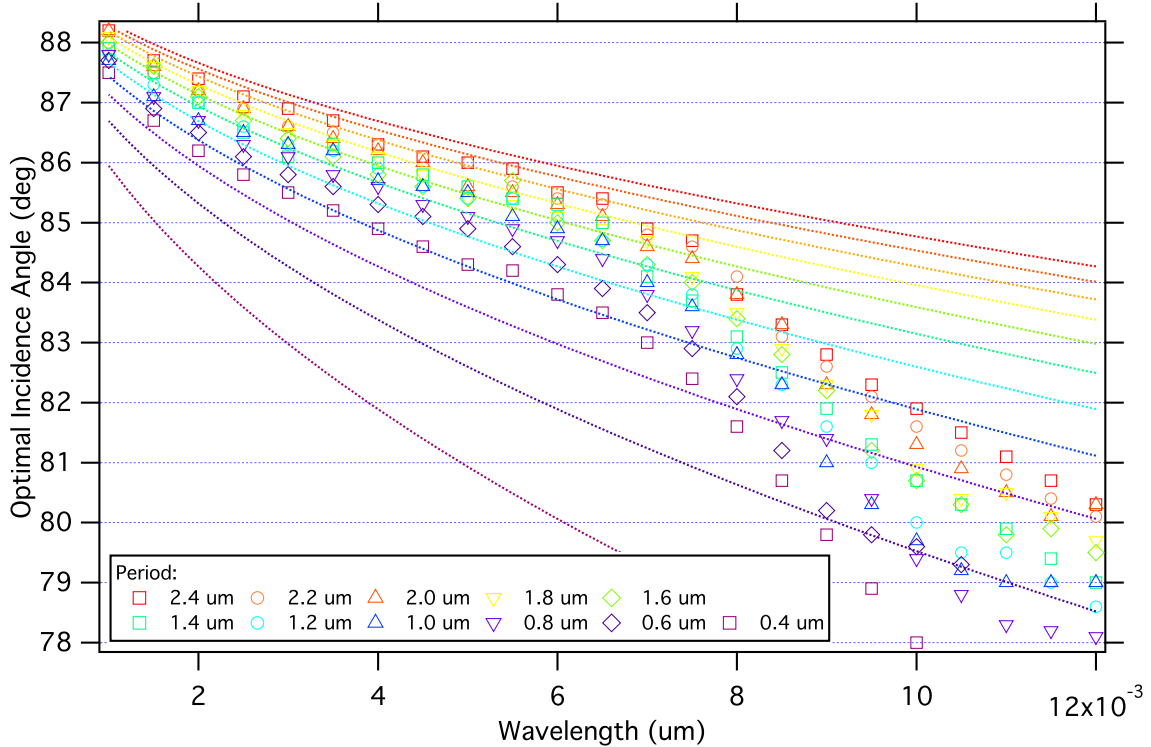


Figure 5.17: Unlike the case of rectangular gratings, the optimal incidence angles for blazed gratings (marked points) do not follow the curves for the +1 order Wood Anomalies (dashed lines). Instead, the optimal incidence needs to be determined through optimization.

5.7 Effect of anti-blaze angle for blazed gratings

Blazed gratings are reported to be most efficient with a perfect anti-blaze angle of 90° [47]. When ordering gratings from a manufacturer, the tolerance for the anti-blaze angle must be specified. In Figure 5.18, we calculate the effect of the anti-blaze angle on the efficiency spectrum. For grazing-incidence optics, it turns out that as long as the anti-blaze angle is greater than approximately eight times the blaze angle, it has almost no effect on the efficiency.

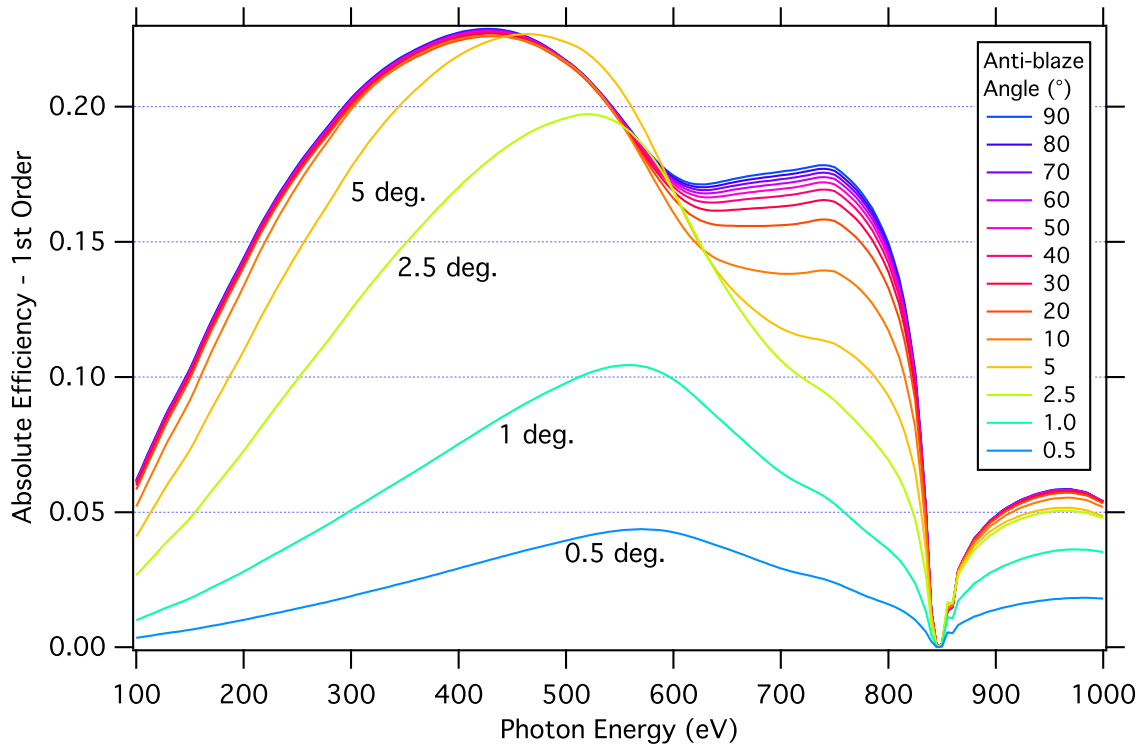


Figure 5.18: These calculations over a range of anti-blaze angles show that as long as the anti-blaze angle is greater than ~ 8 times the blaze angle, it has almost no effect on the efficiency. (Grating: 1200 lines/mm; Nickel coating; 88° incidence; 1.48° blaze angle.)

5.8 Applications to beamline and instrument design

Beamline designers can use the observations in this chapter to guide the design process. Starting with the choice of the groove shape, it is clear that blazed profiles will always offer

the best performance for constant-incidence applications like the spectrometer in Chapter 6. For variable-incidence designs like monochromators, a blazed profile optimized for the centre of the instrument’s wavelength range will lose efficiency at the extremes, but might still offer better performance than a sinusoidal grating, especially if the total range is being divided across multiple gratings. (This can be verified quickly using the constant-included-angle scan in the PEG software.)

Next, a groove density should be chosen that is as low as possible while still providing the required resolution. In the next chapter, we explore a novel way of increasing resolution while maintaining a moderate groove density.

For constant-incidence instruments, designers should consider using the optimal angle discovered in Section 5.6. For rectangular gratings Equation (5.4) can be used. At low photon energies (< 100 eV), the width of the anomaly’s efficiency peak might not be sufficient to cover the desired energy range; using a slightly more grazing incidence angle and re-optimizing the groove geometry tends to widen the peak with an acceptable reduction in the maximum efficiency. For blazed gratings, the optimal incidence should be found through an optimization at the design wavelength and period.

Warning: We should also note here that in most instrument configurations, a lower (more normal) incidence creates a larger acceptance angle for the grating and therefore increases the *geometric* efficiency. The change in the diffraction efficiency as a result of the incidence angle should always be evaluated in conjunction with the change in geometric efficiency.

When choosing a blaze angle, designers should keep in mind that the bandwidth of the blazed efficiency peak increases both with photon energy and groove density: optimizing for low energies near 100 eV creates narrow efficiency peaks; at higher energies, the peaks become wider and the gratings can be more general. Figure 5.9 shows the same increase in generality as a function of groove density.

Finally, our calculations for the effect of the anti-blaze angle (Figure 5.18) show that the tolerance specified for this parameter can be quite large; instead, grating manufacturers should concentrate on achieving a very accurate blaze angle.

5.9 Validation: comparison of theory to experimental results

We have provided these recommendations to beamline designers based on a purely theoretical survey of the factors affecting grating efficiency. For these results to be trustworthy, we need to confirm that the theory in Chapter 3 and the implementations in Chapter 4 are accurate descriptions of the real world. (We move on in Chapter 6 to use these tools to design the gratings and layout for the REIXS beamline spectrometer; before starting that project, we needed our own confirmation of the software's accuracy.)

The published literature on soft x-ray gratings includes only a few measurements of real-world efficiency. This is partly due to the difficulty of completing these measurements, and partly because, after receiving brand new gratings, most beamline builders would rather install them as quickly as possible and start doing their own research, rather than spend time on another beamline characterizing the gratings. This is unfortunate for two reasons. Beamline scientists often do not know the efficiency of their machines, or even whether the gratings they have received are optimal. Additionally, grating theorists do not have a large set of experimental results for validating their calculation methods in the soft x-ray regime.

We found one study by M. Bowler at the SRS light source [6] with a recent set of efficiency measurements for four gratings representing three different types of grating profiles. The gratings include one blazed grating with 1440 lines/mm, one rectangular grating with 600 lines/mm, and two attempted-rectangular gratings that ended up with trapezoidal sides of approximately 57°. The geometry parameters of all of the gratings were well-characterized by the manufacturer after ruling, making them ideal for comparing to theory. (The study also conducted efficiency calculations using the differential method, but we duplicated these calculations as a double-check on our implementations.)

Figures 5.19 through 5.22 show these experimental measurements, combined with our own calculations of the grating efficiency. Table 5.2 provides the geometry parameters, derived from the manufacturer's measurements.

Table 5.2: Geometry parameters and incidence configuration for the gratings in Figures 5.19 to 5.22. The geometry measurements were taken at the centre of the grating; accurate characterization of these gratings after ruling made them ideal for comparing with theoretical calculations. CIA stands for “constant included angle” – a mounting configuration that maintains a constant angle between the incident direction and 1st order.

Profile	Density (lines/mm)	Geometry Parameters	CIA (°)
Blazed	1440	Blaze angle: 2.2°, anti-blaze: 12.8°	160
Rectangular	600	Depth: 22.2 nm, valley width: 1.12 um	167
Trapezoidal	300	Depth: 49.3 nm, valley width: 2.46 um, side angle: 57°	167
Trapezoidal	390	Depth: 54.0 nm, valley width: 1.39 um, side angle: 57°	160

5.9.1 Note on incidence angle

Unlike the constant incidence angle efficiency curves we have been using up to this point, these gratings were designed for use in constant-included-angle monochromators, where the included angle ($\theta_2 + \theta_{2,n}$) between the incident beam and the useful order n is held constant. Therefore, these plots show the efficiency as a function of energy, with an incidence angle that also varies along the x -axis according to this constraint.

5.9.2 Comparison to theory

Of particular interest are the 1st and 2nd order results for the blazed grating in Figure 5.19, since we settled on blazed gratings for the design in Chapter 6. The agreement in the shape and amplitude of the efficiency spectra is very good; we can expect that the real-world efficiency would be slightly lower than predicted due to surface roughness and other effects described in Section 7.3. The agreement for the laminar profile in Figure 5.20 is also very good. Figures 5.21 and 5.22 show a tendency for the calculated results on the trapezoidal gratings to be shifted toward lower energies with respect to the measurements, although the shift is less than 20 eV. Overall, the close agreement between the theoretical and measured efficiencies shown here gives us a high degree of confidence in applying the grating software to optimize real-world beamlines.

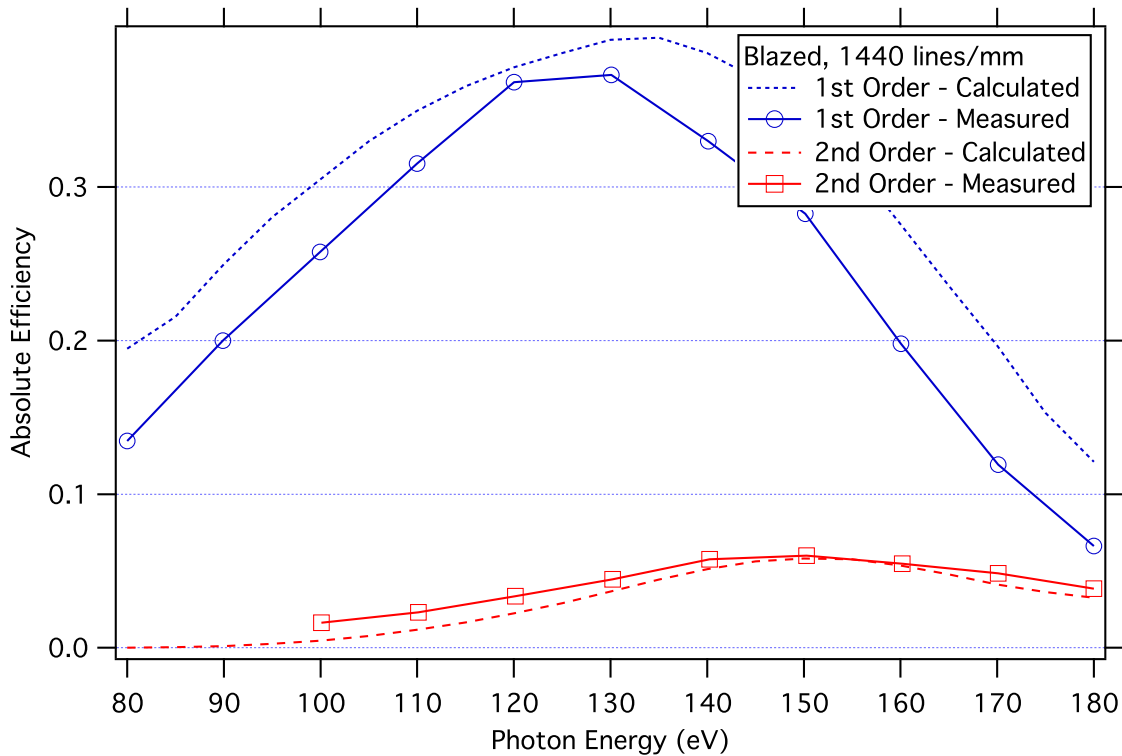


Figure 5.19: Comparison of grating efficiency calculations to diffractometer measurements. Blazed grating, 1440 lines/mm, 2.2° blaze angle, 12.8° anti-blaze angle. Incidence: 160° constant included angle to the 1st inside order.

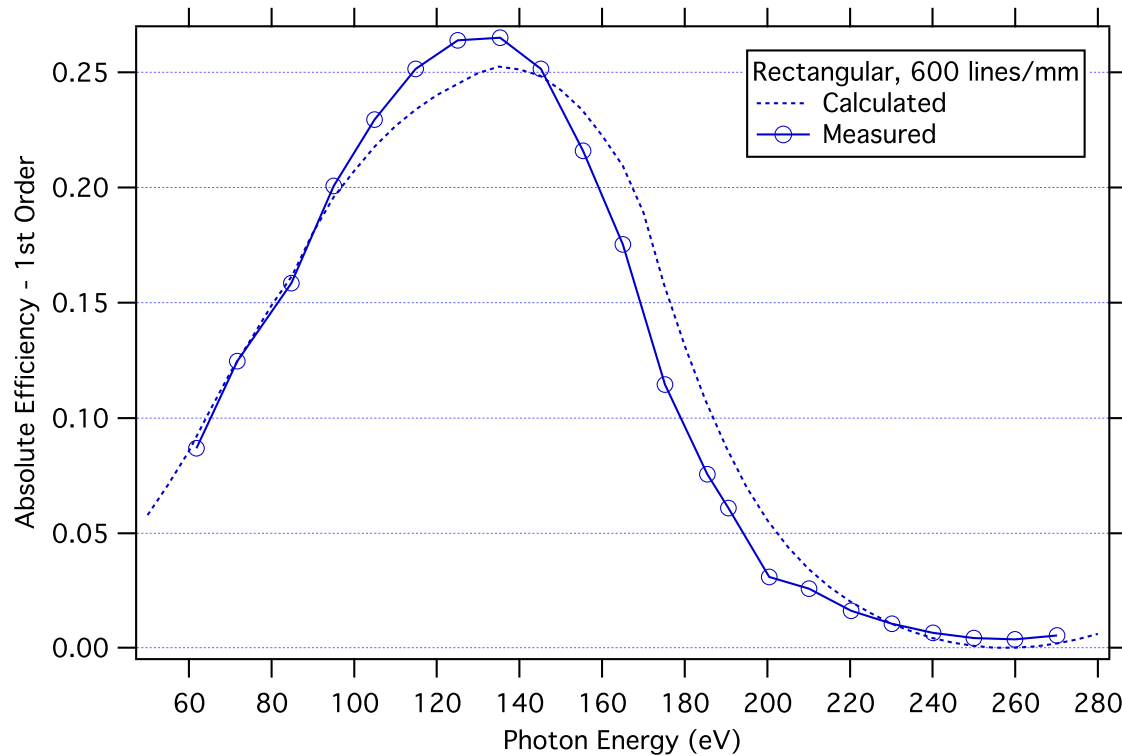


Figure 5.20: Comparison of grating efficiency calculations to diffractometer measurements. Rectangular grating, 600 lines/mm, 22.2 nm depth, 1.12 um valley width. Incidence: 167° constant included angle to the 1st inside order.

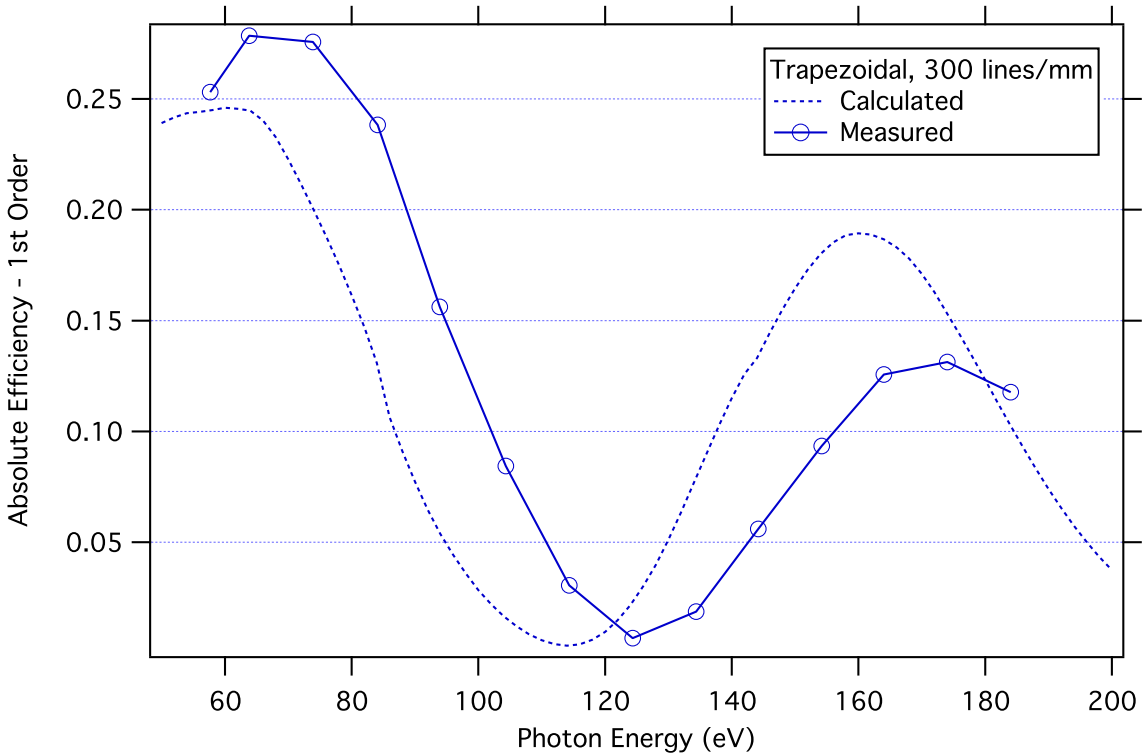


Figure 5.21: Comparison of grating efficiency calculations to diffractometer measurements. Trapezoidal grating, 300 lines/mm, 57° side angles, 49.3 nm depth, 2.46 um valley width. Incidence: 167° constant included angle to the 1st inside order.

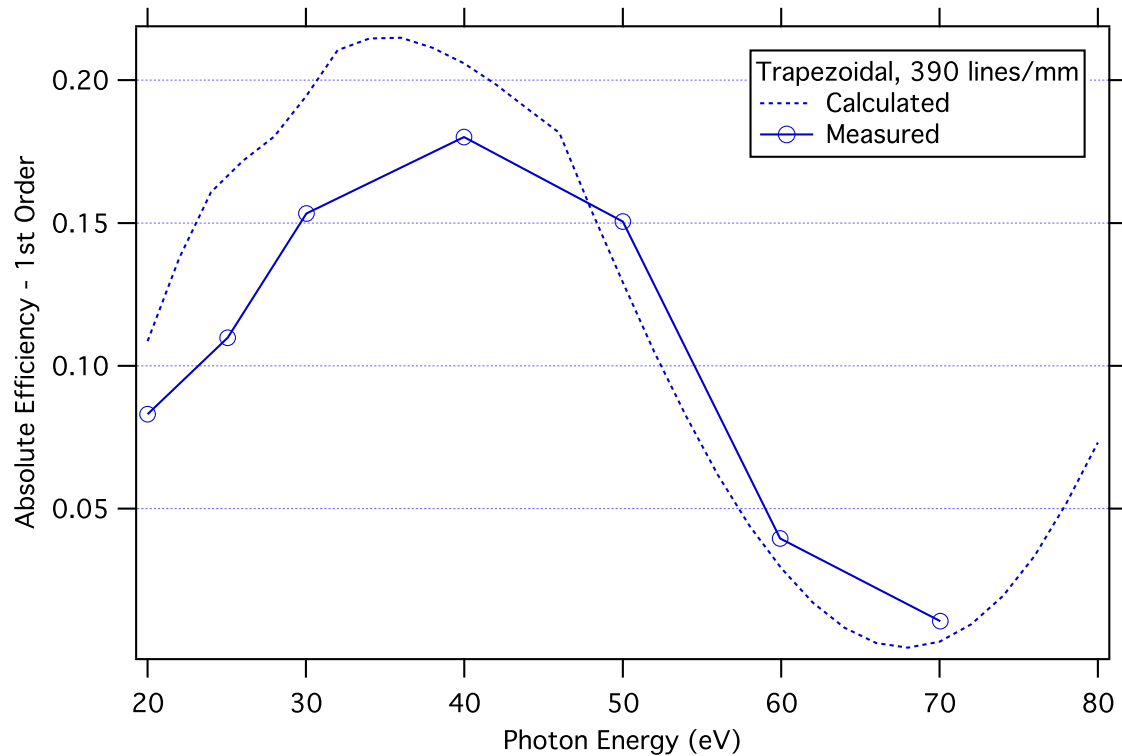


Figure 5.22: Comparison of grating efficiency calculations to diffractometer measurements. Trapezoidal grating, 390 lines/mm, 57° side angles, 54 nm depth, 1.39 um valley width. Incidence: 160° constant included angle to the 1st inside order.

CHAPTER 6

DESIGN: HOW WE APPLIED THESE TOOLS TO MAKE THE REIXS SPECTROMETER OPTICAL DESIGN

6.1 Application to spectrometer design

Up to this point, we have covered the theoretical foundation of grating efficiency, introduced new software tools for performing efficiency calculations, and used these tools to understand how various parameters and conditions affect a grating’s performance. We have also validated the calculation results by comparing against efficiency measurements on a set of real-world gratings.

In this chapter, we describe how we applied these results to the design of the soft x-ray emission spectrometer for the REIXS beamline at the Canadian Light Source.

6.1.1 Design goals

The REIXS beamline at the CLS is intended to facilitate a high-throughput user science program in the field of material science. Academic users apply for beamtime through a peer-reviewed proposal process, and are awarded shifts on the beamline based on the comparative scientific merit of their proposal. These shifts typically range from as short as eight hours, to as long as a week. (A fraction of the total beamtime is set aside for industrial clients, who purchase beamtime or analytical services from the facility.)

For the endstation designers, the challenge of supporting a general user program led to some high-level goals. We wanted to ensure that the spectrometer would be an adaptable “work horse”, applicable to a wide variety of emission experiments. High efficiency was important to minimize the time required for individual scans, maximize the total user throughput

of the beamline, and make the spectrometer useful for dilute samples. At the same time, we wanted to push the resolving power of the machine to be competitive with the highest-resolution spectrometers currently in existence. (If we could somehow exceed world-record resolution without sacrificing these other goals, there could even be a possibility of making new discoveries that would be invisible on existing beamlines.)

The design goals were also influenced by the current focus of the material science research group in the Physics Department at the University of Saskatchewan, with interests in organic biomaterials (DNA and peptides), organic semiconductor and photonic materials, and transition metal oxides.

The performance of the spectrometer was to be derived from the following key strengths:
[40]

1. Superior optimization of the design to specific spectral windows of interest, for analysis of materials containing

- silicon (Si L β emission edge, 92 eV),
- carbon (C K α_1 emission edge, 277 eV),
- nitrogen (N K α_1 emission edge, 392 eV) and
- oxygen (O K α_1 emission edge, 525 eV),

while maintaining acceptable performance for

- soft x-ray transitions in transition metals (L α, β and M α, β edges, 600 eV - 1100 eV).

2. A focus on best achievable performance, instead of a compact, mechanically simple or low-budget design.

3. A mechanical design allowing for superior alignment and calibration.

4. An optical design based on careful, knowledgeable balancing of the tension between efficiency and resolution.

The final key strength was achieved through close teamwork with David Muir, who used ray tracing techniques to quantify and optimize the resolution of our design. His full analysis of spectrometer focussing and resolving power is published in his M.Sc. thesis; some relevant areas of overlap are summarized briefly in this chapter, but for full details we would refer interested readers to Reference [40].

Together, we set a quantitative goal for both efficiency and resolution: 10% efficiency and a resolving power of 2000 at all the emission lines of interest. The design constraints were set by the maximum mechanical length of the spectrometer (the physical space available on the beamline floor was limited to 3m at the time) and the endstation budget of approximately \$1 million.

6.1.2 Comparative examples

Before starting work on the REIXS spectrometer, we examined the designs of existing spectrometers at facilities around the world. (Given that we had never designed a soft x-ray spectrometer before, this was a natural starting point, and one that would ensure that – for lack of original ideas – we would design a machine at least as good as any other in existence.)

We analyzed a variety of machines covering a range of design goals, from mechanical compactness and simplicity of grating/detector motion, to maximum resolution. It turned out to be difficult to accurately compare the stated resolution of the different machines, due to differences in the resolving power criterion and variability in the spatial resolution of their detectors. David resolved this by modelling the optical layout and conducting ray-trace simulations for each one. To decouple the detector performance – which affects the final resolution but is not related to the optical design – from the pure optical performance, we simulated them using a standardized detector with a hypothetical spatial resolution of 20 μm .

Figure 6.1 shows this normalized comparison of spectrometer resolution. For machines offering a choice of gratings, the plot shows the performance attainable by each grating. Among these machines are the SXF spectrometer from Beamline 8.0.1 at the Advanced Light Source [25] (Figure 2.8); another Rowland circle spectrometer, the commercially-available Gamma-data XES350 [19]; and several recent variable line spacing (VLS) designs. Unfortunately, we

were not able to compare the efficiency for these designs, because the exact grating groove parameters are rarely known or published.

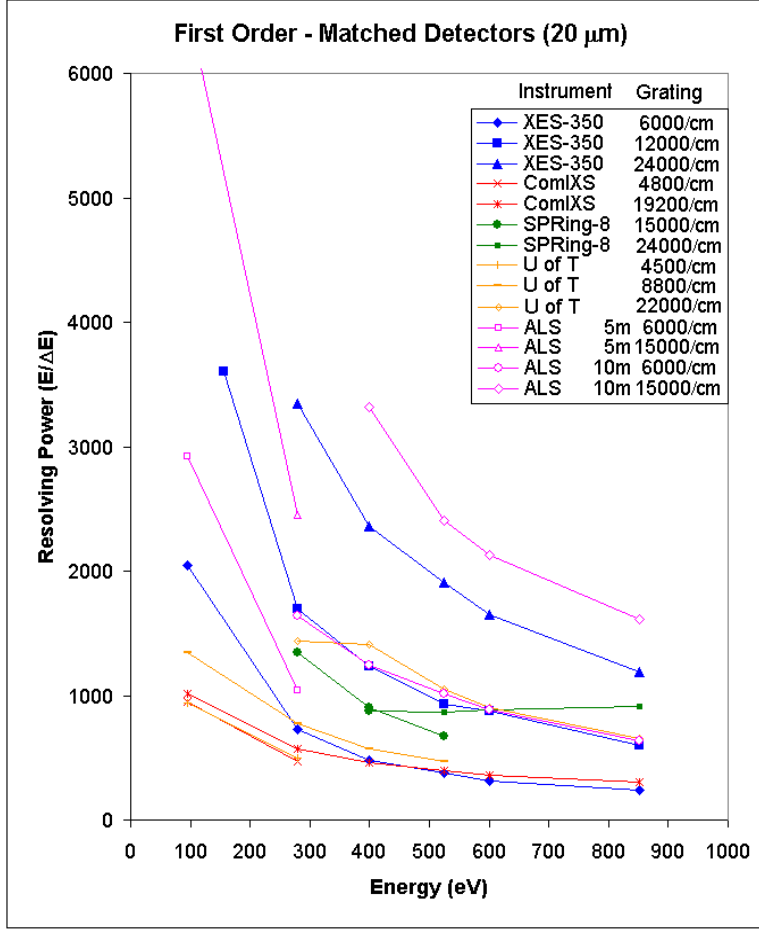


Figure 6.1: Resolving power performance comparison of existing spectrometer designs, calculated with all detectors having a 20 μm pixel size. The legend specifies the spectrometer and grating choice (size and/or line density). Reprinted from Reference [40, Figure 3.2]

6.2 Design Process

The first step in the design process was to choose the focussing configuration of the spectrometer. Based on our comparison of existing designs, we selected the Rowland circle configuration for the reasons in Section 6.2.1.

To determine the number of grating choices to offer, we started by assuming one grating optimized for each emission line of interest: Si (92 eV), C (277 eV), N (392 eV), O (525 eV),

and the transition metal range (600 - 1100 eV) optimized for Fe (725 eV). Eventually, after completing the subsequent steps in the design process, we found that we could merge the medium energy gratings (277, 392 eV) and high energy gratings (525, 725 eV), since there was considerable overlap in their performance. This allowed us to add a fourth grating, intended to cover a large energy range with extremely high efficiency, for studying dilute samples; we called this one the “impurity” (IMP) grating. Later, we added two more gratings, intended to offer impressively high resolution, in the medium energy (HRMEG) and high energy (HRHEG) range; these 3rd order gratings are described in Section 6.3.

Table 6.1: Gratings chosen for the REIXS spectrometer, with their target energies used for optimization, the energy ranges they will be able to cover, and the final optimized grating parameters

Grating	Optimization Energy (eV)	Energy Range (eV)	Groove Density (lines/mm)	Incidence Angle (°)	Coating	Blaze Angle (°)
1 st order						
Low Energy (LEG)	92 eV (Si)	30 - 300	600	86	Au	1.85
Impurity (IMP)	400 eV (N)	75 - 750	900	87	Ni	1.11
Medium Energy (MEG)	400 eV (N)	250+	1200	88	Ni	1.48
High Energy (HEG)	725 eV (Fe)	400+	2000	88	Pt	1.52
3 rd order						
High Res Medium Energy (HRMEG)	280 eV (C)	280+	1800	88	Ni	4.85
High Res High Energy (HRHEG)	725 eV (Fe)	525+	2600	88.25	Pt	4.05

The next step was to determine the grating parameters (line density, profile) and the optical geometry (incidence angle, distances, grating radii, etc.), subject to the focussing constraints, to reach our target resolution and efficiency.

Because of the inherent tension between resolution and efficiency, attempts to establish the grating parameters prompted a carefully-choreographed, swashbuckling duel between the Forces For Efficiency (FFE) and the United Revolutionary Front (URF). This battle became an iterative process, involving a degree of trial-and-error and continuous refinement. In retrospect, the design process we would recommend for future designs is summarized in Figure 6.2. The final grating parameters that affect the efficiency are shown in Table 6.1.

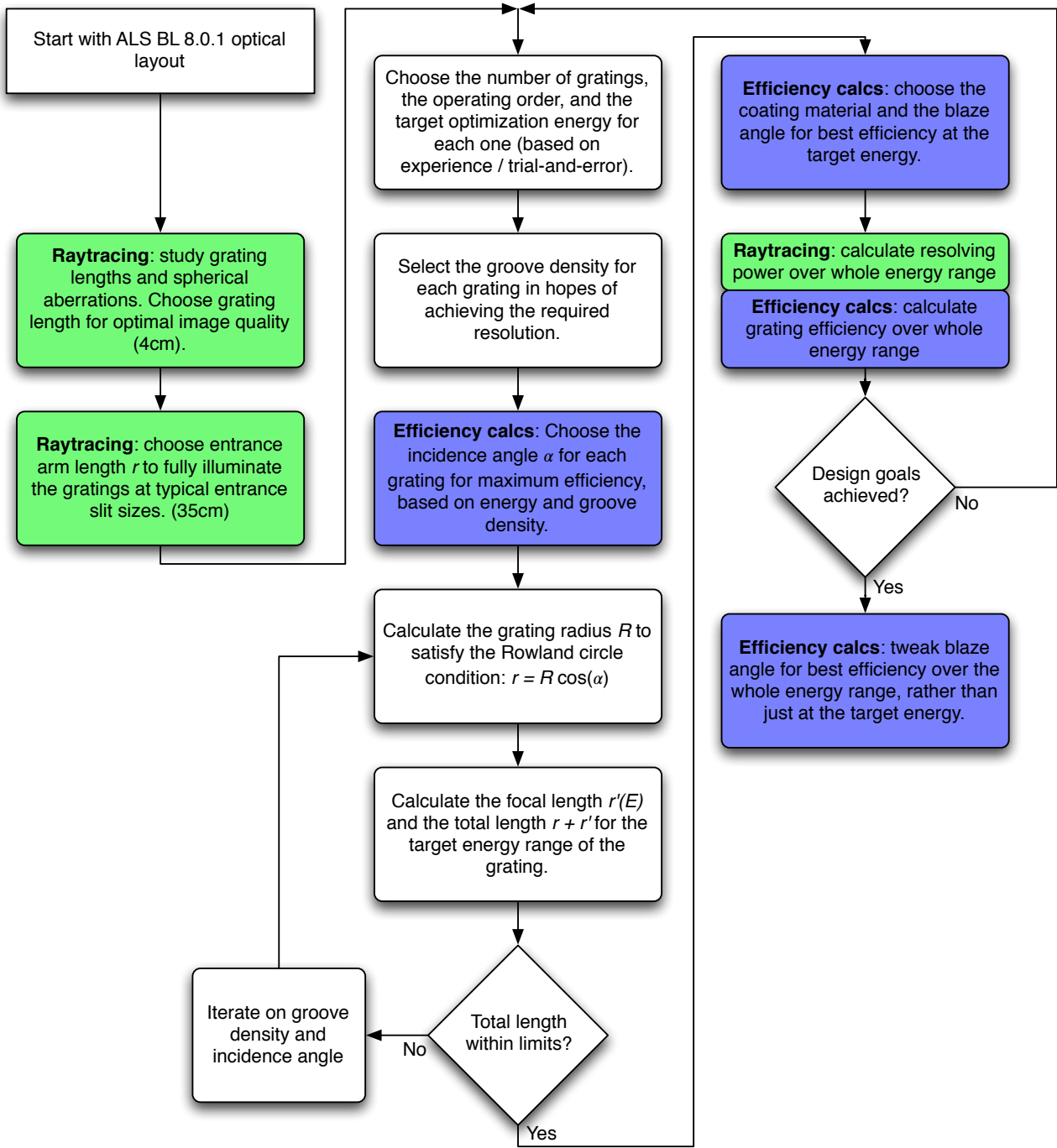


Figure 6.2: Approximation of the process used to design the optics of the REIXS spectrometer.

6.2.1 Justification of design choices

Rowland circle vs. VLS design

We mentioned in Chapter 2 that spectrometer optics must focus as well as disperse light. Some of the designs we surveyed achieved this using VLS gratings, while others employed spherical gratings in the “Rowland circle” configuration. Fortunately, this provided us with a good basis for comparison.

According to Reference [40], the main advantage of VLS gratings is to control the shape of the focal curve – the path in space that the detector must travel along to keep the spectrometer focussed as a function of energy. A flat focal curve simplifies the mechanical design, since the detector then only needs to move along one axis. As Figure 6.3 shows, the VLS correction also shortens the focal curve, so that to handle the same energy range, a spectrometer can be made more compact. Unfortunately, a compact focal curve places the detector closer to the grating and inherently reduces the resolution – as a result, all of the VLS designs we surveyed required very high spatial resolution detectors to maintain just average resolution [40, Table 3.3].

The VLS technique can also be used to minimize aberrations (astigmatism, coma, etc.), but these can only be fully corrected at a single energy; for a general-purpose spectrometer, this is not helpful.¹ Using VLS corrections also removes the flexibility to operate the spectrometer in higher orders: since the formulas for the correction terms depend on the diffraction order, VLS spectrometers behave erratically outside of their design order.

Figure 6.4 compares the detector image of three adjacent energy lines, for a comparable VLS and Rowland circle spectrometer. While requiring a longer focal curve and more complicated detector motion, the Rowland design offers far higher resolution for the same nominal groove density; it would take a large increase in efficiency-robbing line density for the VLS design to keep up with it. Therefore, since we were not constrained by physical size², we selected a Rowland circle optical layout – similar to the ALS Beamline 8.0.1 SXF

¹After completing our Rowland circle design, an external consultant attempted to optimize it by adding VLS terms to correct aberrations. While this worked well at the optimization point of 200 eV, the detector image became heavily defocussed just 50 eV away [40, Figure 5.1].

²At least, we were not constrained beyond the 3 meter limit of the beamline space

spectrometer, as the basis for our design.

Choice of profile: blazed vs. rectangular / sinusoidal

Back in Chapter 4, we saw that optimally blazed gratings have almost double the efficiency of sinusoidal gratings, and even more than that of rectangular gratings (Figure 5.7). Since the ideal blaze angle is energy-dependent, we saw that this optimization comes at the cost of having an efficiency peak centred on the target energy, and comparably lower efficiency outside the peak. However, for high groove densities and high optimization energies, the peaks are wide enough to span the entire soft x-ray range. For low groove densities and low optimization energies – as would be the situation for the LEG – the peak bandwidth is smaller, but still easily covers the design energy range of this grating.

For each grating, we selected blaze angles corresponding to the target energies in Table 6.1, according to Equation (5.1). We then used the efficiency software to optimize the blaze angle at this energy, using the analytical θ_b as a starting point. We then calculated the efficiency curves for these profiles, as well as for optimized sinusoidal and rectangular alternatives, and confirmed that the blazed profile was indeed the clear winner for all the gratings. (For some of the gratings, we tweaked the blaze angle at the end of the design process, since we were willing to accept a small reduction in efficiency at the target energy in exchange for higher overall efficiency integrated across the whole energy range.)

Ruled versus holographic gratings

Section 5.1.1 gave an overview of mechanical ruling and holographic grating manufacturing techniques. To make a pragmatic decision between these two options, we needed to consider the impacts of real-world manufacturing issues. Common errors which happen during ruling and holographic manufacturing are shown in Figure 6.5.

Mechanical ruling engines are designed to be precision machines, but they must be carefully set up and operated to avoid errors. Achieving the specified blaze angle – critical to efficiency – must be accomplished during setup by aligning the diamond tip, ruling a test section of the grating, analyzing the resultant blaze angle with a microscope, adjusting the tip, and tediously repeating this process. Without sufficient quality control, the blaze angle

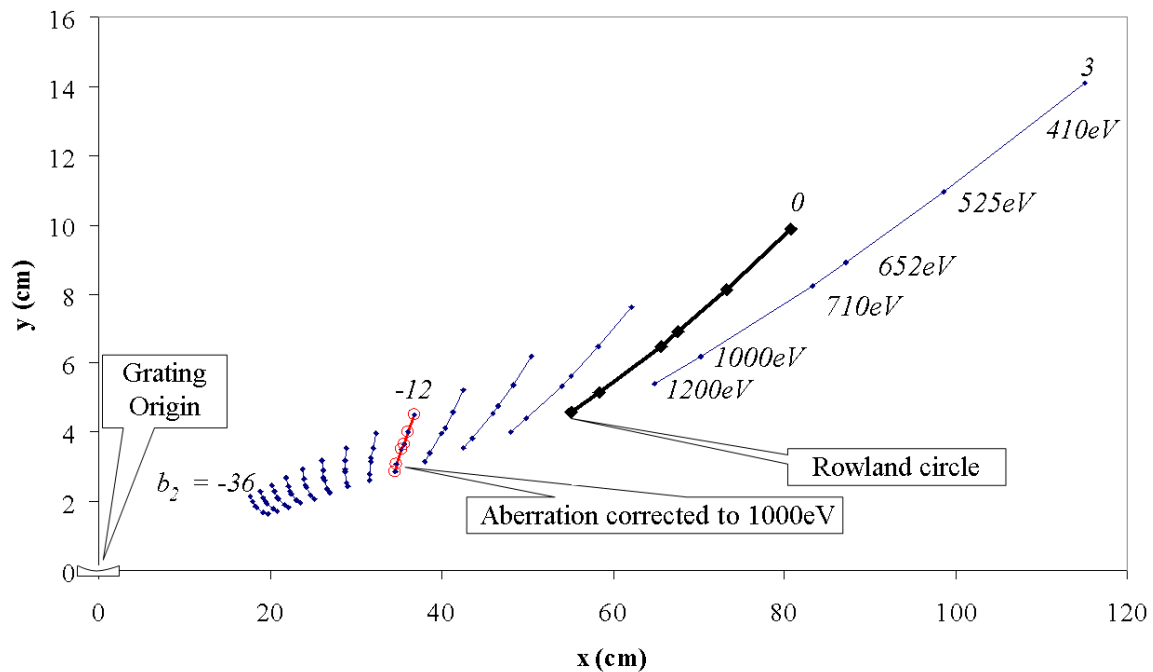


Figure 6.3: The focal curve is the path in space the detector needs to move along to maintain focussing as a function of energy. This plot shows the effect of the b_2 VLS correction term: with a b_2 of 0, the focal curve is the same as the Rowland circle focal curve. A specific b_2 value of -12 (highlighted in red) straightens the focal curve, which could simplify the detector mechanics, but also shortens the focal distance and reduces the resolution at the detector. Reprinted from Reference [40, Figure 2.17].

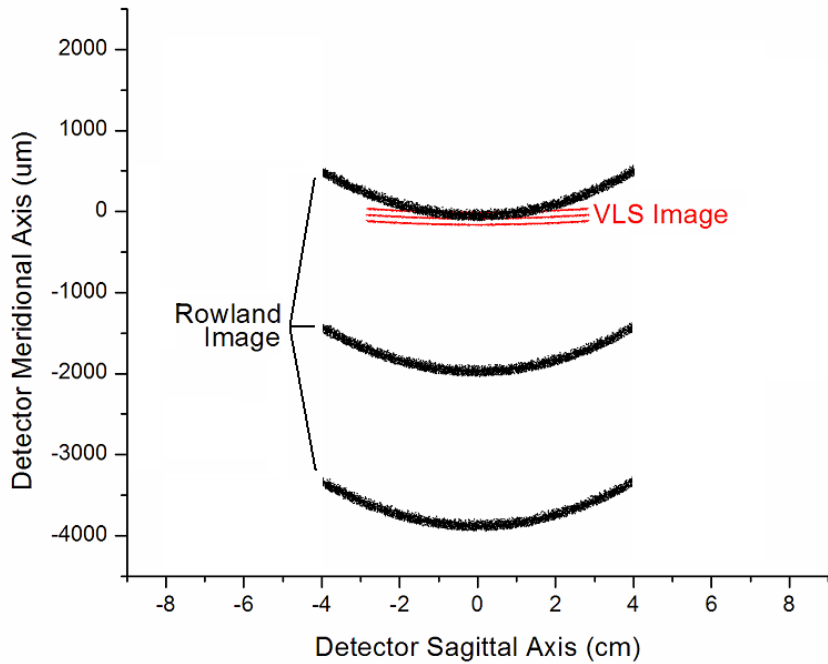


Figure 6.4: Variable line space (VLS) corrections reduce aberrations that cause curvature, as seen in these ray-traced detector images of three adjacent emission lines. However, the increase in resolution due to better focussing is not able to make up for reduced dispersion across the surface of the detector, as compared to the Rowland circle alternative. Reprinted from Reference [40, Figure 2.18].

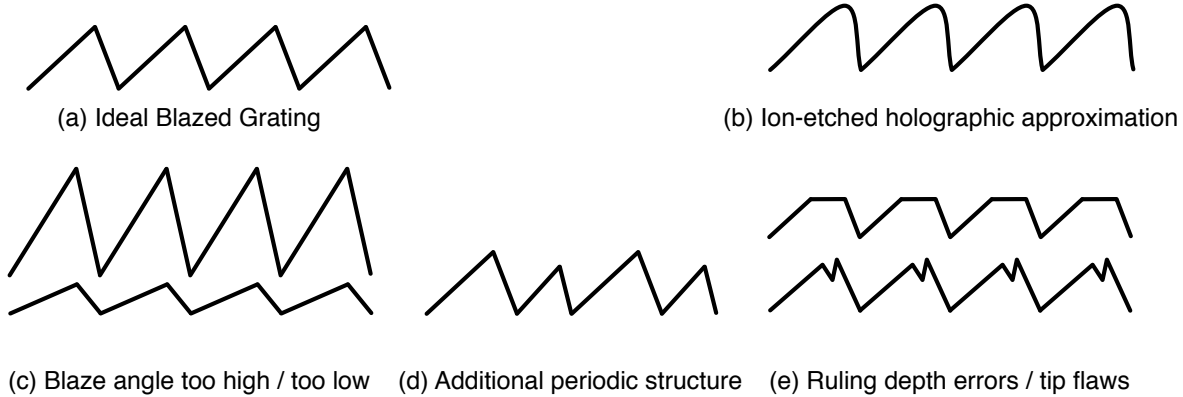


Figure 6.5: Common errors in the manufacture of ruled and holographic gratings. Holographic exposure creates a sinusoidal profile; subsequent ion-etching (b) can only approximate a triangular profile. Ruled gratings can suffer from blaze angle errors (c), or errors due to the shape and/or depth of the diamond tip (e). If the ruling engine introduces periodic errors in the groove position, this additional structure (d) superimposes additional diffraction patterns (ghosts).

can end up high or low by a few tenths of a degree, which could completely eliminate the blazing advantage.

Another concern is whether the grooves end up uniform, and the groove geometry is maintained, across the entire grating. This is essential to both the efficiency and the resolution. If the ruling process creates errors that vary periodically over a series of grooves, this will insert additional periodic structure into the grating and create “ghosts” in the final spectrum: an additional diffraction pattern superimposed over the desired one, with intensity peaks again given by the grating equation, but at a different period. Errors with a period on the same order as the groove spacing create “Lyman ghosts”, which end up far from the spectral lines. Errors with periodicities on the order of millimetres create “Rowland ghosts”, which appear close to and symmetric around the desired spectral lines.

One additional flaw that can occur with ruled gratings happens when the diamond tip fails to penetrate far enough into the metal surface to create the desired profile, resulting in something that looks like Figure 6.5 (e). The profile can also be corrupted by irregularities in the diamond tip, or by bits that break off or are picked up during the ruling process. (One common manufacturing error is for the tip to pick up a shard of metal, and carry it with it for several thousand trips across the grating; this creates an inefficient stripe across an otherwise acceptable grating.) Finally, for maximum efficiency, the anti-blaze angle should be as close to 90° as possible, but in most cases the shape of the ruling tip forces it to be below 30° . (The blazed grating in Figure 5.19 had an anti-blaze angle of 12.8° .) According to the theoretical calculations in Figure 5.18, the anti-blaze angle does not start to seriously affect the efficiency until it goes below ~ 4 times the blaze angle, ie: 5° for a blaze angle of 1.5° .

Holographic gratings overcome many of these disadvantages. They are not susceptible to ghosting, since their grooves are all formed simultaneously, with a period as regular as the wavelengths of an electromagnetic wave.³ They can also be ruled faster and at lower cost – mechanical ruling can take weeks for one grating – so that flaws can be corrected by trial-and-error. Despite these advantages, holographic gratings have their own manufac-

³However, modern interferometrically-controlled ruling engines can inscribe grooves with such precision that they have also virtually eliminated ghosting.

ing challenges. In some cases, variation in the sinusoidal groove depth happens because the intensity of the interference pattern changes across the width of the grating. Traditionally, holographic techniques also have not been able to produce groove densities as high as mechanical ruling engines. The most significant drawback to holographic gratings, however, is their inability to create a true blazed profile, even when using ion etching or the Sheridan method (Figure 6.5 (b)). For this reason alone, we chose mechanical ruling for all six of the spectrometer gratings.

In future work, it would be helpful to characterize the typical groove shape of real-world ion-etched holographic gratings, and update the grating efficiency software to support this additional profile; this could allow for more informed decision-making on whether to use or reject holographic ruling.

6.3 High resolution (3rd order) design

6.3.1 Options for reaching extreme resolution

We mentioned in Section 2.2.2 that the two general ways to increase the resolution of a spectrometer design (besides choosing a better detector) are to move the detector further away from the grating, or to increase the angular dispersion of the grating. Increasing the detector distance requires adjustments to the focussing scheme, and severely reduces geometric efficiency.⁴ This option also is not an option when the constraints on the machine size have been reached. The other method – increasing the angular dispersion – can either be achieved using the groove density, or the diffraction order. As we saw in Figure 5.9, higher groove densities reduce the grating efficiency, and are also constrained by manufacturing limits.⁵

⁴In a Rowland circle design, ray trace testing [40] showed us that the geometric efficiency is proportional to the inverse cube of the detector distance. The reduction in saggital angle captured by the detector causes the first reduction. The grating radius R needs to be increased to maintain focussing, and with spherical gratings, this further increases the saggital dispersion. The entrance distance r also needs to be increased, causing a reduction in the solid angle captured by the grating. This could be compensated by increasing the grating size, but the total grating size is constrained by limits on spherical aberration.

⁵While some ruling engines can now reach extremely high groove densities approaching 10 000 lines/mm, the groove quality and accuracy suffers. For soft x-ray gratings, 3 000 lines/mm seems to be a current effective limit for both mechanical and holographic ruling.

So this leaves three related questions for a designer trying to achieve extreme resolution: what do you when you have hit the machine size limit *and* the groove density manufacturing limit? Does taking these parameters all the way to their limits actually the optimal solution for maintaining efficiency at high resolution? What are the consequences of designing intentionally for a higher diffraction order?

All existing soft x-ray spectrometers seem to be designed for 1st order operation, based on the assumption that diffraction efficiencies in higher orders are too low to be useful. (We have seen users force some Rowland circle designs into 2nd order, when trying to tease out higher resolution.) Although it had never been done before, our survey of efficiency trends hinted that it might actually be more efficient to use gratings in 3rd order, than to triple their groove density or extend the machine size. Based on these results, we attempted to add ultra-high-resolution capabilities to the REIXS spectrometer, by considering gratings specifically optimized for 3rd order operation.

6.3.2 Justification for 3rd order design

A combination of grating efficiency calculations and ray tracing simulations showed that this novel 3rd order design would actually be the *only* way to dramatically increase the resolution of our spectrometer, within the mechanical length constraints that existed at design time. Figure 6.6 shows why the 3rd order design makes sense from an efficiency perspective. From Equation (2.1), we can easily see that switching from 1st order ($n = -1$) to 3rd order ($n = -3$) has the same effect on the angular dispersion (and resolution) as tripling the groove density. The conventional assumption on higher order operation is that even when properly blazed, higher order efficiencies are extremely low compared to the first order. However, we found that at certain points along the efficiency curve, the 3rd order grating efficiency would actually be *higher* than for an equivalent-resolution grating with three times the groove density operated in 1st order. Not only that, but in most cases the hypothetical triple-groove density alternative would be moot: it would be impossible to manufacture such a grating.⁶

⁶Even if it was possible to rule such an ultra-high density grating, decreases in the groove quality would reduce the real-world efficiency through stray light processes described in Section 7.3. In Chapter 7, we char-

Figure 6.6 is based on the efficiency curves for the two 3rd order gratings we ended up adding to the design. For the 1800 line/mm HRMEG grating (a), designed for outstanding resolution near the carbon emission line (280 eV), the efficiency in 3rd order is actually higher than for an equivalent-resolution 5400 line/mm grating optimized for 1st order. (Even with this advantage, we point out again that it would be impossible or very difficult to rule a 5400 line/mm grating with sufficient quality to achieve this theoretical efficiency.) One interesting thing to note is that this advantage in 3rd order efficiency persists even for appropriately-optimized sinusoidal gratings, shown in red.

For the 2600 line/mm HRHEG grating (b), the 3rd order efficiency is comparable but not quite higher than its hypothetical equivalent 7800 line/mm 1st order grating. In this case, however, the 3rd order design is really the only possibility; it would be practically impossible to manufacture the 7800 line/mm grating.

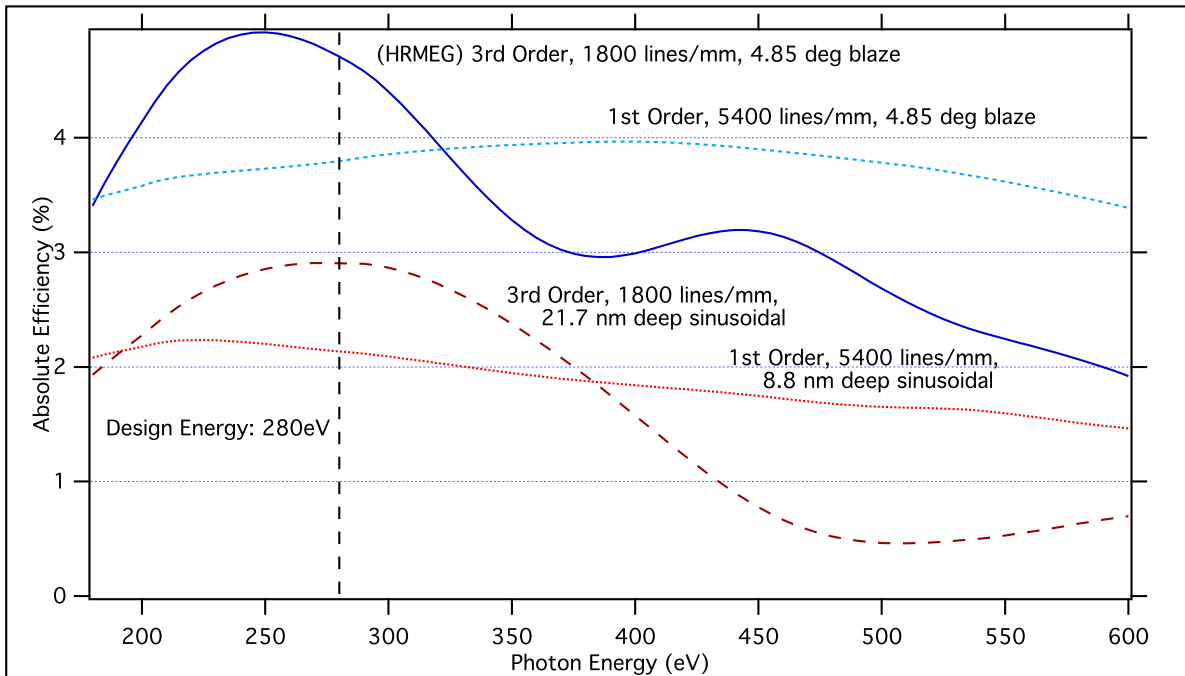
6.4 Coating choices

Back in Chapter 5, we plotted the reflectivity and comparative efficiency for a range of common coating materials (Figure 5.11, 5.12). From these plots it was simple to select the coating with the highest continuous reflectivity over each grating's usable energy range. Since the IMP and MEG were only intended to be used below 800 eV, we chose a nickel coating for its high and near-constant reflectivity. The LEG exploited the gold reflectivity peak at low energies, and we selected platinum for the remaining high-energy gratings. (Iridium and rhodium would have provided nearly equivalent performance, but the grating manufacturer had previous experience in applying platinum coatings.)

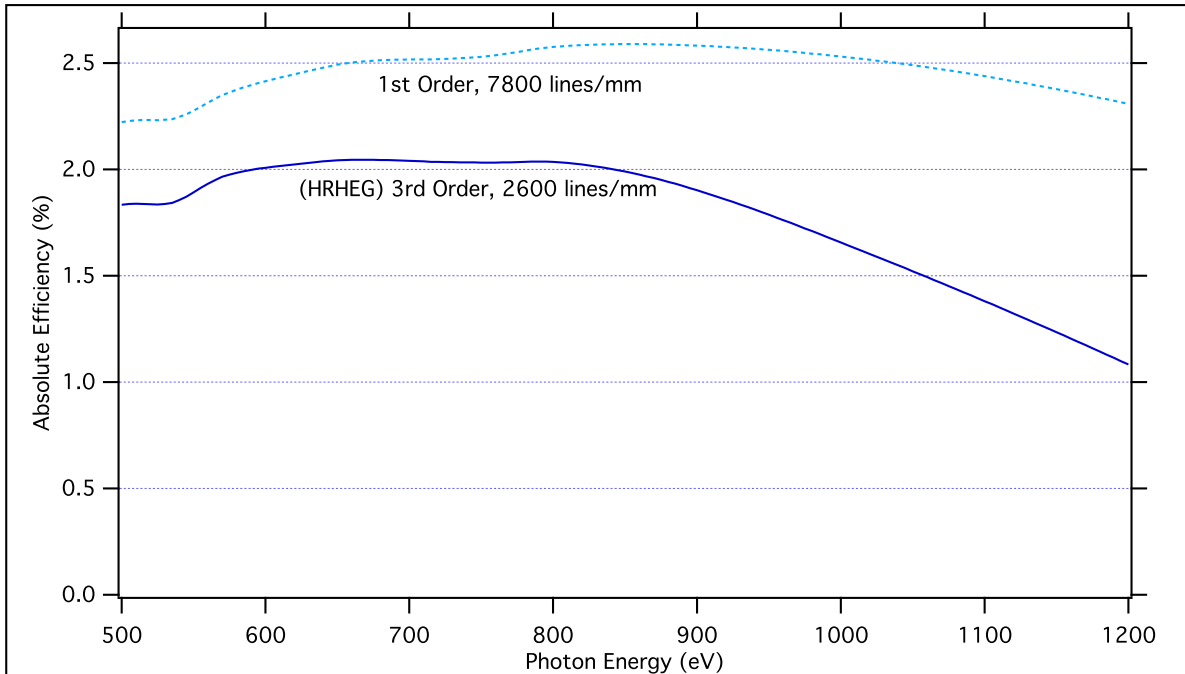
Most of these choices proved to be optimal, but not all. We discovered one serious consequence of using Nickel coatings, which we explore in Chapter 7. It turns out that the surface roughness also has a significant impact on the real-world efficiency, so another factor in the coating choice should be how smoothly it can be applied before or after ruling.

Based on our calculations for the coating thickness (Figure 5.10), we specified a conser-

acterize our own manufactured gratings and find a general reduction in real-world efficiency with increasing groove density, as the ruling process struggles to keep the grooves clean and properly formed.



(a) The 3rd order HRMEG (1800 lines/mm), and an equivalent-resolution 1st-order grating (5400 lines/mm - difficult or impossible to manufacture). The 3rd order efficiency advantage persists even for sinusoidal gratings without the blazing advantage.



(b) The 3rd order HRHEG (2600 lines/mm), and an equivalent-resolution 1st-order grating (7800 lines/mm - impossible to manufacture).

Figure 6.6: At some points along the efficiency curve, the grating efficiency is actually higher in 3rd order than it would be in 1st order for an equivalent-resolution grating with three times the groove density... assuming you could even manufacture such a grating. HRMEG and alternatives: nickel coating, geometry as indicated. HRHEG and alternative: platinum coating, blaze angle of 4.05°.

vative minimum thickness of 40 nm.

6.5 Tolerancing

The combination of efficiency and ray-tracing tools also provided a rigorous way to specify reasonable tolerances for the grating manufacturer. Resolution criteria determined the tolerance for parameters like the groove density and grating figure. To specify the blaze angle limits, we used calculations to determine the amount of error that would cause a 15% relative drop from the nominal efficiency.

6.6 Summary of final design

By combining efficiency and resolution calculations to carefully manage the trade-off between these two goals, we were able to exceed our design targets of 10% theoretical efficiency and 2000 resolving power at all the emission lines of interest, using the LEG, MEG, and HEG gratings. The addition of the impurity (IMP) grating added extremely high efficiency over a large portion of the soft x-ray energy range, and the two 3rd order gratings added massive resolving powers of 14 000 and 10 000 at the carbon and iron lines. (Although their efficiency is substantially lower than the other gratings, the novel usage of the 3rd order was the only way to achieve this kind of resolution within our physical size constraints.)

Table 6.2 shows the predicted resolving power and grating efficiency of our design for all the edges of interest. For those interested in resolution, Figure 6.7 compares the resolving power of our design to the competitors in Figure 6.1. The final optimized grating parameters are included in Table 6.1. In Figures 6.8 through 6.10, we show the theoretical predicted efficiency in 1st, 2nd, and 3rd order for all six gratings. In Chapter 7, we compare these efficiencies with the real-world diffraction performance of the manufactured gratings.

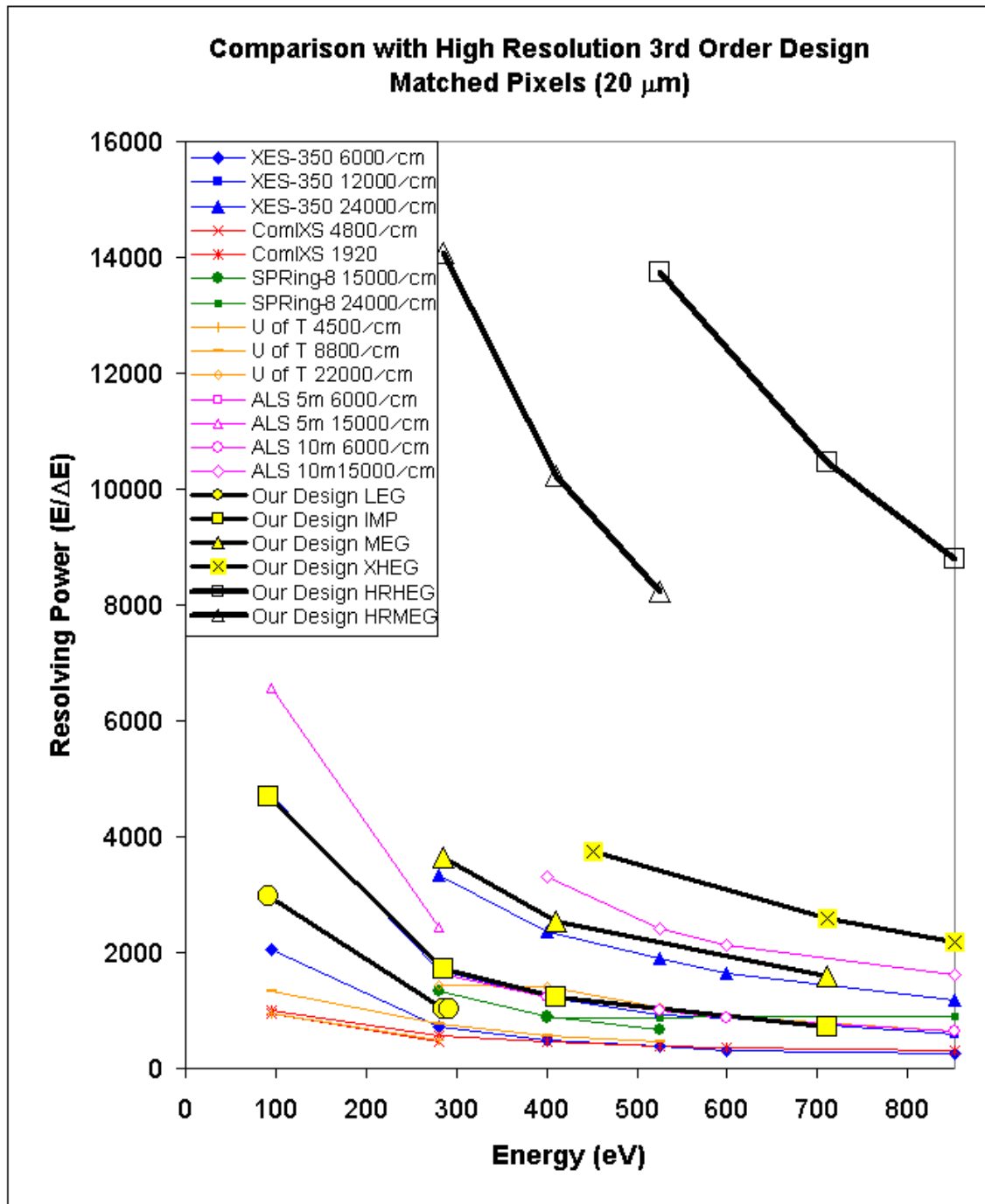
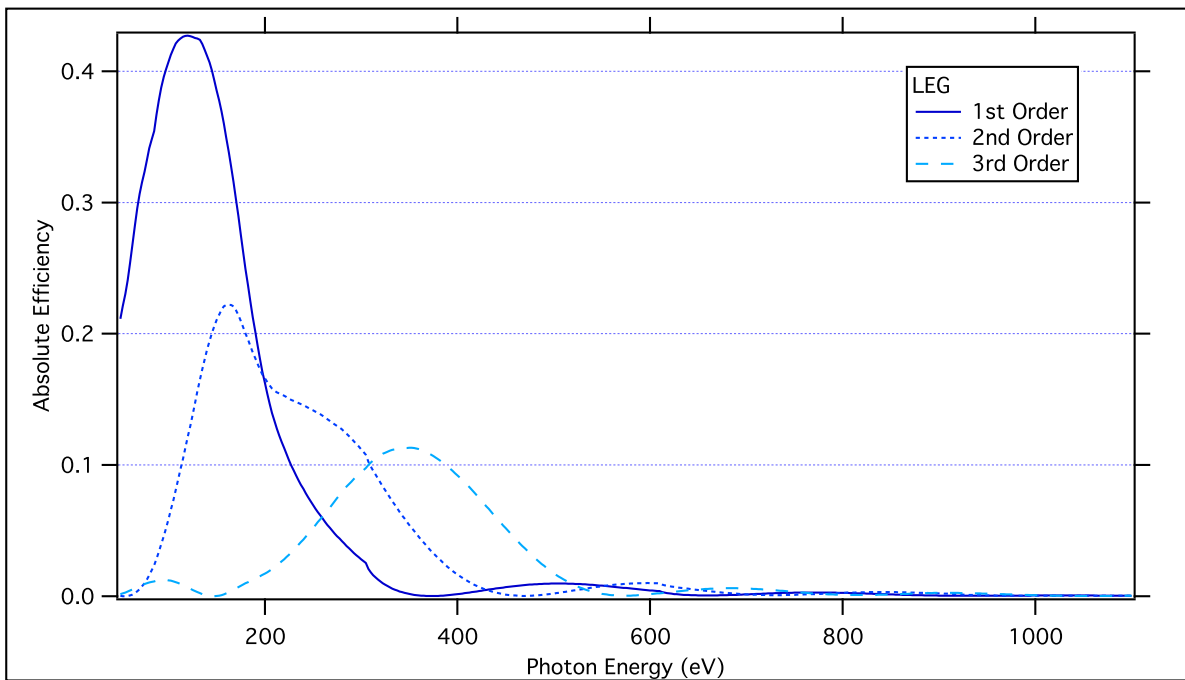
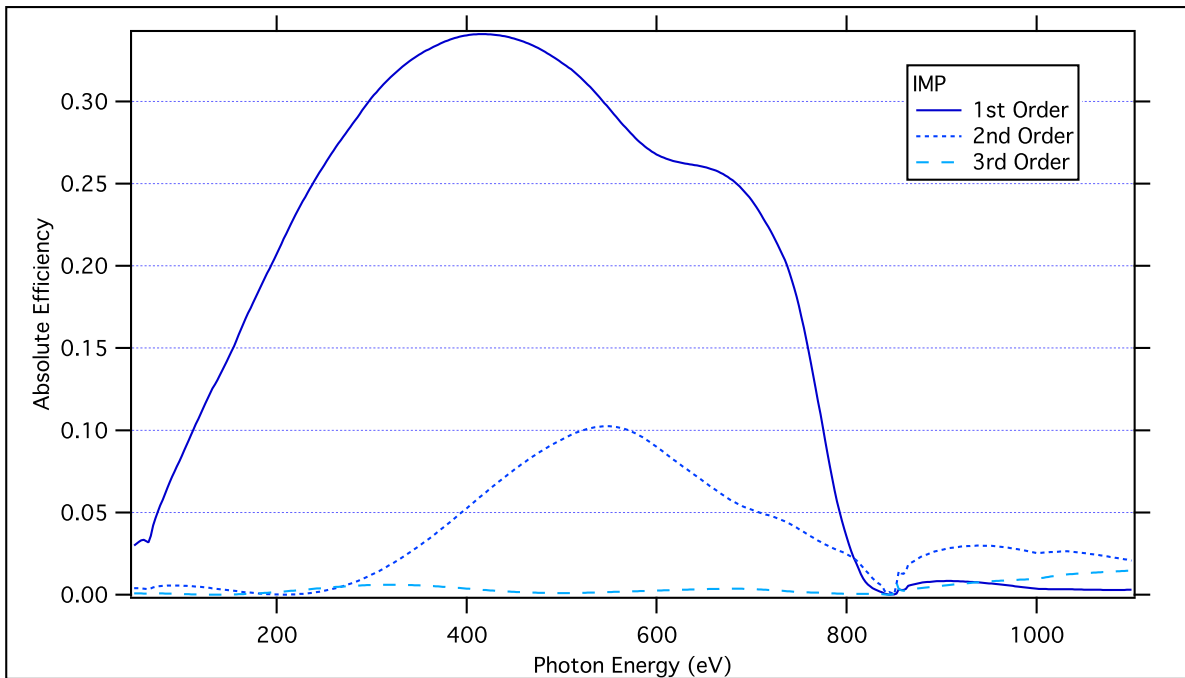


Figure 6.7: The REIXS spectrometer design offers higher predicted resolution than the existing designs we surveyed in Figure 6.1. (The advantage is even more dramatic when considering the 3rd order high resolution gratings.) However, the full strength of the design comes from a knowledgeable balance with grating efficiency, based on our combined calculations. Reprinted from Reference [40, Figure 4.7].

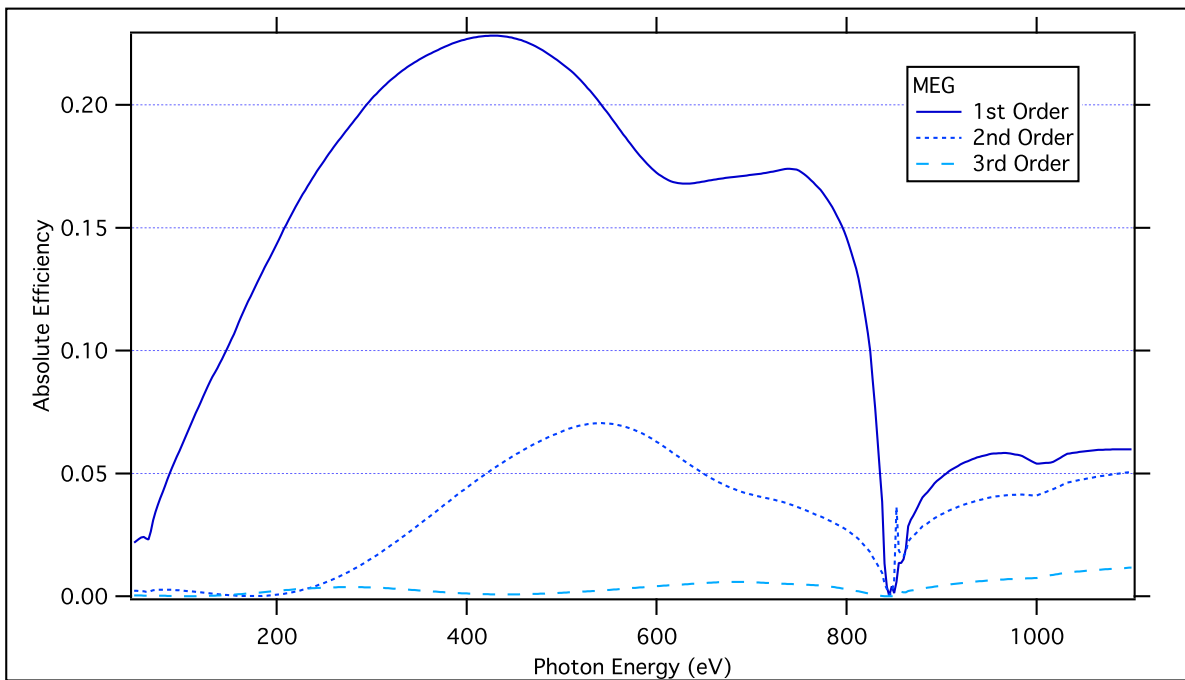


(a) Low Energy Grating (LEG): 600 lines/mm, 1.85 deg. blaze angle, Au coating, for 86 deg. incidence

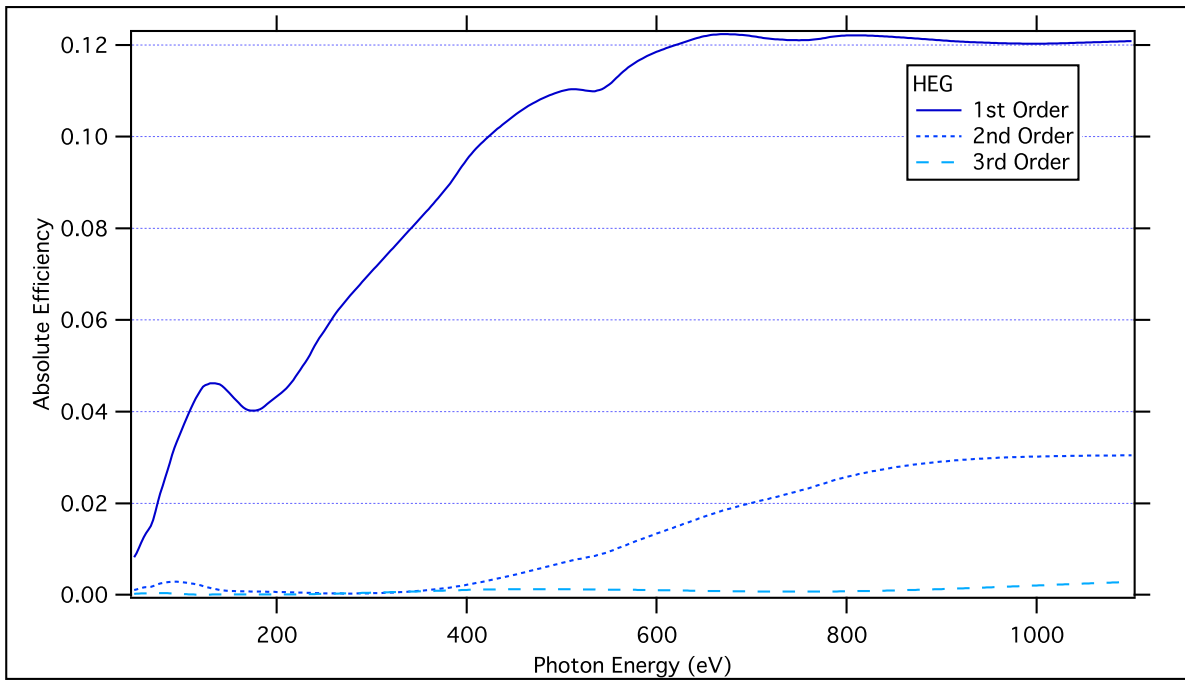


(b) Impurity Grating (IMP): 900 lines/mm, 1.11 deg. blaze angle, Ni coating, for 87 deg. incidence

Figure 6.8: Theoretical diffraction efficiency for the Low Energy Grating and Impurity Grating.

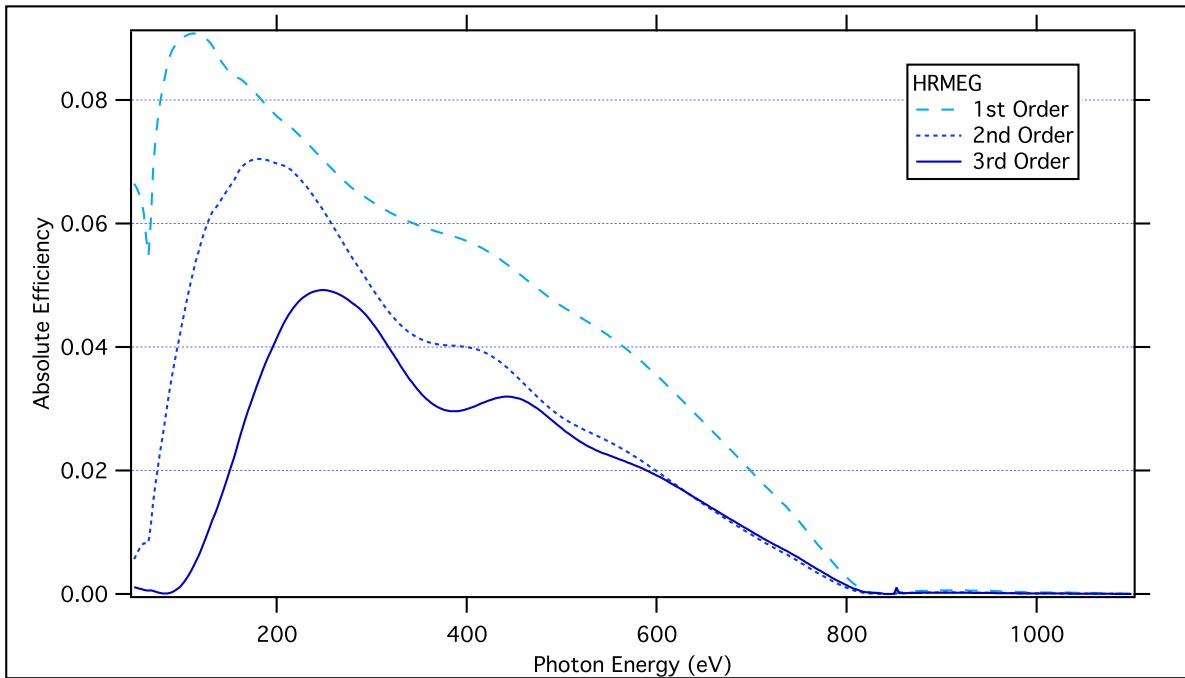


(a) Medium Energy Grating (MEG): 1200 lines/mm, 1.48 deg. blaze angle, Ni coating, for 88 deg. incidence

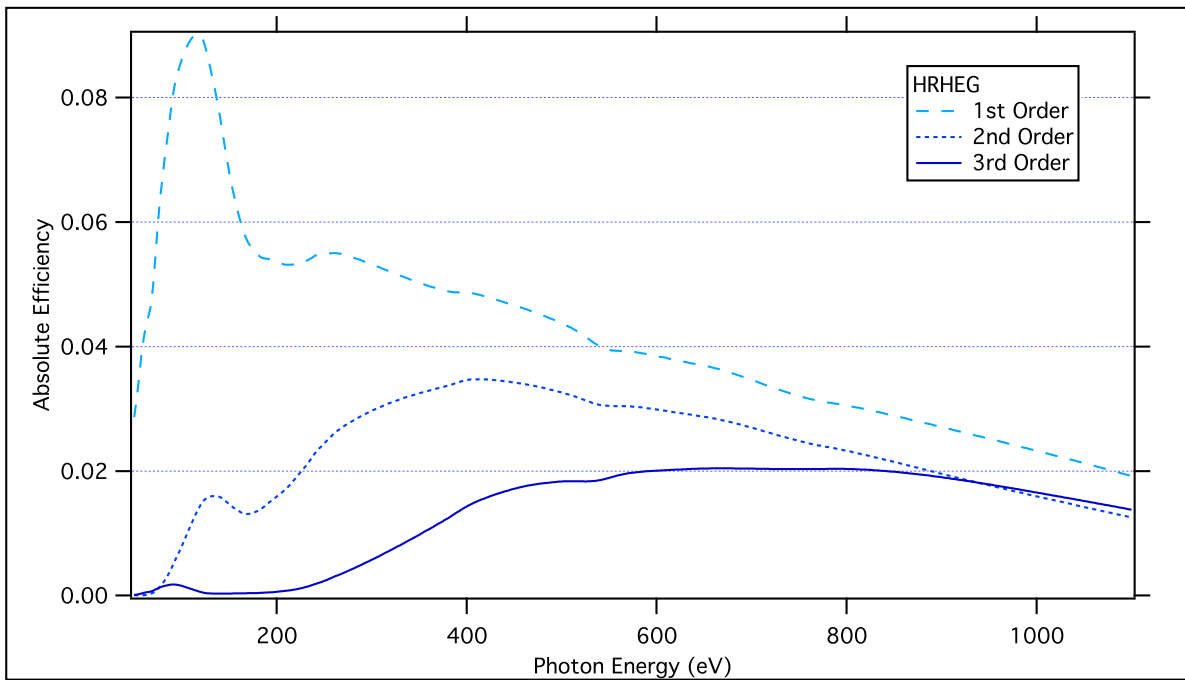


(b) High Energy Grating (HEG): 2000 lines/mm, 1.52 deg. blaze angle, Pt coating, for 88 deg. incidence

Figure 6.9: Theoretical diffraction efficiency for the Medium Energy and High Energy Gratings.



(a) High-res Medium Energy Grating (HRMEG): 1800 lines/mm, 4.85 deg. blaze angle, Ni coating, for 88 deg. incidence



(b) High-res High Energy Grating (HRHEG): 2600 lines/mm, 4.05 deg. blaze angle, Pt coating, for 88.25 deg. incidence

Figure 6.10: Theoretical diffraction efficiency for the High Resolution Gratings, optimized to be used in 3rd order.

Table 6.2: Predicted resolving power (RP, $E/\Delta E$) and grating efficiency (Eff) of the REIXS spectrometer at the emission lines of interest. Values are listed for all gratings where the emission energy lies within the detector's motion range. (Resolving power results are adapted from Reference [40].)

	1st Order Gratings								3rd Order Gratings			
	IMP		LEG		MEG		HEG		HRMEG		HRHEG	
	RP	Eff	RP	Eff	RP	Eff	RP	Eff	RP	Eff	RP	Eff
Si (92 eV)	4693	7.4%	2986	38.7%	10146	5.3%	15580	3.6%				
C (277 eV)	1722	29.1%	1032	3.8%	3646	19.6%	5752	6.7%	14066	4.7%		
N (392 eV)	1226	34.1%			2528	22.8%	4039	9.8%	10227	3.4%	16510	1.5%
Fe (725 eV)	731	23.4%			1588	17.7%	1595	12.2%	6238	0.9%	9468	2.1%

CHAPTER 7

CHARACTERIZATION: HOW WE MEASURED THE ACTUAL GRATING PERFORMANCE, AND ACCOUNTED FOR DIFFERENCES

In the previous chapter, we applied grating efficiency calculations to create and optimize the optical design of the REIXS emission spectrometer. After having the design reviewed by an external consultant, who confirmed our resolution and efficiency predictions [40, Chapter 5], we solicited bids from grating manufacturers and selected Bach Research to mechanically rule the six gratings. Finally, we passed the optical requirements over to a consulting engineer to design the mechanics of the spectrometer, which would be responsible for positioning the entrance slit, gratings, and detector, as well as achieving and maintaining ultra-high vacuum conditions throughout the beam path.

We lamented back in Chapter 5 the lack of published experimental comparisons of grating efficiency – particularly in the soft x-ray regime – and hypothesized that this was because beamline scientists, on receiving new gratings, were often eager to put them into their beamline and start commissioning, rather than spend more time characterizing them. Unfortunately – for us in our role as beamline staff – the construction of the REIXS spectrometer was delayed by a series of serious mechanical design flaws and oversights. Fortunately – for our interests in grating efficiency – this setback provided us with lots of time to characterize the ruling quality and real-world diffraction efficiency of our gratings. Even more fortunately, the characterization process alerted us to serious ruling errors with a few of the gratings, which would have dramatically affected the spectrometer’s resolution and efficiency had they not been discovered. In the end, our characterization of the gratings resulted in several beneficial

outcomes:

- We were able to contribute another set of experimental comparisons to theoretical grating efficiency calculations.
- We discovered a reason to be cautious when specifying nickel-coated gratings, despite nickel's apparently high reflectivity.
- We discovered a serious ruling problem in the HEG grating, which nearly eliminated its ability to diffract in the useful orders, and sent it back to the manufacturer for re-coating and re-ruling.
- We discovered substantial errors in the blaze angle (beyond the manufacturer's specified tolerance) for a few of the gratings; in the case of the HRHEG, the blaze angle was off by so much that we ended up using it as a temporary replacement for the HEG.

This chapter describes these results, based on atomic force microscope (AFM) measurements of the groove profile and soft x-ray diffractometer measurements of the actual grating efficiency. We also compare the calculated and measured grating efficiencies, and offer explanations for the differences.

7.1 AFM measurements of the manufactured grating profile

When we consider a grating like the HEG, with 2000 lines/mm and a blaze angle of 1.52° , it is clear that the physical size of the grooves is extremely small – these are tiny triangles about 500 nm wide and 13 nm tall. Measuring the physical geometry is therefore actually impossible with a visible light microscope.

Instead, we used atomic force microscopy (AFM), an extremely high-resolution technique for measuring the topography of a surface. It uses very sharp-tipped mechanical probe mounted on a piezo-electrically-controlled cantilever to “feel” the surface (Figure 7.1). The tip can either be dragged across the surface (*contact mode*) or electronically oscillated near its resonance frequency (*non-contact mode*) while measuring the change in amplitude, phase

and frequency caused by the tip-sample atomic interaction forces. In both cases, the accurate vertical position of the tip is measured with a laser beam reflected off the back of the cantilever – using either an interferometer or a deflection meter – and the horizontal position of the tip is scanned using piezo drivers. The resolution of the best atomic force microscopes is sufficient to image individual atoms on a surface, although for measuring soft x-ray gratings we only need angstrom-level accuracy.

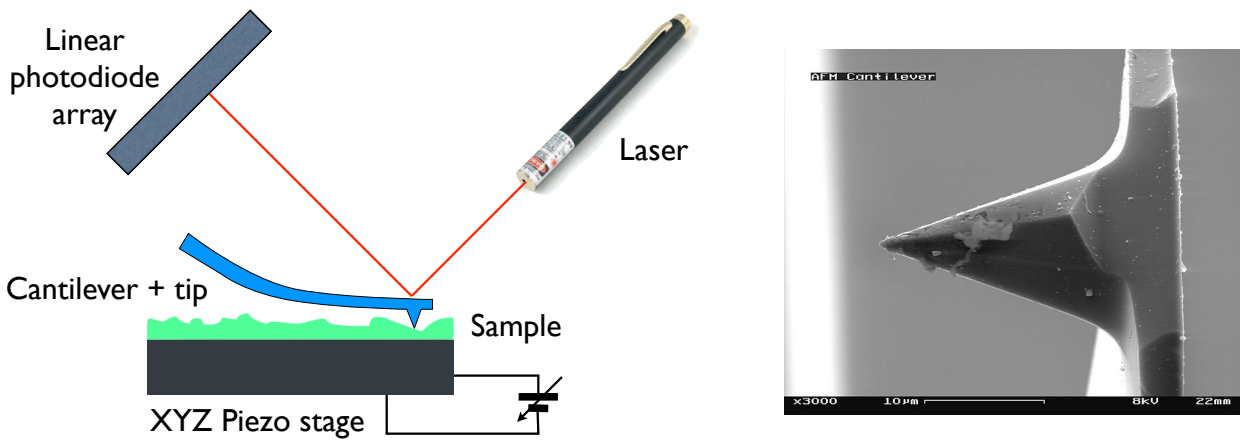


Figure 7.1: Schematic diagram of an Atomic Force Microprobe (AFM), and a Scanning Electron Microscope image of the tip, showing a radius of approximately 10 nm.

One limitation of AFM techniques is that it is easy to produce a two-dimensional map of the relative surface profile in arbitrary units, but difficult to accurately determine the absolute height. In order to measure blaze angles of gratings, we need to measure the height difference from the bottom to the top of the grooves in absolute units, which requires calibration of the AFM using a height standard. (Usually this is a gold mesh with an accurately-known wire size.)

After receiving the gratings from the manufacturer, we first imaged them using the AFM at the University of Saskatchewan Structural Sciences Centre (SSSC). However, we were not able to calibrate the z -axis for these measurements, so with the assistance of Dr. Eric Gullikson, we requested a complete set of measurements using the AFM at the Center for X-Ray Optics at the Lawrence Berkeley National Laboratory.

An example of an AFM scan is given in Figure 7.2, where we show both the two-dimensional image (top) and a cross-section of heights perpendicular to the grooves (bottom),

which reveals the groove profile. Although the grooves should be ideally uniform along their entire length, most of the AFM scans show profile variation across even one image (a distance of just a few micrometers). To determine the average profile shape and average blaze angle, we integrated the two-dimensional image across the groove direction. Since a single AFM scan only spans a few micrometers of the grating, we also need to be careful in extrapolating the results to the entire grating; therefore, we conducted multiple scans at the centre and the corners of the grating.

Figure 7.2 gives an example of the AFM output, for the LEG grating. We present groove profiles for all the gratings starting in Section 7.4, alongside a discussion of their effective diffraction performance.

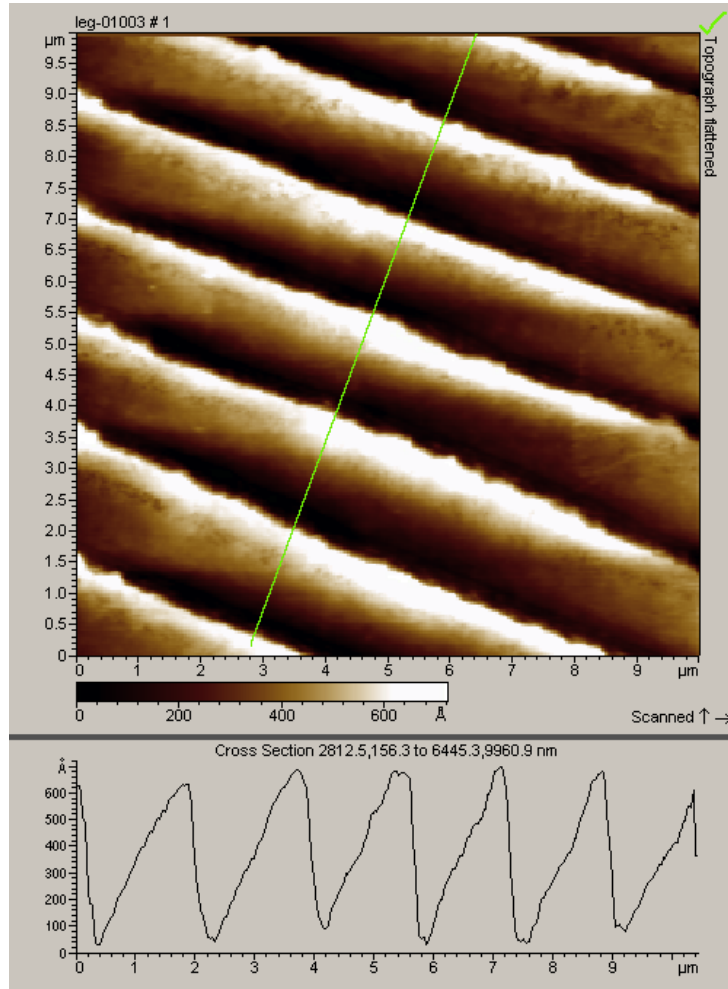


Figure 7.2: The Low Energy Grating has a smooth regular profile, shown in this example image measured using an Atomic Force Microprobe (AFM).

7.2 Diffractometer measurements of actual grating efficiency

To measure the actual grating efficiency, we used the reflectometer on the Calibration and Standards Beamline (6.3.2) at the Advanced Light Source. This beamline was designed specifically for testing the reflectivity of soft x-ray optical components like mirrors, thin films, multilayer coatings, and gratings. It consists of a bending magnet source, a VLS-PGM monochromator with a resolving power of 7000 (Figure 7.3), a higher-order suppressor, and a two-circle reflectometer (Figure 7.4). The beamline optics can focus the monochromator light to a small spot on the sample, or focus at infinite to generate parallel light [74].

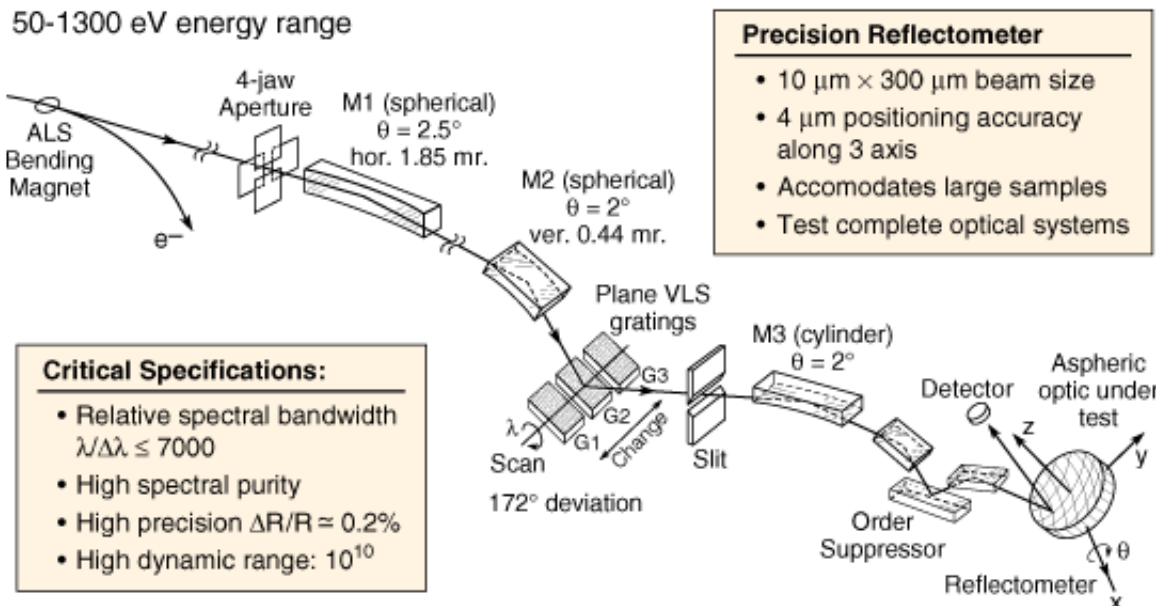


Figure 7.3: The Calibration and Standards Beamline (6.3.2) at the Advanced Light Source consists of a bending magnet source, a VLS-PGM monochromator with three selectable gratings, a higher-order suppressor, and a two-circle reflectometer shown in more detail in Figure 7.4. The curvature of refocussing mirror M3 can be adjusted to image the exit slit onto the sample, or to focus the light at infinite. Reprinted from Reference [11].

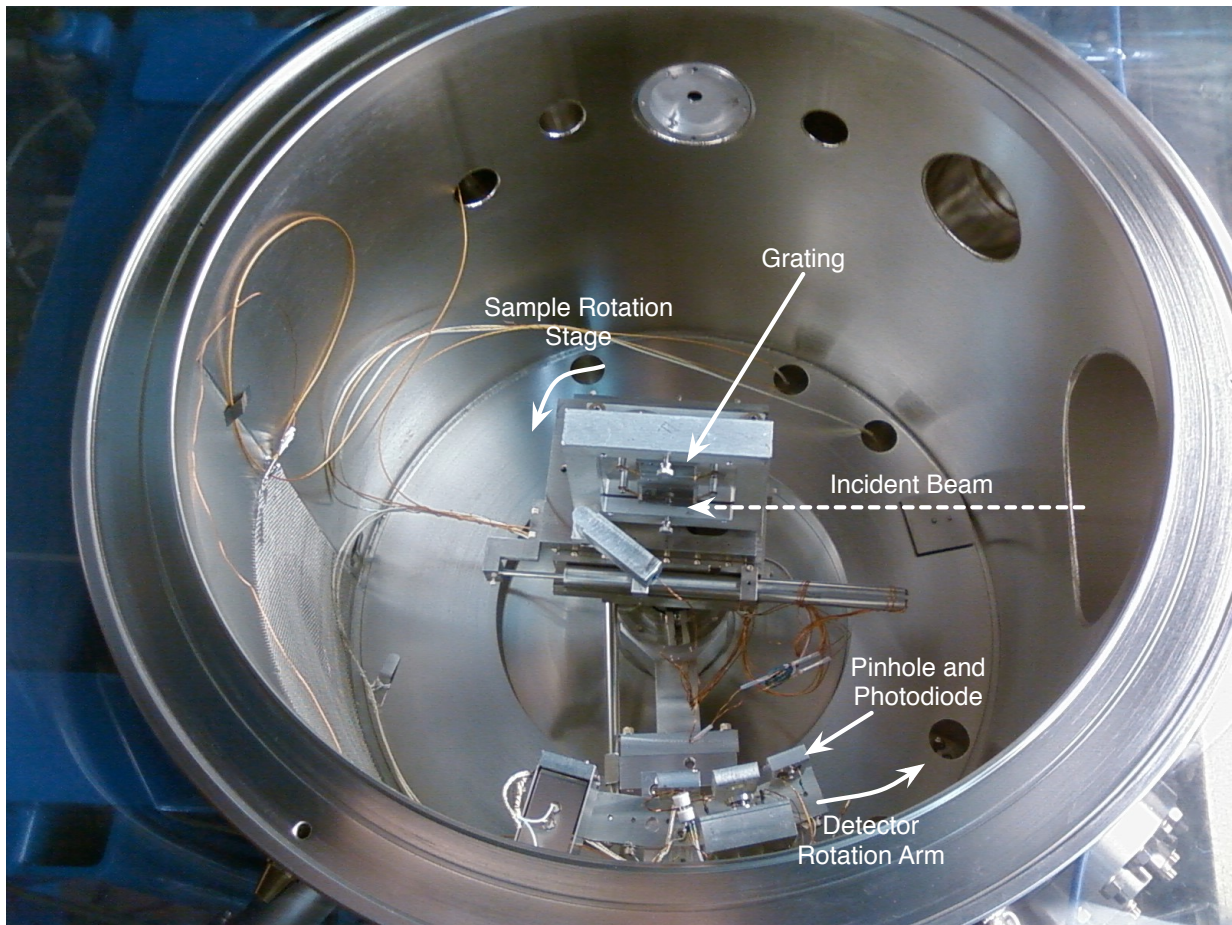


Figure 7.4: The reflectometer on Beamline 6.3.2 at the Advanced Light Source allows for independently setting the angle of the gratings in the beam, and setting the angle of a pinhole photodiode detector. Upstream, filters in the beamline are used to remove contamination from the higher-order light of the monochromator.

7.2.1 Beamlne 6.3.2 reflectometer

The purpose of the reflectometer endstation (Figure 7.4) is to measure the intensity of light reflected off a sample – in our case, a grating – as a function of both incidence and reflection angle. We used it to determine grating efficiency by positioning the grating at the intended incidence angle relative to the incoming beam, measuring the intensity at the angle of the outgoing order, and comparing this to the initial beam intensity. Upstream, the monochromator and order suppressor were used to produce the monochromatic incident beam and set its energy for each datapoint.

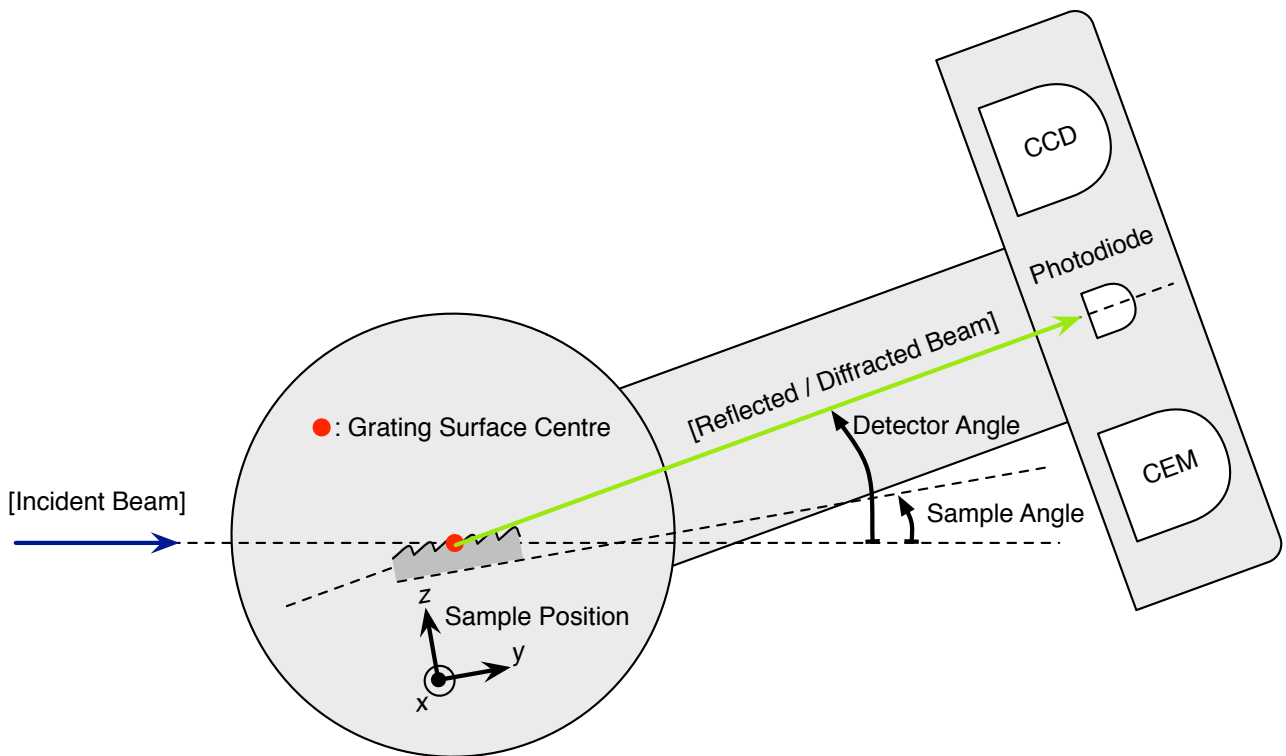


Figure 7.5: In the coordinate convention for the reflectometer, the sample angle is measured up from grazing incidence, and the detector angle is measured up from grazing incidence. The sample position stage (x , y , z) is mounted to the sample angle stage, so that the centre of rotation is always at the height of the beam.

Inside the reflectometer mechanics, a “two-circle goniometer” provided independent control over the angle of the sample and the angle of the detector arm, as well as providing precise

(4 um) positioning to align the sample in x , y , and z . (Figure 7.5 shows the coordinate system convention, with angles measured from grazing incidence or inline with the beam; the “0 degree” sample position would place the grating at perfect grazing incidence, while the “0 degree” position for the detector would capture the incoming beam when unobstructed.) The sample holder could accommodate samples up to 200 mm in diameter, which allowed us to mount two of our gratings side-by-side at once. The detector arm contained a Hamamatsu gallium arsenide photodiode, a channel electron multiplier (CEM, or “channeltron”), and a CCD camera. For all of our grating measurements, we used the photodiode covered by a 2 mm pinhole.

7.2.2 Diffraction experiment procedure

Diffraction efficiency measurements are easily susceptible to a variety of systematic and unintentional errors. The following sections describe in detail the procedure we used for measuring the grating efficiency, and how we dealt with sources of error.

Grating Alignment

To achieve correct incidence angles and accurate detection angles, the grating had to be aligned correctly. In the z -direction (Figure 7.5), the centre of the grating surface had to coincide with the centre of sample rotation, which was also aligned to the height of the beam. In the x -direction (parallel to the grating grooves), the beam had to land on the centre of the grating; otherwise the curvature of the grating would introduce a slope in the saggital direction, and we would end up with conical mounting.

1. To crudely align the grating in the z -direction, the grating angle was set to zero degrees, and the CCD camera was placed at a detection angle of 0 degrees. With the sample moved fully down out of the way in z , this allowed the beam to shine past the grating directly onto the centre of the CCD, confirming the alignment of the beam angle.
2. The grating was then moved upward in z until it just started blocking the beam from reaching the CCD detector, indicating that the surface was now at (or just above) beam height.

3. With the grating blocking the CCD detector in this position, it was translated in x until light returned, indicating that the beam had fallen off the side edge of the grating. This was repeated in the $(-x)$ -direction, providing us with the position of the opposite side; the grating was then positioned midway between these two positions, achieving alignment in x .
4. To accurately complete the alignment in z , the grating was angled at two degrees, and the photodiode detector was positioned to collect reflected (0th order) light at four degrees. As long as the beam was incident on the grating, this would register a signal on the detector. The grating was then translated upward in z until the signal disappeared, indicating that the beam had fallen off the bottom edge of the grating. This z -position was recorded as the bottom grating edge.
5. The grating was then lowered in z until the signal disappeared again, indicating that the beam had fallen off the top edge of the grating. This z -position was recorded as the top grating edge, and then the grating was moved to the average of the two recorded z -positions; this process ensured that the beam was now incident on the exact centre of the grating.

Scanning modes

All of the efficiency plots we calculated in Chapter 6 to predict the REIXS gratings' performance show efficiency as a function of photon energy. We wanted to show our real-world measurements in the same format, which required us to scan the monochromator energy while measuring the intensity of the desired order with the photodiode. Therefore, the detector angle had to change as we changed the monochromator energy, according to the outgoing angle specified by the grating equation (3.19).

If we had known the groove density with high accuracy, we could have calculated the correct diffraction angle and positioned the detector simultaneously while scanning the monochromator energy. However, for brand new gratings, it would be unlikely for the groove density to end up exactly as requested from the manufacturer; in this case we would actually need to conduct a two-dimensional scan: for every photon energy datapoint, we would need to

conduct an angular scan of the photodiode to find the diffraction peaks.¹

For four of the gratings, we did have an accurate groove density, obtained from Power Spectral Density (PSD) measurements taken by the metrology lab at the Canadian Light Source. However, for two of the gratings, the exact groove density was unknown, so we had to use the two-dimensional scan method. Mechanically, this is the simplest way to operate the reflectometer, and an example of the results are shown in Figure 7.6. The procedure was as follows:

1. The monochromator was set to the desired photon energy, and the corresponding filters were selected in the higher-order absorber.
2. The grating was positioned at its specified incidence angle relative to the beam, as it would be during operation of the spectrometer.
3. The photodiode was scanned, recording intensity as a function of outgoing angle.
4. The grating was moved out of the way of the beam, and the photodiode was placed at zero degrees to measure the direct beam intensity; this intensity value was used to normalize the data as described later in this section.
5. The results (Figure 7.6) show the intensity of reflected light as a fraction of the incident beam intensity, as a function of detector angle. The 0th order, 1st order, and 2nd order peaks are clearly seen; we can quickly check that the 0th order peaks show no wavelength dependency and occur at twice the incidence angle. The grating efficiency in the n th order is taken from the height at the centre of the n th diffraction peak.

This time-consuming procedure had to be repeated for every photon energy datapoint that we wanted to test. For the gratings where the groove density was known accurately, we used a more expedient method, which required synchronized scanning of the detector angle and monochromator energy:

¹After completing this scan, we could use the angular position of the diffraction peaks to calculate the actual groove density, but only within a precision determined by the angular extent of the 2mm photodiode pinhole.

1. The higher-order suppressor was configured for the energy range of the scan. (This limited each individual scan to the valid energy range of a single higher-order filter; see Section 7.2.3)
2. The control software was configured to move the detector angle in tandem with the monochromator energy to stay on top of the diffraction peak, using the grating equation and the specified groove density and order.
3. The monochromator energy and the detector angle were scanned together, recording the intensity of the diffracted order at each datapoint.
4. The grating was then moved out of the way of the beam, and the detector angle was set to zero degrees to measure the direct beam. The monochromator energy scan was repeated to measure the incident intensity as a function of energy, to use for normalization (see ‘Normalization’, below).
5. An example of the normalized results is shown in Figure 7.7. They directly show the intensity of diffracted light in the specified order as a fraction of the incident beam intensity, as a function of energy. With this method, it is easier to measure a finely-spaced set of datapoints along the energy axis, to compare with our efficiency prediction plots in Chapter 6.

Wavelength calibration

The monochromator on Beamline 6.3.2 is slitless, therefore its absolute energy calibration is affected by the position of the beam in the ALS storage ring. To calibrate the energy axis of our data, we scanned the monochromator through the absorption edges of the higher-order suppression filters, and compared the onset of the edges with the published values for the binding energies of these elements:

1. For every new energy range, monochromator grating change, or storage ring refill, the sample was moved out of the way and the photodiode was placed at 0 degrees to measure the direct beam.

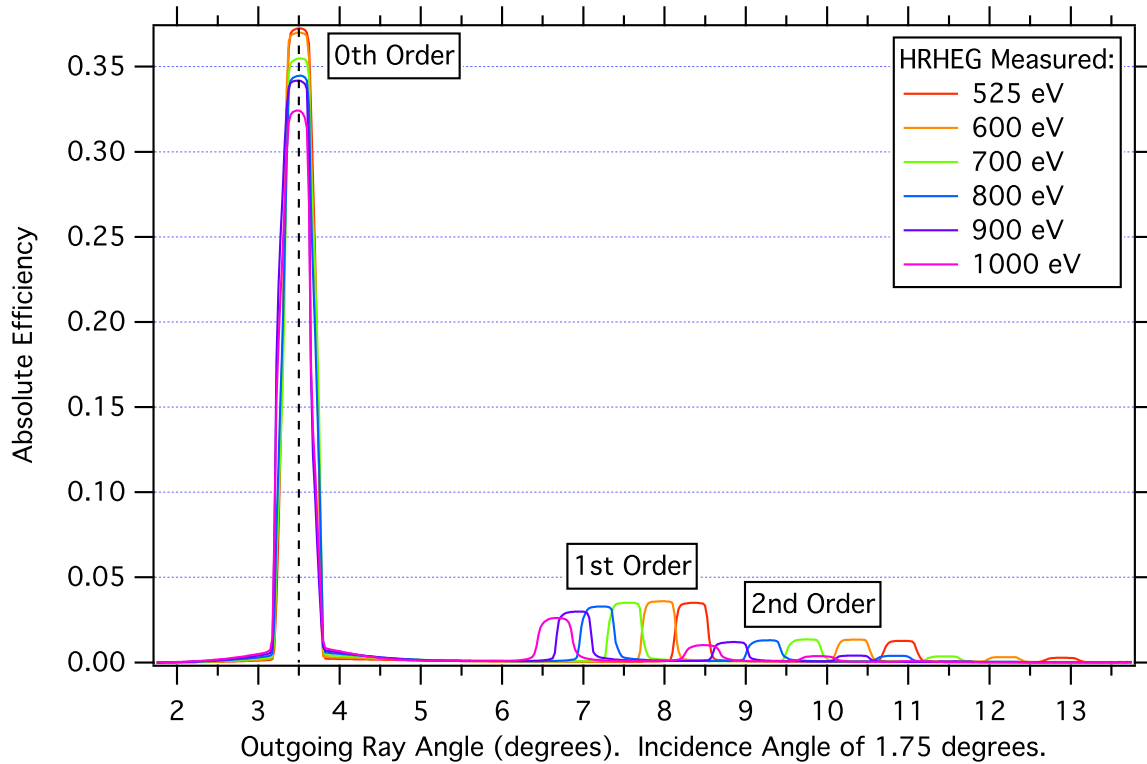


Figure 7.6: The simplest diffractometer experiment scans the detector angle while illuminating the grating with a constant photon energy. The diffraction orders are visible as peaks along the outgoing angle axis (measured up from the incident beam direction at 0°). The 0th order (reflection) peak is easily visible at 3.5° , or twice the incident angle (88.25° , or 1.75° from grazing). Grating: HRHEG.

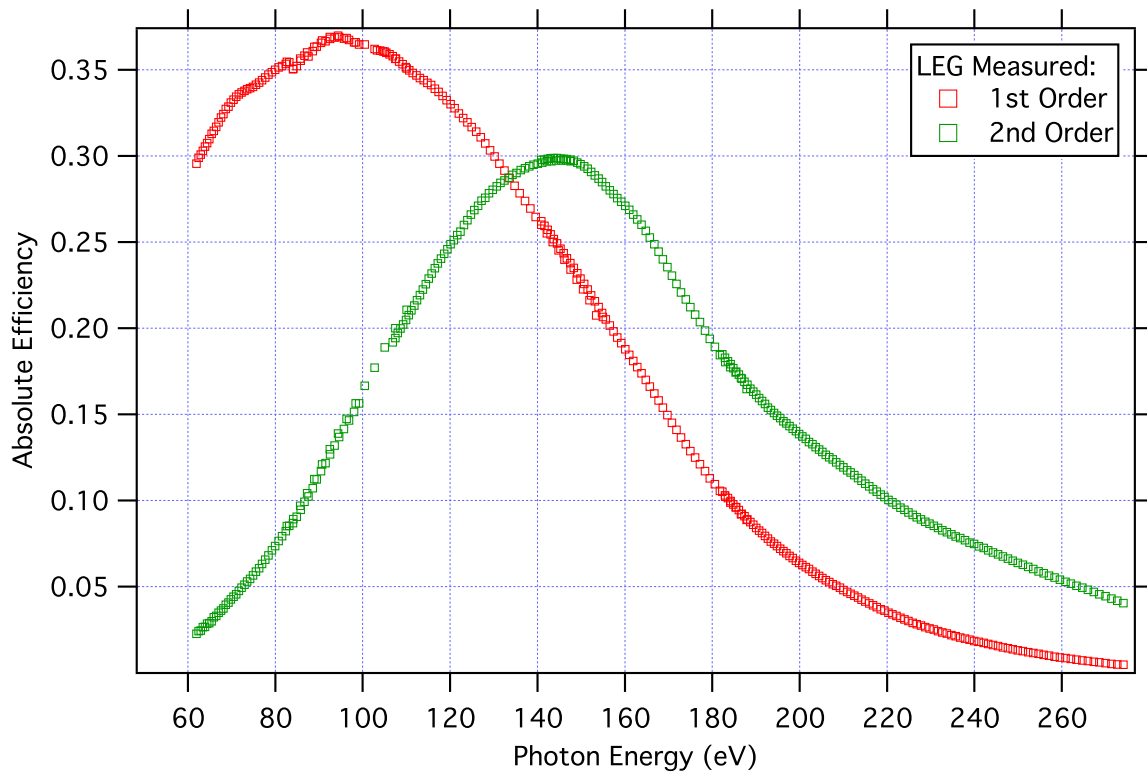


Figure 7.7: When the groove density of a grating is accurately known, the detector angle can be moved in tandem with the monochromator energy to keep it on the diffraction peak as the incident photon energy is scanned. This allows faster, nearly continuous efficiency measurements as a function of photon energy. (Grating: LEG)

2. The monochromator was scanned upward in energy through the onset of the nearest absorption edge of a filter placed in the beam path. (For example, prior to doing scans in the energy range from 82.6 to 112 eV, we installed the silicon filter and scanned across the Si *L*3 absorption edge, located at 99.42 eV.) Essentially, this amounted to measuring a transmission x-ray absorption spectrum of the filter element.
3. The wavelength shift of the onset of the absorption edge (in monochromator wavelength units) away from its theoretical position provided a correction offset that was applied to the wavelength axis for all scans in this range.²

Normalization

Chapter 3 defined grating efficiency as the ratio of the intensities of the *n*th order diffracted beam and the incident beam. In our measurement procedure (above), we used the photodiode to record the intensity of the reflected beam I_r , and subsequently the intensity of the incident beam I_i . The efficiency $e^{(r)}$ would then be

$$e^{(r)} = \frac{I_r}{I_i}$$

Using the same detector to measure both the reflected and incident beam eliminates error due to differences in detector sensitivity. However, because these measurements were not taken simultaneously, it is possible that the incident beam intensity would have changed in the interim; in fact, this would be virtually guaranteed due to decay of the storage ring current over time. Because the light intensity of a bending magnet beamline is proportional to the storage ring current J_{ring} , we can record the ring current at the time of each measurement, and use it to normalize the intensities:

$$e^{(r)} = \frac{I_r/J_{\text{ring},r}}{I_i/J_{\text{ring},i}}$$

Finally, as we identify in the following section, the dominant source of error in low-light photodiode measurements is the *dark current*: an intensity-independent signal from the

²The monochromator control software used wavelength units rather than energy units, so we conducted all of our efficiency scans in wavelength units and converted later from nm to eV, using the photon energy relationship $E = hc/\lambda$.

photodiode that increases with temperature due to thermal generation of electron-hole pairs. With the beam blocked, we measured the dark current I_{dark} for every gain setting of the photodiode, and subtracted this contribution from all measurements to determine the true intensity ratio:

$$e^{(r)} = \frac{(I_r - I_{\text{dark}})/J_{\text{ring},r}}{(I_i - I_{\text{dark}})/J_{\text{ring},i}} \quad (7.1)$$

We used Equation (7.1) to normalize all of the efficiency results in Section 7.4.

7.2.3 Sources of error

In the previous description of our procedure, we briefly mentioned the “higher-order suppressor”, the dark current, and the energy calibration. In this section, we take a look at all of the sources of error which could affect the grating efficiency measurements.

Higher-order contamination

A bending magnet source like the one on Beamline 6.3.2 produces light of all wavelengths, from infrared to hard x-rays; it is the responsibility of the monochromator to extract a single wavelength from this broadband input. The problem with grating monochromators, however, is that the grating equation cannot distinguish between equivalent products of n and λ : light with a wavelength of x nanometers diffracted in 1st order will leave at the same angle as $x/2$ -nanometer light diffracted in 2nd order.³ When both wavelengths are present in the monochromator input, this creates what is known as “higher-order contamination” in the output. Because the monochromator gratings are likely more efficient in 1st order than any other, the intensity of $x/2$ and $x/3$ -nanometer light will be comparatively lower than the desired wavelength, but it will still contaminate the mono output. If this higher-order light were to arrive at the grating under test, it would be diffracted again, introducing additional erroneous peaks into the detector angle scan. (Depending on the ratio of the monochromator and test-grating groove densities, these erroneous peaks could either overlap or fall beside the

³In terms of energy, photons with an energy of y eV will diffract in 1st order to the same angle as $2y$ -eV photons in 2nd order.

“true” diffraction peaks.) Therefore, reflectometry experiments require a method to eliminate this higher-order light before it reaches the sample.

Beamline 6.3.2 has two techniques for higher-order suppression. The first is a variable-incidence mirror with multiple sets of coating stripes. This design exploits the change in reflectivity as a function of incidence angle and energy that we saw (for example) in Figure 5.13. Depending on the desired wavelength, the mirror coating and grazing angle are chosen to provide high reflectivity at the desired wavelength, but significantly lower reflectivity at fractionally shorter wavelengths.

The second technique is a filter wheel containing a set of transmission filters from various elements which may be inserted into the beam path prior to the endstation. The filters are between 300 nm and 1 um thick, and are designed to remove 50% or more of the light at energies above the filter’s absorption edge.

Table 7.1 shows the mirror coating, mirror angle, and filter element that we used for higher-order suppression. The energy ranges of each mirror/filter combination (shown in the left column) restricted the maximum extent of each efficiency scan; for the efficiency results shown in Section 7.4, we have combined multiple scans together.

Monochromator energy calibration

The monochromator is approximately calibrated; entering a desired wavelength into the control software – for example, 2.73 nm – will align the mono grating to diffract light of approximately 2.73 nm out through the exit slit. However, the calibration is not perfect, and it is also affected by shifts in the ALS electron beam orbit position. Therefore, it is important to obtain an absolute wavelength calibration whenever moving to a substantially different wavelength range, changing monochromator gratings, or resuming scans after a storage ring refill.

As described in the procedure, we calibrated the wavelength axis of our efficiency scans (eventually, the energy axis) by conducting transmission absorption spectroscopy on the filter elements in Table 7.1. The difference between the monochromator’s apparent wavelength at the halfway height of the absorption edge, and the wavelength corresponding to the published binding energies for those elements, was used to generate a wavelength offset for nearby

Table 7.1: For higher-order suppression, Beamline 6.3.2 has a variable-incidence mirror and a set of transmission filter elements. The mirror coating, mirror angle, and filter need to be selected based on the energy range of the scan. (Mirror angles are measured from grazing incidence.)

Energy Range (eV)	Mirror	Mirror Angle (°)	Filter
62 - 99		10	Silicon
83 - 112	Carbon		Beryllium
103 - 155		8	Boron
141 - 188		6.2	
182 - 276	Nickel	8	Carbon
275 - 454			[None]
441 - 546			Chromium
544 - 775	[None]		Cobalt
751 - 932			Copper
898 - 1305			Magnesium

scans. (The monochromator's calibration might also suffer from errors which require linear and quadratic scaling corrections, but we assumed that a simple offset would be sufficient over the short length of these scans.)

Photodiode dark current

Photodiodes can be operated in a forward-biased (*photovoltaic*) mode, or in a reverse-biased (*photoconductive*) mode. When used as sensitive detectors of light intensity, the photoconductive mode is almost always used, because it offers faster response times and a linear response to light intensity over many orders of magnitude. In this mode, a reverse bias is applied and – in the absence of light – only a small *dark current* flows through the diode, due to the thermal generation of electron-hole pairs in the $p - n$ junction. When light strikes the $p - n$ junction, incident photons create electron-hole pairs which are swept across the junction by the reverse bias, and create an intensity-dependent *photocurrent*. The total current through the photodiode is measured by a sensitive current amplifier.

The dark current depends on temperature, and slightly on the magnitude of the reverse bias voltage. (In our instrumentation, the reverse bias was affected by the gain setting of the current amplifier.) To account for this, we measured the dark current at every gain setting with the beam turned off, and then subtracted this in the normalization equation (7.1). The dark current measurements were conducted after the diode had been operating under reverse bias for some time (and hopefully had reached operating temperature). Since the dark current increases with temperature, it is possible that exposure to extreme intensity would heat the detector and change the dark current contribution; however, this effect should be negligible for the low intensities observed in our experiment.

Saggital tilt of the grating

The reflectometer mechanics enable the intended rotation of the sample (grating) around the x -axis in Figure 7.5. If the grating surface were tilted away from normal incidence around the y -axis – either due to an offset in the grating mount, or due to the curvature of the grating combined with incorrect alignment in the x -direction – light would be reflected out of the $y - z$ plane. This would create the “conical mount” situation we assumed we could avoid

modelling in Chapter 3, and would also cause the diffracted beam to partially or completely miss the 2 mm pinhole of the photodiode detector. Both of these effects would reduce the observed intensity from what we would expect.

The zero-order alignment test we described in the procedure confirmed that with the grating positioned at 2 degrees, a substantial current was observed on the photodiode at 4 degrees, indicating that a substantial amount of light was staying within the plane of incidence. However, we cannot confirm that the alignment was flawless, and it is possible that the measured efficiencies are lower than they would be under perfect alignment.

Limited beam spot size

The Beamline 6.3.2 optics focus the beam to a spot size of 0.010 mm x 0.3 mm on the grating. Because the grating needs to be aligned on the centre of rotation, there can only be one position for the beam on the grating, and so we could only test the efficiency at this point. If there is variation in the groove profile across the grating, the illuminated part of the grating may not actually be representative of the average efficiency.

It is impossible to overcome this limitation; even if it were possible to fully illuminate the grating, the grating curvature would not be correct to focus the diffracted beam to the same size on the detector as the incident beam would be. Therefore, a small beam size is a necessary compromise to minimize the focussing effect of the grating.

7.3 Real-world grating effects

The comparisons between the predicted and measured efficiencies for each grating are discussed in Section 7.4, and impatient readers might have already beat us there. However, before looking at the results, it might be useful to consider some of the factors that could cause a discrepancy between the two. If there are differences between the predicted and measured efficiency, this would imply one – or more – of three distinct possibilities:

1. That the measurement procedure, due to experimental error, did not measure the actual grating efficiency.

2. That the theory and calculation method do not correctly describe the gratings they attempted to model,
- or,
3. That the real-world gratings, as produced, are different from the ones we modelled.

We dealt with the first possibility in the previous section on sources of error. Before accepting the second possibility, we take a look at some of the ways manufactured gratings differ from ideal ones.

7.3.1 Stray radiant energy

For a perfectly periodic surface, the Rayleigh expansion in Chapter 3 showed that all of the light propagating away from a grating leaves as plane waves in discrete orders. Regardless of the groove shape, no light leaves except at the angles given by the grating equation (3.19). In real-world gratings, deviations from perfect periodicity lead to *stray radiant energy* (SRE), which is a general term for all radiation that leaves at other angles [63]. From conservation of energy, the more SRE that exists, the less energy there is in the desired orders, and the lower the grating efficiency. SRE also affects the resolution of a grating instrument, by increasing the background noise level and contaminating the outgoing angles with light of the wrong wavelength.

Stray radiant energy can be caused by micro-roughness of the grating surface, variation in the height or spacing from groove to groove, and other imperfections such as dust and scratches.

Surface roughness

The grating model in Chapter 3 assumed a perfectly smooth surface, given by the periodic profile $y_p = g(x)$ in Figure 3.1. Unfortunately, both ruling and coating processes invariably leave a certain amount of micro-roughness, shown exaggerated in Figure 7.8. When the surface is rough on the scale of the incident wavelength, it causes diffuse scattering, which is analogous to the diffuse (or non-specular) reflection that would occur off any rough surface. Because this phenomenon affects the entire area of the grating, diffuse scattering from surface

roughness is typically responsible for most of the reduction in real-world grating efficiency (compared to theoretical calculations).

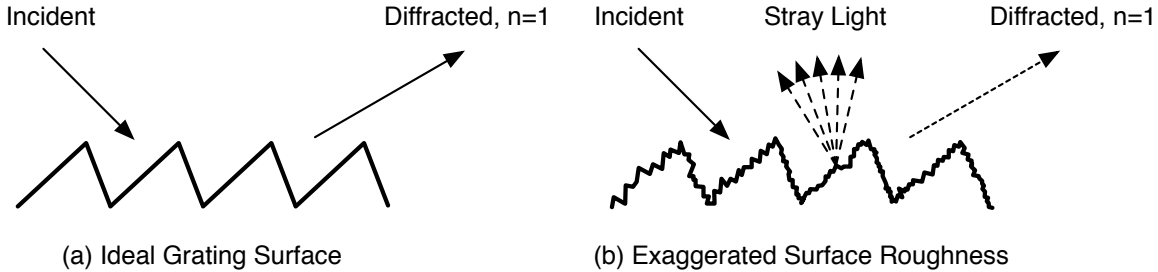


Figure 7.8: Roughness of the grating surface scatters stray light outside the diffraction orders. Typically, surface roughness is responsible for most of the reduction in real-world grating efficiency, compared to theoretical calculations.

Although it might not be clear from Figure 7.8 – which is two-dimensional – diffuse scattering need not be constrained to the plane of incidence. The roughness creates slope variation in both x and z , so scattered light could end up anywhere in the hemisphere above the grating. However, in-plane scattering is stronger than out-of-plane scattering by a factor of $1/\cos\theta$ (where θ is the incidence angle from normal). Therefore, at grazing incidence, the in-plane scattering is dominant [67].

To correct the predicted grating efficiencies for scattering, we need to understand two things:

1. The amount of energy lost to scattering, as a function of roughness, wavelength, incidence angle, and diffraction order.
2. The angular distribution of the scattered intensity. Does it affect all diffraction orders the same way?

Given the randomness of the surface structure, we need statistical methods to answer these questions. Statistically, the surface roughness is characterized by σ , the root mean square (RMS) variation in height from the nominal plane, and by the power spectral density (PSD) function, which describes how the height variation is distributed in frequency.

Even for the simpler (non-grating) case of roughness on flat surfaces, a substantial amount of research has only succeeded in producing a murky swamp of approximate models. In

Reference [14], Elfouhaily and Guerin categorized 260 references – 177 since 1980 – into 30 different methods, before concluding that “there does not seem to be a universal method that is to be preferred systematically. All methods present a compromise between versatility, simplicity, numerical efficiency, accuracy and robustness, with a different weighting in these various fields. [...] No approximate model has fulfilled all listed criteria.”

Even though they only deal with nominally flat surfaces, all of these methods are based on the assumption that a random rough surface can be decomposed into a superposition of sinusoidal gratings⁴, and that scattering can be explained as a diffraction effect from the phase changes created by the “microtopography” of the surface [59]. There are two fundamental approaches: the Rayleigh-Rice theory [61] [62], which is a perturbation approximation for solving the electromagnetic vector wave equation near periodic interfaces, and the Beckmann-Kirchhoff theory, which uses a scalar wave equation and applies the Kirchhoff diffraction formula [3, Chapters 4 and 5]. Both contain approximations; the Rayleigh-Rice methods are only applicable to “smooth” surfaces, where the perturbation from a flat surface is small – i.e., where the RMS roughness is small compared to the wavelength ($\sigma \ll \lambda$). The Beckmann-Kirchhoff methods are appropriate for “rougher” surfaces up to ($\sigma \cos \theta \leq \lambda$), but they contain a small-angle approximation that restricts them to near-normal incidence and scattering angles [59]. (In the extreme case where the roughness is much larger than the wavelength, it becomes more appropriate to handle it using a geometric optics approach, rather than a diffraction approach. In this situation, we can imagine a surface made up of many “microfacets” all reflecting light at different angles; the BESSY raytracing software suite actually uses this approach to model roughness by randomly varying the direction of a mirror’s normal vector (slightly) for each reflecting ray, according to the statistical description of the surface [66].)

Since grating theories are already being used to describe diffuse scattering from rough *flat* surfaces, applying these methods to *actual* gratings is even more difficult; this amounts to creating a superposition of (very high density) gratings, *on the surface of another grating*.

It would be theoretically difficult to analyze “gratings structured on top of gratings”, so instead, we apply some of the results for rough mirrors to come up with an approximate

⁴Obviously, in our case, of much higher groove density than the actual gratings!

correction for our grating efficiencies. Many texts and computer programs use a simple expression called the “Beckmann factor”

$$R' = R \exp \left(- \left(\frac{4\pi\sigma \cos \theta}{\lambda} \right)^2 \right) \quad (7.2)$$

to approximate the reflectivity R' of a real mirror, where R would be the reflectivity of an ideally smooth surface. However, this is subject to the small-angle approximation in the Beckmann approach, and predicts that the reflectivity is essentially unchanged when approaching grazing incidence due to the $\cos^2 \theta$ term in the exponential.

Based on the x-ray-specific work of Sinha et. al. [71], the X-ray Data Booklet [73] gives a correction factor of

$$R' = R \exp \left(- \left(\frac{4\pi\sigma}{\lambda} \right)^2 \sin \theta \operatorname{Re} \left[\sqrt{n^2 - \sin^2 \theta} \right] \right)$$

where n is the complex refractive index.⁵ This was derived from the “distorted-wave Born approximation”, which uses a Rayleigh-Rice-like perturbation approach; it is far more accurate in the limit of grazing incidence.

By analogy from reflectivity (“fraction of incident light reflected”) to grating efficiency (“fraction of incident light reflected in order n ”), we have used the same factor to determine the form of the roughness correction to apply to the grating efficiencies:

$$e'_n = e_n \exp \left(- \left(\frac{4\pi\sigma}{\lambda} \right)^2 \sin \theta \operatorname{Re} \left[\sqrt{n^2 - \sin^2 \theta} \right] \right) \quad (7.3)$$

Since we do not have measurements of each grating’s RMS roughness, we used σ as a free parameter to attempt to fit the theoretical efficiencies to the measured efficiencies; the results are shown in Section 7.4.

Although we do use this mirror expression to correct our predicted efficiencies, it is important to note that roughness on gratings may actually cause different effects than roughness on flat mirrors. Reference [47, Section 10.1.1] reports that the diffuse scattering is not isotropic; within the plane of incidence, the intensity is stronger at angles near the diffraction orders

⁵Reference [73] lists the complex reflection coefficient, instead of the reflectivity. Compared to the expression given there, we have converted from grazing incidence angles to normal incidence angles, and multiplied by the complex conjugate to determine the reflectivity.

than it is between orders. Reference [69] analyzes scattering specifically from gratings, and indicates that the intensity of scattering increases as the fourth power of the energy. Reference [31] looks at sinusoidal gratings illuminated by coherent visible light, and confirms that surface roughness increases the background light level. Finally, Nevot and Croce provide another comprehensive study of rough gratings [44], and come to a result consistent with Sinha et. al. (7.3), although through a different method.

Figure 7.9 shows the reduction in efficiency caused by different amounts of roughness, over the range of soft x-ray energies. These were calculated at grazing incidence using the Sinha approach and a refractive index for platinum. We can observe that they decrease very quickly at high energies / low wavelengths, but this is actually outside the limit of their validity: the Sinha approximation is only valid for RMS roughness much smaller than the wavelength. The Beckmann (7.2) and Sinha (7.3) factors are compared in Figure 7.10 at a grazing angle of 87° ; because of the small-angle approximation, the Beckmann curves show almost no reduction even for substantial roughness.

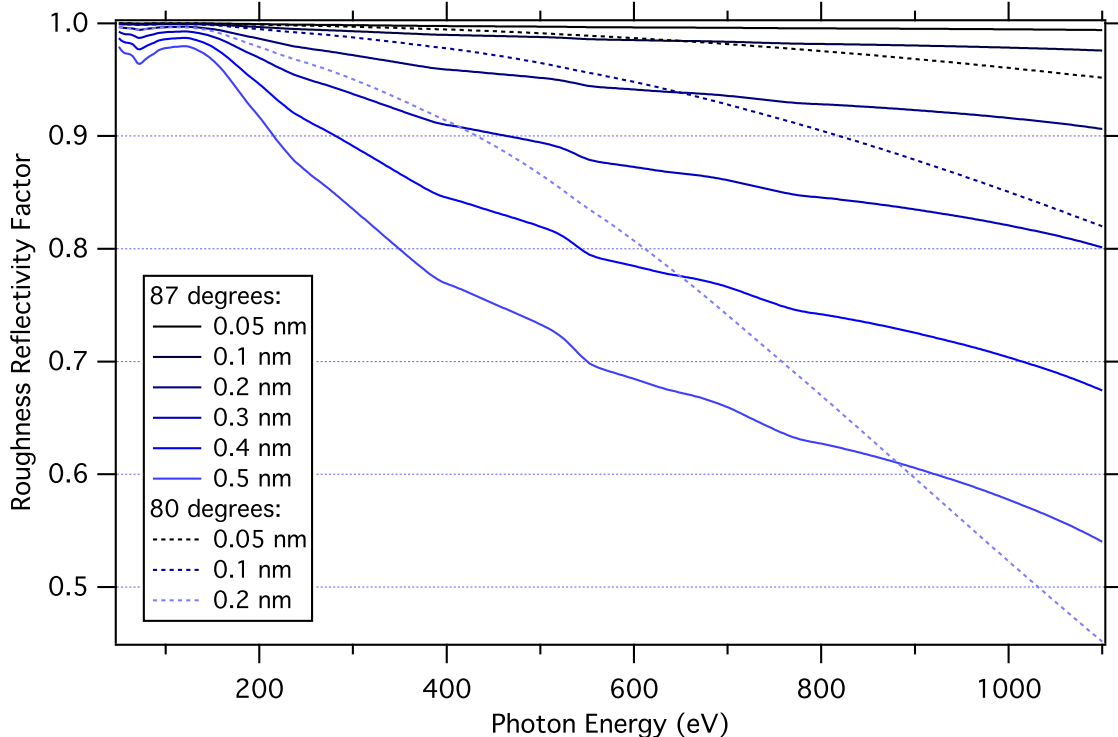


Figure 7.9: The reflectivity factor calculated according to the Sinha expression (7.3) as a function of incidence angle and photon energy, assuming a refractive index of platinum.

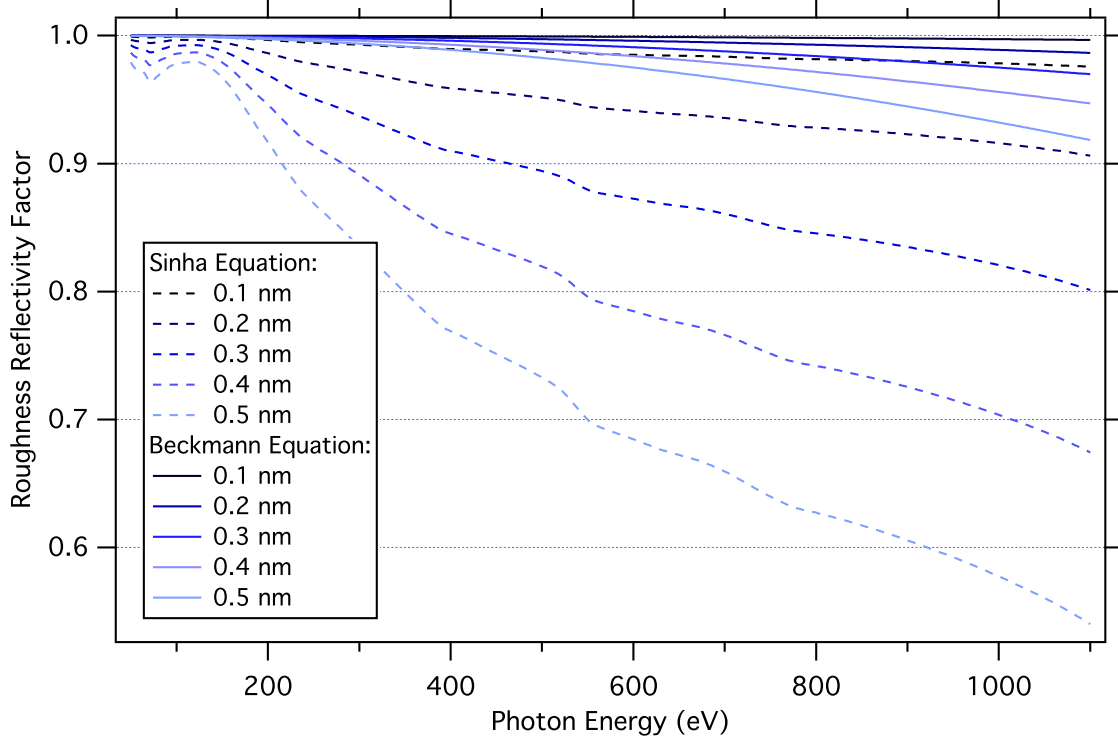


Figure 7.10: A comparison of the Beckmann (solid) and Sinha (dashed) expressions for rough surface reflectivity shows the limitations of both approximations. (The RMS roughness σ is indicated in the legend; the calculations are for 87° incidence assuming a refractive index for platinum.) The Sinha curves incorrectly decrease quickly at high energies (low wavelengths) due to the assumption that $\sigma \ll \lambda$. The Beckmann curves show very little reduction even for substantial roughness because the $\cos(\theta)$ term in the Beckmann Equation is only valid near normal, not grazing incidence.

If these reflectivity approximations are reasonable, they reinforce how important it is to keep the roughness low during manufacturing. Our AFM measurements suggest that re-coating the grating after ruling adds to the roughness, due to the granular nature of the evaporated coating. Due to extensive manufacturing experience, gold coatings are usually the smoothest to apply – as was the case for our LEG. The subsequent platinum and nickel over-coatings on the remaining gratings resulted in a much rougher surface.

Dust, scratches, and pinholes

Dust, scratches, pinholes, and any other out-of-place bumps on the surface also contribute to the stray radiant energy. All of these features act as scattering centres and create diffuse light; we can easily confirm this for visible wavelengths (using our biological photodetectors) when looking at a dirty grating under bright light. Given the challenges of modelling statistically well-behaved surface roughness, we do not even attempt to model these purely random defects, beyond recognizing that they will reduce the overall grating efficiency and contribute to stray light.

Periodic irregularities of the grooves: ghost peaks

In the section on grating manufacturing (Section 5.1.1), we mentioned that periodic errors in the groove position or groove height will create “ghosts”: additional light intensity peaks superimposed over the desired diffraction pattern. This happens because the higher-order structure acts like a superimposed grating with its own periodicity. Just like the other causes of stray radiant energy, if these peaks are present, they will remove energy from the desired diffraction orders, and contaminate the resolution by directing light to the “right place at the wrong wavelength”.

Non-periodic irregularities of the grooves

When ruling a mechanical grating, changes in the elasticity of the metal will allow the tip to penetrate to different depths, causing random (non-periodic) variation in the groove depth from groove to groove. However, we assumed in Chapter 3 that the grooves were ideally periodic; this assumption is at the core of the differential method. Therefore, when the

shape varies across the grooves, it is impossible to model how this will affect the efficiency. Further calculations using the integral method – which does not assume periodicity – might help answer this question.

If the shape changes slowly across the grating, it might be appropriate to model the overall efficiency as the average of several representative gratings with different shapes. However, when the shape changes rapidly or randomly, this will reduce the ability of the grating to form regular interfering plane waves, diminishing the diffraction ability. This has been shown to create a continuous distribution of scattered light which increases as a function of $(1/\lambda^3)$ [69].

Irregularities along the groove: out-of-plane reflection

Another assumption from Chapter 3 was that the grating was invariant along the z direction of the grooves. The same elasticity changes can cause variation in the shape of the profile as the tip travels along the grooves. (This also occurs with holographic gratings, due to variation in the mean intensity of the interference pattern during exposure.) The z -variation can reflect light out of the plane of incidence, and the effect can be diffuse or specular [47].

7.3.2 Manufacturing errors that *can* be modelled

All of the previous real-world grating flaws – surface roughness, dust and scratches, periodic and non-periodic groove irregularities – represent deviation from the theoretical profile in Chapter 3 in ways that cannot be incorporated into the model without breaking our initial assumptions (Section 3.1.4). It is also possible for manufacturing errors to create deviation that we *can* actually model; the best example of this would be the difference between the requested and manufactured groove geometry.

Blaze angle errors shift the efficiency peak

Figure 5.15 showed how small changes in the blaze angle can significantly shift the efficiency peak. For mechanically-ruled gratings, the accuracy of the blaze angle depends on the persistence and perfectionism of the ruling engine operator, who must adjust the diamond tip

angle during setup through tedious trial-and-error. If, after manufacturing, the real blaze angle turns out to be different than what the customer specified, we can measure the true blaze angle using a calibrated AFM and re-calculate the theoretical efficiencies using a better approximation of the profile.

Alternatively, if calibrated AFM measurements are not available, we have determined that the shape of the measured efficiency spectra can provide a strong indication of the real blaze angle. Therefore, we can use a curve-fitting process to choose the best-fit blaze angle that matches the measured to the calculated efficiency curves. For example, using this technique we predicted a blaze angle of 2.0° for the MEG grating, before determining from AFM measurements that the real blaze angle was 2.04° . In Section 7.4, we discuss the fitting process and the blaze angle agreement for each grating.

The same technique can be applied to profiles other than blazed gratings; the first method works as long as the groove geometry can be measured. The second method becomes more time-consuming for profiles like trapezoidal gratings that have more than one adjustable parameter, but this can be accomplished using a multidimensional minimization.

Deviations from ideal groove shapes affect the efficiency spectrum

In both mechanically-ruled and holographic gratings, it is likely for the actual groove shape to differ from the ideal rectangular, blazed, and trapezoidal profiles we showed back in Figure 5.1. If we can determine the actual shape – for example, from AFM measurements – we can still model the grating accurately using the differential theory (as long as the profile is still periodic from groove to groove). Although the `Gradif` software only supports theoretical shapes, the arbitrary groove profile mode of the new PEG software can be used to model the exact measured shape. Figure 7.22 shows an example of an arbitrary profile extracted from measurements of the HEG.

Coating oxidation changes the reflectivity

An unintended consequence of using nickel coated gratings is the unavoidable formation of a thin oxide layer on the surface. We chose nickel gratings for the IMP and MEG with the intention of using them up to the nickel absorption edge near 850 eV. However, as is

obvious from the NiO reflectivity spectrum in Figure 7.11, we should have expected the oxygen absorption edge to significantly affect their efficiency after 543 eV. (Besides reducing the overall efficiency, this causes another problem for spectroscopists: when measuring an oxygen emission spectrum using this grating, the efficiency spectrum of the grating oxide will be superimposed on the actual sample measurement.)

While obviously undesirable to have in retrospect, the effect of a surface oxide on the efficiency can be easily modelled using a coating layer on top of a pure metal substrate. In Section 7.4 we show how a thin layer of NiO on Ni accounts for the measured efficiency of the IMP and MEG gratings, and we predict the thickness of the oxide layer using fitting.

To protect against the formation of a detrimental oxide, in the future we would request that the grating manufacturer evaporate a layer of MgF_2 immediately after applying the primary coating, before exposing the grating to air. In this case, the effect of the MgF_2 layer could also be modelled in the same way.

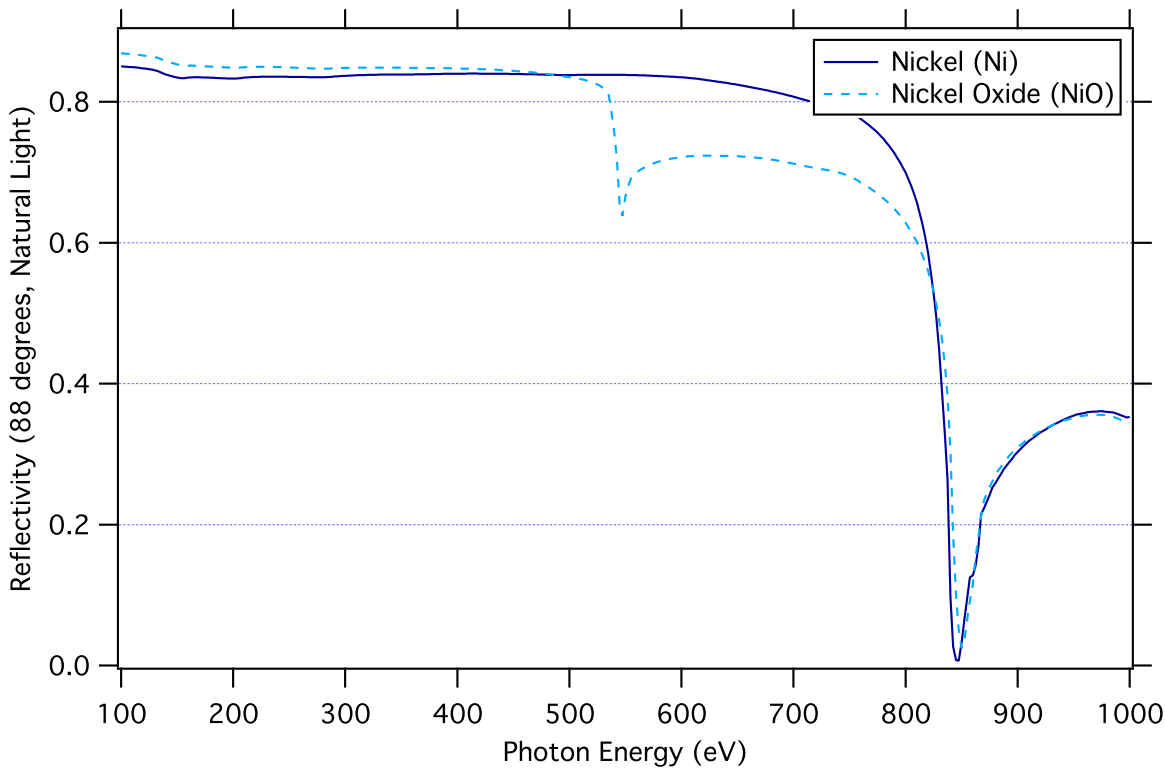


Figure 7.11: Unprotected nickel quickly forms a surface oxide of NiO, which significantly reduces the reflectivity at the Oxygen edge (543 eV)

7.4 Grating results, fitting, and comparison to theoretical efficiencies

We know that no grating can ever be manufactured exactly as specified, so we would expect the real-world efficiencies to be different than our predictions in Chapter 6. Is it possible, however, to account for the discrepancies using the differential method?

Given that we have (a) real efficiency measurements over a range of energies, (b) real measurements of the grating geometry, and (c) the ability to model arbitrary groove profiles, we wondered if it would be possible to use a fitting process to generate theoretical efficiency curves that match the measurements, and then compare the fitted parameters to the actual grating parameters.

In this fitting process, we started with fixed values for the parameters that could be measured exactly. The exact groove densities had been previously determined from power spectral density (PSD) measurements, and confirmed in the diffractometer experiments. We also took the incidence angles as given, since they were accurately known based on the diffractometer encoders. Because the blaze angles derived from the AFM measurements showed considerable variation from groove to groove and were subject to uncertainty in the z -axis calibration, we left these (and the anti-blaze angles) as free parameters in the fitting process. The oxide layer thickness for the Ni gratings and the surface roughness parameter σ in Equation (7.3) were also left as free parameters.

We note that a single efficiency measurement at a single energy would not enable this technique; we need an *efficiency spectrum* measured over a range of energies. The power of the fitting process comes from the fact that each parameter (groove density, incidence, groove geometry, etc.) affects the *shape* of the spectrum in a different way; the spectral shape acts as a “fingerprint” or “hash” of the grating parameters.

In general, we observed that although the shapes of the measured spectra are similar to the calculated curves, the measurements are always lower than predicted in absolute value. This is reasonable to expect, according to the number of real-world effects that act to reduce the efficiency: surface roughness, groove variation and irregularities, etc. Unfortunately, neither

the Sinha (7.3) nor Beckmann (7.2) expressions for roughness can describe this well on their own: both of them decrease too rapidly with increasing energy while providing negligible reduction at low energies, and the size of the required parameter σ ends up far outside the valid range for the Sinha approximation ($\sigma \ll \lambda$).

Instead, it seems that a *constant scaling factor* is required to achieve a good fit between the measured and calculated spectra. (Typical scaling values for our measurements are between 0.5 and 0.8.) Although we have described many factors that could account for the reduction, we currently do not have a rigorous physical derivation for this factor. If it is due to roughness alone, then neither the Beckmann nor Sinha factors are adequate for describing gratings. It is also possible that this could be a measurement effect; for example, focussing or dispersion of the diffractometer beam by the spherical grating on its way to the photodiode would change the apparent intensity; saggital tilt of the grating would cause some light to miss the photodiode.

Reasonable fitting results can be found by using the same scaling factor for the first-order and second-order efficiencies. However, much better agreement in the *shapes of the curves* is found using independent scaling factors for the first-order and second-order curves. Whether this is justifiable depends on the explanation for the scaling factor: both roughness and focussing effects could be affected by the outgoing angle and hence the diffraction order. We present the results for both methods, and summarize them in Table 7.2. It turns out that the process using independent scaling factors predicts blaze angles that agree very closely within error of the AFM estimates. For the nickel coated gratings, it also predicts lower oxide thicknesses than using a common scaling factor.

7.4.1 Low Energy Grating (LEG)

The LEG was one of the easiest gratings to manufacture, due to its low groove density and lack of a secondary coating. It was ruled directly into a layer of gold on the surface of the substrate, and the AFM measurements (Figure 7.12) show a clean triangular profile at the centre of the grating. However, the estimated actual blaze angle based on AFM measurements at the centre of the grating is $2.45^\circ \pm 0.20^\circ$, a substantial difference from the nominal 1.85° we specified.

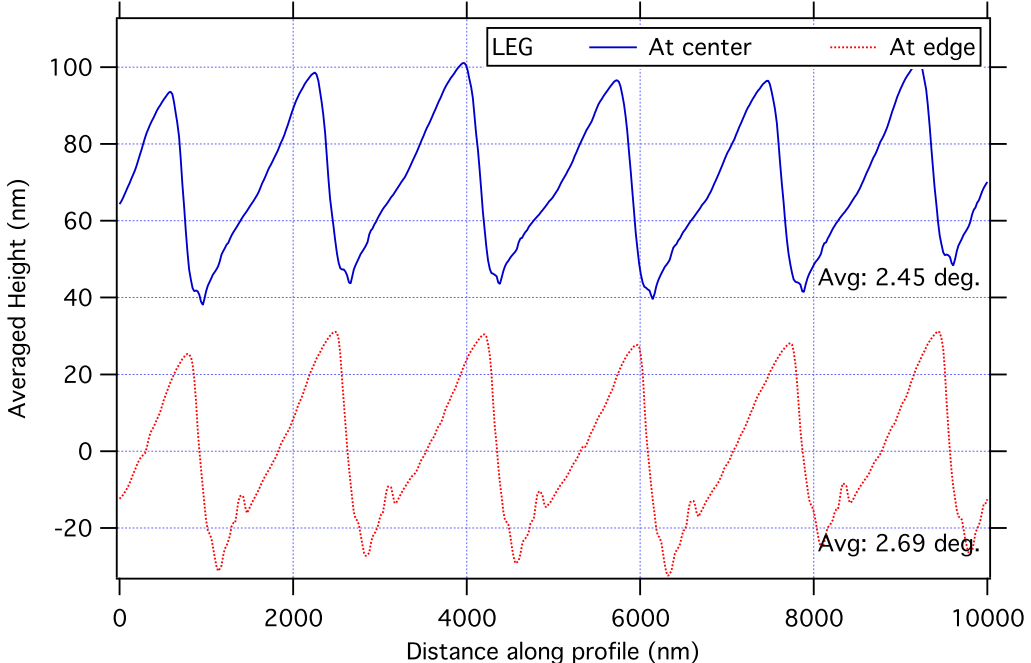


Figure 7.12: AFM measurements of the Low Energy Grating (LEG) profile, averaged along the grooves ($10 \text{ }\mu\text{m} \times 10 \text{ }\mu\text{m}$). The best-fit blaze angle at the centre of the grating is $2.45^\circ \pm 0.20^\circ$.

The effect of the blaze angle error on the measured efficiency is obvious in Figure 7.13: the locations of the efficiency peaks are shifted compared to the theoretical prediction for a nominal grating with 1.85° blazing. A higher blaze angle also increases the second-order peak efficiency at the expense of the first.

When we use a fitting process to match the theoretical curves to the measured efficiency, it predicts a blaze angle of 2.35° , using scaling factors of 0.93 and 0.84 for the first and second orders respectively. The agreement in the shape of the curves is very good (Figure 7.13), and the predicted blaze angle agrees closely with the AFM estimate (2.45°). The high scaling factors compared to the IMP and MEG gratings suggests a high smoothness; it makes sense that the over-coated gratings would be rougher than the bare gold.

If we insist on a common scaling factor for both first and second order, the fitting process predicts a blaze angle of 2.26° and a scaling factor of 0.95. We can see in Figure 7.14 that this reduces the agreement between the measured and fitted curves; it also provides a less accurate prediction of the blaze angle.

Although only a fraction of a degree, the blaze angle error causes a significant reduction

in real-world efficiency. At 140 eV, the theoretical and measured efficiency is less than 0.3, compared to the 0.4 that it could have been with correct blazing. Fortunately, this is still high compared to the other gratings and should be acceptable for all experiments.

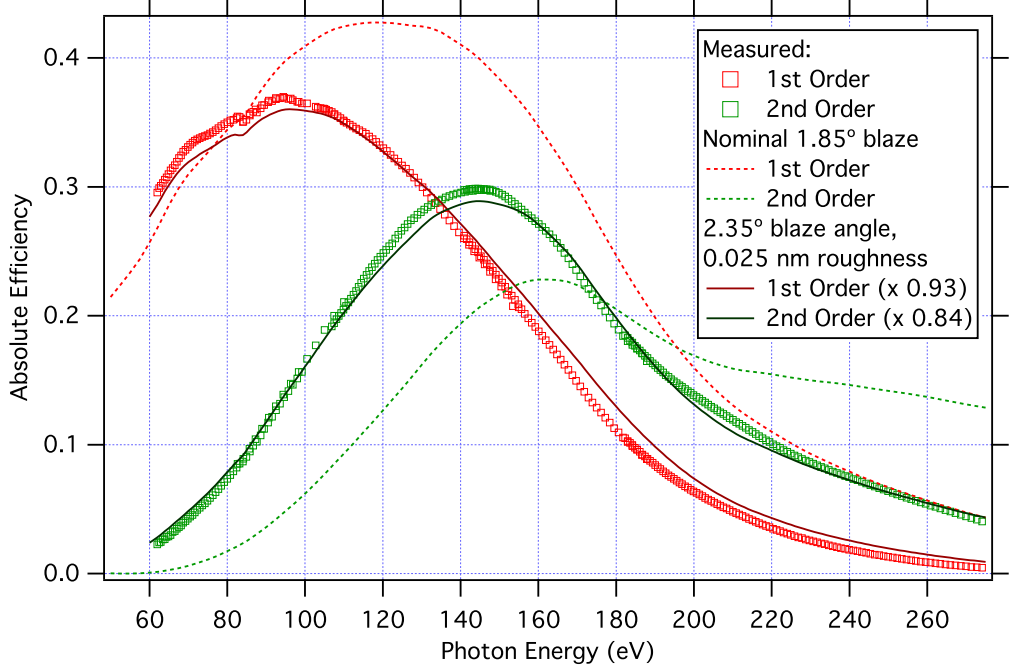


Figure 7.13: The blaze angle error of the manufactured LEG causes the efficiency peak to shift down in energy, and causes a transfer of energy from the first order to the second order. The fitting process predicts a blaze angle of 2.35° and an RMS roughness of 0.025 nm. (This assumes scaling factors of 0.93 and 0.84 for the first and second order respectively.) The predicted blaze angle agrees within error with the AFM estimate (2.45°).

7.4.2 Impurity Grating (IMP)

The AFM measurements of the impurity grating show clean facets on the blazed side (Figure 7.15), although once again the blaze angle is higher than specified: the best-fit angle at the grating centre is $1.60^\circ \pm 0.11^\circ$, compared to the nominal 1.11° . This is consistent with the LEG, which also overshot the nominal blaze angle by $0.4^\circ - 0.5^\circ$.

Originally intended to cover the range from 200 to 800 eV, the IMP suffers a noticeable drop in measured efficiency near 540 eV (Figure 7.16). It is easy to recognize that this occurs at the onset of the oxygen absorption edge (543 eV), suggesting an oxide layer on the surface. Fitting using a common scaling factor for first and second order predicts a blaze angle of

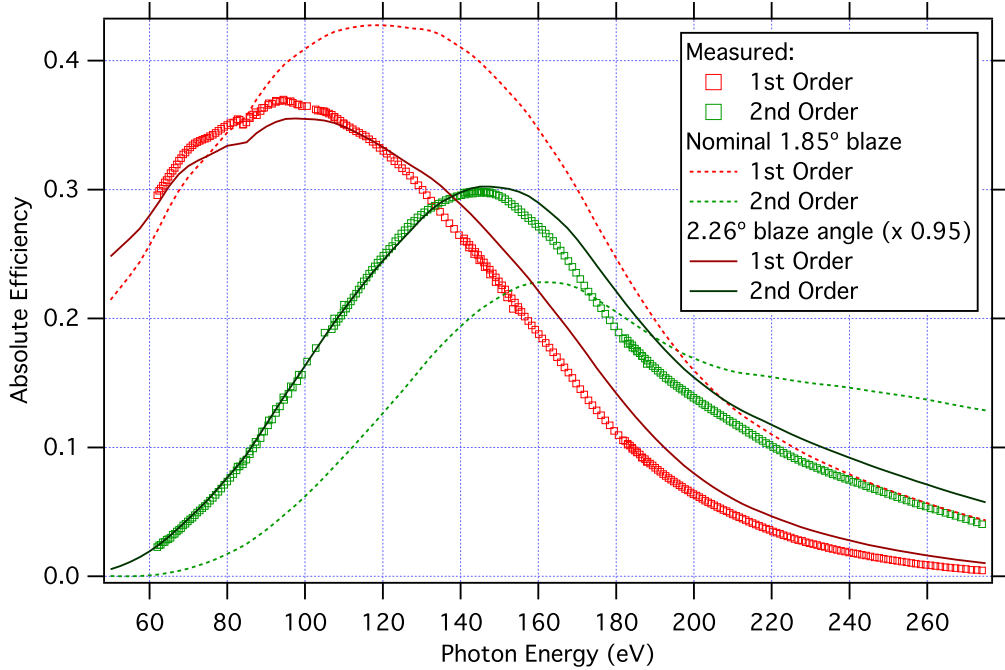


Figure 7.14: When using a common scaling factor for fitting the LEG, we predict a blaze angle of 2.26° and a scaling factor of 0.95. However, this method provides less agreement and a less accurate blaze prediction than using independent scaling factors (Figure 7.13).

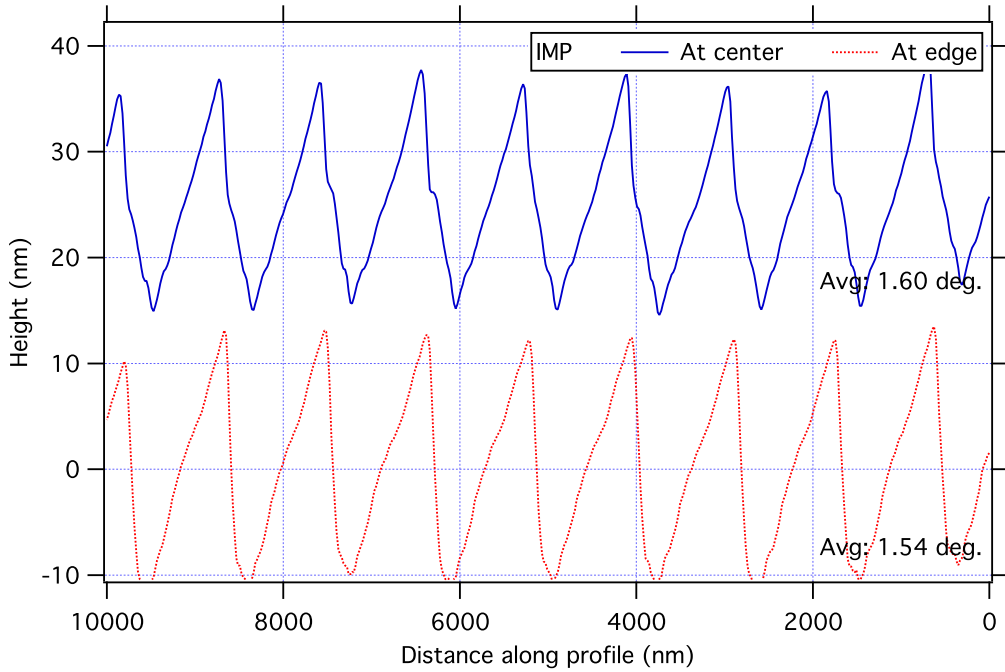


Figure 7.15: AFM measurements of the Impurity Grating (IMP) profile, averaged along the grooves ($10 \mu\text{m} \times 10 \mu\text{m}$). The best-fit blaze angle at the centre of the grating is $1.60^\circ \pm 0.11^\circ$.

1.4° , a scaling factor of 0.9, and a 7 nm coating of NiO on top of the Ni surface (Figure 7.17). However, the best fit to the shape of the curves comes from using separate scaling factors, and suggests that the measured spectrum can be explained by a blaze angle of 1.65° , a 5° anti-blaze angle, a 2.0 nm oxide layer, an RMS roughness of 0.5 nm, and scaling factors of 0.91 and 0.62 respectively (Figure 7.16). We have not found a way to confirm the oxide and roughness predictions, but the blaze angle predicted from fitting agrees closely within error of the AFM estimate (1.60°).

Another interesting observation is that we should not expect the Henke data to be accurate near the oxygen and nickel edges; however, the calculated efficiencies actually reproduce the fine structure visible in the measurements from 540 to 560 eV.

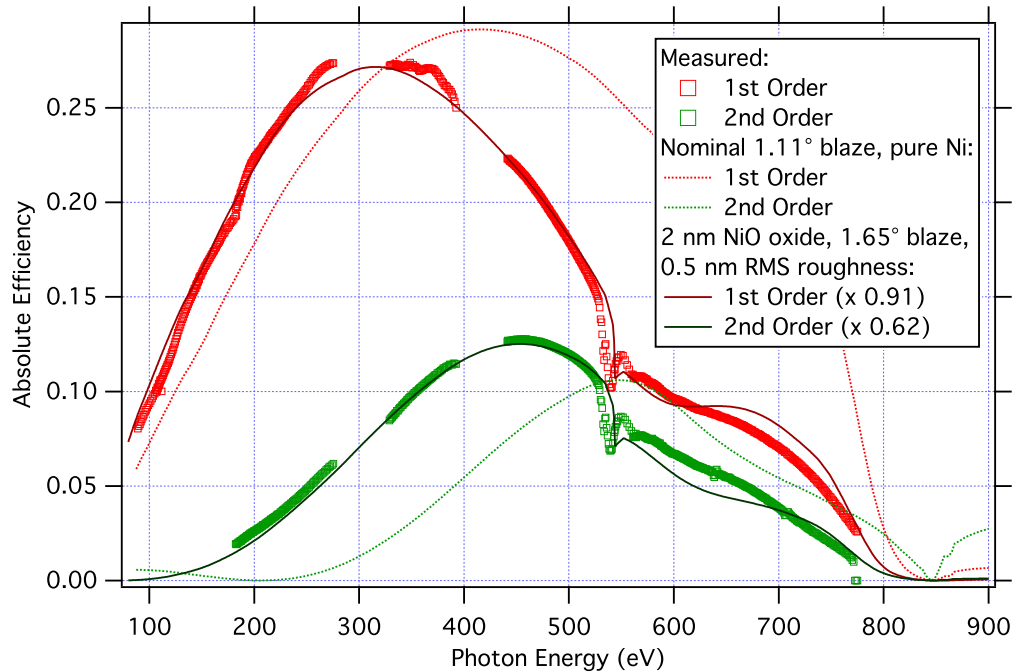


Figure 7.16: Theoretical and measured efficiency of the Impurity Grating (IMP). The best-fit theoretical curve predicts a blaze angle of 1.65° , an anti-blaze angle of 5° , a 2.0 nm oxide layer, and an RMS roughness of 0.5 nm. (This assumes that the first order calculated efficiency is scaled by 0.91, and the second order is scaled by 0.62.) The fitting prediction agrees closely with the AFM estimate of the blaze angle (1.60°).

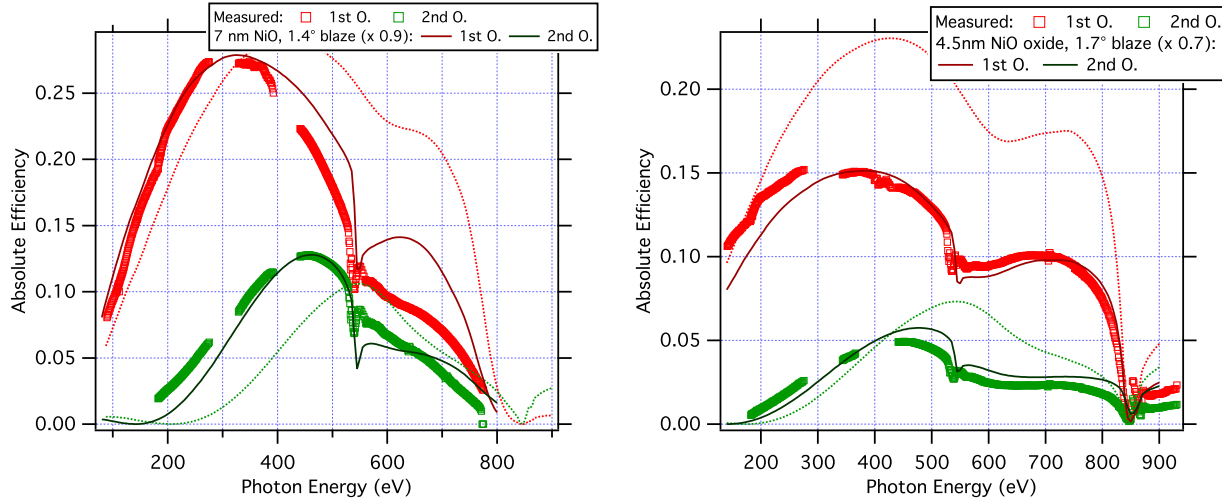


Figure 7.17: Using a common scaling factor for the first-order and second-order efficiency curves reduces the fitting accuracy and reduces the agreement between the predicted and AFM estimated blaze angles. For the impurity grating (left), this process predicts a 1.40° blaze angle, a 7 nm NiO surface layer, and a scaling factor of 0.9. For the MEG (right), it predicts a 1.7° blaze angle, a 4.5 nm NiO layer, and a scaling factor of 0.7.

7.4.3 Medium Energy Grating (MEG)

The MEG, with an increased groove density of 1200 lines/mm, shows a less regular surface than either the LEG or IMP. AFM measurements of the profile (Figure 7.18) estimate an average blaze angle of $2.04^\circ \pm 0.22^\circ$ at the centre of the grating. Again, this is consistently 0.5° higher than the nominal specification of 1.48° .

In efficiency, the nickel MEG suffers the same fate as its oxidized sibling. The measured efficiency (Figure 7.19) is further affected by the error in the blaze angle. The best-fit calculations predict a blaze angle of 1.95° , an NiO oxide layer of 1 nm, and scaling factors of 0.70 (first order) and 0.37 (second order). The lower scaling factors are attributed to the significant groove variation visible in the AFM profile compared to the smoother LEG and IMP. Again, the fitted blaze angle agrees closely with the AFM estimate (2.04°). A worse fit is obtained using a single scaling factor of 0.7, giving a 1.7° blaze angle and 4.5 nm oxide layer.

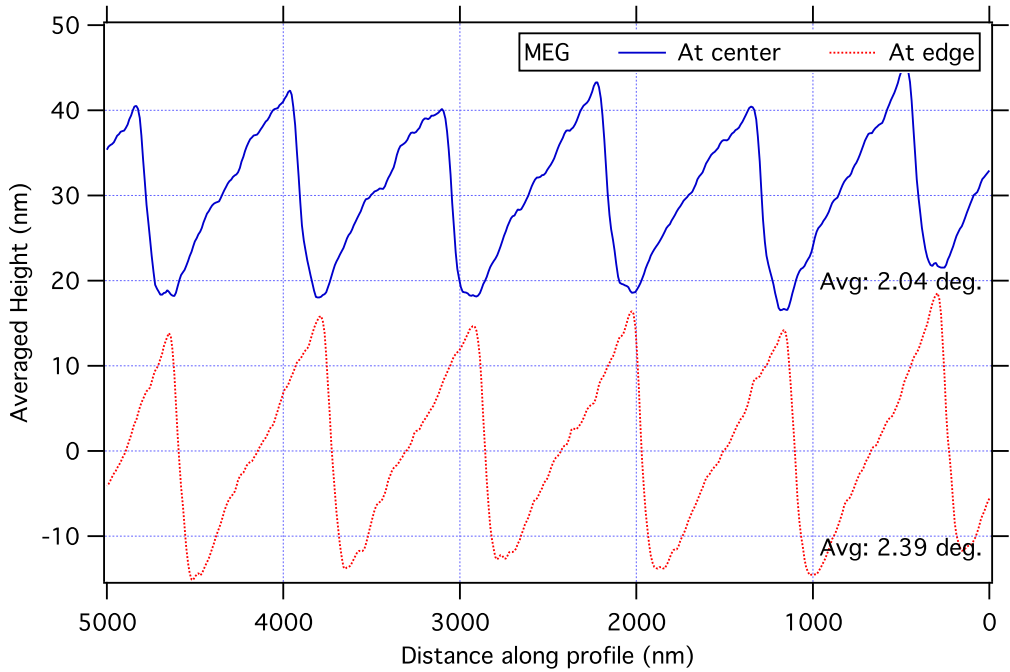


Figure 7.18: AFM measurements of the Medium Energy Grating (MEG) profile, averaged along the grooves ($5 \text{ }\mu\text{m} \times 5 \text{ }\mu\text{m}$). The best-fit blaze angle at the centre of the grating is $2.04^\circ \pm 0.22^\circ$.

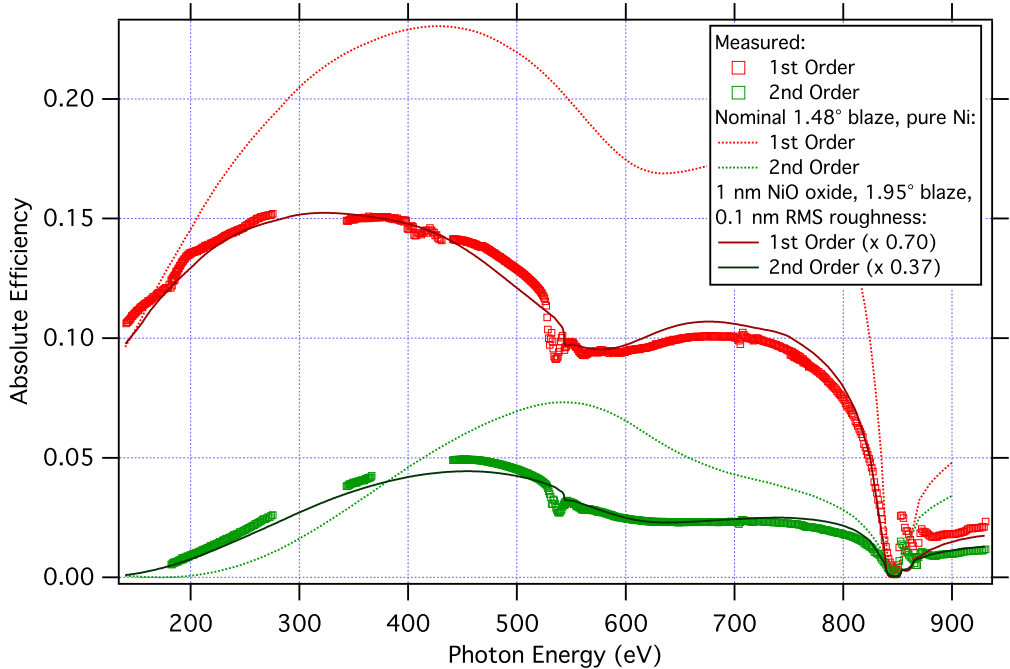


Figure 7.19: The real-world efficiency of the MEG can be explained by the fitting process, which predicts a blaze angle of 1.95° , an anti-blaze angle of 30° , a 1 nm coating of nickel oxide (NiO), and a surface roughness of 0.1 nm RMS. The scaling factors for first and second order are 0.70 and 0.37 respectively.

7.4.4 High Energy Grating (HEG)

When we measured the diffraction efficiency of the HEG grating, we were surprised to observe almost no diffraction in the first and second order (Figure 7.20); initially we thought we had mistakenly mounted it backwards in the diffractometer. On closer inspection, the diffraction peaks were found, but the measured efficiency spectrum is unusably low across the whole energy range.

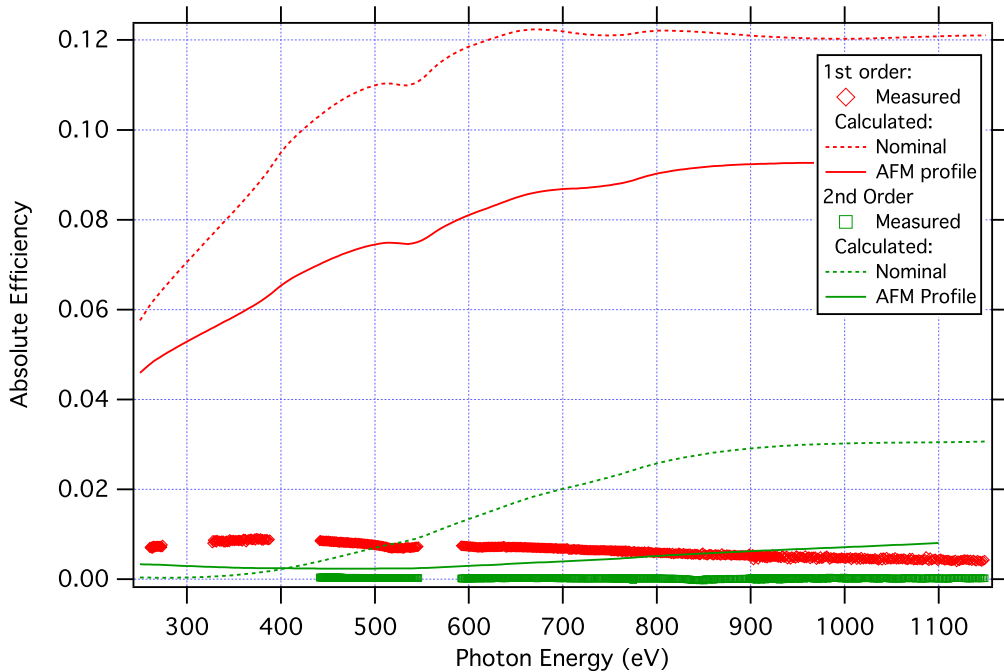


Figure 7.20: Theoretical and measured efficiency of the High Energy Grating (LEG). The solid theoretical curves were calculated using an arbitrary groove shape based on the AFM measurements (Figure 7.22). It cannot fully explain the reduction in real-world efficiency; therefore, we attribute the poor performance to groove-to-groove variation and scatter that we cannot model using the differential method.

What could have caused this? It is easy to see from the AFM measurements of the HEG (Figure 7.21) that something went very wrong in the ruling process. At the centre of the grating, there is a double-peaked structure, and the dimensions differ substantially from groove to groove. We know that the HEG blank was re-ruled after a previous failed attempt by the manufacturer, and we can hypothesize that some structure was left over from the first ruling.

This grating highlights the importance of careful characterization. In this form, the HEG

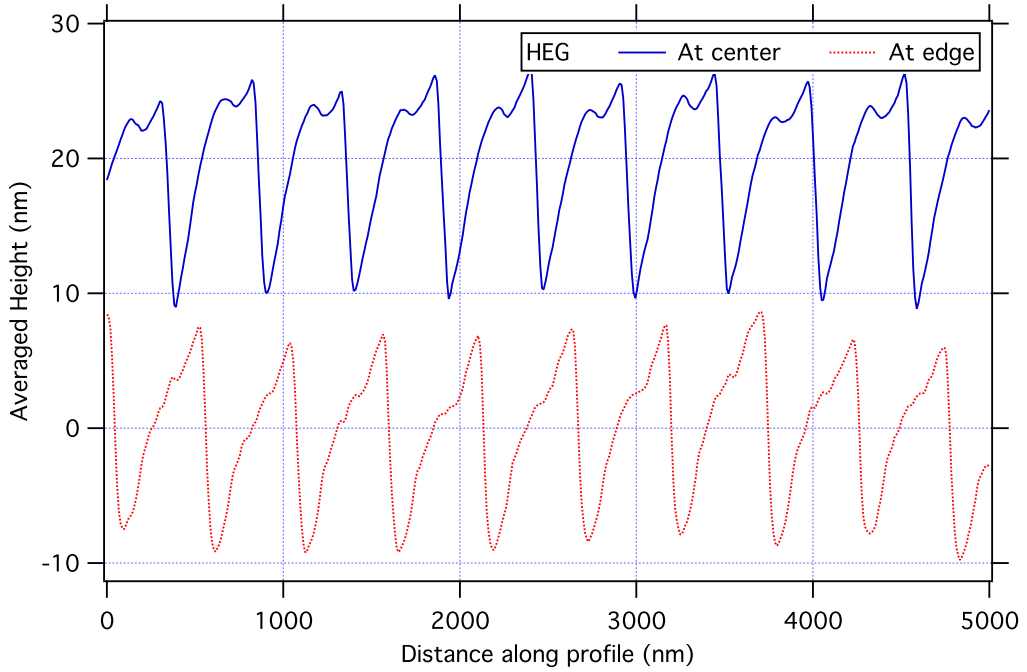


Figure 7.21: AFM measurements of the High Energy Grating (HEG) profile, averaged along the grooves ($5 \text{ um} \times 5 \text{ um}$). Severe ruling errors were apparent. The profile wasn't sufficiently triangular to attempt to fit a blaze angle, so we extracted one of the groove shapes to model as an arbitrary profile (Figure 7.22).

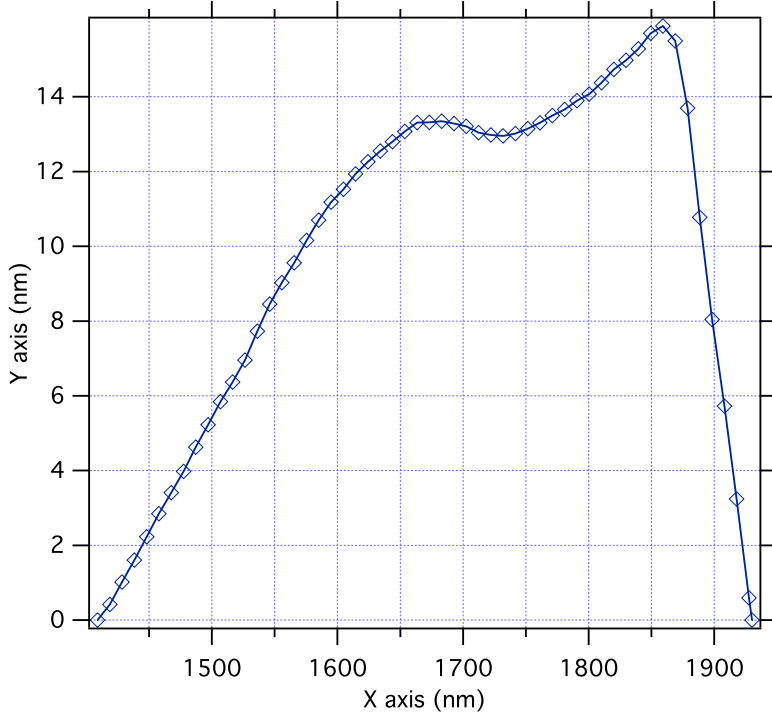


Figure 7.22: Representative profile used to model the real-world HEG, extracted from the AFM measurements in Figure 7.21.

would have been unusable.

Without efficiency and AFM measurements, we would have accepted and installed this grating in the spectrometer, only to be perplexed at the inability to detect anything other than scattered light. Instead, we were able to use this data to persuade the manufacturer to re-rule it one more time.⁶

Could the double-peaked shape of the HEG grooves be responsible for the poor efficiency? This question provided an opportunity to test out the arbitrary profile mode of the new PEG software. We extracted a representative shape from one of the AFM grooves (plotted in Figure 7.22) and used it to specify the set of (x, y_p) points for the profile function $y_p = g(x)$.

The efficiencies calculated using this groove shape are also shown in Figure 7.20. While the double-peaked shape does indeed reduce the theoretical efficiency compared to the nominal profile, it cannot explain the near-zero efficiencies that we measured. Instead, we attribute this to the strong non-periodic variation from groove to groove, which disrupts the formation of diffracting plane waves. (In the limit of complete random variation from groove to groove, the grating simply becomes a rough diffuse surface, scattering in all directions.)

Table 7.2: Comparison of actual and predicted grating parameters, using fitting to match the calculated efficiency spectra to the measured curves. The fitting process was done using a common scaling factor (CF) and independent scaling factors (IF) for the first- and second-order curves, and Equation (7.3) for the surface roughness correction. Using independent scaling factors provides the best agreement with the measurements and very accurate blaze angles compared to the AFM estimates.

	Blaze Angle (°)			Roughness (nm RMS)		Oxide Thickness (nm)	
	Fit (CF)	Fit (IF)	AFM Estimate	Fit (CF)	Fit (IF)	Fit (CF)	Fit (IF)
LEG	2.26	2.35	2.45 ± 0.20	–	0.025	N/A	N/A
IMP	1.40	1.65	1.60 ± 0.11	–	0.5	7.0	2.0
MEG	1.70	1.95	2.04 ± 0.22	–	0.1	4.5	1.0

⁶Coincidentally or un-coincidentally, the manufacturer also purchased their own AFM after this exchange. Currently we are still waiting for delivery of the final grating.

7.4.5 High resolution third-order gratings

The high-resolution third-order gratings (HRMEG and HRHEG) were also characterized using AFM and diffractometer measurements. Unfortunately, the diffractometer measurements were affected by an issue in the diffractometer control software that caused errors in the normalization. It might be possible to correct this problem with post-processing, but at the moment the full efficiency spectra are not ready for publication. We include summary results from the valid measurement points here.

HRMEG

The nickel-coated HRMEG has a measured third-order efficiency peak of 3.5%, but unfortunately the peak occurs at 500 eV instead of the 285 eV design energy. Like the other two nickel gratings, it shows fine structure and a serious decrease in efficiency at the oxygen edge (543 eV). AFM measurements of the HRMEG profile show a beautiful triangular structure (Figure 7.23); unfortunately the best-fit blaze angle is $4.43^\circ \pm 0.30^\circ$ at the centre of the grating. Unlike the other gratings, this is 0.4° *lower* than the nominal 4.85° we requested. Again, the blaze angle error explains why the measured efficiency peak is shifted compared to the nominal calculations, although in this case it shifts to higher instead of lower energies. The effect on the spectrometer performance is nearly a factor of two: instead of the $> 3\%$ third-order efficiency we could get at 285 eV with the proper blaze, we see only 1.5%.

HRHEG

The HRHEG was the most challenging grating to rule due to its extremely high groove density of 2600 lines/mm. As a result, we should not expect a very smooth profile. However, AFM measurements show that this grating is exceptionally far from meeting the blaze angle specification. Figure 7.24 reveals an extremely high blaze angle of $6.34^\circ \pm 0.28^\circ$ – more than two degrees higher than the required 4.05° . Since accurate blazing is essential for exploiting the third-order efficiency peak, it was unfeasible to use this grating in the role we originally designed it for: the third-order efficiency is less than 0.5% at 400 eV, and decreases to 0.28% at the design energy of 725 eV.

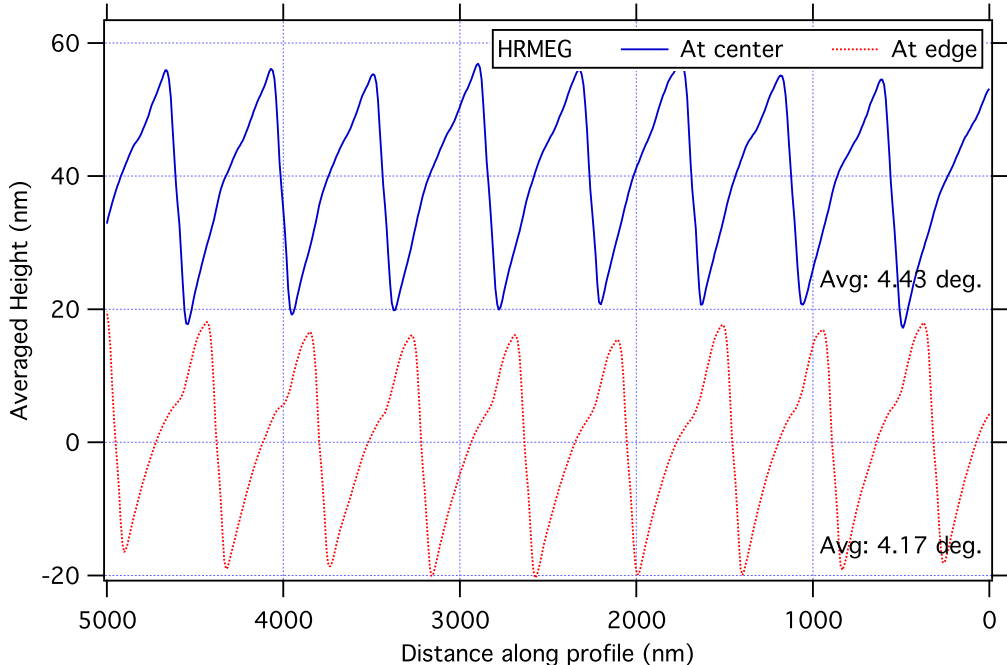


Figure 7.23: AFM measurements of the HighRes Medium Energy Grating (HRMEG) profile, averaged along the grooves ($5 \text{ }\mu\text{m} \times 5 \text{ }\mu\text{m}$). The best-fit blaze angle at the centre of the grating is $4.43^\circ \pm 0.30^\circ$.

However, this blaze angle error had an unintended but lucky consequence: it actually makes the HRHEG ideally blazed for *first order* operation from 400 eV to 900 eV. (Although the efficiencies are low due to the extreme groove density, it was measured to give 2% efficiency at 400 eV, and > 1% efficiency at 800 eV.) Simultaneously, the failure of the HEG left us lacking a general first-order grating to support experiments above 530 eV. Therefore, we had the idea to install the HRHEG in the spectrometer as a temporary first-order HEG replacement until the manufacturer was done re-ruling the actual HEG. Fortunately, the manufacturer also had a spare blank (substrate) for the HRHEG, so they could proceed with ruling another copy of it as well. This example again highlights the value of careful characterization from an engineering perspective.

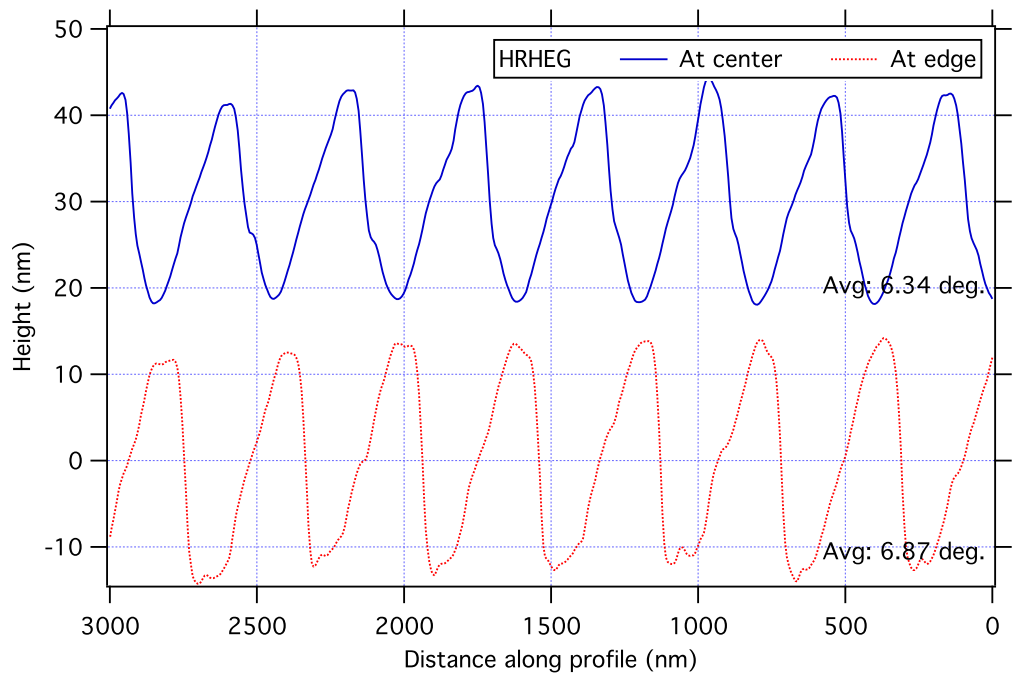


Figure 7.24: AFM measurements of the HighRes High Energy Grating (HRHEG) profile, averaged along the grooves ($3 \text{ um} \times 3 \text{ um}$). The best-fit blaze angle at the centre of the grating is $6.34^\circ \pm 0.28^\circ$.

CHAPTER 8

WHAT NEXT: REAL-WORLD RESULTS AND OPPORTUNITIES FOR FUTURE WORK

The famous Robert Feynman opened his 1965 Nobel Prize lecture by noting,

“We have a habit in writing articles published in scientific journals to make the work as finished as possible, to cover all the tracks, to not worry about the blind alleys or to describe how you had the wrong idea first, and so on. So there isn’t any place to publish, in a dignified manner, what you actually did in order to get to do the work...” [15]

In this chapter, we include enough early commissioning results from the REIXS beamline to show that the design process produced a promising, feasible spectrometer-in-progress. More importantly, however, we highlight the loose ends, blind alleys, and open questions that provide ongoing opportunities for future research.

8.1 Spectrometer assembly, commissioning, and preliminary results

After completing the optical design, we passed the requirements to a mechanical engineering firm to design the hardware that would position and interface all the spectrometer components. Unfortunately, the firm shut down its operations immediately after rushing an early version of their design into production. In addition to the grating manufacturing issues mentioned in Chapter 7, we had to correct many serious mechanical and system design flaws in the original assembly, which delayed the completion of the spectrometer by two years. The issues are too numerous to detail completely, and outside the scope of this thesis, but we highlight some major examples:

- The detector vacuum chamber, with a mass of approximately 1200 kg, is lifted vertically into position by a ball screw drive and motor. The ball screw was not equipped with a passive or active brake, so that loss of power to the lift motor would cause the chamber to instantly fall from the raised position (up to 1 meter). If this had occurred, it could have destroyed the detector hardware. More seriously, it posed a deadly hazard to users who could have been pinched or crushed if they were standing or reaching within certain regions of the machine.
- The six-axis kinematic positioning system for the gratings did not have sufficient range to manoeuvre all six gratings into their operating positions.
- The in-vacuum power supply and output signal cables for the detector were routed in a parallel bundle with unshielded stepper motor cables, causing electrical noise that swamped the actual detector signals. The high voltage cables were required to apply up to four kilovolts, but were only rated for two kilovolts.
- The original design required the detector's four-channel preamplifier to be sealed and placed in-vacuum beside the detector. However, the housing for the preamplifier could not maintain a positive seal. Instead, we created a miniaturized re-design of the preamplifier using modern surface-mount components, which could be sealed using a standard UHV tube and flange.

We also spent a substantial amount of time determining how to align the optical components and process the detector images. We developed processes and data acquisition software to

- focus the incident beam on the sample for maximum brightness,
- align all optical components for proper focussing of the detector image, as a function of energy,
- analyze the detector images, correcting for the curvature caused by the curved gratings and masking hot spots caused by light ionizing the detector housing,
- correct for non-linearity in the detector position sensing, and

- compute the scale for the spectrum energy axis based on the spectrometer geometry.

Refining these processes is an ongoing effort. However, in the spring of 2012, all of this work culminated in forming the first useful emission spectra from the REIXS beamline. In Figure 8.1, we show an example of the nitrogen K α emission line of hexagonal boron nitride (hBN), taken with the IMP grating. From the observed count rate, we calculated that the spectrometer has an end-to-end throughput approximately four to six times higher than the Beamline 8.0.1 spectrometer¹, with comparable resolution. This spectrum was developed in 20 minutes, producing 1892380 total counts.

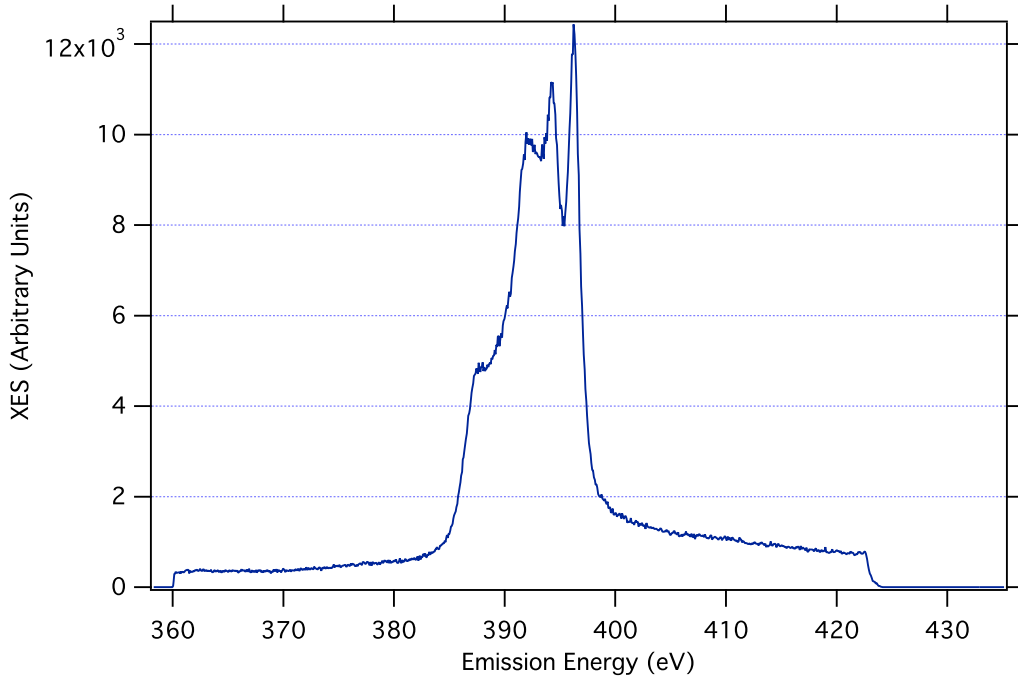


Figure 8.1: Nitrogen K α emission line of hexagonal boron nitride (hBN), taken using the IMP grating in 20 minutes. Total counts: 1892380.

Figure 8.2 shows the same spectrum measured using the medium energy grating. The emission line covers more of the detector window, offering the possibility for higher resolution. (The energy axis for this spectrum is in raw detector pixels instead of calibrated in eV.)

Using the HRMEG in third order should offer even higher resolution. However, the low efficiency of the grating requires long count times to develop even poor statistics (Figure 8.3).

¹Unfortunately, the upstream beamline produces substantially less flux than Beamline 8.0.1, so the efficiency difference is practically negated for users.

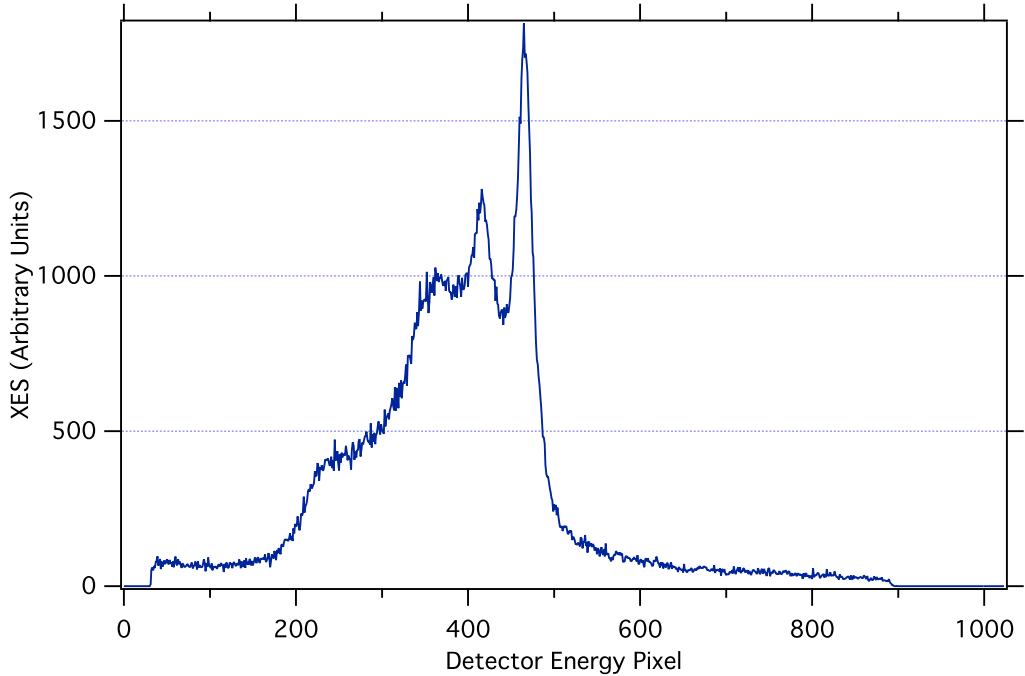


Figure 8.2: Nitrogen K α emission line of hexagonal boron nitride (hBN), taken using the MEG. It offers the possibility for higher resolution than the IMP (Figure 8.1) at the expense of efficiency. (The energy axis for this plot is not calibrated.) Total counts: 288792.

Over this time, thermal expansion of the machine due to room temperature cycles causes the detector's central energy to shift, which reduces the resolution.² Work is still ongoing to focus the spectrometer for operation with the HRMEG, as well as stabilize the room temperature.

8.2 Future work: confirmation and extension of the fitting process

We were surprised by the close agreement between the fitted and measured efficiency curves in Chapter 7. The strong agreement between the fitted and AFM blaze angles suggests that we might actually be able to use efficiency measurements to characterize the profile and surface structure of gratings, especially when these are difficult to measure directly. Several questions provide opportunities for future research:

²The temperature stabilization problem occurs with the other gratings as well, but becomes more significant at higher resolution and longer count times.

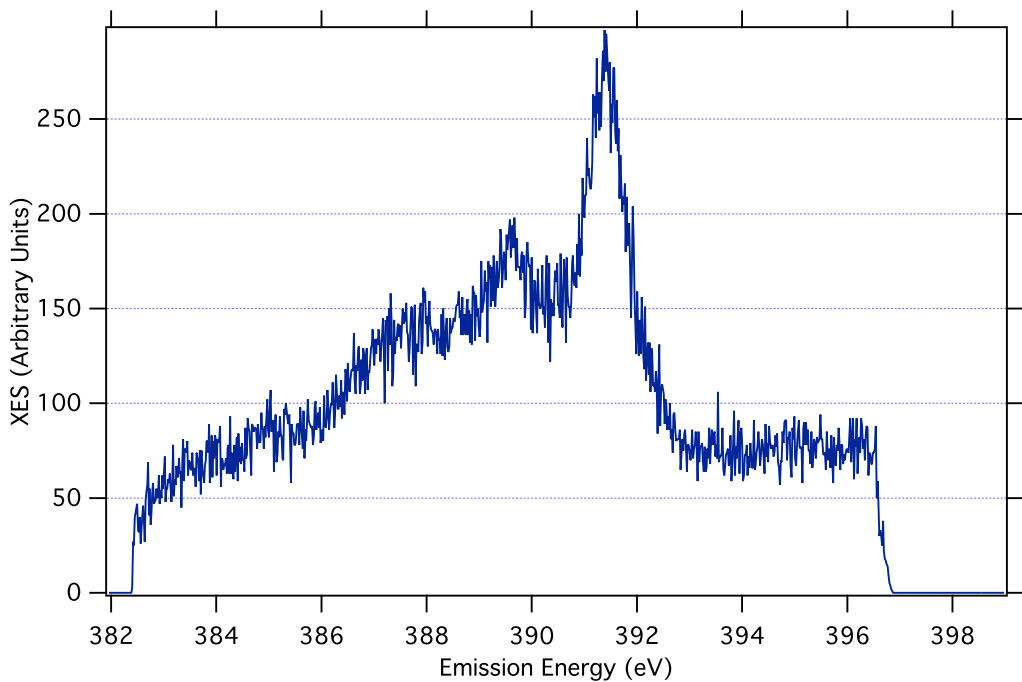


Figure 8.3: Nitrogen K α emission line of hexagonal boron nitride (hBN), taken using the HRMEG in third order. The low count rate requires long count times; however, temperature shifts in the room cause the central detector energy to shift over this time, reducing the resolution. Work is still ongoing to focus the spectrometer for operation with the HRMEG, as well as stabilize the room temperature. Total counts: 112973.

1. Can the surface roughness and oxide thickness be measured experimentally to confirm the fitting predictions?
2. How many parameters can be fit simultaneously? Which parameters have overlapping and which have orthogonal effects on the shape of the efficiency spectra?
3. Without any prior knowledge of the nominal groove shape, could we predict the exact groove profile?

Finally, we recognized in Chapter 7 that neither the Sinha nor Beckmann expressions provide a satisfactory description of surface roughness on gratings. Both assume that the scattering due to roughness is independent of the diffraction order. Additionally, the Beckmann expression is only valid near normal incidence, and the Sinha expression is only valid for roughness parameters much smaller than the wavelength. It would be desirable to continue searching for a rigorous and general method to incorporate roughness into the calculated diffraction efficiencies.

8.3 Future work: Efficiency calculation improvements and software-as-a-service

One of our secondary goals was to encourage beamline designers to consider the grating efficiency at design time. To support this goal, we would like to make grating calculation and optimization tools as complete and accessible as possible.

Within the existing software, we need to add the ability to compute TM efficiency.

Currently, we can optimize gratings using the solver to do single efficiency evaluations within a third-party or simple brute-force optimization tool. However, it would be helpful to integrate a global optimizer into the software itself. The optimizer should be able to accept an arbitrary set of grating parameters or ranges with constraints, and find the combination of parameters for maximum efficiency in the desired order. Since optimization is resource-intensive, it should be able to run in parallel on high-performance computing platforms.

Finally, to make all of these tools as accessible as possible, we would like to build a web application to replace the `Gradif` interface shown in Chapter 4. Instead of downloading,

compiling, reading the documentation, and running the command-line software, users would have instant access to calculation and optimization services through their web browser. By exploiting cloud computing resources such as Amazon's Elastic Cloud Compute (EC2) platform, results could be made available almost instantly, encouraging users to experiment and freely explore.

REFERENCES

- [1] J. Andrewartha, G. Derrick, and R. McPhedran. A general modal theory for reflection gratings. *Optica Acta: International Journal of Optics*, 28(11):1501–1516, 1981.
- [2] Y. Aoyagi and S. Namba. Blazed ion-etched holographic gratings. *Optica Acta: International Journal of Optics*, 23(9):701–707, 1976.
- [3] P. Beckmann and A. Spizzichino. *The Scattering of Electromagnetic Waves from Rough Surfaces*. The Artech House radar library. Artech House, 1987.
- [4] I. Botten, M. Craig, R. McPhedran, J. Adams, and J. Andrewartha. The dielectric lamellar diffraction grating. *Optica Acta: International Journal of Optics*, 28(3):413–428, 1981.
- [5] L. Botten, M. Craig, R. McPhedran, J. Adams, and J. Andrewartha. The finitely conducting lamellar diffraction grating. *Optica Acta: International Journal of Optics*, 28(8):1087–1102, 1981.
- [6] M. Bowler, P. Finetti, D. Holland, I. Humphrey, F. Quinn, and M. Roper. Theoretical and measured performance of diffraction gratings. *Nuclear Instruments and Methods in Physics Research Section A: Accelerators, Spectrometers, Detectors and Associated Equipment*, 467–468, Part 1(0):317 – 320, 2001. 7th Int. Conf. on Synchrotron Radiation Instrumentation.
- [7] L. Braicovich, J. van den Brink, V. Bisogni, M. M. Sala, L. J. P. Ament, N. B. Brookes, G. M. De Luca, M. Salluzzo, T. Schmitt, V. N. Strocov, and G. Ghiringhelli. Magnetic excitations and phase separation in the underdoped $\text{La}_{2-x}\text{Sr}_x\text{CuO}_4$ superconductor measured by resonant inelastic x-ray scattering. *Phys. Rev. Lett.*, 104:077002, Feb 2010.
- [8] C. B. Burckhardt. Diffraction of a plane wave at a sinusoidally stratified dielectric grating. *J. Opt. Soc. Am.*, 56(11):1502–1508, Nov 1966.
- [9] S. M. Butorin, J.-H. Guo, M. Magnuson, P. Kuiper, and J. Nordgren. Low-energy d - d excitations in MnO studied by resonant x-ray fluorescence spectroscopy. *Phys. Rev. B*, 54:4405–4408, Aug 1996.
- [10] G. D. Byrne and A. C. Hindmarsh. A polyalgorithm for the numerical solution of ordinary differential equations. *ACM Trans. Math. Softw.*, 1(1):71–96, Mar. 1975.
- [11] Center for X-Ray Optics. Calibration and standards beamline 6.3.2 at the ALS. Available at: <http://cxro.lbl.gov/als632/> (July 2012).

- [12] Center for X-Ray Optics. X-ray interactions with matter calculator. Available at: http://henke.lbl.gov/optical_constants/ (July 2012).
- [13] F. M. F. de Groot, J. C. Fuggle, B. T. Thole, and G. A. Sawatzky. *2p* x-ray absorption of *3d* transition-metal compounds: An atomic multiplet description including the crystal field. *Phys. Rev. B*, 42:5459–5468, Sep 1990.
- [14] T. M. Elfouhaily and C.-A. Guérin. A critical survey of approximate scattering wave theories from random rough surfaces. *Waves in Random Media*, 14(4):R1–R40, 2004.
- [15] R. Feynman. Nobel lecture: The development of the space-time view of quantum electrodynamics, December 1965. Available at: http://www.nobelprize.org/nobel_prizes/physics/laureates/1965/feynman-lecture.html.
- [16] G. Fowles. *Introduction to Modern Optics*. Dover Books on Physics Series. Dover Publications, 1989.
- [17] J. v. Fraunhofer. Kurzer bericht von den resultaten neuerer versuche über die gesetze des lichtes, und die theorie derselben (Short account of the results of new experiments on the laws of light, and their theory). *Annalen der Physik*, 74(8):337–378, 1823.
- [18] J. v. Fraunhofer, J. Ames, and W. Wollaston. *Prismatic and diffraction spectra*. Harper's scientific memoirs. Harper & brothers, 1898.
- [19] Gammadata. Soft x-ray emission spectrometer Scienta XES 350. Available at: http://www.vgscienta.com/_resources/File/XES350%20data%20sheet%20web.pdf (July 2012).
- [20] L. Goray. Numerical analysis of the efficiency of multilayer-coated gratings using integral method. *Nuclear Instruments and Methods in Physics Research Section A: Accelerators, Spectrometers, Detectors and Associated Equipment*, 536(1-2):211–221, 2005.
- [21] L. Goray and S. Y. Sadov. Numerical modelling of gratings in sensitive cases. *OSA Trends in Optics and Photonics Series*, 75 (Diffractive Optics and Micro-Optics):365, 2002.
- [22] L. I. Goray and J. F. Seely. Efficiencies of master, replica, and multilayer gratings for the soft-x-ray-extreme-ultraviolet range: Modeling based on the modified integral method and comparisons with measurements. *Appl. Opt.*, 41(7):1434–1445, Mar 2002.
- [23] B. Henke, E. Gullikson, and J. Davis. X-ray interactions: Photoabsorption, scattering, transmission, and reflection at $E = 50\text{--}30,000$ eV, $Z = 1\text{--}92$. *Atomic Data and Nuclear Data Tables*, 54(2):181 – 342, 1993.
- [24] P. J. and B. M.J. Diffraction par un reseau conducteur nouvelle methode de resolution. *Journal of Modern Optics*, 17(6):469–478, 1970.

- [25] J. J. Jia, T. A. Callcott, J. Yurkas, A. W. Ellis, F. J. Himpel, M. G. Samant, J. Stöhr, D. L. Ederer, J. A. Carlisle, E. A. Hudson, L. J. Terminello, D. K. Shuh, and R. C. C. Perera. First experimental results from IBM/TENN/TULANE/LLNL/LBL undulator beamline at the Advanced Light Source. *Review of Scientific Instruments*, 66(2):1394–1397, 1995.
- [26] G. Kirchhoff. Zur theorie der lichtstrahlen. *Annalen der Physik*, 254(4):663–695, 1883.
- [27] R. D. L. KRONIG. On the theory of dispersion of x-rays. *J. Opt. Soc. Am.*, 12(6):547–556, Jun 1926.
- [28] L. Li. Formulation and comparison of two recursive matrix algorithms for modeling layered diffraction gratings. *J. Opt. Soc. Am. A*, 13(5):1024–1035, May 1996.
- [29] L. Li. Use of Fourier series in the analysis of discontinuous periodic structures. *J. Opt. Soc. Am. A*, 13(9):1870–1876, Sep 1996.
- [30] S. Lindau. The groove profile formation of holographic gratings. *Optica Acta: International Journal of Optics*, 29(10):1371–1381, 1982.
- [31] E. Marx, T. A. Germer, T. V. Vorburger, and B. C. Park. Angular distribution of light scattered from a sinusoidal grating. *Appl. Opt.*, 39(25):4473–4485, Sep 2000.
- [32] D. Maystre. Sur la diffraction d'une onde plane par un reseau metallique de conductivite finie. *Optics Communications*, 6(1):50 – 54, 1972.
- [33] J. A. McLeod. EXAFS study of amorphous selenium. Master's thesis, University of Saskatchewan, April 2010.
- [34] M. G. Moharam and T. K. Gaylord. Rigorous coupled-wave analysis of planar-grating diffraction. *J. Opt. Soc. Am.*, 71(7):811–818, Jul 1981.
- [35] M. G. Moharam and T. K. Gaylord. Diffraction analysis of dielectric surface-relief gratings. *J. Opt. Soc. Am.*, 72(10):1385–1392, Oct 1982.
- [36] M. G. Moharam and T. K. Gaylord. Rigorous coupled-wave analysis of metallic surface-relief gratings. *J. Opt. Soc. Am. A*, 3(11):1780–1787, Nov 1986.
- [37] M. G. Moharam, D. A. Pommet, E. B. Grann, and T. K. Gaylord. Stable implementation of the rigorous coupled-wave analysis for surface-relief gratings: enhanced transmittance matrix approach. *J. Opt. Soc. Am. A*, 12(5):1077–1086, May 1995.
- [38] F. Montiel, M. Neviere, and P. Peyrot. Waveguide confinement of Cerenkov second-harmonic generation through a graded-index grating coupler: Electromagnetic optimization. *Journal of Modern Optics*, 45(10):2169–2186, 1998.
- [39] MPI Forum. MPI: A Message-Passing Interface Standard. Version 1.3, May 30 2008. Available at: <http://www.mpi-forum.org/docs/docs.html> (July 2012).

- [40] D. Muir. Design of a high performance soft X-Ray emission spectrometer for the REIXS beamline at the Canadian Light Source. Master's thesis, University of Saskatchewan, 2006.
- [41] M. Neviere and F. Montiel. Electromagnetic theory of multilayer gratings and zone plates. In R. B. Hoover and A. B. C. Walker, editors, *SPIE Proceedings (Multilayer and Grazing Incidence X-Ray/EUV Optics III)*, volume 2805, pages 176–183. SPIE, 1996.
- [42] M. Nevière and E. Popov. *Light propagation in periodic media: differential theory and design*. Optical engineering. Marcel Dekker, 2003.
- [43] M. Nevière, P. Vincent, and R. Petit. Theory of conducting gratings and their applications to optics. *Nouvelle Revue d'Optique*, 5(2):65, 1974.
- [44] Névet, L. and Croce, P. Caractérisation des surfaces par réflexion rasante de rayons x. application à l'étude du polissage de quelques verres silicates. *Rev. Phys. Appl. (Paris)*, 15(3):761–779, 1980.
- [45] Ocean Optics Inc. USB4000-UV-VIS Miniature Fiber Optic Spectrometer. Available at: <http://www.oceanoptics.com/Products/usb4000uvvis.asp> (July 2012).
- [46] OpenMP Architecture Review Board. OpenMP application program interface version 3.0, May 2008. Available at: <http://www.openmp.org/mp-documents/spec30.pdf> (July 2012).
- [47] C. Palmer and E. Loewen, editors. *Diffraction Grating Handbook*. Newport Corporation, sixth edition, 2005. Also available online at: <http://gratings.newport.com/library/handbook/handbook.asp> (July 2012).
- [48] W. Peatman. *Gratings, mirrors, and slits: beamline design for soft X-ray synchrotron radiation sources*. Gordon and Breach Science Publishers, 1997.
- [49] H. Petersen, C. Jung, C. Hellwig, W. B. Peatman, and W. Gudat. Review of plane grating focusing for soft x-ray monochromators. *Review of Scientific Instruments*, 66(1):1–14, 1995.
- [50] R. Petit. Contribution à l'étude de la diffraction par un réseau métallique. *Rev. Opt.*, 45:249–276, 1966.
- [51] R. Petit and L. Botten. *Electromagnetic theory of gratings*. Topics in current physics. Springer-Verlag, 1980.
- [52] R. Petit and M. Cadilhac. Electromagnetic theory of gratings: some advances and some comments on the use of the operator formalism. *J. Opt. Soc. Am. A*, 7(9):1666–1674, Sep 1990.
- [53] A. Pietzsch, Y.-P. Sun, F. Hennies, Z. Rinkevicius, H. O. Karlsson, T. Schmitt, N. Strocov, V. J. Andersson, B. Kennedy, J. Schlappa, A. Föhlisch, J.-E. Rubensson, and F. Gel'mukhanov. Spatial quantum beats in vibrational resonant inelastic soft x-ray scattering at dissociating states in oxygen. *Phys. Rev. Lett.*, 106:153004, Apr 2011.

- [54] A. Pomp. The integral method for coated gratings: Computational cost. *Journal of Modern Optics*, 38(1):109–120, 1991.
- [55] E. Popov, B. Chernov, M. Nevière, and N. Bonod. Differential theory: application to highly conducting gratings. *J. Opt. Soc. Am. A*, 21(2):199–206, Feb 2004.
- [56] E. Popov and M. Nevière. Grating theory: new equations in Fourier space leading to fast converging results for TM polarization. *J. Opt. Soc. Am. A*, 17(10):1773–1784, Oct 2000.
- [57] E. Popov and M. Nevière. Maxwell equations in Fourier space: fast-converging formulation for diffraction by arbitrary shaped, periodic, anisotropic media. *J. Opt. Soc. Am. A*, 18(11):2886–2894, Nov 2001.
- [58] E. Popov, M. Nevière, B. Gralak, and G. Tayeb. Staircase approximation validity for arbitrary-shaped gratings. *J. Opt. Soc. Am. A*, 19(1):33–42, Jan 2002.
- [59] H. Ragheb and E. R. Hancock. The modified Beckmann-Kirchhoff scattering theory for rough surface analysis. *Pattern Recognition*, 40(7):2004 – 2020, 2007.
- [60] J. Rayleigh. *The theory of sound*. Number 2 in The Theory of Sound. Macmillan, 1896.
- [61] L. Rayleigh. On the dynamical theory of gratings. *Proceedings of the Royal Society of London. Series A, Containing Papers of a Mathematical and Physical Character*, 79(532):399–416, 1907.
- [62] S. O. Rice. Reflection of electromagnetic waves from slightly rough surfaces. *Communications on Pure and Applied Mathematics*, 4(2-3):351–378, 1951.
- [63] Richardson Gratings Laboratory. Technical note 9: Scattered light, stray light, and diffraction gratings. Available at: <http://gratings.newport.com/information/technotes/technote9.asp/> (July 2012).
- [64] H. Rowland. *The physical papers of Henry Augustus Rowland*. The Johns Hopkins Press, Baltimore, 1902. Also available online at: <http://archive.org/details/physicalpaper00rowlrich> (July 2012).
- [65] T. T. S. T. Peng and H. L. Bertoni. Theory of periodic dielectric waveguides. *IEEE Trans. Microwave Theory and Techn.*, MTT-23:123–123, 1975.
- [66] F. Schäfers. The BESSY raytrace program RAY, 2007. Available at: http://www.helmholtz-berlin.de/media/media/grossgeraete/optische_syst/publications/2008/paper_schaefers_ray_springer_2007.pdf (July 2012).
- [67] D. Schwartz. X-ray optics, August 2002. Available at: http://www2.astro.psu.edu/~niel/astro485/xrayschool/schwartz-xray_optics.pdf (July 2012).

- [68] J. F. Seely, Y. A. Uspenskii, Y. P. Pershin, V. V. Kondratenko, and A. V. Vinogradov. Skylab 3600 groove /mm replica grating with a scandium-silicon multilayer coating and high normal-incidence efficiency at 38-nm wavelength. *Appl. Opt.*, 41(10):1846–1851, Apr 2002.
- [69] M. R. Sharpe and D. Irish. Stray light in diffraction grating monochromators. *Optica Acta: International Journal of Optics*, 25(9):861–893, 1978.
- [70] N. K. Sheridan. Production of blazed holograms. *Applied Physics Letters*, 12(9):316–318, May 1968.
- [71] S. K. Sinha, E. B. Sirota, S. Garoff, and H. B. Stanley. X-ray and neutron scattering from rough surfaces. *Phys. Rev. B*, 38:2297–2311, Aug 1988.
- [72] J. E. Stewart and W. S. Gallaway. Diffraction anomalies in grating spectrophotometers. *Appl. Opt.*, 1(4):421–429, Jul 1962.
- [73] A. C. Thompson and D. Vaughan, editors. *X-ray Data Booklet*. Lawrence Berkeley National Laboratory, University of California, second edition, Jan. 2001. Also available online at: <http://xdb.lbl.gov> (July 2012).
- [74] J. H. Underwood, E. M. Gullikson, M. Koike, P. J. Batson, P. E. Denham, K. D. Franck, R. E. Tackaberry, and W. F. Steele. Calibration and standards beamline 6.3.2 at the advanced light source. *Review of Scientific Instruments*, 67(9):3372, sep 1996.
- [75] S. Weart. *Selected papers of great American physicists: the bicentennial commemorative volume of The American Physical Society 1976*. American Institute of Physics, 1976. Also available online at: <http://www.aip.org/history/gap/Rowland/Rowland.html> (July 2012).
- [76] A. Wirgin. Selected papers from the URSI symposium. *Alta. Freq.*, 38:327–338, 1969.
- [77] R. W. Wood. On a remarkable case of uneven distribution of light in a diffraction grating spectrum. *Proceedings of the Physical Society of London*, 18(1):269, 1902.
- [78] P. Zeeman. On the influence of magnetism on the nature of the light emitted by a substance. *Astrophysical Journal*, 5:332, 1897.